

## **INFORMATION TO USERS**

This manuscript has been reproduced from the microfilm master. UMI films the text directly from the original or copy submitted. Thus, some thesis and dissertation copies are in typewriter face, while others may be from any type of computer printer.

The quality of this reproduction is dependent upon the quality of the copy submitted. Broken or indistinct print, colored or poor quality illustrations and photographs, print bleedthrough, substandard margins, and improper alignment can adversely affect reproduction.

In the unlikely event that the author did not send UMI a complete manuscript and there are missing pages, these will be noted. Also, if unauthorized copyright material had to be removed, a note will indicate the deletion.

Oversize materials (e.g., maps, drawings, charts) are reproduced by sectioning the original, beginning at the upper left-hand corner and continuing from left to right in equal sections with small overlaps. Each original is also photographed in one exposure and is included in reduced form at the back of the book.

Photographs included in the original manuscript have been reproduced xerographically in this copy. Higher quality 6" x 9" black and white photographic prints are available for any photographs or illustrations appearing in this copy for an additional charge. Contact UMI directly to order.

**UMI**

A Bell & Howell Information Company  
300 North Zeeb Road, Ann Arbor, MI 48106-1346 USA  
313/761-4700 800/521-0600



NORTHWESTERN UNIVERSITY

THE FORMATION, TRANSPORT PROPERTIES AND  
MICROSTRUCTURE OF 45° [001] TILT GRAIN BOUNDARIES IN  
YBa<sub>2</sub>Cu<sub>3</sub>O<sub>7-x</sub> THIN FILMS

A DISSERTATION

SUBMITTED TO THE GRADUATE SCHOOL  
IN PARTIAL FULFILLMENT OF THE REQUIREMENTS

for the degree  
DOCTOR OF PHILOSOPHY

Field of Materials Science and Engineering

By

Boris Vukan Vuchic, B. V.,

, Ph.D.,

EVANSTON, ILLINOIS  
December 1995

**UMI Number: 9614858**

**Copyright 1995 by  
Vuchic, Boris Vukan**

**All rights reserved.**

---

**UMI Microform 9614858  
Copyright 1996, by UMI Company. All rights reserved.**

**This microform edition is protected against unauthorized  
copying under Title 17, United States Code.**

---

**UMI**  
300 North Zeeb Road  
Ann Arbor, MI 48103

© Copyright by Boris Vukan Vuchic 1995  
All Rights Reserved

# **Abstract**

**The Formation, Transport Properties and  
Microstructure of 45° [001] Tilt Grain Boundaries in  
YBa<sub>2</sub>Cu<sub>3</sub>O<sub>7-x</sub> Thin Films**

Boris V. Vuchic

Most high angle grain boundaries in high-T<sub>c</sub> superconductors exhibit weak link behavior. The Josephson-like properties of these grain boundaries can be used for many device applications such as superconducting quantum interference devices (SQUIDs). The structure-property relationship of different types of 45° [001] YBa<sub>2</sub>Cu<sub>3</sub>O<sub>7-x</sub> thin film grain boundary junctions are examined to study their weak link nature.

A technique, termed sputter-induced epitaxy, is developed to form 45° [001] tilt grain boundaries in YBa<sub>2</sub>Cu<sub>3</sub>O<sub>7-x</sub> thin films on (100) MgO substrates. A low voltage ion bombardment pre-growth substrate treatment is used to modify the epitaxial orientation relationship between the thin film and the substrate in selected regions. By modifying the orientation of the thin film, grain boundary junctions can be placed in any configuration on the substrate. A variety of pre-growth sputtering conditions in conjunction with atomic force microscopy and Rutherford backscatter spectrometry are used to determine the role of the ions in modifying the substrate surface. Sputter-induced epitaxy is

extended to a multilayer MgO/LaAlO<sub>3</sub> substrate , allowing integration of the sputter-induced epitaxy junctions into multilayer structures.

The low temperature transport properties of the sputter-induced epitaxy junctions and a set of bi-epitaxial grain boundaries are studied. Individual grain boundaries are isolated and characterized for resistance vs. temperature, current vs. voltage as a function of temperature and magnetic field behavior. Resistive and superconducting grain boundaries are compared. Microstructural analysis is performed using scanning electron microscopy, transmission electron microscopy and high resolution electron microscopy (HREM). Marked differences are observed in the microstructure of resistive and superconducting grain boundaries. HREM studies suggest the importance of the local atomic scale structure of the grain boundary in transport properties. A phenomenological grain boundary model is proposed to describe the structure-property relationship of the boundaries.



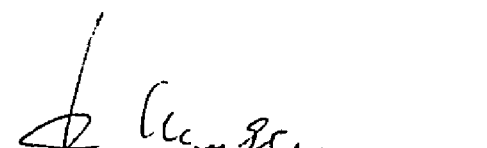
Professor Laurence D. Marks

Thesis Co-Advisor

Dept. of Materials Science and Engineering

Northwestern University

Evanston, Illinois



Dr. Karl L. Merkle

Thesis Co-Advisor

Materials Science Division

Argonne National Laboratory

Argonne, Illinois

## **Dedication**

To my wife, Sandra Lee Mathews

## Acknowledgments

There are many people to whom I owe a deep gratitude for making my experience as a graduate student truly exceptional. First, I would like to express my thanks to my thesis advisors. Both Professor Laurie Marks and Dr. Karl Merkle provided me with the support and encouragement needed during the course of this research. I have been extremely fortunate to work with and learn from these two outstanding scientists. Much of the work within this thesis would not have been possible without high quality thin films. I would like to thank Professor R.P.H. Chang and his group at Northwestern University, and in particular Ken Dean, Bruce Buchholz and Dr. Steve Duray for providing excellent thin films. I would like to acknowledge Dr. Yun Yu Wang and Professor Vinayak Dravid for assistance with the PEELS measurements and discussion of the results. I am also grateful to Dr. Hong Zhang for assistance with the HREM multislice calculations. I would also like to acknowledge Peter Baldo at Argonne National Lab for performing the Rutherford Backscattering measurements.

There were many people at both Northwestern University and Argonne National Laboratory who helped make research enjoyable. At Northwestern they included Ganesh, Kevin, Howard, Manolo, Tony, Gretchen, Tracey, Ravi, Brad, Greg, Jon, Doug S., Frank and Ken. I would like to thank the Interface Studies group and other Argonne staff past and present, Mary, Yufei, Steve, Russ, Dean, David, Chris, Tim, Jeff F., Roseann, Chuck, John and Jules.

I am especially indebted to all the members of Nevin's F.C. who provided an outlet when necessary. I would also like to thank my family and friends who were always encouraging.

Most of all I would like to thank my wife, Sandy. Her constant support, patience and understanding will always be remembered.

This work was supported by the U.S. Department of Energy, Office of Basic Energy Sciences-Materials Science under contract W-31-109-Eng-38, the National Science Foundation Office of Science and Technology Centers under contract DMR 91-20000 and the Argonne Division of Educational Programs.

# Table of Contents

Abstract.....	iii
Acknowledgments .....	vi
Table of Contents.....	viii
List of Tables .....	xi
List of Figures .....	xii
Chapter I. Introduction.....	1
Chapter II. Background and Literature Survey .....	7
II.1. High-Temperature Superconductivity .....	7
II.1.1. YBa <sub>2</sub> Cu <sub>3</sub> O <sub>7-x</sub> Structure.....	8
II.1.2. YBa <sub>2</sub> Cu <sub>3</sub> O <sub>7-x</sub> Properties .....	15
II.2. YBa <sub>2</sub> Cu <sub>3</sub> O <sub>7-x</sub> Thin Films .....	24
II.2.1. Epitaxy .....	24
II.2.2. Ion Beam Modification .....	27
II.2.3. Substrates.....	30
II.2.4. Thin Film Growth.....	31
II.2.4.1. Thin Film Growth Techniques.....	35
II.2.4.2. Thin Film Characterization .....	38
II.3. High-Tc Grain Boundaries .....	39
II.3.1. Misorientation Angle .....	42
II.3.2. Grain Boundary Structure .....	47
II.3.3. Grain Boundary Chemistry .....	50
II.3.4. Direct Transport Properties .....	55
II.3.4.1. Resistive Transition .....	55
II.3.4.2. Current-Voltage Characteristics .....	56
II.3.4.3. Magnetic Field Properties .....	58
II.3.5. Grain Boundary Models .....	61
II.4. YBa <sub>2</sub> Cu <sub>3</sub> O <sub>7-x</sub> Junctions.....	64
Chapter III. Experimental Procedure .....	70
III.1. Equipment .....	70
III.1.1. Low Voltage Ion Mill .....	70
III.1.2. Electron Backscatter Detector.....	75
III.1.3. Cryogenic Transport Measurement System.....	77
III.2. Experimental Method .....	87
III.2.1. Grain Boundary Formation .....	88
III.2.2. Thin Film Growth .....	93
III.2.3. Grain Boundary Isolation.....	94
III.2.4. Low Temperature Transport Measurements .....	100
III.2.5. Grain boundary TEM Sample Preparation .....	103
III.2.6. Electron Microscopy .....	107
Chapter IV. Sputter-Induced Epitaxy .....	109
IV.1. Formation of Sputter Induced Epitaxy Grain Boundaries .....	109

IV.1.2. Thin Film Junctions on MgO .....	109
IV.1.2. Sputter Induced Epitaxy Junctions .....	111
IV.1.2.1. Pre-growth Sputter Conditions.....	117
IV.1.2.1.1. Masking Techniques .....	117
IV.1.2.1.2. Sputtering Conditions .....	121
IV.1.3. Rutherford Backscattering Spectrometry .....	126
IV.1.3.1. Background .....	126
IV.1.3.2. RBS on Pre-Sputtered Substrates .....	127
IV.1.3.2.1. Standard Pre-Sputter Conditions .....	127
IV.1.3.2.2. Modified Pre-Sputter Conditions .....	131
IV.1.3. Surface Profile.....	139
IV.2. Transport Properties .....	147
IV.2.1. Resistance-Temperature .....	147
IV.2.1.1. TAPS and Thermally Activated Conduction Paths .....	157
IV.2.2. Current-Voltage Characteristics .....	160
IV.2.3. Magnetic Field Behavior .....	172
IV.3. Microstructure .....	179
IV.3.1. Scanning electron microscopy.....	179
IV.3.2. Transmission Electron Microscopy .....	184
IV.3.3. Parallel Electron Energy Loss Spectroscopy .....	211
IV.4. Conclusions .....	216
V. Multilayer Sputter-Induced Epitaxy .....	219
V.1. Grain Boundary Formation.....	219
V.1.1. Sputter Induced Epitaxy Conditions .....	220
V.1.2. Surface Morphology .....	222
V.2. Transport Properties .....	228
V.2.1. Resistance-Temperature .....	228
V.2.2. Current-Voltage.....	231
V.2.3. Magnetic Field Behavior.....	236
V.3. Conclusions .....	240
VI. Bi-Epitaxial Grain Boundary Junctions.....	242
VI.1. Thin Film Growth .....	242
VI.2. Transport Properties .....	249
VI.2.1. Resistance-Temperature Characteristics.....	249
VI.2.2. Current-Voltage Characteristics .....	257
VI.2.3. Magnetic Field Behavior .....	262
VI.2.4. Noise Measurements .....	268
VI.3. Microstructure .....	270
VI.3.1. Transmission Electron Microscopy .....	270
VI.3.2. High Resolution Electron Microscopy .....	285
VI.4. Structure - Property Relations .....	292
VII. Grain Boundary Model .....	294

VII.1	Asymmetric Parallel Junction Model.....	294
VII.2.	Transport Properties .....	305
	VII.2.1. Resistance-Temperature .....	305
	VII.1.2. Current-Voltage .....	306
	VII.1.3. Magnetic Field.....	307
VII.2.	Microstructure.....	310
VII.3.	Structure-Property Relationship .....	312
VIII.	Conclusions and Future Work .....	314
Appendix I. Structure-Property Relationship in $\text{YBa}_2\text{Cu}_3\text{O}_{7-x}$ Thin Film Grain Boundaries: A Grain Boundary Model .....		321
	References.....	357

## List of Tables

Table		Page
Table 2.1.	The crystal structure and transition temperature of several high-T <sub>C</sub> superconductors (from Shaked <i>et al.</i> 1994).	9
Table 2.2.	The atomic positions and site occupancies for both the orthorhombic and tetragonal phases of YBCO (Jorgensen <i>et al.</i> 1987).	14
Table 2.3.	Various substrates used for YBCO thin film growth and accompanying materials properties (Giess <i>et al.</i> 1990; Hollmann <i>et al.</i> 1994).	32
Table 2.4.	Comparison of low-T <sub>C</sub> and high-T <sub>C</sub> transition temperatures, penetration depths and coherence lengths (from Russek 1990).	40
Table 4.1.	Results of YBCO thin film growth for different pre-sputter conditions.	123
Table 4.2.	Different substrates attempted for sputter-induced epitaxy.	125
Table 4.3.	RBS data for pre-sputtered MgO substrates under different conditions. Ar and W counts are the integrated counts over the entire peak after a modeled background is removed.	132
Table 4.4.	RBS results for a series of incident angles. Ar and W counts as a percentage of the counts at 90°.	133
Table 7.1.	Synopsis of transport data for three representative types of grain boundary junctions.	309

## List of Figures

Figure		Page
Figure 2.1.	Schematic diagram of the $\text{YBa}_2\text{Cu}_3\text{O}_{7-x}$ unit cell structure.	11
Figure 2.2.	Variation in critical temperature and copper valence as a function of oxygen stoichiometry (from Marezio <i>et al.</i> 1991).	12
Figure 2.3a.	The d.c. Josephson effect shown by the normalized critical current vs. applied magnetic field for a uniform critical current density distribution (from Van Duzer 1981).	20
Figure 2.3b.	A schematic of Josephson current flow across a Josephson junction as a function of applied magnetic field (from Van Duzer 1981).	20
Figure 2.3c.	The variation of the Josephson tunneling current for an in-line junction with normalized lengths of ( $L/\text{Josephson penetration depth} = 2, 5 \text{ and } 15$ ) (from Van Duzer 1981).	21
Figure 2.3d.	A diagram of a resistively shunted junction. The junction is modeled with a capacitive element, a resistor and a Josephson junction in a parallel circuit (from Van Duzer 1981).	21
Figure 2.4.	Basic thin film growth modes.	26
Figure 2.5a.	Incident ion interactions with a target (from Chapman 1980).	28
Figure 2.5b.	Atom/ion yield ratio ( $S$ ) as a function of angle of incidence (from Chapman 1980).	28
Figure 2.6a-c.	The formation of a screw dislocation during growth around a substrate defect (from Mannhart 1993).	34

Figure 2.6d.	Thin film growth via step flow mechanism, propagating the screw dislocation through the film (from Mannhart 1993).	34
Figure 2.7.	Schematic drawing of pulsed organo-metallic beam epitaxy (POMBE) thin film growth system.	37
Figure 2.8a.	The normalized critical current density as a function of misorientation angle for [001] tilt grain boundaries (from Dimos <i>et al.</i> 1990).	45
Figure 2.8b.	The normalized critical current density as a function of total misorientation angle in bicrystal grain boundaries (from Dimos <i>et al.</i> 1990).	45
Figure 2.9.	The critical current density as a function of misorientation angle in asymmetric bicrystal grain boundaries (from Ivanov <i>et al.</i> 1991a).	46
Figure 2.10.	Histogram of grain boundary misorientations in polycrystalline thin films on MgO (from Shin <i>et al.</i> 1989).	49
Figure 2.11a.	Normalized oxygen pre-edge intensity as a function of oxygen content (from Browning <i>et al.</i> 1993).	53
Figure 2.11b.	Normalized oxygen pre-edge intensity across an asymmetric and symmetric grain boundary. The asymmetric grain boundary is represented by the circles (from Browning <i>et al.</i> 1993).	53
Figure 2.12a.	Bicrystal and bi-epitaxial grain boundary junctions.	66
Figure 2.12b.	Step-edge and sputter-induced epitaxy grain boundary junctions.	67
Figure 3.1.	Low-voltage ion mill chamber schematic.	72
Figure 3.2.	Low-voltage ion mill sample stage.	73
Figure 3.3.	Schematic diagram of the formation and imaging of backscattered electron Kikuchi patterns in the SEM.	76

<b>Figure 3.4.</b>	Schematic diagram of helium flow cryostat (from Jirmanus 1990).	78
<b>Figure 3.5.</b>	Sample stub for cryogenic transport measurements.	80
<b>Figure 3.6.</b>	Schematic drawing of low-temperature measurement system. Note: all electrical equipment is attached to common ground.	81
<b>Figure 3.7.</b>	A schematic representation of the four-probe measurement across the microbridge. Voltage drop measurements are taken across the various channels. The grain boundary can be located across any part of the microbridge.	82
<b>Figure 3.8.</b>	Hysteretic voltage-current characteristics of sample exhibiting thermal heating.	83
<b>Figure 3.9.</b>	Sputter-induced epitaxy $45^\circ$ [001] tilt grain boundary junction.	89
<b>Figure 3.10.</b>	Bi-epitaxial substrate forming [001] $45^\circ$ tilt grain boundary junction.	92
<b>Figure 3.11.</b>	An optical micrograph of a patterned microbridge with $100\ \mu\text{m}$ spaced parallel bi-epitaxial grain boundary junctions.	95
<b>Figure 3.12.</b>	Secondary electron image of a $40\ \mu\text{m}$ wide microbridge patterned into a YBCO thin film on MgO.	96
<b>Figure 3.13.</b>	Mask design for silver evaporation of contact pads.	98
<b>Figure 3.14.</b>	An optical micrograph of a patterned YBCO thin film with evaporated silver contact pads (substrate diameter is 3 mm).	99
<b>Figure 3.15.</b>	Secondary electron micrograph of patterned microbridge on a YBCO thin film with 10 gold wire leads attached.	102

- Figure 3.16. An optical micrograph of a TEM sample using monochromatic sodium light. The thickness fringes are due to interference contrast from the top and bottom sample surfaces. The microbridge width is 40  $\mu\text{m}$ . 105
- Figure 3.17. An optical micrograph, using monochromatic light, showing perforation of a TEM sample at the microbridge. The microbridge width is 40  $\mu\text{m}$ . 106
- Figure 4.1a. Pre-growth sputter treatment for sputter-induced epitaxy samples. 112
- Figure 4.1b. Schematic of YBCO thin film orientation after deposition. 112
- Figure 4.1c. Directional ion beam etching forms a narrow region of modified epitaxy due to contamination from redeposition of the photoresist mask. 113
- Figure 4.1d. Schematic diagram of focused ion beam technique that uses medium energy gallium ions to create a narrow damaged region in the substrate. The YBCO film is subsequently either polycrystalline in the region or contaminated with diffused gallium. 114
- Figure 4.2a. A secondary electron micrograph of a sputter-induced epitaxy grain boundary junction with a polycrystalline "interface" region. 119
- Figure 4.2b. An optical image of a high quality sputter-induced grain boundary junction. The junction is centered in the 3 mm diameter disk and is barely discernible. 120
- Figure 4.3a. RBS spectrum for a MgO substrate irradiated for 3 minutes with 250 eV ions and a beam current density of 1 mA/cm<sup>2</sup>. 128
- Figure 4.3b. Magnified image of high energy loss regime from inset in figure 4.3a. 128

- Figure 4.4.** Experimental and calculated RBS spectra. The 129 simulation of the RBS spectrum is done using 1 monolayer of argon and 0.1 monolayer of tungsten in the top 10 Å of the substrate. 130
- Figure. 4.5.** TRIM calculation of argon and tungsten ion penetration 136 into a MgO substrate. 137
- Figure 4.6a.** Integrated counts of argon and tungsten as a function of 136 irradiation time. 138
- Figure 4.6b.** Normalized counts of argon and tungsten as a function 137 of angle of incidence. Counts are normalized to values for 90° incidence. 139
- Figure 4.6c.** RBS spectra from varying ion incidence angles. 140
- Figure 4.7a.** AFM image of an unspattered region on a (100) MgO 141 substrate prior to annealing. 142
- Figure 4.7b.** AFM image of a pre-sputtered substrate (300 eV argon 142 for 3 minutes) prior to annealing. 143
- Figure 4.8a.** AFM image of the edge delineating the pre-sputtered 143 and unspattered regions of the substrate after an oxygen plasma anneal. 144
- Figure 4.8b.** Line scans of step region in figure 4.8a. showing 144 roughness values for the unspattered region (top scan) and sputtered region (bottom scan). The middle scan shows the step edge height. 145
- Figure 4.8c.** AFM image of unspattered region after anneal in an 145 oxygenated plasma. 146
- Figure 4.8d.** AFM image of a pre-sputtered region (300 eV argon 146 ions for 3 minutes) after anneal in fully oxygenated plasma. 147
- Figure 4.9.** Resistance vs. temperature curve for a polycrystalline 148 grain boundary region. 149

Figure 4.10a.	Resistance vs. temperature characteristics for a grain boundary junction formed with a metal mask.	151
Figure 4.10b.	Resistance vs. temperature for sample in figure 4.10a.	152
Figure 4.10c.	Magnified foot-like structure from (b.), with calculated fit to a set of parallel thermally activated transport passages.	152
Figure 4.11a.	Resistance vs. temperature for photoresist masked sample.	153
Figure 4.11b.	Magnified foot region for resistance vs. temperature.	153
Figure 4.11c.	R-T log plot demonstrating the grain boundary resistance is above the noise level of the measuring instruments.	154
Figure 4.12a.	Schematic diagram of a polycrystalline region showing a percolative current path. The path of least resistance crosses grain boundaries with different transition temperatures as indicated. All of the regions along the path must be superconducting before a continuous path across the polycrystalline area is fully superconducting.	155
Figure 4.12b.	Schematic diagram of a single grain boundary region. The first region that has a detectable transition will provide a continuous superconducting path across the grain boundary.	155
Figure 4.13a.	I-V curve for a polycrystalline grain boundary region at T=35 K.	161
Figure 4.13b.	I-V curves for a polycrystalline grain boundary region at different temperatures.	161
Figure 4.14a.	I-V characteristic for sputter-induced grain boundary junction with RSJ model fit ( $\beta_C=0$ ).	162
Figure 4.14b.	I-V characteristics for temperatures from 10 K to 70 K for a sputter-induced grain boundary junction.	162

- Figure 4.15. I-V characteristics and RSJ fit for sputter-induced grain boundary junction at 4.2 K. 163
- Figure 4.16a-c. I-V characteristics for (a). T=10 K, (b). T=20 K and (c). 166 T=30 K.
- Figure 4.16d-f. I-V characteristics for a grain boundary at (d). T=70 K, 167 (e). T=77 K and (f). T=80 K.
- Figure 4.17. I-V characteristics at 4.2 K, 20 K, 30 K, 40 K, 50 K, 60 K, 168 70 K, 77 K, and 80 K showing transition from RSJ type behavior to flux-flow behavior.
- Figure 4.18. Critical current as a function of temperature. The calculated curve follows  $I=I_C(1-T/T_C)^2$ . 169
- Figure 4.18b. Critical current as a function of temperature for a different grain boundary than figure 4.18a. 170
- Figure 4.19. Grain boundary normal state resistance as a function of temperature. 171
- Figure 4.20. Low magnetic field behavior of a sputter-induced epitaxy grain boundary junction. 175
- Figure 4.21. Low magnetic field behavior for a sputter-induced grain boundary junction. 176
- Figure 4.22. Patterson function of magnetic field data from figure 4.20. 177
- Figure 4.23. A SEM image of a sputter-induced epitaxy grain boundary junction. The insets are the corresponding backscattered electron Kikuchi patterns for the grains indicating a 45° rotation about the [001] axis. 181
- Figure 4.24a. Bright field TEM image of a sputter-induced grain boundary junction. The grain boundary (indicated by the arrows) meanders significantly. 186

- Figure 4.24b. Corresponding dark field TEM image to figure 4.24a. 188  
The image highlights how much boundary meanders  
(the arrows are the same locations in the boundary as in  
figure 4.24a).
- Figure 4.25. Diffraction pattern of a polycrystalline "interface" 189  
region observed in samples made with a poorly  
contacting metal mask.
- Figure 4.26a. TEM image of a sputter-induced grain boundary with a 190  
 $\text{Y}_2\text{O}_3$  particle at the boundary. The boundary is  
asymmetrically faceted.
- Figure 4.27a. An image of a 100 nm long asymmetric facet at the 193  
grain boundary. The (100) planes of the left grains are  
parallel to the (110) planes of the adjacent grain.
- Figure 4.27b. Asymmetric facets along a length of a sputter-induced 195  
epitaxy grain boundary.
- Figure 4.28a. A region of a grain boundary that curves 90°, but 198  
maintains the asymmetric facets along the entire length.  
The region indicated by the arrow is magnified in figure  
4.28b.
- Figure 4.28b. Magnified region of the grain boundary in figure 4.28a. 200  
The boundary is stepped with asymmetric microfacets  
maintaining the local asymmetry. The "step" regions  
have reversed symmetry of the "ledge" regions.
- Figure 4.29. Two asymmetrically faceted regions of the grain 202  
boundary connected by an unfaceted region.
- Figure 4.30a. A HREM image of an asymmetric facet. There is a 204  
small step in the boundary accommodated by a reversal  
in symmetry.
- Figure 4.30b. A 40 nm long asymmetric facet along a grain boundary. 206  
The boundary maintains the grain structure to within  
one plane of the grain boundary plane.

Figure 4.31.	HREM through focus simulation set from 0 defocus in -100 Å steps (upper right to lower left going down the columns). The thickness is 114 Å.	208
Figure 4.32a.	HREM image and image simulation of a sputter-induced epitaxy grain boundary. The simulation is at -400 Å defocus and a sample thickness of 114 Å.	209
Figure 4.32b.	HREM image and simulation of grain boundary junction. The simulation is for a defocus of -700 Å and a sample thickness of 114 Å.	210
Figure 4.33a.	PEELS spectrum of a grain region in the sample with the two gaussian fit.	213
Figure 4.33b.	PEELS spectrum of a grain boundary region in the sample with the two gaussian fit.	213
Figure 4.34.	Seven spectra from along the grain boundary.	214
Figure 4.35.	Normalized pre-edge intensity along the grain boundary in 2 nm steps.	215
Figure 5.1a-b.	Schematic diagram of the multilayer sputter-induced epitaxy process.	221
Figure 5.2.	An SEM image of a multilayer sputter-induced epitaxy grain boundary junction. The grain boundary lies between the two arrows. The corresponding backscattered electron Kikuchi patterns (insets) show a 45° rotation about the [001] axis. The sample is inclined relative to the beam to maximize grain boundary contrast.	225
Figure 5.3.	An SEM image of a 5 µm wide strip of rotated grain forming two parallel junctions. The sample is inclined relative to the beam so the micron marker is only valid in the direction along the boundary.	227
Figure 5.4a.	Resistance vs. temperature for a grain and grain boundary in a multilayer sputter-induced junction sample. Measuring current is 0.5 µA.	229

Figure 5.4b.	Transition region of R-T curve showing the foot-like structure of grain boundary and sharp transition for grain.	229
Figure 5.5a.	Resistance vs. temperature curve for multilayer sputter-induced grain boundary junction using a 1 $\mu$ A measuring current.	230
Figure 5.5b.	R-T curve showing extended foot-like structure of grain boundary transition due to a larger measuring current (1 $\mu$ A).	230
Figure 5.6a.	I-V characteristics of multilayer sputter-induced grain boundary junction at 5 K.	232
Figure 5.6b.	I-V characteristics of grain boundary junction at 40 K. A RSJ model fit is shown using $\beta_c=0$ .	232
Figure 5.6c.	I-V characteristics of grain boundary junction at 60 K.	233
Figure 5.7.	I-V characteristics of grain boundary and grain at 10 K, 40 K, and 60	233
Figure 5.8a.	Critical current dependence on temperature for a multilayer sputter-induced grain boundary junction.	234
Figure 5.8b.	Normal state resistance vs. temperature for a multi-layer sputter-induced grain boundary junction.	235
Figure 5.9.	Voltage vs. applied magnetic field for a multilayer sputter-induced grain boundary junction. The applied current bias is 0.2 mA.	237
Figure 5.10.	Voltage vs. applied magnetic field for field applied parallel to the grain boundary and the thin film surface.	238
Figure 5.11.	Patterson function of magnetic field data in figure 5.9. The pattern exhibits a Moire interference between two frequencies.	239

- Figure 6.1a. SEM image of two parallel bi-epitaxial grain boundaries 245  
100  $\mu\text{m}$  apart. The inset backscattered electron Kikuchi  
patterns confirm the 45° rotation about [001]. The  
difference in precipitation in the two grains is due to the  
substrate materials used.
- Figure 6.1b. Secondary electron image of a POMBE grown bi- 246  
epitaxial grain boundary junction. The density of  
precipitates is higher in the YBCO grown on the cerium  
oxide substrate region.
- Figure 6.1c. A secondary electron image of a set of bi-epitaxial grain 247  
boundary junctions. The higher concentration of  
smaller precipitates are in the YBCO grown on the  
strontium titanate regions of the substrate.
- Figure 6.1d. A secondary electron image of a bi-epitaxial grain 248  
boundary junction. The higher concentration of  
precipitates is in the YBCO grown on the strontium  
titanate.
- Figure 6.2a. R-T curve for a POMBE grown bi-epitaxial grain 250  
boundary with resistive behavior.
- Figure 6.2b. Superconducting transition of the grain with a  $T_c=90.5$  250  
K.
- Figure 6.2c. R-T curve of resistive grain boundary with grain 251  
resistance subtracted out.
- Figure 6.2d. R-T curve of grain boundaries with grain resistance 252  
removed. The curve fit is with a series of thermally  
activated conduction paths.
- Figure 6.3a. R-T curve of PLD grown bi-epitaxial junctions. 255
- Figure 6.3b. R-T curve showing foot-like structure due to TAPS. 255
- Figure 6.3c. Superconducting transition of grain and double "hump" 256  
transition onset in grain boundaries.

- Figure 6.4. I-V characteristics of PLD grown bi-epitaxial grain boundary junction exhibiting weak link behavior at 5 K. 258
- Figure 6.5a. I-V characteristics of bi-epitaxial junction at 9.6 K and 0.24 G applied magnetic field. RSJ model fit with no capacitance. 259
- Figure 6.5b. Enlarged transition region showing slight deviations from the RSJ model. 259
- Figure 6.6. I-V characteristics of a bi-epitaxial grain boundary junction at a series of temperatures from 8.8 K to 40 K. 260
- Figure 6.7. Critical current vs. temperature for a grain boundary junction fitted with a  $(1-T/T_c)^2$  fit. 261
- Figure 6.8a. I-V characteristics of two bi-epitaxial grain boundaries on one sample showing markedly different behavior. Measurement at T=5 K, applied magnetic field=-1.25 G. 263
- Figure 6.8b. I-V characteristics of same boundaries as in figure 6.8a. at T=5 K, applied magnetic field =1.5 G. 263
- Figure 6.9. Voltage vs. applied magnetic field perpendicular to the film surface stepped in 0.01 G increments. 265
- Figure 6.10. Voltage vs. applied magnetic field perpendicular to the film surface from -1 G to 1 G. 265
- Figure 6.11. Voltage vs. increasing and decreasing applied magnetic field. 266
- Figure 6.12. Voltage vs. applied magnetic field to -18 G. 266
- Figure 6.13. Patterson function of magnetic field data in figure 6.9. 267
- Figure 6.13a. Bright field micrograph of a resistive bi-epitaxial grain boundary. The two arrows indicate the ends of the grain boundary. 272

- Figure 6.13b.** Bright field micrograph of a resistive bi-epitaxial grain boundary. The arrows marked A show two different type of disruptions at the boundary. The arrows marked B show the boundary. 274
- Figure 6.14.** A region of the resistive grain boundary showing significant disruption along the boundary length. 276
- Figure 6.15a.** A bright field image of a superconducting bi-epitaxial grain boundary. The arrows denote similar locations in the corresponding bright field images. The arrow A is a precipitate at the boundary. 280
- Figure 6.15b.** A dark field image corresponding to the figure 6.15a. The arrows indicate similar positions in the micrographs. 282
- Figure 6.15c.** A dark field image of the opposing grain from figure 6.15b. The arrows indicate similar positions along the boundary. Note that the region denoted by the arrow A remains dark in both images. 284
- Figure 6.17.** A HREM image of a POMBE grown bi-epitaxial junction. A 1 nm disordered region is seen at the boundary. 287
- Figure 6.18a.** A HREM image of a PLD grown bi-epitaxial junction. The boundary is well structured and exhibits some (100)(110) asymmetric facets. 289
- Figure 6.18b.** A HREM image of PLD grown bi-epitaxial grain boundary. The arrow indicates a region where the grain boundary plane is inclined relative to the beam direction. 291
- Figure 7.1** Circuit diagram to simulate grain boundary junction. A series of parallel Josephson junctions shunted by resistors, analogous to a resistively shunted interferometer. The junctions have unequal critical currents. 296

Figure 7.2a.	Comparative region of the grain boundary junction with parallel junction shunted by resistive regions.	296
Figure 7.2b.	Schematic diagram of the grain boundary junction showing the total critical current for three different applied flux states.	297
Figure 7.3.	The dependence of the critical current on applied flux for a 2 junction model. The dotted line is for two junctions with unequal critical currents (from Van Duzer 1981).	302
Figure 7.4.	The critical current response for two parallel junctions with self-induced fields included. The lower two curves break down the currents in either junction.	302
Figure 7.5.	The effect of self inductance on the difference of the maximum and minimum critical currents. At higher self-inductances the peak to valley ratio in the I(B) relation diminishes.	303
Figure 7.6.	The $I_c(B)$ behavior for an asymmetric (unequal critical currents) junction with self-induced fields.	303
Figure A1a.	The critical current vs. magnetic field behavior for a bi-epitaxial grain boundary junction at 5 K.	337
Figure A1b.	The critical current vs. magnetic field behavior for increasing and decreasing field with hysteretic behavior.	337
Figure A2.	The Patterson function for the bi-epitaxial grain boundary junction characteristics shown in figure A1a.	338
Figure A3.	The magnetic field behavior for a sputter-induced epitaxy sample at 5 K.	339
Figure A4.	The Patterson function for the curve in figure A2.	339
Figure A5.	The critical current vs. magnetic field behavior for a multilayer sputter-induced epitaxy sample.	340

<b>Figure A6.</b>	The corresponding Patterson function for figure A5.	340
<b>Figure A7a.</b>	A micrograph of a sputter-induced epitaxy grain boundary showing the variation in the microstructure. The boundary has a precipitate (arrow) and exhibits different regions of faceting along its length.	341
<b>Figure A7b.</b>	A schematic representation of a grain boundary with precipitates and different types of grain boundary structure (faceted and non-faceted) along its length. The corresponding variation in critical current density and the phase along the boundary length.	341
<b>Figure A8a.</b>	The simulated critical current vs. magnetic field behavior for a grain boundary with minimal magnetic field penetration into the superconducting regions.	342
<b>Figure A8b.</b>	The corresponding Patterson function for figure A8a with a very narrow central peak.	342
<b>Figure A9a.</b>	The simulated critical current vs. magnetic field behavior for a grain boundary with larger penetration of the field into the superconducting region than figure A8.	343
<b>Figure A9b.</b>	The corresponding Patterson function for figure A9a with a broadening central peak relative to figure A8b.	343
<b>Figure A10a.</b>	The simulated behavior for a junction with almost complete penetration of the superconducting regions (virtually the same penetration as in the normal regions).	344
<b>Figure A10b.</b>	The corresponding Patterson function for figure A10a with the central peak removed showing a further broadening of the central peak.	344
<b>Figure A10c.</b>	The Patterson function for figure A10a without the central peak removed showing exhibiting a triangular shape expected for a standard Fraunhofer pattern.	345

<b>Figure A11a.</b>	The real part of the critical current traversing the boundary with relatively uniform magnetic field penetration. The inset is an enlargement of a region of the curve.	346
<b>Figure A11b.</b>	The imaginary part of the critical current traversing the boundary corresponding to figure A11a.	346
<b>Figure A12a.</b>	The real part of the critical current traversing the boundary with non-uniform magnetic field penetration. The inset is an enlargement of a region of the curve.	347
<b>Figure A12b.</b>	The imaginary part of the critical current traversing the boundary corresponding to figure A12a.	347
<b>Figure A13a.</b>	The simulated behavior for a grain boundary with a relatively small average superconducting region distribution. This graph is a good match with the bi-epitaxial data.	348
<b>Figure A13b.</b>	The Patterson function for figure A13a.	348
<b>Figure A14a.</b>	The simulated behavior for a grain boundary with a 10-fold increase in the size of the conduction paths across the boundary. This matches the experimental results for the sputter-induced epitaxy grain boundaries.	349
<b>Figure A14b.</b>	The corresponding Patterson function for figure A14a that is in good agreement with figure A6.	349
<b>Figure A14c.</b>	Enlargement of figure A14b to show Moire interference pattern in Patterson function.	350
<b>Figure A15.</b>	The simulated behavior for a grain boundary with small precipitates.	350
<b>Figure A16.</b>	The simulated behavior for the identical boundary as in figure A15 except for double the size for the precipitates.	351
<b>Figure A17.</b>	The same grain boundary as in figure A13, but for microbridge that is twice as wide. There is an increase in the higher frequency modulations relative to figure A13.	351

# Chapter I. Introduction

This thesis studies the formation, structural characteristics and transport properties of 45° [001] tilt  $\text{YBa}_2\text{Cu}_3\text{O}_{7-x}$  (YBCO) thin film grain boundaries. A pre-growth ion beam substrate modification technique on (100)  $\text{MgO}$ , termed sputter-induced epitaxy, has been developed to form 45° grain boundary junctions in YBCO thin films. The effect of the ion beam on the  $\text{MgO}$  has been studied to determine the cause of the epitaxial modification. The sputter-induced epitaxy has been extended to work on multilayer substrates so that bulk substrates other than  $\text{MgO}$  can be used. The transport properties and microstructure of the sputter-induced epitaxy junctions have been compared to bi-epitaxial grain boundary junctions with similar 45° [001] tilt boundaries. The microstructure and the transport properties of the different grain boundaries varied significantly, and suggest some of the key elements of grain boundary transport. A grain boundary model, consistent with the observations, consisting of a series of parallel Josephson junctions is developed to phenomenologically describe the junction behavior.

The advent of high critical temperature (high- $T_c$ ) materials has created a unique opportunity to exploit superconducting phenomena for practical applications. The realization of these opportunities has been inhibited by many materials issues stemming from the complex nature of the oxide materials. One of the major differences between the high- $T_c$  and low- $T_c$  superconductors is the magnitude of the coherence length, which is significantly shorter in the high- $T_c$

samples, for YBCO  $\lambda_{a-b} = 1\text{-}1.5 \text{ nm}$  (see table 2.4)(Welp *et al.* 1989). The short coherence length implies that any distortions, structural or chemical, on this length scale will diminish the superconducting properties in the region. In the high- $T_c$  materials, most high angle grain boundaries behave as weak links with reduced critical current density,  $J_c$ , and critical temperature,  $T_c$ , across the grain boundary relative to the bulk grain (Dimos *et al.* 1988; Dimos *et al.* 1990). The weak links are detrimental for many bulk applications that require high supercurrent densities, such as transmission lines, magnetically levitated trains and high field magnets. The weak link high angle grain boundaries, however, often display the Josephson effects that can be used for many microelectronic applications. This thesis studies the useful Josephson properties of these junctions ultimately for development of potential applications.

The Josephson effects are based on the macroscopic quantum superconducting wavefunction that exists in the superconducting state. The interference of two superconducting wavefunctions across a barrier provides extreme sensitivity to magnetic fields and various forms of radiation. Josephson junctions that exhibit these effects can be used to form numerous practical devices. One of the most useful applications is to form a superconducting quantum interference device (SQUID). SQUIDs currently have the best sensitivity to magnetic flux of any known technology by approximately four orders of magnitude (compared to a flux gate magnetometer). These devices can be used for unique biomagnetic applications (such as magnetoencephalograms (MEG) and magnetocardiograms (MCG)), non-destructive evaluation and geophysical applications that require high magnetic field sensitivity. The significant potential for SQUIDs has stimulated research to

develop and understand the weak link nature of high angle high-T<sub>C</sub> thin film grain boundaries, which can be used to make these devices.

The first part of this thesis describes a technique developed to form reproducible 45° [001] tilt grain boundary junctions. High quality epitaxial single crystal YBCO thin films grown on MgO form a cube-on-cube orientation ([001] YBCO || [001] MgO and [110] YBCO || [110] MgO). By using a low-voltage ion beam to modify the substrate surface, the epitaxial orientation of the YBCO film can be altered to [001] YBCO || [001] MgO and [100] YBCO || [110] MgO. Therefore by sputtering a predetermined region of the substrate, grain boundary junctions can be selectively formed in the YBCO thin film. This result is interesting both from a thin film epitaxy perspective and for studying the weak link nature of grain boundaries and forming junctions in high-T<sub>C</sub> superconductors.

Sputter-induced epitaxy is a unique method to control the epitaxial orientation relation between the substrate and the thin film. The role of the ions in the substrate modification process was studied using both Rutherford Backscattering Spectroscopy and Atomic Force Microscopy. The accelerated ions have two primary effects on the substrate. First there is a surface roughening of the MgO creating distorted regions on the substrate. The second effect is the implantation of both argon and tungsten into the substrate surface. By understanding these mechanisms, in principle this technique can be extended to other materials systems where grain boundaries are integral in controlling properties (e.g. ferroelectric materials). Sputter-induced epitaxy is one of the first examples of epitaxy modification using strictly a pre-growth ion

beam process. The simplicity and versatility of this method makes it an attractive technique for numerous applications.

One of the drawbacks of sputter-induced epitaxy is the limitation of the technique to bulk MgO substrates. Ion beam modification of other substrates did not have the same effect on the YBCO epitaxy as on (100) MgO. Therefore, in order to use a bulk substrate other than MgO, a novel multilayer approach was developed. A layer of (100) MgO was deposited on a bulk (100) LaAlO<sub>3</sub> substrate. The film was then partially irradiated with a low voltage argon ion beam. The resulting film had a cube-on-cube orientation on the unspattered region and an epitaxial condition [001] YBCO || [001] MgO and [110] YBCO || [100] MgO on the presputtered region. The major implication of this result is that the grain boundary junctions can be formed on any substrate or multilayer that a high quality epitaxial MgO layer can be grown on. This is a tremendous advantage for integration into other materials systems such as semiconductors or ferroelectrics.

The weak link nature of the sputter-induced epitaxy junctions and a set of 45° [001] bi-epitaxial junctions was studied by comparing the microstructure and transport properties of the different junctions. Numerous cryogenic transport studies were made to study the individual grain boundary properties. Measurements of resistance - temperature, current - voltage as a function of temperature and critical current as a function of magnetic field were made to characterize the transport properties of the junctions. The sputter-induced epitaxy grain boundary junctions had the highest critical current densities of all the junctions measured. Two types of bi-epitaxial grain boundaries were identified, resistive and superconducting. The superconducting grain

boundaries all exhibited resistively shunted junction behavior without capacitance, and strong oscillations in the critical current as a function of small applied magnetic fields. The transport properties are compared between the junctions to gain a better understanding of the role of the microstructure in the weak link behavior.

The analysis of the microstructure elucidated significant differences in the three types of grain boundary junctions. All of the grain boundaries meandered on a length scale of hundreds of nanometers indicating inhomogeneous structure along the boundary. The resistive bi-epitaxial junctions exhibited structural disorder along the entire length of the boundary. The major difference between the sputter-induced epitaxy junctions and the bi-epitaxial junctions was the amount of microfaceting along the boundary. Both types of grain boundaries were relatively free of precipitation and second phases, but the sputter-induced epitaxy had long uniform low-index plane asymmetric facets along its length.

The combination of the microstructural and transport data supports a model of a series of Josephson junctions parallel to a set of thermally activated resistors. The model suggests that the magnetic field behavior of the junctions can not be explained by a constant phase shift across the boundary. There is a variation of critical currents across the junction which will modify the local magnetic flux seen by each junction. The strongly coupled regions are related to the local structure at the grain boundary. The model demonstrates the complexity of the grain boundary junctions and the difficulty in forming junctions with reproducible transport properties necessary for applications.

The thesis first details relevant background information on superconductivity, thin film growth and grain boundary junctions in high-T<sub>C</sub> thin films. Chapter three describes the experimental procedure developed to form the grain boundaries using sputter-induced epitaxy and to characterize the microstructure and transport properties of individual grain boundary junctions. Then the experimental results on the sputter-induced epitaxy junctions are presented. First the mechanism for the modified orientation is discussed followed by the transport and microstructural analysis of the sputter-induced epitaxy junctions. The technique is then extended to a multilayer system, with a description of the process of forming the grain boundaries and the studies of the transport properties and microstructure. Chapter six describes the results of experiments on the bi-epitaxial grain boundaries. Finally, in chapter seven and appendix one, the different grain boundaries are all compared and a grain boundary model is presented which helps in understanding the microstructure - transport property relationship of the grain boundary junctions.

## **Chapter II. Background and Literature Survey**

High critical temperature (high- $T_c$ ) superconductors are materials that go through a superconducting transition at a relatively high temperature (generally  $> 25$  K), as compared to the low- $T_c$  materials. This chapter reviews the relevant background information on high- $T_c$  materials, thin films and grain boundaries. These topics all help in understanding the weak link nature of most high-angle grain boundaries. Some basic concepts of superconductivity including the Josephson effects are described with particular emphasis on the high- $T_c$  superconductors. Epitaxial thin film deposition and characterization is discussed with respect to the techniques used in this work. The role of grain boundaries in the high- $T_c$  superconductors will be detailed and previous work on superconducting grain boundaries will be highlighted. Finally all the work will be brought together in a description of the current technology of  $\text{YBa}_2\text{Cu}_3\text{O}_{7-x}$  (YBCO) thin film grain boundary junctions, one of the first commercially viable products developed from the high- $T_c$  superconductors.

### **II.1. High-Temperature Superconductivity**

Superconductivity was first discovered in 1911 by Kamerlingh Onnes upon cooling mercury to 4.2K (de Bruyn Outboter 1987). This began a long study of the fascinating physical phenomenon where certain materials lose all electrical resistance below a critical temperature,  $T_c$ . Since that time many materials, both pure metals and alloys, have been shown to be superconducting. The research which ensued after Onnes's discovery eventually uncovered many

unique properties of the superconductors and after 45 years a consistent theory explaining the phenomenon was developed (Bardeen-Cooper-Schrieffer or BCS theory)(Bardeen *et al.* 1957). In 1986 Bednorz and Muller (Bednorz *et al.* 1986) discovered a material La-Ba-Cu-O, with a perovskite structure, which was a superconductor with a transition temperature of 30K, ushering in the age of high-temperature superconductors. This immediately stimulated research for related new compounds with higher transition temperatures. Eventually yttrium was used as a substitute for the lanthanum creating a new cuprate superconductor,  $\text{YBa}_2\text{Cu}_3\text{O}_{7-x}$ , with a  $T_c=92$  K (Wu *et al.* 1987). This discovery had an immediate impact on research since the transition temperature was above the boiling point of liquid nitrogen making superconductivity much more economically viable than using the low- $T_c$  materials. Since 1987, several other high- $T_c$  superconductors were discovered (see Table 2.1), including the bismuth-, thallium- and mercury- based systems(Maeda *et al.* 1988; Sheng *et al.* 1988; Putilin *et al.* 1993). However, none of them has been as extensively studied as  $\text{YBa}_2\text{Cu}_3\text{O}_{7-x}$ . The research in this work involves only  $\text{YBa}_2\text{Cu}_3\text{O}_{7-x}$  due to the high-quality epitaxial thin films that can be made and are necessary for grain boundary junctions with good transport properties. It is important to realize that significant progress has been made in this area of research in a short period of time, and despite the lack of immediate commercial success, there is still significant potential for these materials.

### II.1.1. $\text{YBa}_2\text{Cu}_3\text{O}_{7-x}$ Structure

$\text{YBa}_2\text{Cu}_3\text{O}_{7-x}$  has an oxygen-deficient perovskite structure (see figure 2.1). The structure is anisotropic with the orthorhombic lattice parameters for

Material	Abbrev.	Structure (300 K)	Lattice Constant (Å)	T <sub>C</sub> (K)
(Nd,Sr,Ce) <sub>2</sub> CuO <sub>4-x</sub>		Tetragonal	a= 3.86 c=12.50	35
(La,Ba) <sub>2</sub> CuO <sub>4</sub>		Tetragonal	a= 3.79 c=13.29	38
YBa <sub>2</sub> Cu <sub>3</sub> O <sub>7-x</sub>	123	Orthorhombic	a= 3.82, b=3.89 c=11.68	92
YBa <sub>2</sub> Cu <sub>4</sub> O <sub>8</sub>	124	Orthorhombic	a= 3.84, b= 3.87 c=27.24	80
Y <sub>2</sub> Ba <sub>4</sub> Cu <sub>7</sub> O <sub>14</sub>	247	Orthorhombic	a= 3.85, b= 3.87 c=50.29	95
Bi <sub>2</sub> Sr <sub>2</sub> CaCu <sub>2</sub> O <sub>8</sub>	2212	Tetragonal	a= 5.41 c=30.93	112
TlBa <sub>2</sub> CaCu <sub>2</sub> O <sub>7</sub>	1212	Tetragonal	a= 3.86 c=12.75	103
Tl <sub>2</sub> Ba <sub>2</sub> Ca <sub>2</sub> Cu <sub>3</sub> O <sub>10</sub>	2224	Tetragonal	a= 3.85 c=35.88	125
HgBa <sub>2</sub> CuO <sub>4+x</sub>		Tetragonal	a= 3.88 c=9.51	98
(Ba,Sr)CuO <sub>2</sub>	Infinite Layer	Tetragonal	a= 3.93 c= 3.47	90
(Ba <sub>1-x</sub> K <sub>x</sub> )BiO <sub>3</sub>		Cubic	a= 4.29	30

Table 2.1. The crystal structure and transition temperature of several high-T<sub>C</sub> superconductors (from Shaked *et al.* 1994).

$x=0.07$  being  $a=3.82 \text{ \AA}$ ,  $b=3.89 \text{ \AA}$  and  $c=11.68 \text{ \AA}$ . Table 2.2 lists the atomic positions and occupancies of all the atoms in the unit cell for  $x=0.07$ . Figure 2.1 shows the orthorhombic unit cell with labels to differentiate the oxygen atom sites and copper atom sites. The properties of  $\text{YBa}_2\text{Cu}_3\text{O}_{7-x}$  are highly dependent on the oxygen stoichiometry. The oxygen content varies from  $x=0$  to  $x=1$ , with a structural orthorhombic ( $\text{Pmmm}$ ,  $a \neq b$ ) to tetragonal ( $\text{P}4/\text{mmm}$ ,  $a=b$ ) with a phase transition occurring at  $x=0.6$  (Jorgensen *et al.* 1987; Jorgensen *et al.* 1990; Marezio 1991; Cava *et al.* 1990). The O(2), O(3) and O(4) sites (see figure 2.1) remain fully occupied for the entire range of oxygen stoichiometry, but the O(1) site is removed as the oxygen content is decreased, forming the tetragonal cell.

Figure 2.2 shows the dependence of  $T_c$  on the oxygen content and the corresponding change in copper valence. There are two  $T_c$  plateaus in the plot, the first is termed the 90 K plateau for  $0 < x < 0.2$  and actually is slightly decreasing in this range from  $T_c=92 \text{ K}$ . The second plateau is for  $0.3 < x < 0.5$  and is termed the 60 K plateau. The phase transition is directly related to the superconducting behavior, with the orthorhombic phase being superconducting and the tetragonal phase being semiconducting. The unit cell has two  $\text{CuO}_2$  planes (with O(2) and O(3)) that carry the supercurrent(Cava *et al.* 1990), and two CuO chains (with O(1)) that act as charge reservoirs and supply the planes with charge carriers. As the oxygen content is decreased, oxygen from the chains is removed until there are no O(1) sites occupied at  $x=1$ . The two plateau behavior has been attributed to a change in valence of the Cu(2) atom which lies in the  $\text{CuO}_2$  planes (Marezio 1991). From the 90K plateau to the 60K plateau there is a drop in valence of approximately 0.03 v.u./Cu, decreasing the

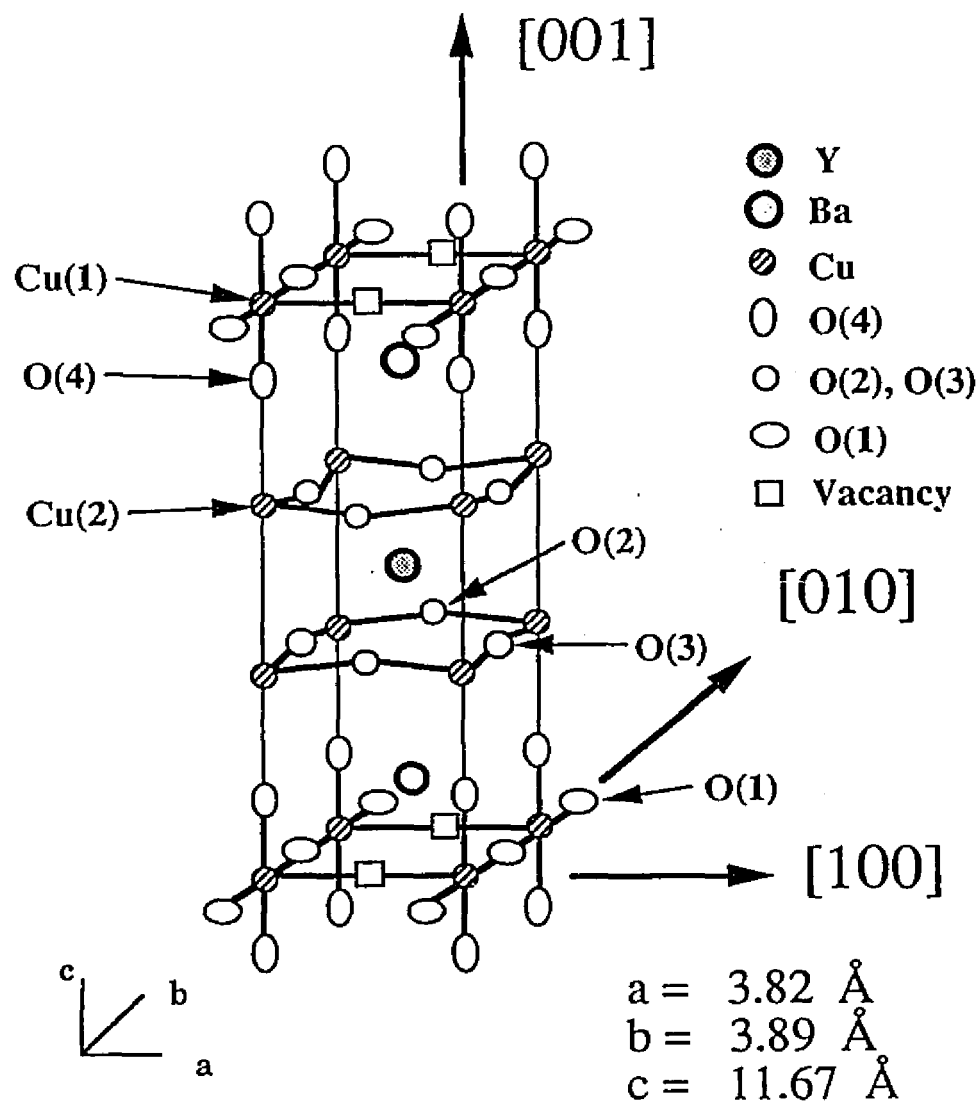


Figure 2.1. Schematic diagram of the  $\text{YBa}_2\text{Cu}_3\text{O}_{7-\chi}$  unit cell structure.

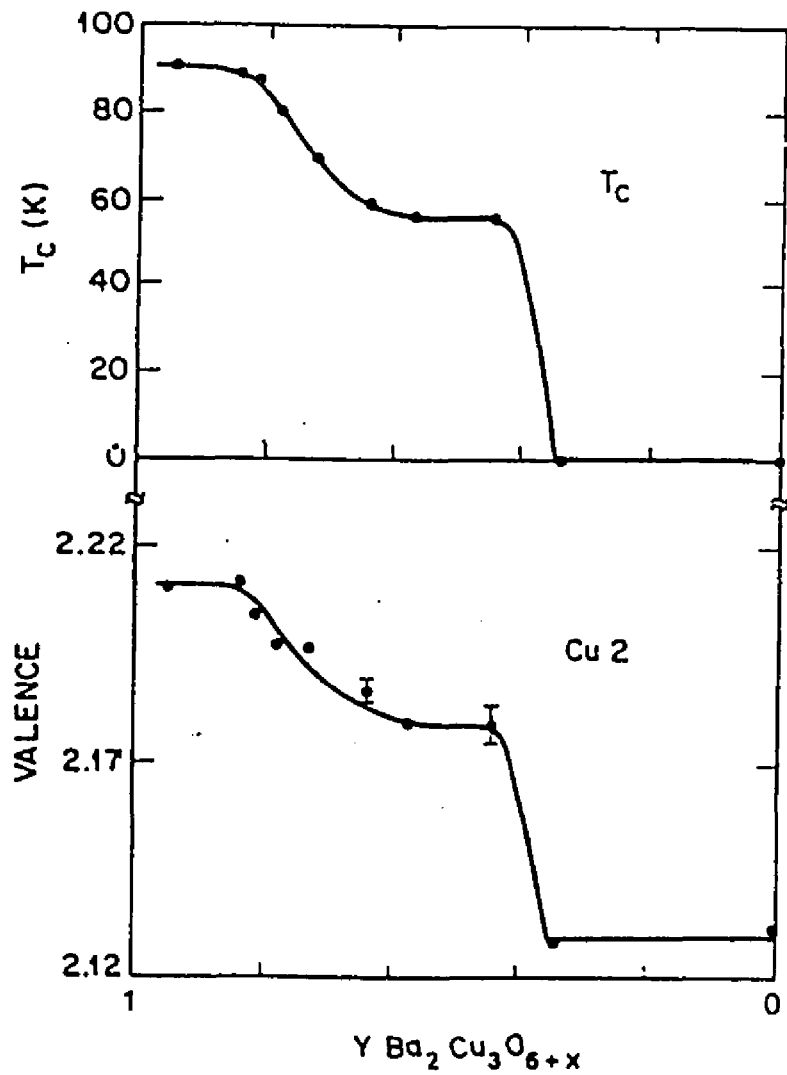


Figure 2.2. Variation in critical temperature and copper valence as a function of oxygen stoichiometry (from Marezio et al. 1991).

hole concentration, and at the structural phase transition, the Cu cation valence abruptly decreases another 0.05 v.u./Cu. The role of the oxygen stoichiometry in the variation of  $T_c$  is very important. Local deviations in oxygen stoichiometry due to defects or otherwise can cause a local difference in the critical temperature. This is potentially critical for grain boundaries where it has been postulated that a different oxygen concentration at the boundary could locally suppress  $T_c$  in certain regions. These assumptions and their validity will be discussed in detail later.

In measuring YBCO samples, an issue of concern is the formation of twins due to the phase transition from tetragonal to orthorhombic during cooldown. (110) type twins are formed where the a- and b- axes reverse, in order to relieve strain. Thin films in particular can be highly twinned because of the structural constraint of the substrate. The role of twin boundaries in single crystals has been studied by various groups (Kwok *et al.* 1990; Gyorgy *et al.* 1990; Welp *et al.* 1994; Fleshler *et al.* 1993). Twin boundaries do not exhibit any weak link behavior, such as a depressed critical current density. They do, however, act as weak flux pinning sites, which can increase the critical current density in low magnetic fields. Highly twinned thin films have been measured, and also do not exhibit any weak link behavior. Therefore there is no significant effect of twins on the measurements in these samples that can be confused with the grain boundary behavior.

Due to the very small variation between the a- and b- lattice parameters (1.8%), they are often not distinguished. However, the large anisotropy between the a/b axes and the c-axis plays an integral role in many materials

Atom	x	y	z	Occupancy
<b>YBa<sub>2</sub>Cu<sub>3</sub>O<sub>6.71</sub></b>		<b>Orthorhombic</b>		
Y	0.5	0.5	0.5	1
Ba	0.5	0.5	0.1895(3)	2
Cu(1)	0.0	0.0	0.00000	1
Cu(2)	0.0	0.0	0.3574(3)	2
O(1)	0.0	0.5	0.0	0.65(2)
O(2)	0.5	0.0	0.3767(4)	2
O(3)	0.0	0.5	0.3804(5)	2
O(4)	0.0	0.0	0.1542(5)	2
O(5)	0.5	0.0	0.0	0.06(2)
<b>YBa<sub>2</sub>Cu<sub>3</sub>O<sub>6.42</sub></b>		<b>Tetragonal</b>		
Y	0.5	0.5	0.5	1
Ba	0.5	0.5	0.1914(3)	2
Cu(1)	0.0	0.0	0.00000	1
Cu(2)	0.0	0.0	0.3590(3)	2
O(1)	0.0	0.5	0.0	0.42(3)
O(2)	0.5	0.0	0.3792(2)	4
O(4)	0.0	0.0	0.1508(5)	2

Table 2.2. The atomic positions and site occupancies for both the orthorhombic and tetragonal phases of YBCO (Jorgensen *et al.* 1987).

properties. Therefore properties will usually be quoted for the a-b direction and the c-direction separately.

### II.1.2. $\text{YBa}_2\text{Cu}_3\text{O}_{7-x}$ Properties

Despite the many differences between the low- $T_c$  and high- $T_c$  superconductors, many of the concepts developed for low- $T_c$  materials have been used to explain certain phenomena or just as a starting point for understanding the new materials.  $\text{YBa}_2\text{Cu}_3\text{O}_{7-x}$  is a type II superconductor, with highly anisotropic properties due to the crystal structure of the material and the conduction along the Cu-O planes (there is very weak coupling between planes along the c-axis). For the study of grain boundary behavior in high- $T_c$  materials it is important to understand the concept of Cooper pairs and the Josephson effects. The modeling of Josephson junctions in particular has been borrowed from the low- $T_c$  systems, but has not been completely successful in explaining junction behavior in the high- $T_c$  materials. This section will develop some of these ideas as a basis for explaining grain boundary junction behavior in  $\text{YBa}_2\text{Cu}_3\text{O}_{7-x}$ .

In order to develop the theory of the Josephson effects, it is necessary to understand that charge is carried during superconduction in Cooper pairs. L.N. Cooper (Cooper 1956) determined that by adding electrons to a zero-temperature Fermi gas the electrons have a tendency to form electron pairs to reduce the total system energy. These electron pairs, called Cooper pairs, consist of two electrons with opposite spins, have a total charge of  $2e$  and a total mass of  $2m$ , where  $e$  is the charge of the electron, and  $m$  is the mass of the electron. The electrons that form the Cooper pair maintain phase coherence and

are therefore "correlated" over a mean distance called the coherence length. The coherence length is defined as:

$$\xi = \frac{h v_f}{2\Delta\pi^2} \quad (2.1)$$

where  $v_f$  is the Fermi velocity and  $2\Delta$  the energy gap. The phenomenon is actually macroscopic, where all paired electrons in an uninterrupted superconductor exist in a single quantum mechanical state. If there is a disruption in the superconducting material on the order of or greater than the coherence length, superconducting properties can be diminished or destroyed. The coherence length for many low- $T_c$  materials is on the order of 10-100 nm, but for  $\text{YBa}_2\text{Cu}_3\text{O}_{7-x}$  the coherence length is only  $\xi_{a-b}=15 \text{ \AA}$  and  $\xi_c=3 \text{ \AA}$  (*Oh et al.* 1988; *Welp et al.* 1989). The large anisotropy in the coherence length is due to the conduction in the a-b planes, and only weak coupling along the c-axis. These values for the coherence length are at low temperature, and will decrease as the temperature approaches  $T_c$ . Any distortion in the material on this length scale, either structural or chemical, can create a region of weakened superconductivity by disrupting the coherence of Cooper pairs. These regions are called weak links and usually exhibit a depressed critical current density across the weakened region. The short coherence length is why grain boundaries may exhibit weak link behavior in the high- $T_c$  materials (this will be discussed extensively in section II.3).

The Josephson effects are a result of the macroscopic phase coherence and the behavior of paired superconducting electrons at a conduction barrier (e.g. a normal metal, or insulating layer). *Giaever*(*Giaever* 1960) showed that

quasiparticle tunneling could occur across a barrier by creating a potential drop across it. Soon afterwards, Josephson predicted that Cooper pairs could tunnel through a thin insulating layer even without bias across the barrier (Josephson 1962). The type of structure (superconductor-barrier-superconductor) that exhibits the Josephson effect is called a Josephson junction (a type of weak link), and was soon verified experimentally by Anderson and Rowell (Anderson *et al.* 1963). The resulting critical current of Cooper pairs tunneling through the insulating layer is dependent on the interference of the two macroscopic superconducting states from the material on either side of the junction, and results in the d.c. Josephson effect (eq. 2.2).

$$I_c = I_{c\max} \sin(\phi_1 - \phi_2) \quad (2.2)$$

where  $I_c$  is the measured critical current of the junction,  $I_{c\max}$  the maximum critical current of the junction, and  $\phi_1$  and  $\phi_2$  the phases of the macroscopic wavefunction from the two adjacent superconducting regions on either side of the junction. This can be related to the critical current density by the relation  $J_c = I_c / A$ , where  $A$  is the cross-sectional area of the junction. In high-T<sub>C</sub> grain boundaries, the area is not easily defined because of meandering chemical and structural inhomogeneities along the boundary, which significantly change the cross-sectional area. This effect has not been treated clearly in the literature, but can modify  $J_c$  values significantly (this issue will be discussed in detail later). The derivation by Josephson shows that the phase difference between the two superconducting regions can be varied by an applied magnetic field as is shown, for a specific junction configuration, in equation 2.3.

$$I_c = I_{c0} \left| \frac{\sin(\frac{\pi\phi}{\phi_0})}{(\frac{\pi\phi}{\phi_0})} \right| \quad (2.3)$$

The magnetic field is given in terms of fractions of flux quanta ( $\phi/\phi_0$ ). The expression for the critical current in eq. 2.3 assumes a uniform rectangular junction configuration with homogeneous current flow across the junction, and a constant phase shift along the junction (these assumptions are not necessarily valid in high-T<sub>c</sub> grain boundary junctions and will be detailed later). When an applied magnetic field of one flux quantum is applied there is perfect destructive interference between the wave functions and no net critical current is observed across the junction. Constructive interference of the wavefunctions leads to local maxima in the critical current density across the junction (see figure 2.3a-b.). In the general case, the critical current of the junction as a function of magnetic field is the Fourier transform of the integrated current density along the junction (eq. 2.4).

$$J_c(H) = \left| \int_{-\infty}^{+\infty} J_c(x) e^{i\beta x} dx \right|$$

where,  $\beta = (2\lambda + d) \frac{2\pi H}{\phi_0}$  (2.4)

where x is the distance along the junction,  $\lambda$  the London penetration depth, d the thickness of the junction, H the applied magnetic field and  $\phi_0$  the flux quantum ( $h/2e$ ). The Josephson effect is directly dependent on the coherence length in the sample because the barrier must be on the order of the coherence length to allow tunneling across the junction. If the barrier is too thin phase coherence can be

maintained without disruption, while if the barrier is too thick the tunneling effect is minimal.

For larger tunneling currents, a magnetic field can be self-induced by the currents, modifying the junction characteristics. The Josephson penetration depth,  $\lambda_J$ , is the distance from the edge of the junction that carries most of the tunneling currents. The Josephson penetration depth is used as a criterion to determine if self-field effects are important. It can be calculated using equation 2.5 as

$$\lambda_J^2 = \frac{h}{4\pi e J_c \mu (2\lambda + d)} \quad (2.5)$$

where  $\lambda$  is the London penetration depth and  $d$  the barrier thickness (for high- $T_C$  usually  $\lambda \gg d$ ). The Josephson penetration depth becomes important for "wide" junctions where the width,  $W$ , of the junction (see figure 2.3c.) exceeds  $4\lambda_J$  ( $W > 4\lambda_J$ ). For distances greater than this width, the Josephson current is mostly contained at the edges of the junction and very little tunneling current is maintained in the center of the junction. The current on the edges induces a magnetic field that decreases the phase difference in the center of the sample. The applied magnetic field becomes the sum of the external field and self-fields induced by the supercurrent.

Josephson junctions also exhibit an a.c. effect. For a given applied d.c. voltage  $V$ , an alternating current is set up across the junction with a characteristic frequency,  $f$  (eq. 2.6).

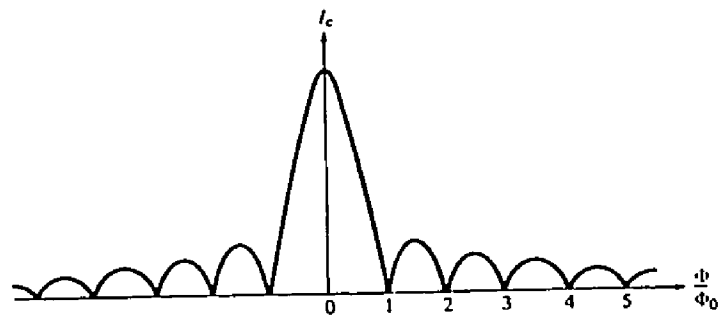


Figure 2.3a. The d.c. Josephson effect shown by the normalized critical current vs. applied magnetic field for a uniform critical current density distribution (from Van Duzer 1981).

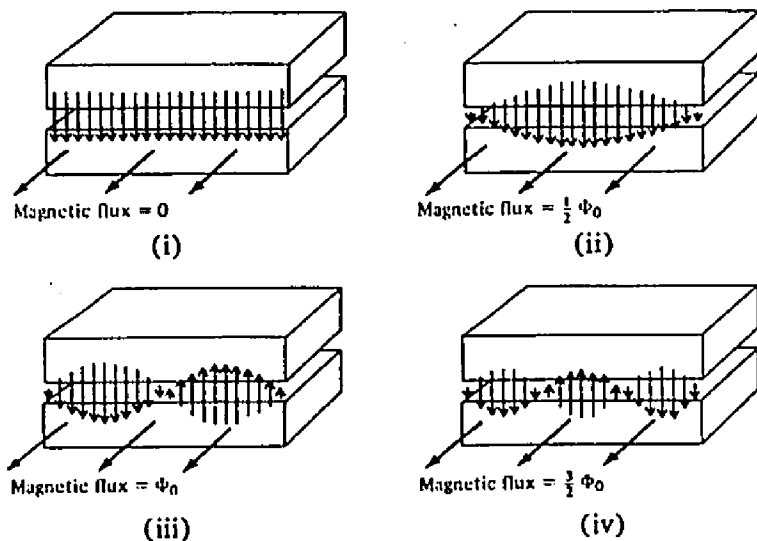


Figure 2.3b. A schematic of Josephson current flow across a Josephson junction as a function of applied magnetic field (from Van Duzer 1981).

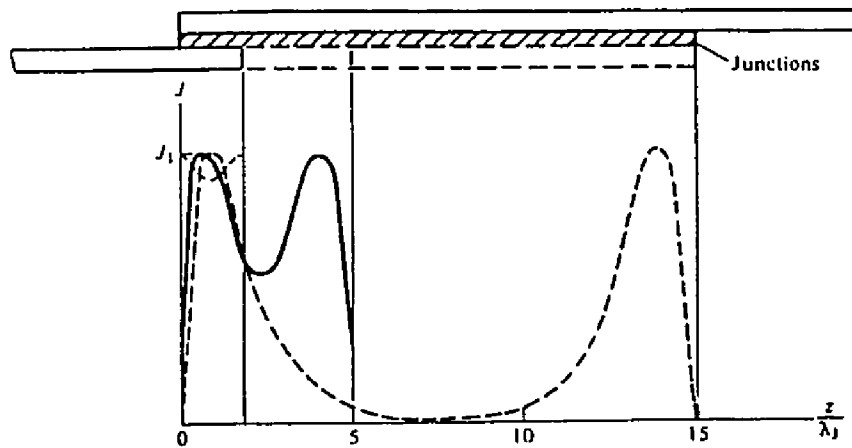


Figure 2.3c. The variation of the Josephson tunneling current for an in-line junction with normalized lengths of ( $L/\lambda_J$ ) penetrations depth=2, 5 and 15) (from Van Duzer 1981).

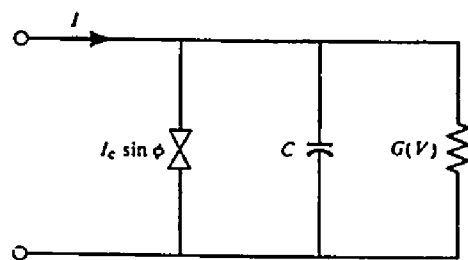


Figure 2.3d. A diagram of a resistively shunted junction. The junction is modeled with a capacitive element, a resistor and a Josephson junction in a parallel circuit (from Van Duzer 1981).

$$f = \frac{2eV}{h} \quad (2.6)$$

The alternating current is a consequence of a shift of  $\pi$  in the phase difference across the junction. This phase shift causes a current reversal across the junction and thus sets up a characteristic frequency related to the applied voltage. The frequency can be observed using an alternating field of high frequency microwave irradiation that couples with the alternating current. When the frequency of the alternating current is an integer value of the microwave frequency, an additional offset (d.c.) current is added creating characteristic steps (also known as Shapiro steps) (Shapiro *et al.* 1964).

The current-voltage characteristics of Josephson junctions can be modeled using the resistively shunted junction model (Van Duzer *et al.* 1981; Barone *et al.* 1982; Stewart 1968; McCumber 1968). This model uses a shunt resistance and capacitance with the Josephson junction (see eq. 2.7 and figure 2.3d.) to give

$$I = I_c \sin(\phi) + GV + C \frac{dV}{dT} \quad (2.7)$$

Putting this equation in terms of  $f$ , the differential equation becomes:

$$\frac{I}{I_c} = \beta_c \frac{d^2\phi}{d\theta^2} + \frac{d\phi}{d\theta} + \sin \phi \quad (2.8)$$

and

$$\beta_c = \frac{\omega_c C}{G} = \left( \frac{4\pi e}{h} \right) \left( \frac{I_c}{G} \right) \frac{C}{G}$$

where  $\beta_c$  is the Stewart-McCumber parameter,(Stewart 1968; McCumber 1968) the ratio of the capacitance to the conductance at a given frequency, a characteristic of the junction. The higher the capacitance of the junction, the more linear the current-voltage characteristics.

Josephson junctions are classified as "weak links" that are strictly defined as regions of weakened superconductivity. The junctions have decreased critical current densities relative to the adjacent material. Various types of weak link junctions, using different configurations, have been made in the low- $T_c$  materials including superconducting-normal-superconducting (S-N-S), superconducting-insulating-superconducting (S-I-S), Dayem bridge(Dayem *et al.* 1967)(microbridges with constricted superconducting regions on the order of the coherence length) and point-contact tunnel junctions. All of these junctions display the Josephson effect in some way. One method to differentiate the various junctions is to analyze the  $I_c(T)$  behavior. According to Ambegaokar and Baratoff(Ambegaokar *et al.* 1963), the temperature dependence of the critical current of a S-N-S junction is proportional to  $(1-T/T_c)^2$  in the vicinity of  $T_c$ , but for a S-I-S junction the critical current is proportional to  $(1-T/T_c)$ .

It is important to note that the junction behavior described by Josephson was for low- $T_c$  materials, and has been applied to the high- $T_c$ . The application of the knowledge of these systems to high- $T_c$  is due to the thorough understanding of low- $T_c$  junctions, not necessarily due to empirical fitting to the data. The junctions formed using high- $T_c$  are significantly more complex due to the short coherence length and anisotropic structure, which demand much better control over materials to form high-quality reproducible junctions.

The major difficulty in analyzing the transport data lies in separating intrinsic from extrinsic junction behavior.

## II.2. $\text{YBa}_2\text{Cu}_3\text{O}_{7-x}$ Thin Films

High quality epitaxial  $\text{YBa}_2\text{Cu}_3\text{O}_{7-x}$  thin films are the major reason devices have been developed using this material. In order to form controlled junctions and devices for integrated circuits it is necessary to reproducibly form good epitaxial films on various substrates and to grow multilayers. Thin films of other high- $T_c$  materials have not been made with as much control, and therefore have not been used for device fabrication. Numerous techniques including coevaporation, laser ablation, sputtering and metal-organic chemical vapor deposition have been used to produce these films (Schieber 1991a; Schieber *et al.* 1991b). This section deals with thin film issues in depositing complex oxide films.

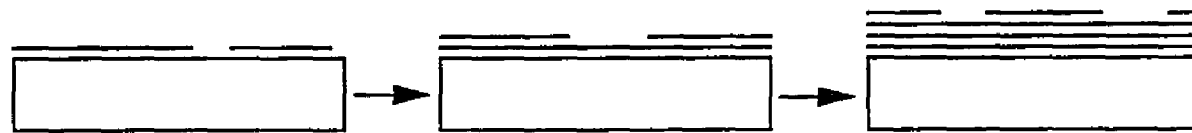
### II.2.1. Epitaxy

All of the thin film grain boundary junctions discussed in this thesis rely on epitaxial  $\text{YBa}_2\text{Cu}_3\text{O}_{7-x}$  thin films. Epitaxy describes a fixed orientation relationship between a substrate and a thin film. There are two different types of epitaxial conditions, the first being homoepitaxy where the substrate and the film are the same material. The second type of epitaxy is heteroepitaxy where the thin film is a different material from the substrate. In these experiments all the films were grown in a heteroepitaxial condition where the thin film was  $\text{YBa}_2\text{Cu}_3\text{O}_{7-x}$  and the substrates varied. Two of the primary issues in heteroepitaxy are the lattice mismatch between the deposited thin film and the

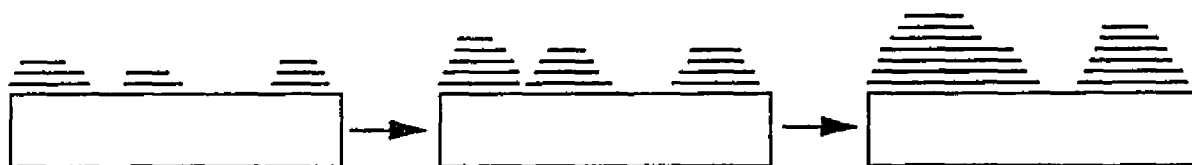
substrate, and the difference in the coefficients of thermal expansion. Table 2.3 shows various substrates used, the misfits with  $\text{YBa}_2\text{Cu}_3\text{O}_{7-x}$  and the coefficients of thermal expansion.

The importance of lattice misfit can be shown by characterization of the structural film quality. An example of this is  $\text{YBa}_2\text{Cu}_3\text{O}_{7-x}$  on  $\text{MgO}$  where the mismatch is 8.8% compared to  $\text{YBa}_2\text{Cu}_3\text{O}_{7-x}$  on  $\text{SrTiO}_3$  with a mismatch of only 0.3% along the a-axis. The films initially grown on  $\text{MgO}$  were often polycrystalline with two favorable orientations (recently high quality single crystal epitaxial films have been grown on  $\text{MgO}$ ), whereas the films on  $\text{SrTiO}_3$  were typically single crystal. In general, epitaxy can be maintained in thin films with as much as a 15% lattice misfit.

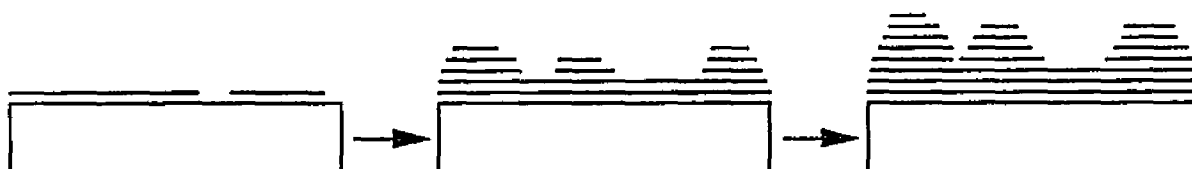
There are different types of growth modes for thin films (see figure 2.4) (Pashley 1985). A thin film can grow layer-by-layer if there are stronger binding forces between the thin film and the substrate than between atoms in the film. Layer-by-layer growth continues if the binding energy to the thin film free surface is stronger than the binding energy to a bulk crystal. If this is not the case, three dimensional nuclei will form on top of the layers and this is termed Stranski-Krastanov growth mode. The third method of thin film growth is Volmer-Weber growth, where the film nucleates and grows in three dimensions until there are enough nuclei to cover the entire surface. The actual method of growth for YBCO is termed ledge growth. Ledge growth comes from formation of favorable ad-sites at steps in the thin film, and is caused by imperfect substrate surfaces. This is discussed in more detail in section II.2-4.



Layer Growth



Island Growth



Stranski-Krastanov

Figure 2.4. Basic thin film growth modes.

### II.2.2. Ion Beam Modification

Part of this dissertation is devoted to a new technique in epitaxy control using a pre-growth ion beam treatment. Several processes may occur when an ion beam interacts with a solid surface (see figure 2.5a.) (Chapman 1980). First, an accelerated ion can be reflected off the surface (this is the basis for ion scattering spectroscopy, which is used to study surface layers). Second, a secondary electron can be ejected from the sample. The ion can also be implanted into the material upon impact, or the incident ion can create lattice defects or modify the surface structure. Finally, the resulting impact of an incident ion can result in the ejection of material. This process is known as sputtering, and in combination with the damage that modifies the substrate surface, is the important aspect of ion bombardment that relates to this work.

The sputtering process is based on the collision between the substrate material and the incident ion beam. In a simple binary collision the energy transfer is given by eq. 2.9., where  $m_i$  is the mass of the incident ion and  $m_t$  is the mass of the target material.

$$\frac{E_t}{E_i} = \frac{4m_i m_t}{(m_i + m_t)^2} \cos^2 \theta \quad (2.9)$$

The sputtering process deals with multiple collisions that are made up of individual collisions based on eq. 2.9. The sputter yield,  $S$ , is the number of target atoms ejected per incident ion (eq. 2.10)

$$S = \frac{3\alpha}{4\pi^2} \frac{4m_i m_t}{(m_i + m_t)^2} \frac{E}{U_0} \quad (2.10)$$

where  $U_0$  is the surface binding energy of the target and  $\alpha$  is a monotonically increasing value of  $m_t/m_i$ . From this equation it is seen that the sputter yield is

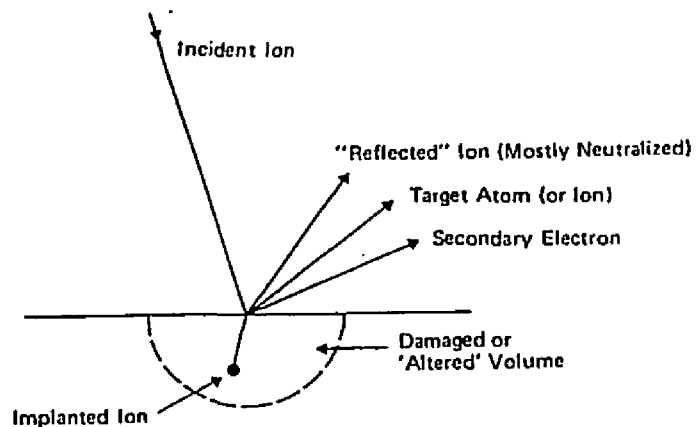


Figure 2.5a. Incident ion interactions with a target  
(from Chapman 1980).

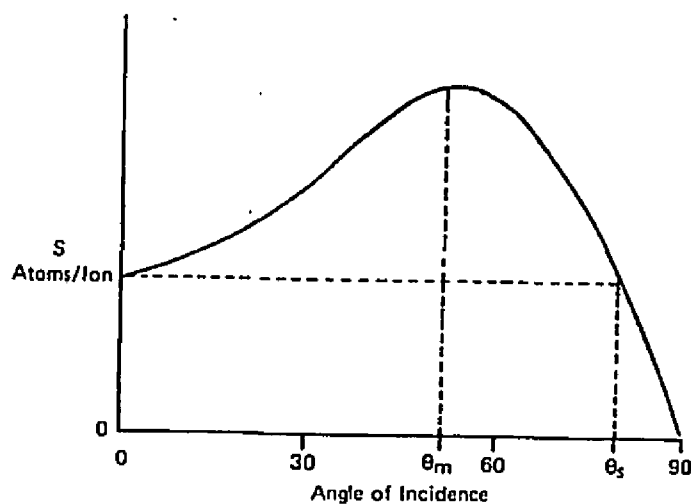


Figure 2.5b. Atom/ion yield ratio ( $S$ ) as a function of angle of incidence (from Chapman 1980).

directly proportional to the incident ion energy and inversely proportional to the surface binding energy. The yield follows eq. 2.10 only up to incident ion energies of approximately 1 keV, above which energy there is saturation of the energy transferred to the surface layers, as the ions penetrate further into the target. The sputter yield is also highly dependent on the angle of incidence. The maximum atom/ion yield typically varies significantly depending on the sample material (Cheney *et al.* 1965). The yield follows generically a curve such as figure 2.5b., where the yield goes through a maximum and drops off at higher incident angles because of the large reversal of momentum necessary to eject material (Chapman 1980).

There has been significant research on the modification of thin film growth using a variety of ion beam techniques both before and during deposition. These techniques include a low-energy substrate sputter prior to thin film growth, ion beam assisted deposition, reactive ion implantation and ion beam stitching (Baglin 1989; Baglin 1991; Baglin 1994; Baglin 1994). Substrate pre-sputtering with low energy (100-1000eV) inert ions (e.g. Ar<sup>+</sup> ions) will remove contaminants from the substrate surface. Pre-sputtering can preferentially sputter the surface to form a different surface chemistry from the bulk substrate. The pre-sputter treatment can also roughen the substrate surface for purposes of adhesion. Ion beam assisted deposition (IBAD) uses low-energy ions to bombard the surface during deposition. This is typically used to increase thin film density and to remove intrinsic stress formed during deposition. Very low energy ions (20-100eV) have been used to alter the growth mode of a thin film from Stranski-Krastanov to layer-by-layer by removing the island formations. Reactive ion implantation uses reactive ion species implanted after

deposition to increase fracture toughness by creating a layer of active ions. Ion beam stitching uses higher-energy ions to create cascades which increases adhesion properties (Baglin 1994; Baglin 1994).

Many of these ion beam techniques have been used for high- $T_C$  thin films, and some new techniques have been developed to control thin film morphology (e.g. step edge junctions). Recently, IBAD has been used to aid the formation of thick films on flexible substrates. Despite the wide use of ion beams in these various capacities (both for high- $T_C$  and other material systems), it is important to note that none of these techniques uses strictly a pre-growth sputter treatment to modify the epitaxial condition of the deposited thin film. Such a technique has been developed to control grain boundary formation for this thesis.

### II.2.3. Substrates

Numerous substrates are used for high- $T_C$  thin film growth depending on the specific requirements of the thin film to be deposited. There are several considerations in selecting a substrate. These considerations are separated into two categories, one is the requirements of the system environment on the substrate (e.g. a microwave environment has different substrate requirements than magnetic fields). Second, the considerations for the substrate-thin film growth relationship. Only this second aspect will be dealt with here (with some properties related to system requirements listed in Table 2.3). The lattice parameters, the crystal structure and the bonding are important in facilitating epitaxial growth and in determining the epitaxial orientation that can dominate. The coefficient of thermal expansion is important to determine the local strain

state of the thin film, whether it is in compression or tension. The chemical composition of the substrate also can affect the deposited film, for example yttria-stabilized zirconia interdiffuses into  $\text{YBa}_2\text{Cu}_3\text{O}_{7-\text{x}}$  to form  $\text{BaZrO}_2$ . The interdiffusion or chemical reaction of the substrate with the thin film can severely affect the properties of the deposited film by either doping a region or forming precipitates. Grain boundaries are particularly sensitive to diffusion because the lower density usually increases diffusion rates. The actual surface structure is important, e.g.  $\text{MgO}$  is hygroscopic and typically forms a hydroxide on the surface creating a rough surface structure which is not ideal for thin film deposition. Many "new" substrates have been developed in the process of trying to find the ideal substrate for complex oxide thin films. Development in this area has clearly penetrated into other fields such as ferroelectric materials, which also can be complex oxides. The benefit of research in the development of high- $T_C$  materials clearly extends beyond merely direct applications of superconductivity.

Other concerns for systems integration include appropriate substrate optical and electrical properties. Of course cost is always an issue especially when it comes to large scale fabrication. As an example of the difficulty in matching all the properties,  $\text{LaAlO}_3$  has excellent optical properties, but goes through a phase transition at around  $500^\circ\text{C}$  creating a highly twinned substrate, and is very expensive. Table 2.3 has several of the typical substrates used and their properties.

#### II.2.4. Thin Film Growth

Substrate	Melting Temp. (C)	Lattice Constant (Å)	Lattice Mismatch w/ YBCO (% w.r.t. YBCO)	Coeff. therm. exp. ( $10^{-6}/K$ )	Dielectric Constant (e) (1 MHz, @ 293 K)	Loss tan d (1 MHz, @ 293K)
SrTiO <sub>3</sub>	2080	a=3.905	a=2.3% b=0.4%	10.4	277	0.0125
LaAlO <sub>3</sub>	2100	a=3.79	a=-0.8% b=-2.6%	10	23	0.007
LaGaO <sub>3</sub>	1715	a=5.52 b=5.49 c=7.77	a=1.8% b=0.0%	10.3	25	0.0018
NdGaO <sub>3</sub>	1670	a=5.43 b=5.50 c=7.70	a=1.3% b=-0.1%	10	20.2	0.002
MgO	2825	a=4.21	a=10.2% b=8.2%	12.6	9.62	0.0091
ZrO <sub>2</sub> (5% Y)	2550	a=4.14	a=8.4% b=6.4%	9.2	27.5	0.0054
LaSrGaO <sub>4</sub>		a=3.84 c=4.23	a=0.5% b=-1.0%			
YAlO <sub>3</sub>	1875	a=3.66 c=3.76	a=-4.5% b=-5.4%	5-10	16	0.001
CeO <sub>2</sub>	2600	a=5.41	a=0.0% b=-1.8%	10	21.2	
YBCO		a=3.82 b=3.89 c=11.68	---	11		

Table 2.3. Various substrates used for YBCO thin film growth and accompanying materials properties (Giess *et al.* 1990; Hollmann *et al.* 1994).

The growth of  $\text{YBa}_2\text{Cu}_3\text{O}_{7-x}$  thin films has been studied by numerous groups (Schlom 1992a; Schlom *et al.* 1992b). Thin films have been grown in various epitaxial orientations ((001), (100), (103), etc.) on many different substrates ( $\text{SrTiO}_3$ ,  $\text{LaAlO}_3$ ,  $\text{MgO}$ ,  $\text{YSZ}$ , etc.) and using a variety of techniques (pulsed laser ablation, organo-metallic chemical vapor deposition, co-evaporation, etc.). Extensive studies using both atomic force microscopy (AFM) and transmission electron microscopy (TEM), have examined the growth mechanism for  $\text{YBa}_2\text{Cu}_3\text{O}_{7-x}$  thin films (Streiffer *et al.* 1990; Mannhart *et al.* 1993). It has been shown that the growth of  $\text{YBa}_2\text{Cu}_3\text{O}_{7-x}$  is much faster in the a-b direction than in the c direction. The thin film forms nuclei of 2-3 unit cells high which then propagate in the a-b direction. These steps in the film act as favorable ad-sites for the depositing film.

Observations of thin films using AFM have identified screw dislocations emanating from the substrate surface. This type of growth occurs by disruptions at the substrate surface and then incoherent growth of the film around the inclusion (see figure 2.6a-c.). The screw dislocation propagates through the film by ledge growth, which spirals upwards as it grows laterally. This screw dislocation growth is very clearly shown in STM images, which resolve ledge heights of 11 Å or one unit cell (Mannhart *et al.* 1993). The growth mechanism has been termed step flow growth since it is neither layer-by-layer growth, island growth or Stranski-Krastanov growth (see figure 2.6d.).  $\text{YBa}_2\text{Cu}_3\text{O}_{7-x}$  is highly sensitive to substrate defect sites such as steps or dislocations, which serve as nucleation sites for screw dislocations and promote step flow growth. In the absence of substrate imperfections, another growth mode might dominate, but this has not been observed. The ledge growth

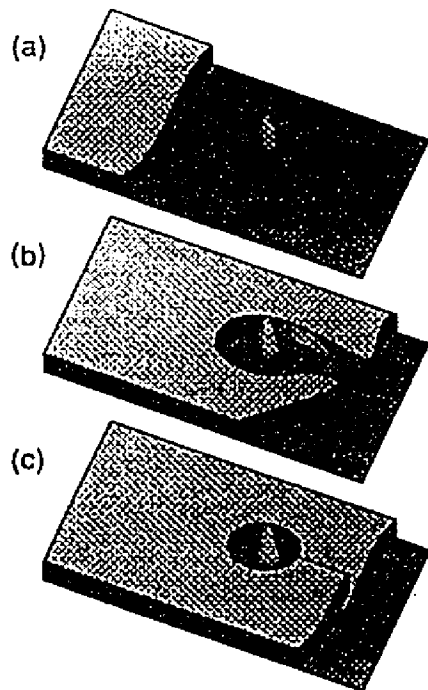


Figure 2.6a-c. The formation of a screw dislocation during growth around a substrate defect (from Mannhart 1993).

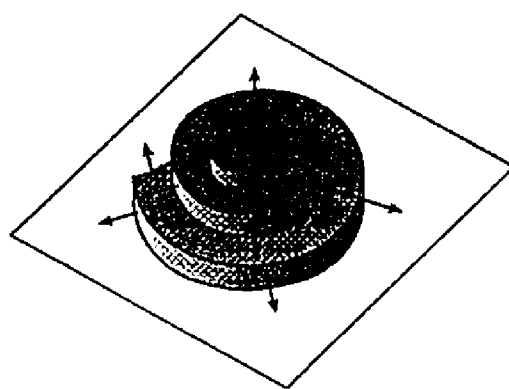


Figure 2.6d. Thin film growth via step flow mechanism, propagating the screw dislocation through the film (from Mannhart 1993).

mechanism occurs on all of the common substrate materials for  $\text{YBa}_2\text{Cu}_3\text{O}_{7-x}$  thin films. The spiral ledge growth is of importance in grain boundaries because it is part of the reason for meandering grain boundaries, which will be discussed later.

#### II.2.4.1. Thin Film Growth Techniques

There has been significant progress in thin film growth of high- $T_c$  superconductors since the initial epitaxial films were made using co-evaporation (Chaudhari *et al.* 1987). Numerous techniques have been used to grow films including laser ablation, co-evaporation, sputter deposition, molecular beam epitaxy and chemical vapor deposition (Schieber 1991a; Schieber *et al.* 1991b). Each technique has advantages and disadvantages detailed elsewhere (see Schieber *et al.* 1991b for more details). For this work only pulsed organometallic beam epitaxy (POMBE)(Duray *et al.* 1991; Buchholz *et al.* 1994) and pulsed laser ablation were used and will be discussed.

Organometallic chemical vapor deposition (OMCVD) is a basic technique that uses organo-metallic precursors to react with the substrate to deposit a film. There are many advantages to this deposition method including commercial scalability, multiple sources (for deposition of different or more complex materials), high control of deposition variables, capability of producing uniform, large area films and multilayers, *in-situ* multilayers and a relatively low cost. The major efforts in this area have been due to the scale-up abilities, which have been extremely successful in the semiconductor area. Some of the disadvantages include the large number of variables to control, high growth

rates will decrease crystal quality and often produce rough surface morphology, and precipitation due growth close to thermodynamic equilibrium conditions.

POMBE is a relatively new thin film deposition method which uses computer controlled feedback loops to control oxide film growth in a microwave oxygen plasma with atomic level accuracy (see figure 2.7). Both solid and/or liquid organometallic precursors can be pulsed to control deposition rates and stoichiometries of the thin films. The volatilized beta-diketonate organometallic sources were transported to the substrate using a helium carrier gas. The specific sources used for the  $\text{YBa}_2\text{Cu}_3\text{O}_{7-x}$  and  $\text{MgO}$  deposition were  $\text{Y}(\text{dipivaloylmethanate})_3$ ,  $\text{Cu}(\text{dipivaloylmethanate})_2$ ,  $\text{Mg}(\text{dipivaloylmethanate})_2$  and  $\text{Ba}(\text{hexafluoroacetylacetone})_2 \cdot \text{tetraglyme}$ . The background oxygen pressure in the chamber during deposition is between  $10^{-2}$  and  $10^{-3}$  torr, so the mean free path of the precursor molecule is on the order of the chamber size, creating an organometallic beam epitaxy condition. A quartz crystal monitor measures the organometallic transport rates and the computer control provides a feedback loop to adjust the individual delivery times. For  $\text{YBa}_2\text{Cu}_3\text{O}_{7-x}$ , the pulse sequence is (-Cu-Ba-Cu-Y-Cu-Ba-) in atomic scale increments. The system also features a remote oxygen plasma, which is induced by a 2.45 GHz microwave generator and provides atomic oxygen to the reaction. Therefore no post-deposition anneal is required to make a fully oxygenated superconducting sample. The oxygen plasma is also turned on prior to growth to clean the substrate, which is typically held at growth temperature ( $620^\circ\text{C}$  to  $800^\circ\text{C}$ ) for 30 minutes before deposition. Another major advantage of the system is the ability to have multiple precursors so that

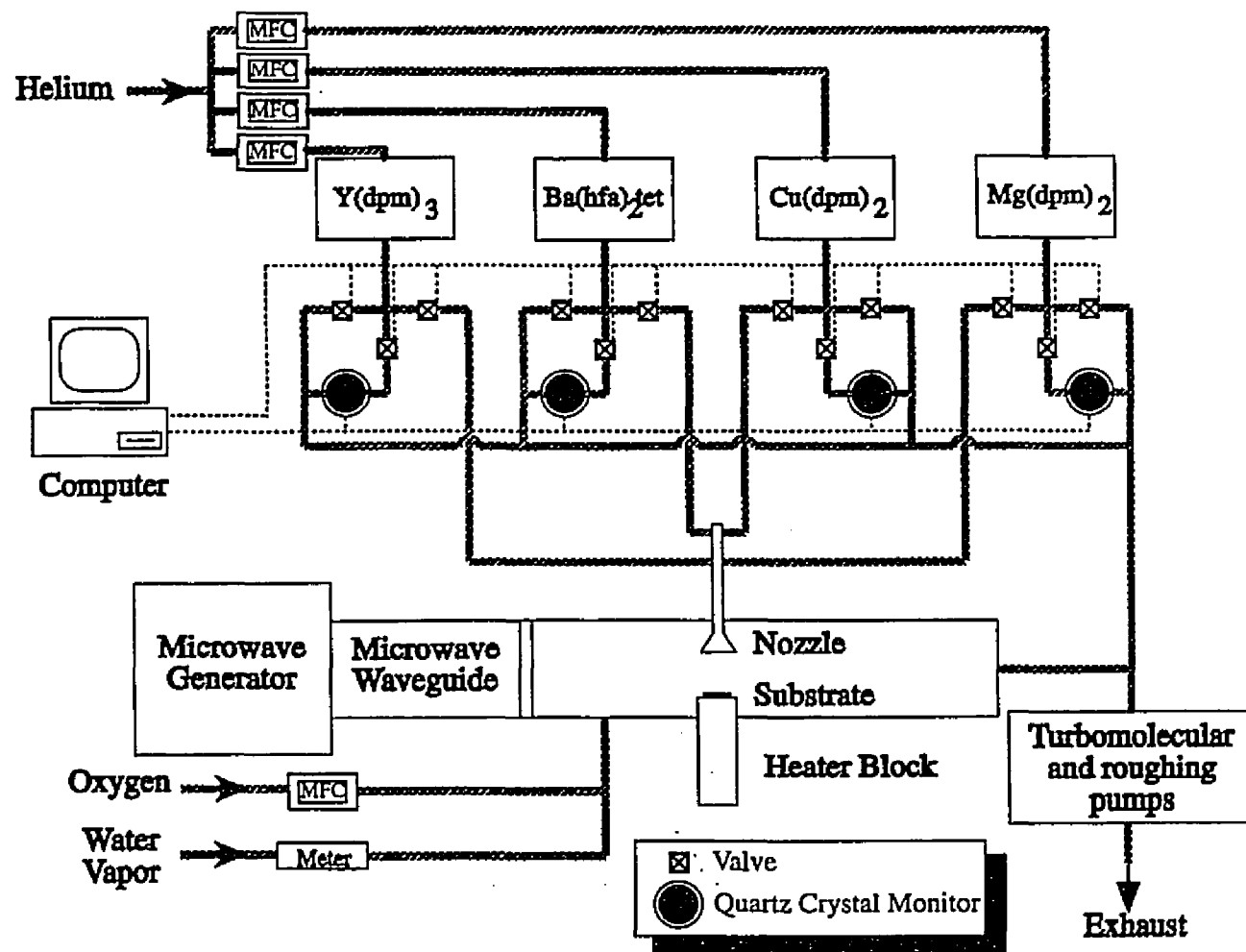


Figure 2.7. Schematic drawing of pulsed organo-metallic beam epitaxy (POMBE) thin film growth system.

multilayers can be deposited. In this study both  $\text{YBa}_2\text{Cu}_3\text{O}_{7-x}$  films and  $\text{MgO}$  films from the POMBE system were used.

Pulsed laser deposition typically uses an ultra-violet laser (e.g. halogen gas excimer laser) to ablate a stoichiometric target onto a substrate. Laser ablation can work in high  $\text{O}_2$  pressures to allow *in-situ* deposition of thin films. Other advantages of this technique are fast growth rates, smooth surface morphology and generally high quality films. It is relatively simple to deposit several different materials by using stoichiometric targets, whereas with OMCVD separate pre-cursors are needed for each element and stoichiometry is more difficult to control. The drawbacks for pulsed laser deposition are that sputter balls can form, only small area deposition is possible (about 1 in.<sup>2</sup>) and there is non uniform thickness across the substrate. Conductus has developed a method to raster the beam for larger scale deposition (up to 2 in.<sup>2</sup>) at slower growth rates.

#### II.2.4.2. Thin Film Characterization

A variety of *ex-situ* techniques can be used to structurally and chemically characterize thin films. Many *in-situ* techniques are available, however the high ambient pressures in both POMBE and PLD prevent some of their uses, and others were not available in the deposition systems used. X-ray diffraction techniques are used for many purposes, but in this experiment they provided specifically phase identification, information on epitaxial orientation and epitaxial quality. Scanning electron microscopy (SEM) was used to analyze the surface morphology of the thin films. The composition of precipitates on the surface of the films was typically identified using energy dispersive x-ray

spectroscopy (EDS). Structural characterization in the SEM was performed using electron backscattered Kikuchi patterns (EBSP), which is discussed in detail in chapter 3. EBSP gives local crystallographic information with a spatial resolution as small as 0.25  $\mu\text{m}$ . This technique allowed the orientation relationship between the substrate and the thin film to be identified as well as between grains in the film. It is a non-destructive technique which is relatively surface sensitive (typical electron beam penetration of approximately 200-300  $\text{\AA}$ ). Smoothness of surfaces can be analyzed using atomic force microscopy (AFM). AFM uses displacements of a small cantilever beam measured using a laser, to map out surface morphology. This technique was specifically used to analyze the surface of the MgO substrates both prior to and after irradiation. Both transmission electron microscopy (TEM) and high resolution electron microscopy (HREM) are destructive techniques to study the structure and chemistry of thin films and will be discussed in detail later.

### II.3. High-T<sub>c</sub> Grain Boundaries

The discovery of high-temperature superconductors provided intense excitement in the technological possibilities of these materials. This enthusiasm was tempered by fundamental materials issues, which prevented immediate implementation of these materials. The most obvious problems were that these materials were extremely complex in both structure and chemistry, and were difficult to form in various configurations necessary for different applications due to their brittle nature. Another materials difficulty was also quickly realized, the weak-link behavior of grain boundaries (Ekin *et al.* 1987). Due to the relatively short coherence length (see Table 2.4) of the high-T<sub>c</sub> materials

Material	T <sub>C</sub> (K)	Penetration Depth, λ <sub>0</sub> (nm)	Coherence Length, ξ <sub>0</sub> (nm)
Al	1.18	16	1600
Pb	7.2	37	83
Nb	9.2	39 80	38 10-30
NbTi	9.2-10		
NbN	13-16	300-600	4-7
Nb <sub>3</sub> Sn	17-18	170	6-8
Nb <sub>3</sub> Ge	21-23	150	3
YBCO	92	140	1-1.5 0.3

Table 2.4. Comparison of low-T<sub>C</sub> and high-T<sub>C</sub> transition temperatures, penetration depths and coherence lengths (from Russek 1990).

relative to the low-T<sub>c</sub> materials, any structural or chemical defect on the order of 1 nm would disrupt the superconductivity. High-angle grain boundaries proved to provide sufficient distortion to locally reduce the order parameter at the boundary and create a weak link.

A weak link is strictly defined as a region of weakened superconductivity. In the case of grain boundaries, they behave as regions with depressed critical current densities relative to a single grain. This behavior is highly detrimental for high-critical current applications such as transmission lines. In these applications, as much supercurrent needs to be passed through the material as possible, so regions of depressed critical current are not desired. There is significant work being done in bulk samples to attempt to increase the grain size or make mostly low angle grain boundaries with higher critical current densities than high angle grain boundaries, using techniques such as melt-texturing. Studies of single grain boundaries in bulk samples (described later) have been done to analyze their superconducting behavior (Babcock *et al.* 1990; Schindler *et al.* 1992; Schindler *et al.* 1994; Sarma *et al.* 1994; Field *et al.* 1992; Field *et al.* 1995). The detrimental aspects of high-angle grain boundaries forced the development of epitaxial thin films without grain boundaries on numerous substrates to avoid weak links.

The weak link behavior of grain boundary junctions can be favorable under certain circumstances. The high-angle grain boundaries exhibit some of the Josephson effects discussed earlier. If properly controlled these effects can be used in numerous active device applications, where the response of the junction can be used. One of the applications is to use the magnetic field properties of a grain boundary junction as a detector. The first commercial

high- $T_c$  device was made using a bi-epitaxial grain boundary junction in a superconducting quantum interference device (SQUID). SQUIDs can be used as magnetic field sensors for biomagnetics (magnetic resonance imaging), and geophysical applications. Other applications for Josephson like grain boundary junctions include receivers (radar), DC voltage standard and multiplier, A/D and D/A converter, digital integrated circuits, logic gates for computers and memory cells. With the advent of high-temperature superconductivity and the reduced cooling needs, there obviously is large motivation for developing high quality Josephson junctions for applications. This work is concerned with the favorable aspects of grain boundary junctions. Some of the junctions have been used in actual applications, and others are being developed for potential implementation. The study will address the weak link nature of the grain boundaries to better understand and ultimately improve the junction characteristics.

### II.3.1. Misorientation Angle

The first major systematic effort to understand the role of grain boundary weak links was by Dimos *et al.* (Chaudhari *et al.* 1988; Dimos *et al.* 1988; Dimos *et al.* 1990). This work used  $\text{YBa}_2\text{Cu}_3\text{O}_{7-\text{x}}$  thin films grown on  $\text{SrTiO}_3$  bicrystal substrates to study the normalized grain boundary critical current density as a function of grain boundary misorientation angle. Bicrystals were made by sintering two single crystal substrates misoriented by a given angle, to form a substrate template for the film deposited on top. In bicrystals with primarily [001] tilt and twist grain boundaries, it was shown that the normalized critical current density decreased exponentially for misorientation angles  $>10^\circ$  (see

figure 2.8a-b.). (Note: A tilt grain boundary is defined by a rotation to form the boundary about an axis parallel to the grain boundary plane. A twist boundary is defined by a rotation of the grain about an axis perpendicular to the grain boundary plane.) The decreased critical current density was approximately two orders of magnitude less than that of the grain for the highest misorientation angles 35°-40°. The strong decrease in critical current density was attributed to the structural disorder at the grain boundary which locally depressed the order parameter, or the density of Cooper pairs. The grain boundaries showed strong oscillations of the critical current in small applied magnetic fields, while there was no variation in the critical current of the grains, confirming weak link behavior. The current steps resulting from a single grain boundary under microwave irradiation were observed, demonstrating that the a.c. Josephson effect exists in these boundaries (Gross *et al.*). Ivanov *et al.* (Ivanov *et al.* 1991a; Ivanov *et al.* 1991b) studied nominally asymmetric (as opposed to Dimos *et al.*, who studied predominantly symmetric tilt boundaries) grain boundaries on yttria-stabilized zirconia (YSZ) substrates as a function of misorientation angle(see figure 2.9) (a symmetric grain boundary is defined as a boundary which is a mirror plane for the structure on the either side, and will be discussed more later). Ivanov(Ivanov *et al.* 1991a) also found an exponential decrease in the critical current density of the grain boundary as a function of misorientation angle confirming the result by Dimos *et al.* This work also questioned the role of the macroscopic symmetry of the grain boundary. This will later be shown to be important, but uncontrolled due to the domination of microfaceting and meandering locally at the grain boundary.

Other work has shown that certain high-angle grain boundaries can support "weak-link-free" behavior (Chan *et al.* 1990; Babcock *et al.* 1990; Eom *et al.* 1991; Eom *et al.* 1993). The first major work that directly measured a high angle grain boundary without weak link behavior was Babcock *et al.* (Babcock *et al.* 1990). This study describes a bulk bicrystal with 90° tilt and a 90° twist grain boundaries in parallel. These grain boundaries did not have any significant variations in I-V characteristics as a function of applied field, and the critical current density (albeit relatively low, about  $10^3$  A/cm<sup>2</sup>) did not diminish significantly across the boundary. The behavior was attributed to the bulk nature of the crystal, which is not constrained by a substrate as in the thin films, and can therefore choose lower energy configurations. The authors said the grain boundary properties were possibly attributable to the fact that it was in a near coincident site lattice configuration (NCSL). Coincident site lattice (CSL) models, however, are strictly geometric constructs without any energetic considerations. No work has consistently correlated NCSL grain boundaries to improved transport properties.

Eom *et al.* studied (103) YBa<sub>2</sub>Cu<sub>3</sub>O<sub>7-x</sub> thin films on (101) LaAlO<sub>3</sub> and (101) SrTiO<sub>3</sub> substrates with specific 90° grain boundaries both [010] twist grain boundaries and [010] basal plane faced tilt boundaries (Eom *et al.* 1993). The 90° [010] twist boundaries exhibited non-weak link type behavior. The implication of this result is that in step-edge junctions one of the junctions is strongly coupled (see discussion below). Therefore, some specific high-angle grain boundaries have been shown to support almost as much critical current as the grains.

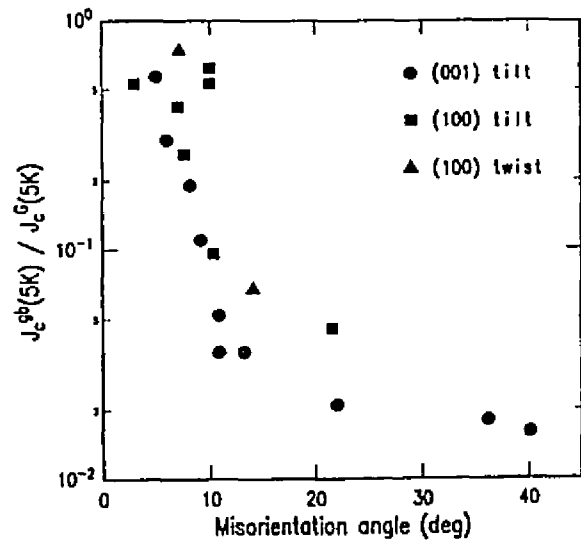


Figure 2.8a. The normalized critical current density as a function of misorientation angle for [001] tilt grain boundaries (from Dimos et al. 1990).

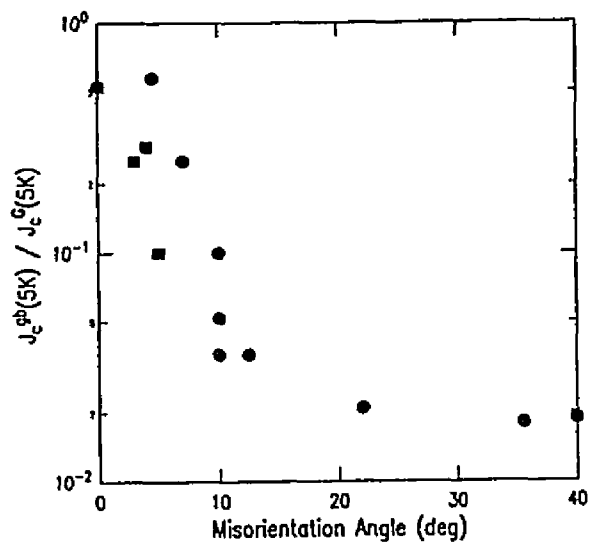


Figure 2.8b. The normalized critical current density as a function of total misorientation angle in bicrystal grain boundaries (from Dimos et al. 1990).

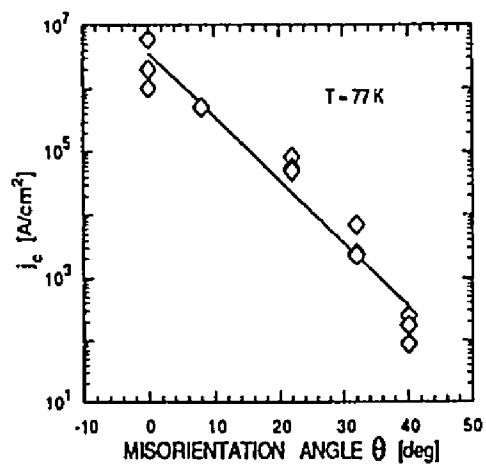


Figure 2.9. The critical current density as a function of misorientation angle in asymmetric bicrystal grain boundaries (from Ivanov et al. 1991).

The grain boundaries in this study are all  $45^\circ$  [001] tilt grain boundaries and therefore are in the high-angle weak-linked regime. They were designed to be macroscopically both symmetric and asymmetric. All the boundaries were formed in YBCO thin films using both POMBE and pulsed laser deposition.

### II.3.2. Grain Boundary Structure

The transport properties of the grain boundary can be affected by both macroscopic and microscopic structural features. Distortions on the order of the coherence length will prevent phase coherence across the boundary. Therefore the structure of the grain boundary on microscopic and macroscopic length scales can strongly affect the conduction of Cooper pairs across the junction. On a relatively large scale, grain boundaries can be interrupted by both precipitates and second phases. The occurrence of second phases and precipitates is highly dependent on the specific conditions and the method of growth used. If there is a large degree of non-stoichiometry there are more precipitates that often disrupt the grain boundary, and prevent supercurrent from traversing the boundary in that region. This is very clearly seen in the case of bulk, melt-textured samples that often have large  $\text{Y}_2\text{Ba}_3\text{Cu}_5\text{O}_{10}$  particles forming as a second phase, often intersecting the grain boundary (Wang *et al.* 1993).

Numerous studies have looked at grain boundaries in YBCO thin films using TEM (Zandbergen *et al.* 1990; Gao *et al.* 1991b; Laval *et al.* 1991; Alarco *et al.* 1993; Chisholm *et al.* 1993; Eom *et al.* 1993; Jia *et al.* 1993; Marshall *et al.* 1993; Zhu *et al.* 1993a; Traeholt *et al.* 1994b). On a microscopic scale the grain boundary structure can vary, especially in thin film grain boundaries which

typically do not follow the template of the substrate (bicrystal, bi-epitaxial etc.). This structural behavior has been labeled meandering and has been seen in various samples (Traeholt *et al.* 1994b; Miller *et al.* 1995). Meandering occurs on a length scale of hundreds of angstroms to hundreds of nanometers (deviation from the template substrate boundary) and has been related to the growth rate of the thin film. The slower the growth rate of the film, the smaller the amount of meandering, which implies that it is due to grain growth across the substrate boundary due to the faster growth in the a-b direction than in the c-direction. This also means that the macroscopic symmetry of the boundary does not match the microscopic symmetry (this will be discussed with respect to transport and chemistry later). The role of the variation will be discussed in detail later, both in the difference between symmetry and asymmetry and the uniformity of symmetry along the boundary.

The local symmetry of the grain boundary can potentially play an important role in the conduction across the boundaries (discussed more in the following section). The local symmetry of the grain boundary essentially defines the relation of the grain boundary plane to the two adjacent grains. If the grain boundary plane is a mirror plane, the boundary is symmetric, if not, it is asymmetric. There are numerous symmetric and asymmetric configurations possible for a given misorientation and they are specifically identified using the plane normal of the two adjacent grains at the grain boundary and a rotation angle. Typically due to meandering it is very difficult to isolate the independent transport properties of the different facets (discussed in detail later). This is why the macroscopically symmetric and asymmetric bicrystals did not necessarily identify the difference in the transport properties between

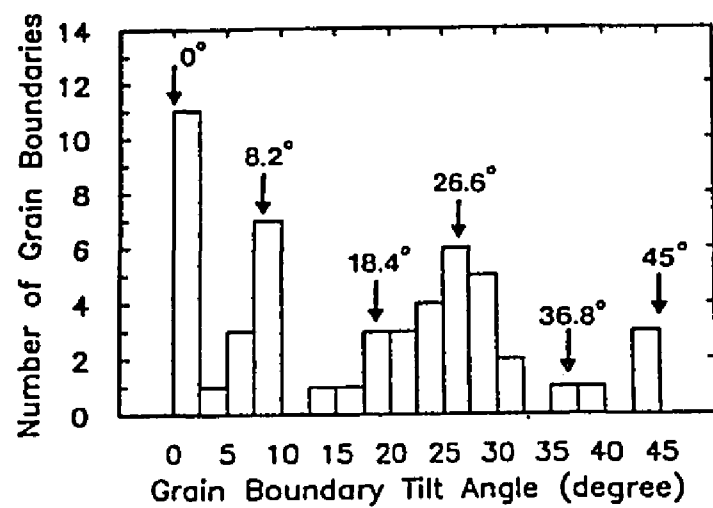


Figure 2.10. Histogram of grain boundary misorientations in polycrystalline thin films on MgO (from Shin et al. 1989).

the symmetries. Finally, and perhaps most importantly, structural disorder localized at the grain boundary can strongly affect the grain boundary properties. The combination of these different structural disorders can all potentially play a role in the weak link properties of the grain boundary junction behavior.

Specific TEM/STEM analysis of YBCO grain boundaries on MgO substrates have been studied by several groups (Tietz *et al.* 1988; Carter *et al.* 1989; Shin *et al.* 1989; Norton *et al.* 1990; Gao *et al.* 1991a; Gao *et al.* 1991b; McKernan *et al.* 1992; Neumann *et al.* 1993a; Hwang *et al.* 1990; Ramesh *et al.* 1990a; Ramesh *et al.* 1990b; Ramesh *et al.* 1991). When films were initially grown on MgO substrates, the samples were polycrystalline and formed several different orientation relations between the MgO and YBCO (Shin *et al.* 1989; Hwang *et al.* 1990; Ramesh *et al.* 1990a; Ramesh *et al.* 1990b; Ramesh *et al.* 1991). The films grew [001] epitaxial but the a-b axes of the film had several favored orientations with the substrate. Two predominant high angle grain boundaries that formed were 27° and 45° [001] tilt (see figure 2.10). Evidence for meandering was clearly seen, and there was some microfaceting for specific misorientations. One of the major interests in grain boundaries on MgO is that they are formed "naturally" as opposed to a forced epitaxial relation such as with the bicrystal or bi-epitaxial junctions. A few studies of the transport have been done, but they were on randomly isolated high-angle grain boundaries, without specific knowledge of the misorientation.

### II.3.3. Grain Boundary Chemistry

The chemical composition of the grain boundary is also potentially very important in controlling the transport properties. As previously mentioned, a large variation in local chemistry can result in second phases and precipitates at the grain boundary which disrupt the supercurrent transport. There are also other more subtle effects such as small local variations in stoichiometry at the boundary. Studies of the grain boundary composition in bulk  $\text{YBa}_2\text{Cu}_3\text{O}_{7-x}$  samples have shown some stoichiometric variation at the grain boundary (Babcock *et al.* 1989; Kroeger *et al.* 1988; Chiang *et al.* 1988). Auger electron spectroscopy demonstrated that grain boundaries varied significantly in composition, but tended to be Cu rich and O deficient (Kroeger *et al.* 1988; Chiang *et al.* 1988). Babcock *et al.* (Babcock *et al.* 1989) used energy dispersive x-ray spectroscopy (EDS) to study the local boundary composition with a 5-8nm spatial resolution. Within this resolution the grain boundary had a slight increase in Cu and decrease in O content in some regions, but no variation across other regions. This is consistent with the argument that there are modulations in the local chemistry along the boundary. In thin film grain boundaries on MgO, Shin *et al.* (Shin *et al.* 1989) used EDS to measure the local chemical composition. In the thin film case no variation was seen across the grain boundary within a stated 10 Å spatial resolution. A consistent explanation of the stoichiometry at the grain boundary in these two cases can be that in bulk samples there is less control over local stoichiometry compared to thin films. Therefore, the thin film grain boundaries will not be enriched with cations. None of the experiments correlated the local chemical composition to the grain boundary misorientation.

As mentioned above, there can be an oxygen deficiency locally at the grain boundary, which can cause a difference in the local hole carrier concentration. Decreasing the oxygen content in  $\text{YBa}_2\text{Cu}_3\text{O}_{7-x}$  to  $x=0.6$ ,(see  $\text{YBa}_2\text{Cu}_3\text{O}_{7-x}$  structure above) leads to a semiconducting phase, with the oxygen content related to the superconducting properties by the number of hole carriers available. Work by Nücker *et al.*(Nücker *et al.* 1988; Nücker *et al.* 1989; Nücker *et al.* 1990)demonstrated a correlation between the oxygen content and the oxygen pre-edge structure using electron energy loss spectroscopy (EELS) on bulk samples. The hole carriers were determined to be at the oxygen (4) sites connecting the planes and the chains, as opposed to being equally distributed among all the oxygen sites in the unit cell.

Spatially localized hole carrier concentrations were determined using parallel electron energy loss spectroscopy (PEELS) both using a field emission gun transmission electron microscope and scanning transmission electron microscopes by numerous groups (Browning *et al.* 1992; Batson 1993; Browning *et al.* 1993; Dravid *et al.* 1993; Zhu *et al.* 1993b; Babcock *et al.* 1994). Quantification of spectra from both fully oxygenated and oxygen-deficient samples using a three gaussian fit to the pre-edge was done to confirm that the hole carrier concentration was related to the YBCO superconducting properties (see figure 2.11a.) (Browning *et al.* 1992). Work by Browning *et al.*(Browning *et al.* 1993) on a symmetric 36° tilt boundary and an asymmetric 29° tilt boundary using PEELS showed that structurally there was a small unidentified region (potentially amorphous) along the asymmetric grain boundary, but a well structured symmetric grain boundary. The PEELS spectrum of the asymmetric grain boundary was oxygen depleted in a region of 20-40 Å on both sides of the

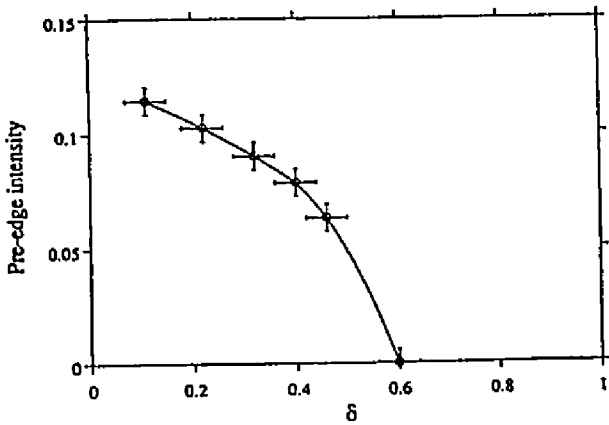


Figure 2.11a. Normalized oxygen pre-edge intensity as a function of oxygen content (from Browning et al. 1993).

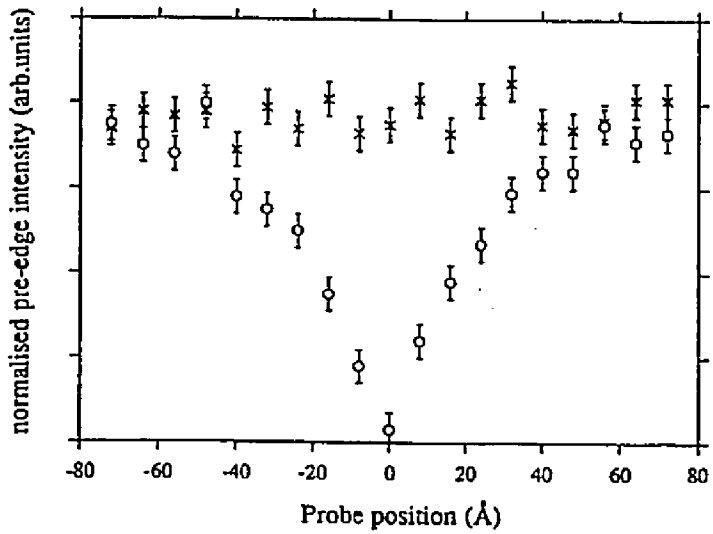


Figure 2.11b. Normalized oxygen pre-edge intensity across an asymmetric and symmetric grain boundary. The asymmetric grain boundary is represented by the circles (from Browning et al. 1993).

boundary (see figure 2.11b.). The symmetric grain boundary, however, did not have an oxygen depletion. This result suggests that there could be a difference in the transport properties of symmetric and asymmetric grain boundaries, but no transport measurements were made. Zhu *et al.*(Zhu *et al.* 1993b) studied two different facets of the same grain boundary. They looked at the effect of the grain boundary plane on the oxygen pre-edge structure using PEELS. The two different grain boundary planes had different hole carrier concentrations despite having the same misorientation angle. One part of the grain boundary had a depleted region (within the resolution of a 2 nm probe), and the second region with a different grain boundary plane did not have a depletion.

Another issue is whether there is any variation along the grain boundary. None of the previous studies mentioned looked at the variation along the grain boundary. Dravid *et al.* (Dravid *et al.* 1993) studied the hole carrier concentration along bulk grain boundaries. The hole carrier concentration was related to the oxygen content, and exhibited a change between approximately O<sub>6.85</sub> and O<sub>6.5</sub>. This result was on a variety of grain boundaries both symmetric and asymmetric with varying misorientation angles, which were not correlated to the depletion. Babcock *et al.*(Babcock *et al.* 1994) studied electromagnetically characterized bulk bicrystals using PEELS. They correlated hole carrier depletion with weak-link behavior using a 2 nm probe stepped across the grain boundary. Weak-linked grain boundaries had a depletion in the hole carrier concentration at the boundary, but the strongly coupled junctions (as measured by decrease in critical current as a function of applied magnetic field) did not show a depletion. Even re-oxygenated samples of weak-

linked grain boundaries remained depleted (although increased relative to pre-anneal measurements).

The chemistry of the grain boundary appears to play an important role in the weak link behavior. It is difficult, however, to distinguish between the local composition and the effect of the misorientation. Part of the chemical effects could be due to the local structure (as shown by Browning)(Browning *et al.* 1993), and will be discussed in detail in the results.

#### II.3.4. Direct Transport Properties

Significant work has been done on the transport properties of grain boundary junctions. A wide variety of junctions have been studied using numerous techniques. The most important and relevant studies concerning direct transport measurements of individual grain boundary junctions are reviewed in this section.

##### II.3.4.1. Resistive Transition

The resistive transition is used to identify the critical temperature and study some of the normal state properties of the grain boundaries. Since a grain boundary is surrounded by two grains, there are usually two resistive transitions. First a transition for the bulk superconducting material, followed by a transition for the grain boundary (if it is a weak link, and the measurement is sufficiently sensitive). The reason for the lower  $T_c$  of a weak linked grain boundary is because of the depressed critical current density. The resistance is measured as a function of temperature for a given applied current. Therefore the critical temperature is determined by the applied current, which dictates the

resistance sensitivity of the measurement (and is directly related to the sensitivity to the critical current). This value is always reached in a weak linked grain boundary, prior to the grains due to the depressed critical current. Low-field SQUID measurements of the Meissner effect are typically used to measure the bulk  $T_c$ , but cannot detect the grain boundary transition because it is not a significant volume fraction of the sample. The normal state resistance has been generally shown to be temperature-independent (Gross 1992). Most of the variation with temperature in  $I_c R_n$  is therefore due to the temperature dependence of the critical current.

The grain boundary junction resistance has also been attributed to thermally activated phase slippage (TAPS) (Gross *et al.* 1990; Ambegaokar *et al.* 1969). TAPS is caused by thermal fluctuations that disrupt the phase coherence of a Josephson junction. If the phase slips by  $2\pi$ , there is a finite resistance across the junction. Experimental evidence has demonstrated the effect of TAPS on the transition due to the high operating temperature of the junctions relative to the low- $T_c$  junctions where this is not a significant effect (Gross *et al.* 1990).

#### II.3.4.2. Current-Voltage Characteristics

Current-Voltage characteristics can be used to describe several aspects of grain boundary junctions. First, the basic I-V measurement gives the critical current ( $I_c$ ) of the region measured. The current is ramped up across a junction until a specific offset voltage is measured (typically  $1 \mu V$ ). This value is defined as the critical current above which the sample is in the normal state. There are other criteria that can be used such as a given resistivity, which are discussed elsewhere (see Ekin(Ekin 1989)). The weak link grain boundary behavior can be

isolated from the adjacent grains because the grains remain superconducting and have no voltage drop during the transition of the boundaries. Therefore the transition to the normal state of the grain boundary can be readily analyzed without the superposition of the grain characteristics. The weak link behavior of individual grain boundary junctions isolated by Chaudhari *et al.* (Chaudhari *et al.* 1988), was first identified by current-voltage measurements. Dimos *et al.* showed an exponential decay of the normalized critical current density when the misorientation angle exceeded approximately 10° (described previously). After the transition to the normal state, the normal state resistance can be identified ( $R_N$ ) by determining the slope of the I-V characteristics when at high voltages. Gross (Gross 1992) showed that  $R_N$  is typically independent of temperature for most types of junctions. The  $I_C R_N$  value is a characteristic value of the junction and is an important design parameter for applications. This value is the voltage that can be placed across the junction, and determines the necessary circuit parameters for a given device.

The shape of the I-V characteristic can be indicative of the type of junction behavior. Lathrop *et al.* (Lathrop *et al.* 1991; Moeckly *et al.* 1993) used the resistively shunted junction model for the I-V characteristics in weak-linked grain boundaries on MgO. The grain boundaries were found by making microbridges smaller than the average grain size to randomly isolate individual grain boundaries, however these were never directly correlated to misorientation angle. Depending on the value of the Stewart-McCumber parameter,  $\beta$ , the curve can vary from a sharp voltage onset (junction capacitance = 0) to a gradual voltage onset (larger capacitance values). At

higher temperatures, close to  $T_c$ , the I-V curve can become more rounded, indicating a flux-flow type behavior as opposed to the RSJ-type behavior.

One way of identifying the type of junction is to analyze the critical current as a function of temperature close to  $T_c$ . Ambegaokar *et al.* (Ambegaokar *et al.* 1963) demonstrated that the scaling behavior of a junction can identify the difference between low- $T_c$  S-N-S and S-I-S type junctions. The temperature dependence of the critical current is predicted to be proportional to  $(1-T/T_c)^n$ ,  $n=1$  for a S-I-S junction and  $n=2$  for a S-N-S junction. However, recent theoretical predictions suggest that the reduced coherence length in the high- $T_c$  materials would give  $n=2$  for both S-I-S and S-N-S junctions making them indistinguishable (Deutscher *et al.* 1987). This has not been confirmed experimentally. Grain boundaries on MgO exhibited  $I_c \propto (1-T/T_c)^n$  with  $n=2$  type behavior. This type of behavior was attributed to S-N-S junctions, but no clear N layer was identified.

Significant information can be obtained from the I-V data, but some key issues remain unresolved. The critical current only measures the total supercurrent traversing the junction. It does not identify whether the  $J_c$  fluctuates as a function of position, i.e. whether  $J_c$  is uniform across the junction, or varies along the junction. This is one of the key questions in identifying the weak link behavior across the grain boundary. Also, virtually all the transport work on these junctions was not directly studied with respect to microstructural features.

#### **II.3.4.3. Magnetic Field Properties**

The magnetic field behavior of the grain boundary junction can provide unique information on the uniformity of the supercurrent distribution along the boundary length. Two different magnetic field regimes are usually studied to determine the junction behavior. Small magnetic fields are used to identify oscillations in the critical current as a function of applied magnetic field below  $H_{c1}$  (approximately 200 G for YBCO). Large magnetic fields are used to study residual critical currents, which can be described by models of inhomogeneous junctions. The scale of the inhomogeneities along the grain boundary as a function of applied field follows eq. 2.11: (Mayer *et al.* 1993)

$$\Delta x = \frac{\Phi_0}{2B_{\max}\lambda_L} \quad (2.11)$$

where  $\Delta x$  = the real space size of the superconducting region

$\Phi_0$  = the flux quantum

$B_{\max}$  = the maximum applied magnetic field

$\lambda_L$  = the London penetration depth

Also "weak-link-free" grain boundaries have been identified by high field measurements with no degradation in the critical current density of the grain boundary (Babcock *et al.* 1990; Eom *et al.* 1991).

Several studies have looked at the magnetic field dependence of grain boundaries in high-T<sub>c</sub> superconductors. A couple of the studies (Eom *et al.* 1993; Babcock *et al.* 1990) showed that specific high-angle grain boundaries (90° [100] twist and [100] tilt) maintain high critical currents at large applied fields, and are therefore strongly coupled junctions. In the case of weak-link grain boundaries the magnetic field behavior is related to the coupling across the junction.

The magnetic field dependence of the critical current density of thin film weak-link grain boundary junctions has been studied on 45° grain boundaries

on MgO, (Lathrop *et al.* 1991) bicrystal grain boundaries,(Mayer *et al.* 1993; Sarnelli *et al.* 1993b; Sarnelli *et al.* 1993c; Daumling *et al.* 1992; Froehlich *et al.* 1995), bi-epitaxial grain boundaries(Rosenthal *et al.* 1991), and bulk grain boundaries (Schindler *et al.* 1992). Lathrop *et al.* (Lathrop *et al.* 1991)modeled magnetic field data using an inhomogeneous critical current distribution along the grain boundary. While not perfect, the data certainly hinted that this type of current distribution could be consistent with the results. The magnetic field oscillation as a function of grain boundary width was analyzed, using bi-epitaxial junctions, by Rosenthal *et al.*(Rosenthal *et al.* 1991). They showed that the scaling of the lobe width,  $\Delta B$  (the spacing between valleys in the  $I_c(B)$  data), scaled as  $1/w^2$  as opposed to the usual  $1/w$  behavior. Mayer *et al.* determined that the critical current dependence on the width of the boundary did not saturate indicating that the current was not limited to the Josephson penetration depth.

In high applied magnetic fields (2-12 T) a residual current is typically observed across the grain boundary junctions (Sarnelli *et al.* 1993b; Sarnelli *et al.* 1993c; Daumling *et al.* 1992; Froehlich *et al.* 1995). Small oscillations are still observed in the critical current at these high fields. This has been explained by Sarnelli *et al.* (Sarnelli *et al.* 1993c)as inhomogeneities on the length scale of the coherence length (Dayem-bridge model explained below). Froehlich *et al.* (Froehlich *et al.* 1995) describes the grain boundary as regions of strongly varying critical current densities with length scales from nm to  $\mu\text{m}$  (discussed more below). This work assumed a constant phase variation along the boundary which will later be shown to be incorrect. The combination of high and low magnetic field measurements definitely suggests length scales for

inhomogeneities of the grain boundary, but the key is to identify microstructural features that may cause this behavior.

### II.3.5. Grain Boundary Models

Numerous attempts have been made to model the grain boundaries both using transport data and microstructural data. The models tend to be relatively simplistic and based on empirical data, however, they do provide insight into the weak link behavior of grain boundaries. The first model suggested was by Dimos *et al.* (Dimos *et al.* 1988) who said that the dislocation spacing along the grain boundary was proportional to the magnitude of the critical current density. Therefore, for small angle grain boundaries the dislocation spacing is roughly proportional to  $1/\theta$  and has a similar degradation in  $J_c$  as the misorientation angle drops. The dislocation cores were believed to have a depressed order parameter, i.e. a reduced number of Cooper pairs due to structural distortions, or the dislocations could act as preferential penetration sites for magnetic flux. The spacing in between the dislocations was considered strongly coupled, and therefore as this region diminished, so did  $J_c$ . TEM work by Gao *et al.* confirmed that low angle grain boundaries consisted of a series of discrete edge dislocations with a finite core structure whose dimensions are commensurate with the strong decrease in  $J_c$  as a function of  $\theta$  (Gao *et al.* 1991a). Low angle grain boundary models breaks down for higher angle grain boundaries where dislocation cores overlap. A clear shortcoming of such models is the relation to typical microstructures of high-angle grain boundaries, which never exhibit perfectly periodic dislocation spacings as assumed by the model (this will be discussed in chapter VII and appendix I).

The transport properties of the junctions were attributed by Gross to be due to resonant tunneling across the boundary (Gross 1992). The model is based on an S-I-S structure where the insulator consists of a high density of defect states (presumably oxygen vacancies) at the boundary. There are two tunneling processes across the boundary, direct and indirect. The direct tunneling results in Cooper pairs directly traversing the boundary. In the indirect tunneling process, pairs of electrons tunnel to defect sites in the insulator before tunneling to the second grain. This model successfully describes some of the transport properties of the boundary. However, it definitely does not explain the critical current variation at low applied magnetic fields. The magnetic field data are essential in understanding the current distribution along the boundary. The S-I-S junction is also not directly correlated to microstructural features along the boundary.

A third model was developed by Sarnelli *et al.* (Sarnelli *et al.* 1993a; Sarnelli *et al.* 1993c) based on residual currents across grain boundary junctions in high magnetic fields. This model, called the Dayem bridge model, is a series of Dayem bridges lying in parallel along the grain boundary separated by normal regions. A Dayem bridge is a constriction in a superconductor down to the size of the coherence length, and was first developed for low- $T_c$  materials (Dayem *et al.* 1967). This model predicts weak links on the order of a few nm in length lying in parallel with normal paths. The other corroborating evidence is that the I-V characteristics of the junctions agree with the RSJ model (as does the Dayem bridge). Close to  $T_c$  the Dayem bridge model predicts a dependence of  $I_C(1-T/T_c)^n$  with  $n=2$ ; however other data suggests that Dayem bridges have  $n=1.5$  dependence (Likharev 1979). A theoretical calculation of the magnetic

field behavior for a similar set of Josephson junctions in parallel shows that a residual critical current persists due to the inductance of the coupled junctions (Miller *et al.* 1991). One of the difficulties with this model is that experimentally a set of parallel Dayem bridges have not been measured, and little data is available on the transport properties of these junctions in general.

The Dayem bridge model was developed further by Dravid *et al.* (Dravid *et al.* 1993). They found a modulation of the hole carrier concentration along the grain boundary and related it to a modified Dayem bridge model. In this model superconducting regions are surrounded by regions with varying oxygen stoichiometry. These regions would have different electromagnetic properties, which would affect the electromagnetic properties of the grain boundary. It was also stated that the distance between the different regions was greater than the coherence length of approximately 1.5 nm, and would generally be approximately 20-50 nm in size. It should be noted that the data were not directly correlated to either microstructure or specific grain boundary misorientations.

Another model, called the filamentary model, was proposed by Moeckly *et al.* (Moeckly *et al.* 1993). This model is a composite superconductor, consisting of superconducting filaments shunted by normal conduction paths (essentially superconducting filaments in a non-superconductive matrix). The superconducting filaments are assumed to be randomly connected at the grain boundary. By studying the electromigration of oxygen it was determined that the non-superconductive matrix is due to oxygen disorder in the basal plane. The average lateral dimension of the filaments was estimated to be between the coherence length (1.5 nm) and a correlation length determined from magnetic

field data (60 nm). The model was not correlated to microstructural features and was only fit to transport data. Likewise the grain boundaries studied were randomly isolated on MgO substrates and found to be mostly 27° and 45° tilt grain boundaries, but the actual misorientation was not related to the transport properties.

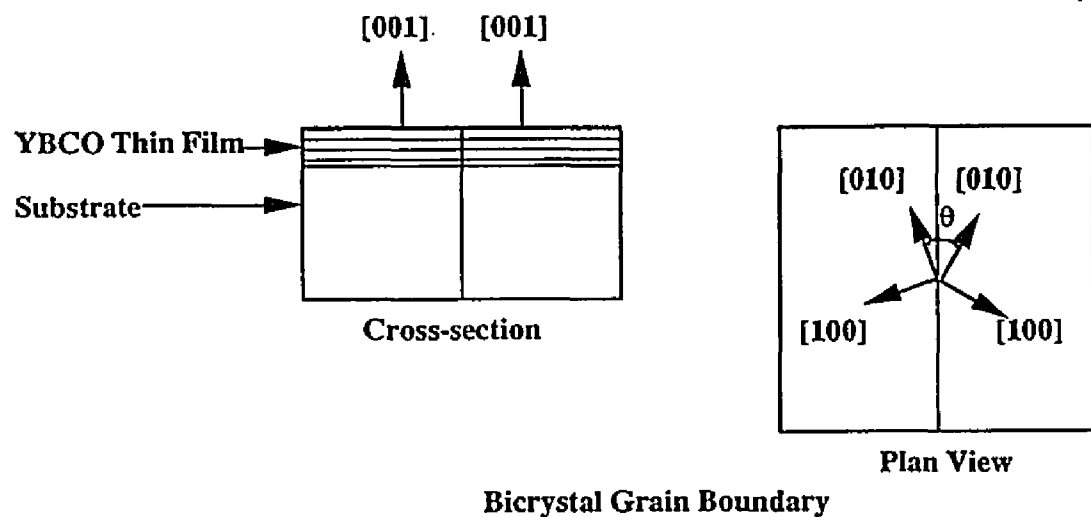
All of these models are successful in describing certain aspects of grain boundary weak-link behavior. However, none of them are completely consistent with all the data, and the details of the boundary are not well known (e.g. distances and sizes of normal regions, etc.). Also, a thorough and consistent agreement between the microstructure and transport properties has not been determined.

#### II.4. $\text{YBa}_2\text{Cu}_3\text{O}_{7-x}$ Junctions

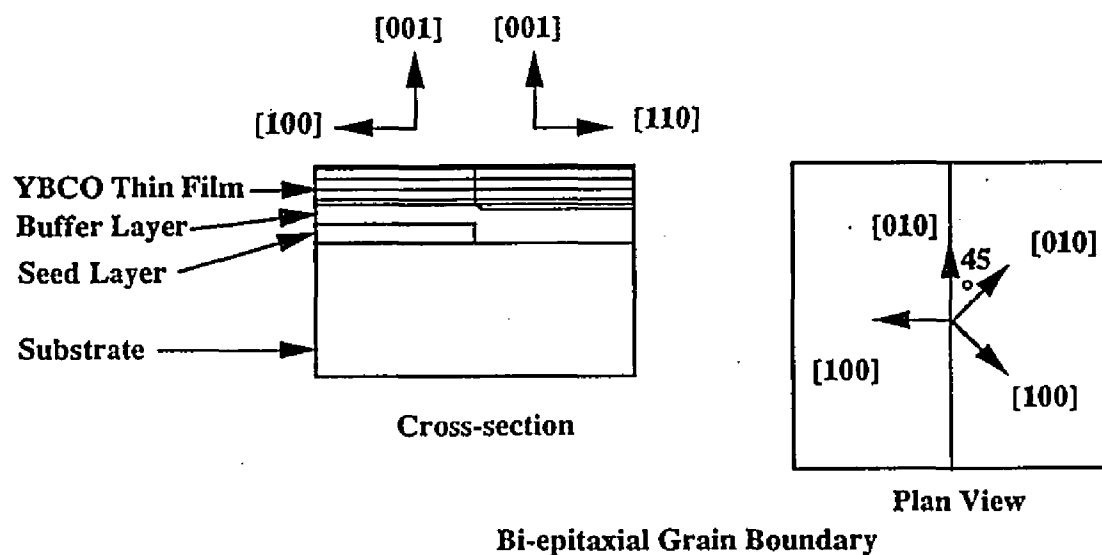
High quality high- $T_c$  grain boundary Josephson junctions with reproducible transport properties are difficult to make due to basic materials issues. Since the coherence length is on the order of 15 Å, there must be significant control over the materials growth to form reproducible transport properties in junctions. The first junctions made were based on thin film high angle grain boundaries since they could be formed relatively easily (see figure 2.12 a-b.). By using various epitaxial conditions to control the grain boundary formation, several different techniques were used to make grain boundary junctions including bicrystals,(Dimos *et al.* 1988; Dimos *et al.* 1990) steep step-edges,(Jia *et al.* 1991; Jia *et al.* 1992; Daly *et al.* 1991) bi-epitaxial(Char *et al.* 1991a; Char *et al.* 1991b) and sputter-induced epitaxy (Vuchic *et al.* 1995a; Vuchic *et al.* 1995b; Chew *et al.* 1992b).

Initially bicrystals were used,(Dimos *et al.* 1988; Dimos *et al.* 1990; Ivanov *et al.* 1991a) where two bulk substrates were misoriented to the desired angle and sintered together to form an epitaxial substrate with two different epitaxial orientations. The substrates can be aligned in numerous configurations including symmetric and asymmetric tilt, as well as twist boundaries. Various materials were used such as SrTiO<sub>3</sub>, yttria stabilized zirconia (YSZ) and MgO (Lu *et al.* 1993). This technique forms relatively high-quality junctions with decent reproducibility, but is expensive due to the bicrystal cost. Another drawback is that the grain boundary can be formed in only one position along the substrate, which is fine for superconducting quantum interference devices (SQUID), but not good if multiple junctions are necessary for other applications. Also it is more difficult to form multilayers due to propagation of the bicrystal template into the subsequent layers deposited.

The second type of junction called the step-edge junction is made by forming a steep step in the substrate (Daly *et al.* 1991; Jia *et al.* 1991; Jia *et al.* 1992; Jia *et al.* 1993). The step is typically made using an ion beam to remove part of the substrate (usually LaAlO<sub>3</sub>, but others have been used) and form a step approximately 100 nm deep. The film is then deposited with a c-axis epitaxy on the upper and lower ledges, but an a-axis film is formed along the step edge. The junction then consists of two grain boundary junctions, one at the top step edge, which is a symmetric tilt grain boundary, and a grain boundary at the lower edge which is less well defined. The upper junction has been studied by measuring films with analogous grain boundary configurations (Eom *et al.* 1991; Eom *et al.* 1993). These grain boundaries appear to be strongly coupled and maintain a large supercurrent in field. The lower junction is probably more

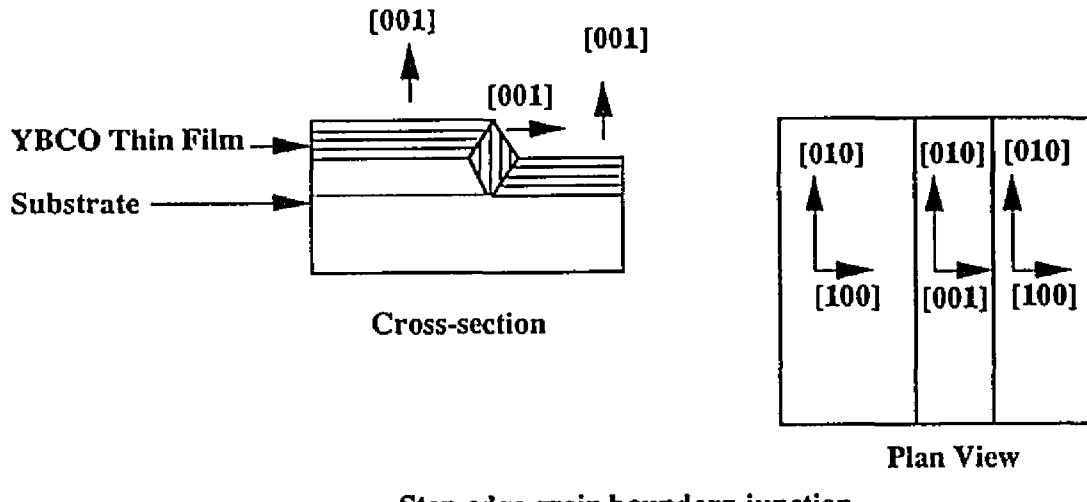


Bicrystal Grain Boundary

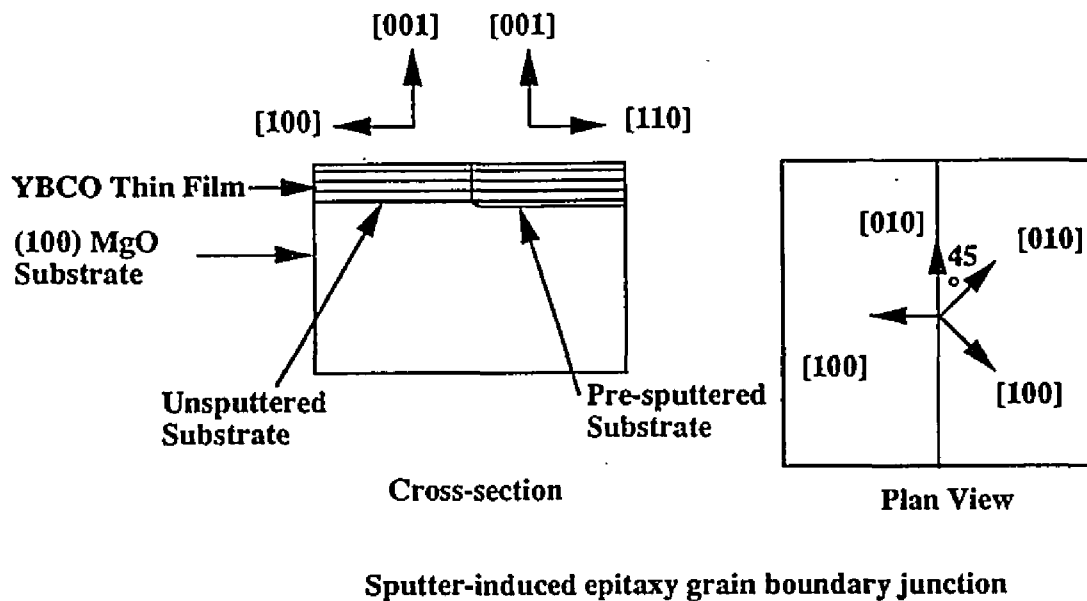


Bi-epitaxial Grain Boundary

Figure 2.12a. Bicrystal and bi-epitaxial grain boundary junctions.



Step-edge grain boundary junction



Sputter-induced epitaxy grain boundary junction

Figure 2.12b. Step-edge and sputter-induced epitaxy grain boundary junctions.

responsible for the weak link behavior, but is unfortunately more difficult to form reproducibly. The step-edge technique can be used to make junctions in virtually any configuration on a substrate. There are three major drawbacks in using the step-edge junctions. First, it is difficult to make reproducible junctions, especially from chip to chip. The second drawback is the limitation in the misorientation angle between the grains (the grain boundaries are all between a- and c- axis grains), and two grain boundaries are more difficult to control than one. Finally, due to the step edge it is difficult to form planar multi-layer configurations for integration with other materials systems.

One of the first high-T<sub>c</sub> commercial products was developed using another type of grain boundary junction called a bi-epitaxial junction (Char *et al.* 1991a; Char *et al.* 1991b). A 45° [001] tilt grain boundary is formed by modifying the epitaxial condition on two different parts of the substrate. The substrate consists of a YSZ base followed by layers of CeO<sub>2</sub>, PrBa<sub>2</sub>Cu<sub>3</sub>O<sub>7-d</sub>, SrTiO<sub>3</sub>, MgO, CeO<sub>2</sub> (see table 2 for lattice mismatch). The CeO<sub>2</sub> is then selectively sputtered away . The roles of these various layers in producing a 45° tilt grain boundary are as follows. The relation between the CeO<sub>2</sub> and Y-Ba-Cu-O is such that Y-Ba-Cu-O[110] || CeO<sub>2</sub>[100]. On SrTiO<sub>3</sub> the epitaxial relation is Y-Ba-Cu-O[100] || SrTiO<sub>3</sub>[100], therefore the epitaxial growth on the CeO<sub>2</sub> will be rotated 45° with respect to the thin film orientation on the SrTiO<sub>3</sub>. Some substrates have also been grown where a final layer of CeO<sub>2</sub> or SrTiO<sub>3</sub> have been added as a buffer. The grain boundary remains rotated since the epitaxial relation is CeO<sub>2</sub>[110] || SrTiO<sub>3</sub>[100]. These junctions are limited in the misorientation angle (45° [001] tilt grain boundary) and by relatively low I<sub>c</sub>R<sub>n</sub> products. The advantage is that the technique can produce junctions in any configuration

(limited by photolithographic capabilities). Since the bi-epitaxial junction is based on multi-layers it can be integrated into other multi-layer systems.

Sputter induced epitaxy is another technique developed to form 45° [001] grain boundary junctions (Vuchic *et al.* 1995a; Vuchic *et al.* 1995b; Chew *et al.* 1992b). This technique will be described in detail in the body of this thesis and compared in more detail with the other junctions mentioned above.

Most recently junctions have been made using superconducting-normal-superconducting step-edge structures (see figure 2.10) (Char *et al.* 1994). These junctions are not based on grain boundaries, but on epitaxial  $\text{YBa}_2\text{Cu}_3\text{O}_{7-\text{x}}$  thin films interrupted by 1-10 nm of a normal material. The advantage of this technique over grain boundary junctions is the ability to control the junction transport properties by modifying the normal material, or changing the thickness. However, there are many materials issues in forming uniform junction regions including chemical compatibility, interdiffusion, lattice parameter match and similar coefficients of thermal expansion. These issues are beyond the scope of this thesis and are described elsewhere (Olsson *et al.* 1993).

Each junction technique has its advantages for specific applications. For example the best SQUIDs are made from bicrystals since only two junctions in parallel are required. Bi-epitaxial junctions are good for multi-layer systems and where arrays of junctions are needed. The sputter-induced grain boundary junctions described later are tremendously simple to form and have potential as a junction technology. This work studies some of the important microstructural aspects of these junctions so that they can be better understood, and ultimately controlled to the extent where they can be developed for routine commercial use.

# **Chapter III. Experimental Procedure**

This chapter describes in detail the procedure used in this study. The specific equipment used and developed for the experiments will be discussed. Finally there will be a description of the general techniques and methodologies developed to perform the pre-sputter treatment for the sputter-induced grain boundaries, the cryogenic transport measurements and the structural characterization.

## **III.1. Equipment**

Several pieces of equipment were developed and used in this research. These included a low voltage ion mill designed and built for both substrate pre-treatments and thin film patterning. An electron backscatter detector was acquired for determination of local crystallographic information from thin film samples. Also a cryogenic four-probe measurement system was built to perform a variety of low temperature measurements on grain boundary junctions. This section describes the relevant aspects of the aforementioned equipment with respect to the experiments performed.

### **III.1.1. Low Voltage Ion Mill**

A low voltage ion mill was designed for two primary functions in the experimental procedure. First, it was used to pre-irradiate MgO substrates prior to thin film growth for the sputter-induced epitaxial junctions (the ion mill has

also been used to form step-edges and for general sputtering purposes). The ion source was also used to pattern thin films with microbridges for transport measurements by sputtering the thin film covered by metal or photoresist contact masks. The sputter-induced epitaxy process is based on the pre-sputter treatment in the ion mill, therefore the ion mill and chamber will be described in detail.

Schematics of the ion source chamber and the sample stage are shown in Figs. 3.1 and 3.2. The source is a Kaufman type Ion Tech Model 3.0-1500-100 Ion Source, which uses a heated tungsten filament as a cathode to emit electrons. The magnetic field from the pole pieces causes the electrons to have a long trajectory prior to reaching the anode. These electrons ionize argon gas that flows through the source creating positively charged ions. The ions are then accelerated through the accelerator grids with a final energy between 50 eV to 1000 eV. The accelerator grids are 3 cm in diameter and are made from graphite. There is also a tungsten neutralizer filament that is beyond the accelerator and emits electrons to help collimate the ion beam (by providing negatively charged electrons to prevent repulsion between ions) and prevents ion backstreaming towards the accelerator grids. A graphite aperture is also typically placed in front of the neutralizer to further collimate the beam. The beam current density, usually approximately  $1 \text{ mA/cm}^2$ , is measured using the current from the sample stub, and the value varies with the specific beam conditions.

The sample sits on a holder 4 inches from the accelerator grid in a high vacuum chamber that is a 6-way cross with four 8-inch flanges and two 6-inch flanges. A cryopump with a pumping speed of 660 liters/second (for argon)

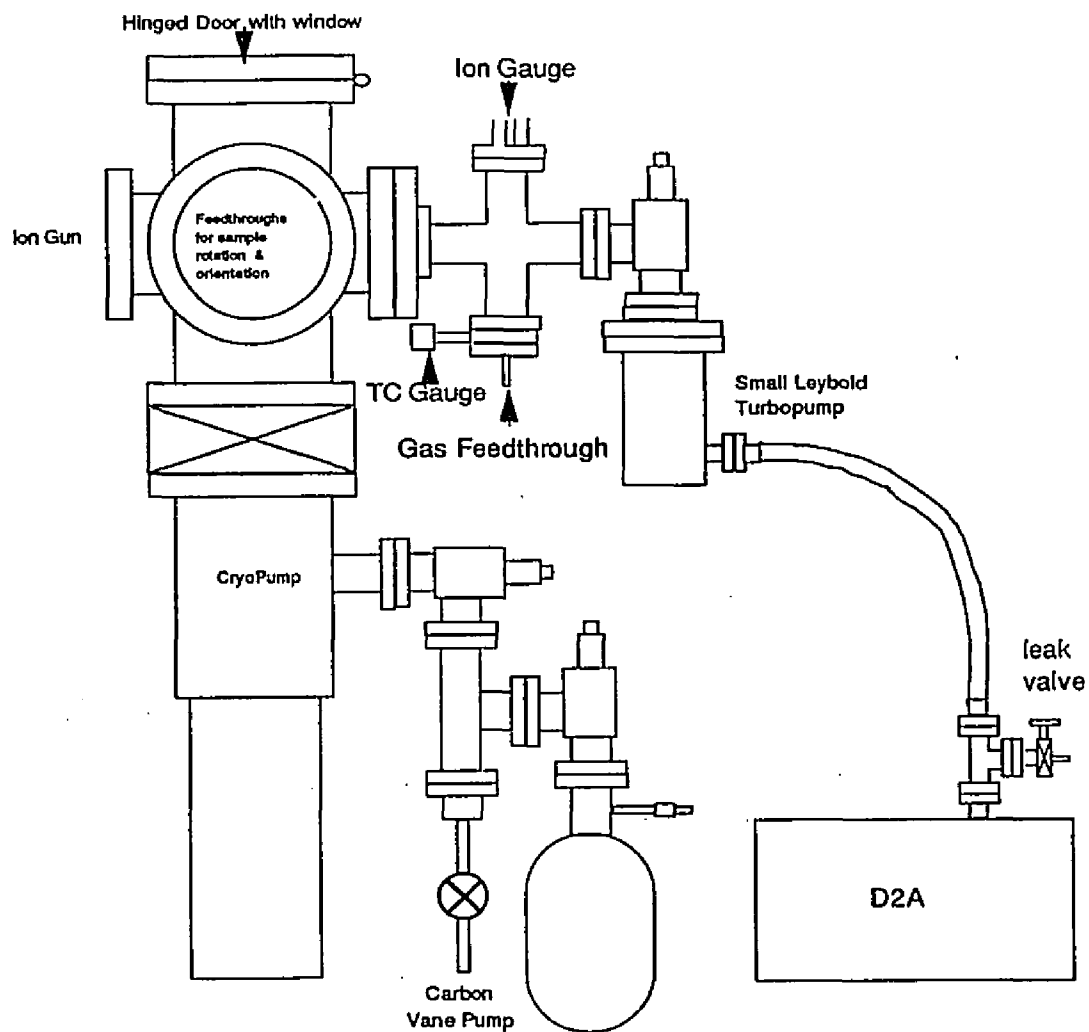


Figure 3.1. Low-voltage ion mill chamber schematic.

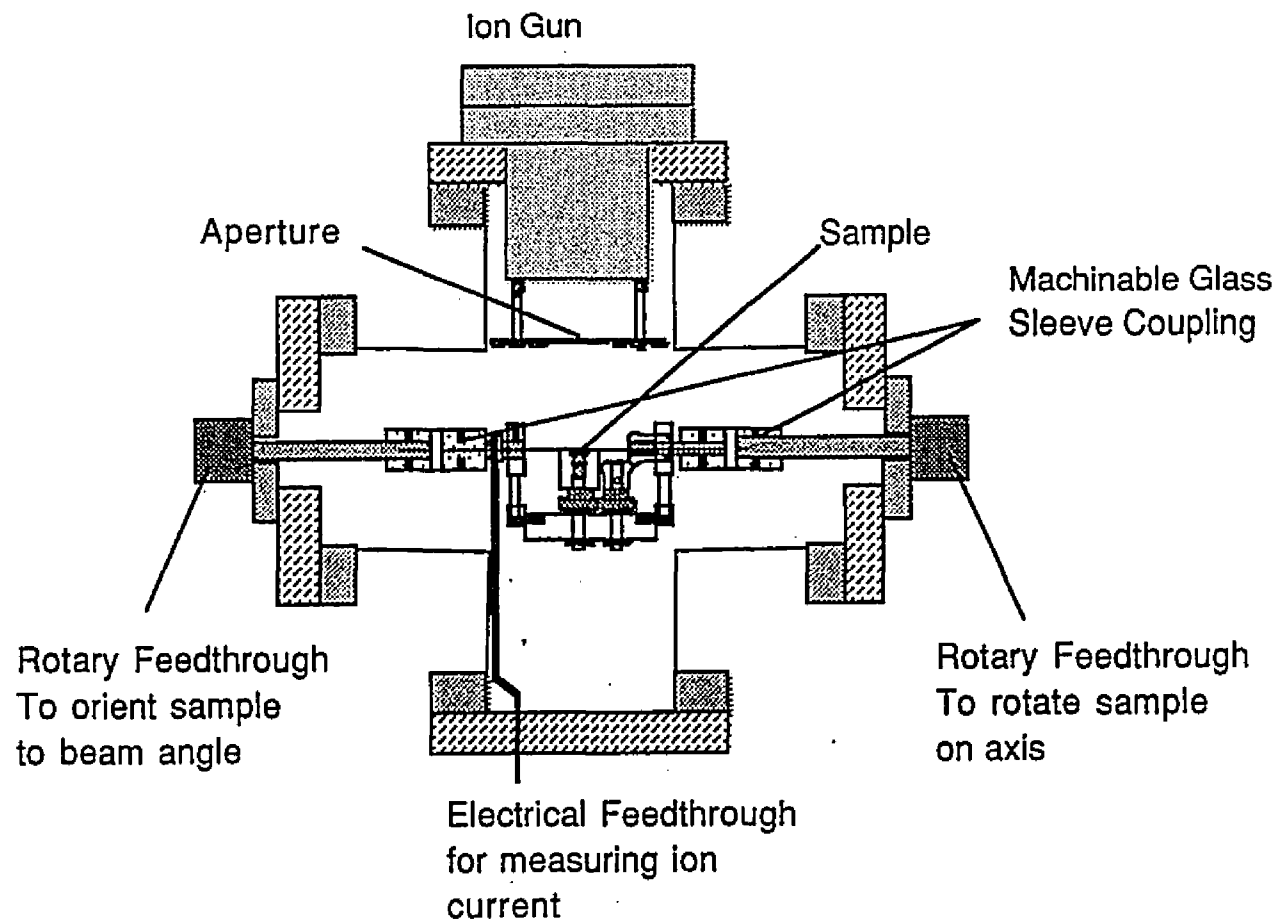


Figure 3.2 Low voltage ion mill sample stage.

and a throughput of 300 standard cubic centimeters (sccm) of argon sits directly below the chamber on one of the 8-inch flanges. This pump maintains a base pressure of  $5 \times 10^{-7}$  Torr without any gas flow, and approximately  $1-2 \times 10^{-4}$  Torr with 3 sccm of argon gas flowing. Cryopumps use helium to cool a cold head to approximately 10-14 K. This method allows for clean pumping without any contamination from pump oil (as is typical with diffusion and roughing pumps). The cryopump can be isolated from the chamber using a gate valve, providing straightforward sample exchange. A hinged door allows the sample stub to be accessed and a small turbo pump (backed by a small roughing pump and isolated by a valve) evacuates the chamber to as low as  $9 \times 10^{-6}$  Torr before crossing over to the cryopump. A thermocouple gauge and an ion gauge are used to measure the chamber pressure at all times. This system allows a turn around time as short as 15 minutes between samples.

The stage assembly is supported by two rotary feedthroughs on opposite 8 in. flanges (see figure 3.2). The stage allows  $360^\circ$  rotation about the normal axis of the stub, and  $360^\circ$  rotation about the axis of the rotary feedthrough (with the sample lying on the axis). A motor drive is set up to rotate the stage about the stub normal at approximately 10 rpm (often used to provide uniform sputtering). A tantalum shield is affixed to the stage and can be rotated to block the beam. This shield is used to protect the sample while beam conditions are being set. Several different stages can be used depending on the specific requirements including a standard Gatan ion mill holder, but for the substrate pre-growth sputtering and thin film patterning, a copper block (modified to accommodate various masks) was used to act as a large thermal mass to minimize beam heating. The sample is typically affixed to the copper stub using

silver paint to maximize thermal contact and conduction between the sample and stub. The sample stage is electrically isolated from the chamber using insulating Macor pieces. The current from the sample can be read, and the sample maintained at ground potential. The stage can also be connected to a liquid nitrogen cold finger for cooling to further reduce beam heating. The details of the sputtering conditions for particular applications will be discussed later.

### III.1.2. Electron Backscatter Detector

An electron backscatter detector was used to determine the local crystallographic orientation of the thin film  $\text{YBa}_2\text{Cu}_3\text{O}_{7-x}$  samples. The basic principle of an electron backscatter detector is to image inelastically scattered electrons which meet a simple Bragg condition upon leaving the sample (see figure 3.3). The inelastically scattered electrons form the equivalent of a point source in the sample (with electrons scattered in all directions). Some of the electrons are completely backscattered and are subsequently elastically scattered as they leave the sample (Venables *et al.* 1973; Dingley *et al.* 1990; Dingley 1991). These electrons therefore have crystallographic information from the crystal and form Kikuchi patterns that describe the orientation of the grain. The Kikuchi patterns are imaged on a special phosphor screen that is particularly sensitive to the electron energies of these electrons (to eliminate noise). The phosphor screen is imaged by a low-light CCD camera and then displayed on a video monitor. The image is typically integrated over 10 frames and an integrated background is subtracted from the image to improve the image quality.

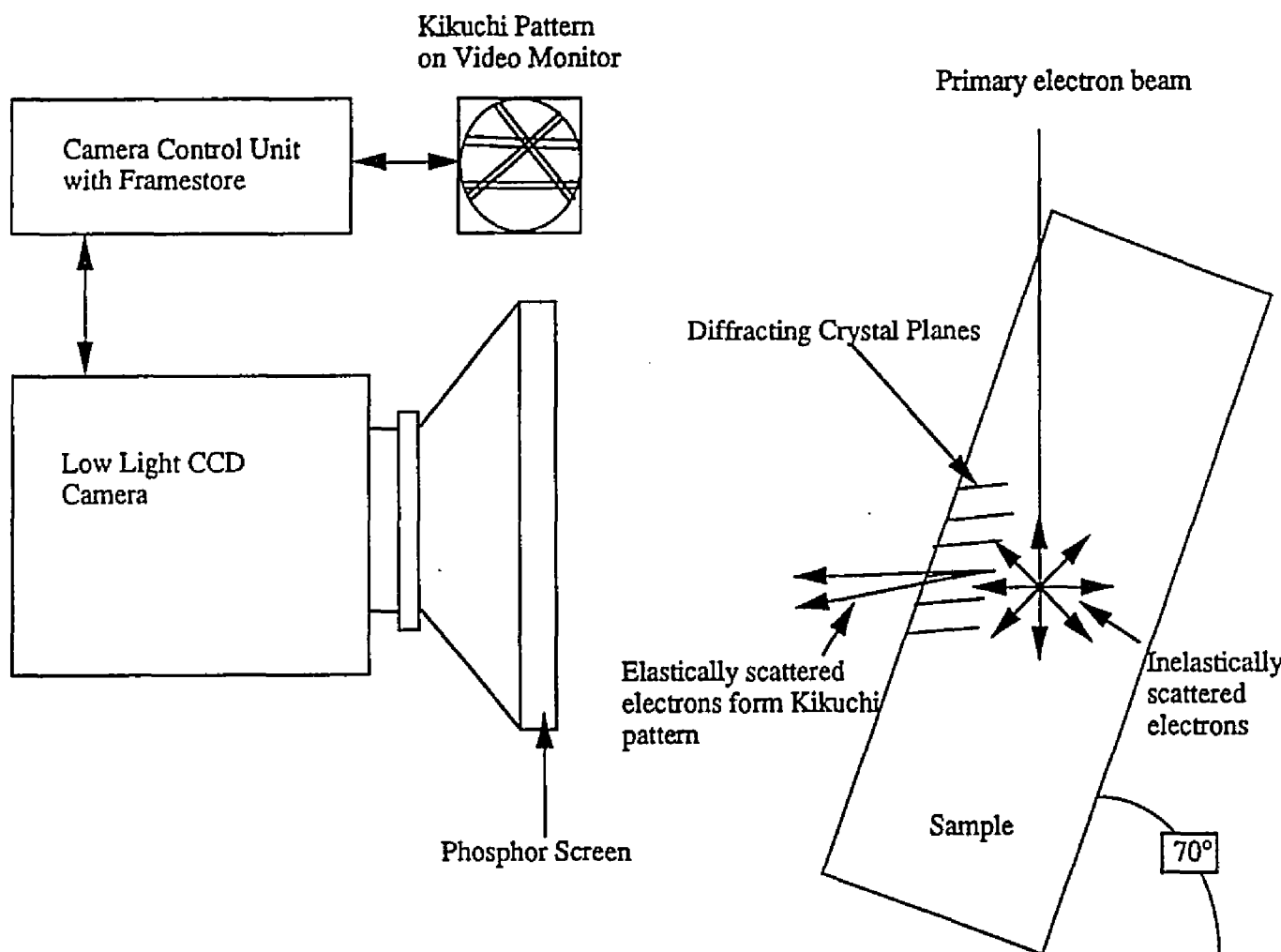


Figure 3.3. Schematic diagram of the formation and imaging of backscattered electron Kikuchi patterns in the SEM.

The spatial resolution of this technique is limited by the probe size, beam spreading, and sample quality. Grain sizes as small as  $0.25 \mu\text{m}^2$  have been resolved in stainless steel, but more typically the smallest detectable grains are on the order of  $0.5\text{-}1\mu\text{m}^2$ . The technique is highly sensitive to any surface distortion or contamination, but this was not a major problem for the  $\text{YBa}_2\text{Cu}_3\text{O}_{7-x}$  thin films. The accelerating voltage was 15 kV to insure sufficient signal. Due to the near surface sensitivity of the technique, the signal was always from the thin film, not the substrate.

### III.1.3. Cryogenic Transport Measurement System

A four probe low-temperature direct transport system was developed to perform all the low-temperature measurements. The system is based on a cryostat that uses flowing cold helium gas from a liquid helium reservoir to cool a copper cold finger. A schematic of the Janis Research designed cryostat is shown in figure 3.4 (Jirmanus 1990). The cryostat consists of a copper cold finger stub with 10 leads (see figure 3.5). The leads are brought from the feedthrough to the stage in twisted pairs to cancel self inductance due to the current transport along the wires. The cold finger is then surrounded by a radiation shroud to prevent radiative heating. An outer container is placed around the radiation shroud and a roughing pump is used to pull vacuum on the entire configuration. The vacuum provides thermal insulation from the external environment.

The copper stage has two silicon diode thermometers to measure the temperature at both ends of the stage. It was found that using a copper shield around the sample stage provided better thermal stability for the measurements.

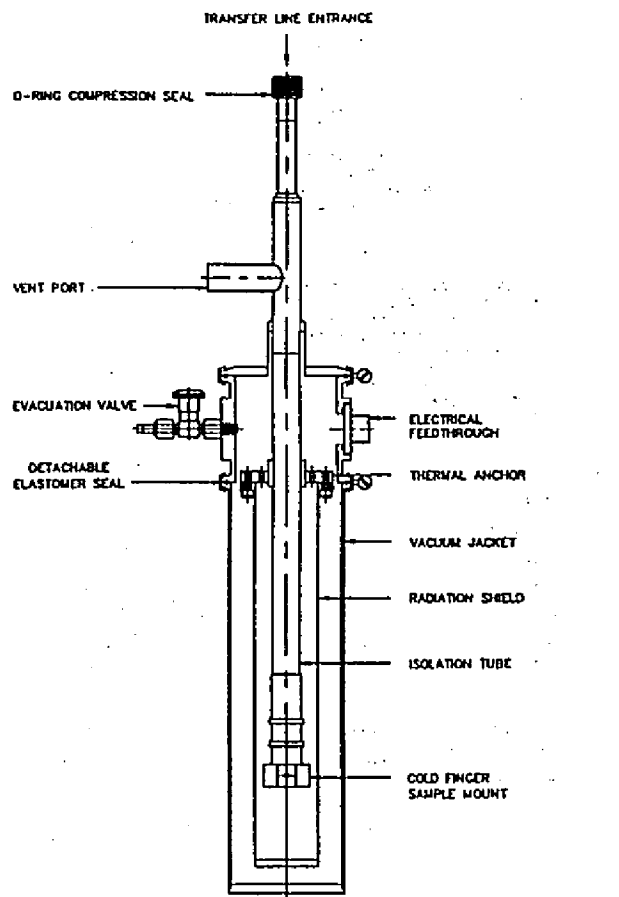


Figure 3.4. Schematic diagram of helium flow cryostat (from Janus).

Type N Apiezon grease was used to connect the sample to the stage, because it has high thermal conductivity and is electrically insulating. The sample was placed on the copper stub and the gold leads from the sample were soldered onto the pins. The advantage of a flow cryostat is that the temperature can be cycled very easily unlike closed cycle systems. Measurements could be taken at a variety of temperatures with excellent control. The lowest limit of the temperature, however, is 4.2 K (unlike closed cycle systems which can go lower). Another drawback of the system is that the sample sits in vacuum, not in the helium vapor. This means that the thermal conduction is done through the substrate, and not with direct contact between the sample and the helium. Therefore at higher current biases, and with poor thermal conducting substrates, evidence of heating due to poor conduction can sometimes be observed. An example of sample heating is shown in figure 3.8. As the current bias is increased, under sample heating conditions, the voltage drop across the sample increases with time. Therefore the voltage value for a given current bias is higher on the way down (after the sample was sitting with a current for a longer period of time) than on the way up and the sample displayed hysteretic behavior. Another effect that is sometimes present is a slight temperature gradient across the sample that creates a finite voltage. This offset voltage was left in all the I-V data (many people typically subtract it out from the measurement), but removed from the R-T data to confirm superconductivity.

The configuration of the measurement scheme is shown in figure 3.6. The four probe technique is used to remove contact resistance from the measurement by driving a current across two leads and measuring the voltage drop across two different leads (see figure 3.7). The voltage drop is a passive

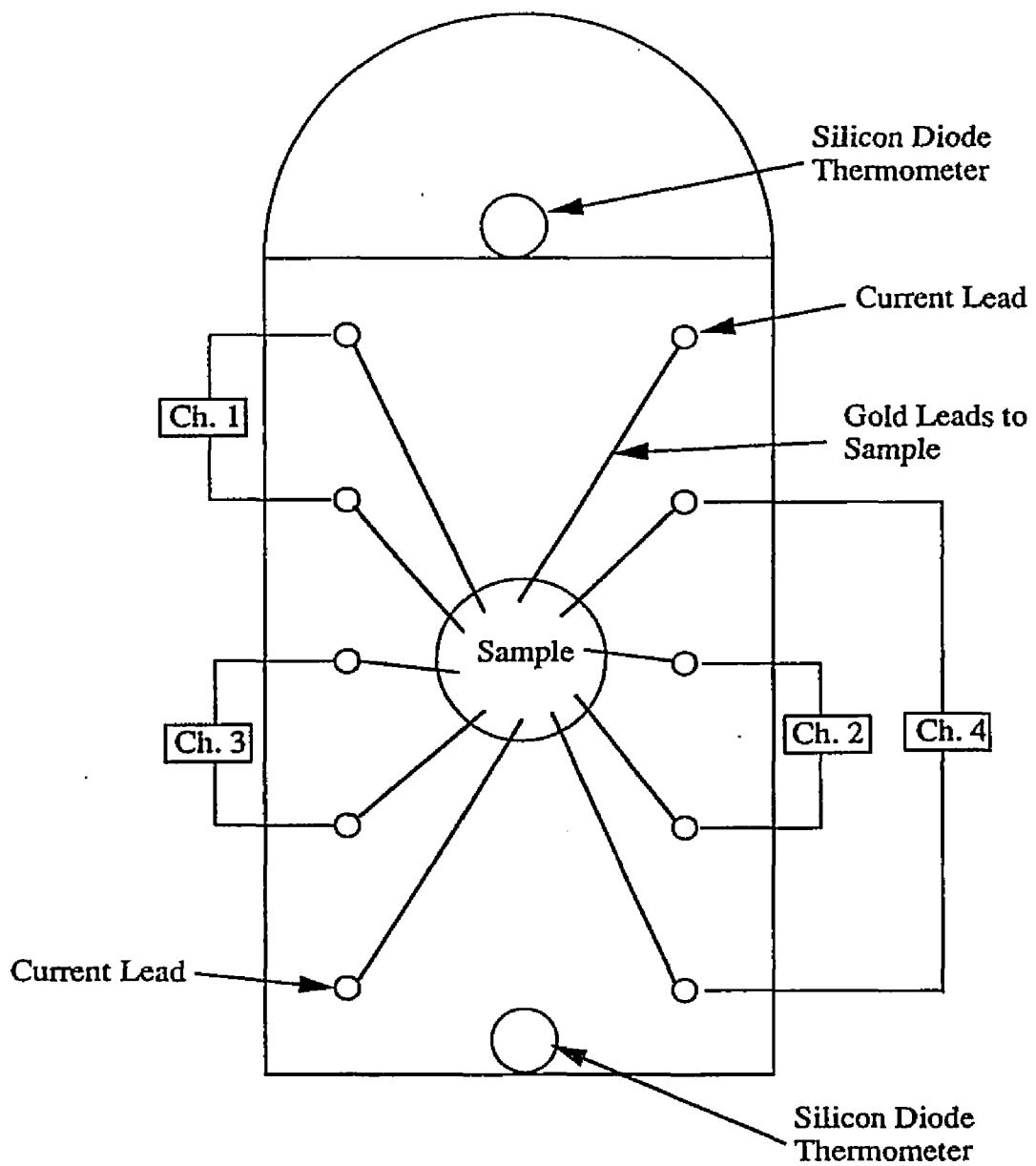


Figure 3.5. Sample stub for cryogenic transport measurements

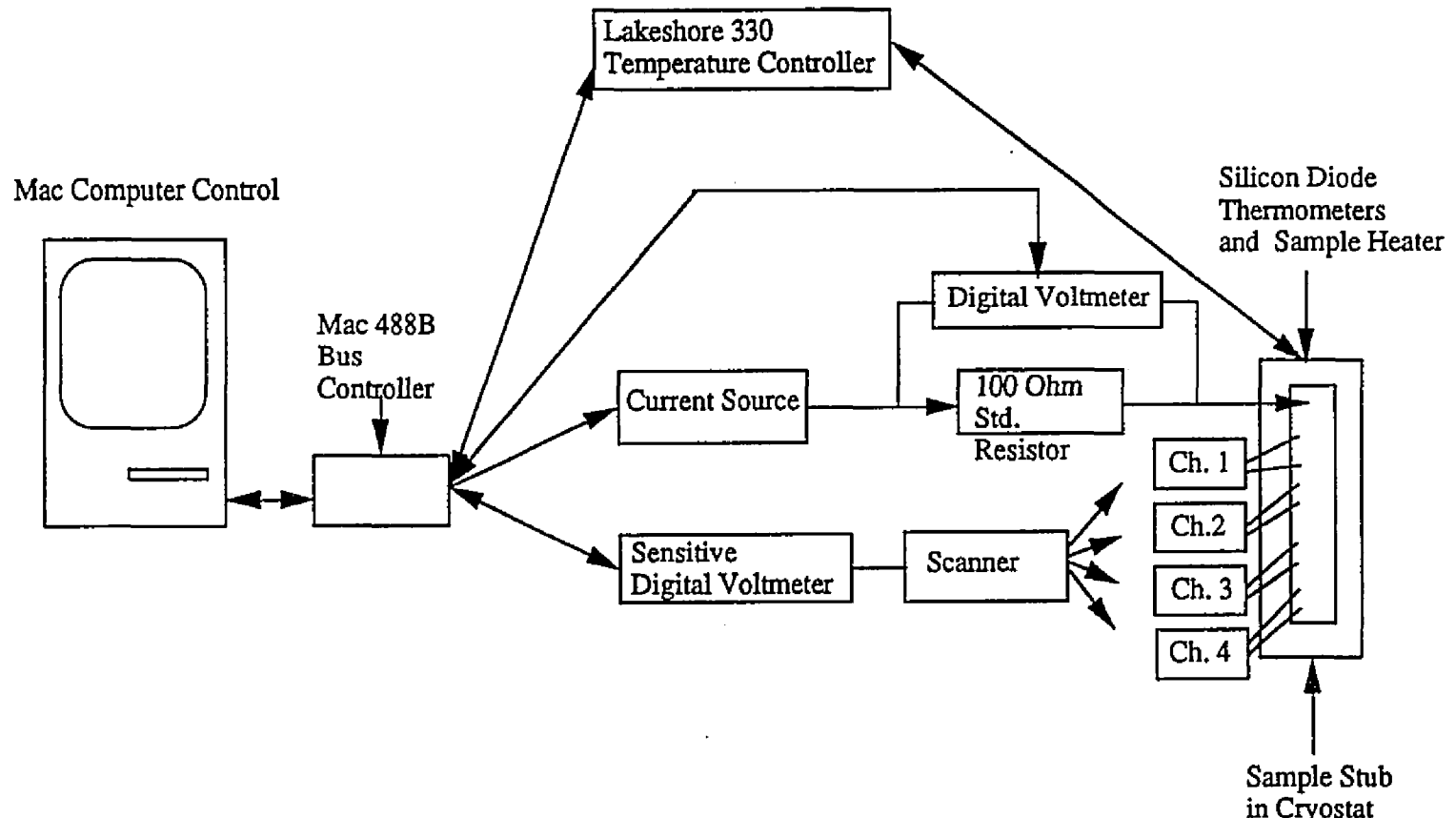


Figure 3.6. Schematic drawing of low-temperature measurement system. Note: all electrical equipment is attached to common ground.

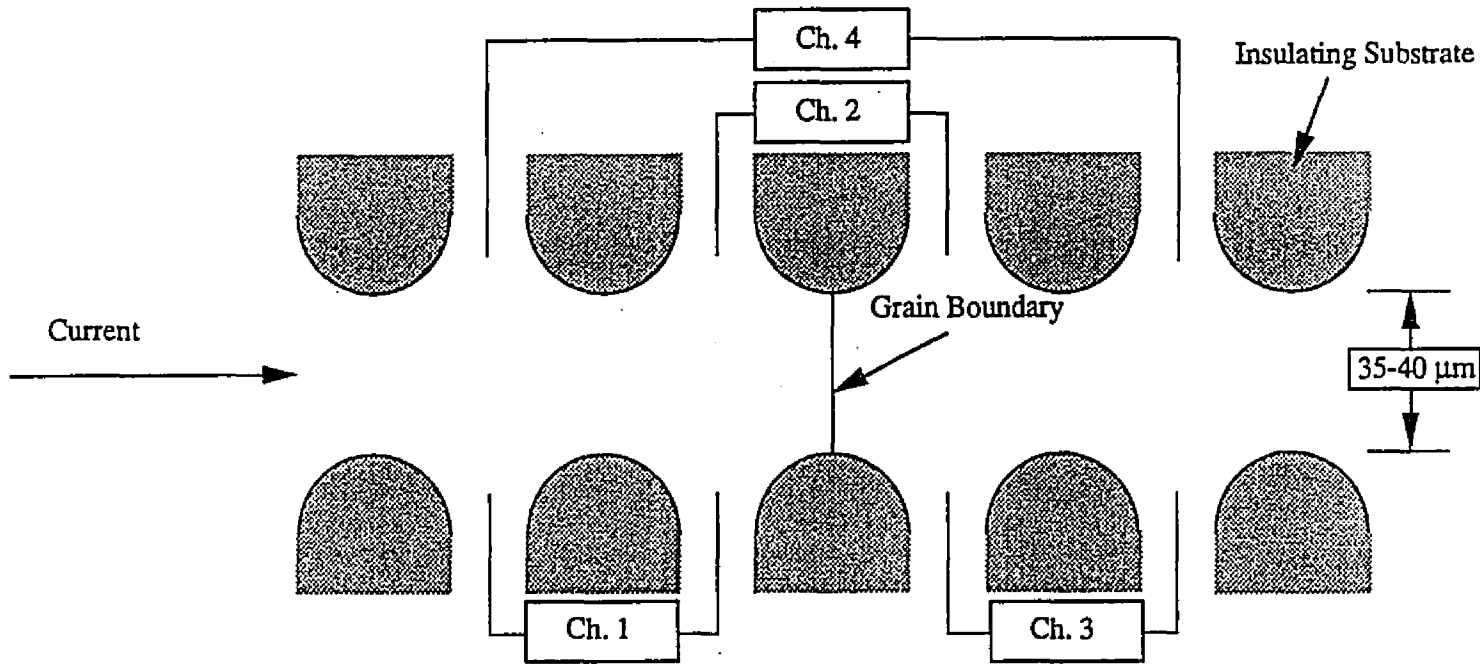


Figure 3.7. A schematic of the four-probe measurement across the microbridge. The voltage drop measurements are taken across the various channels. The grain boundary can be located across any part of the microbridge.

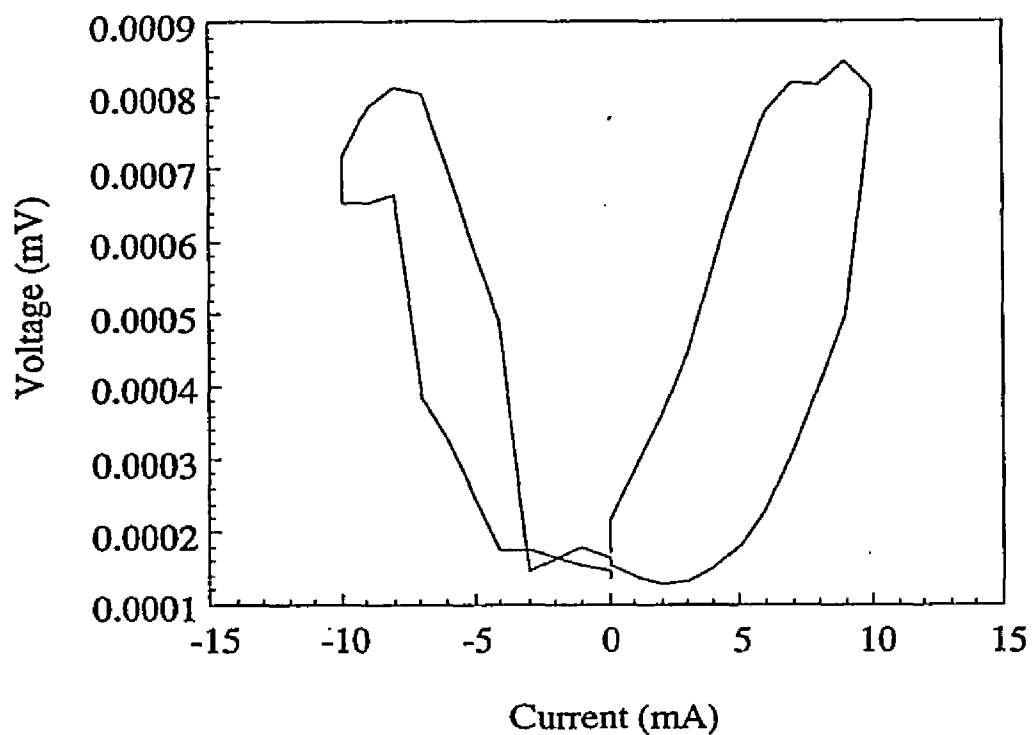


Figure 3.8. Hysteretic voltage-current characteristics of sample exhibiting thermal heating

measurement with vanishingly small amounts of current being drawn due to the high impedance, so the contact resistance is not measured. The measurements performed in this system include resistance vs. temperature ( $R-T$ ), current vs. voltage ( $I-V$ ),  $I-V$  as a function of applied magnetic field, and  $I-V$  as a function of temperature. Note that the measurement is a current-biased technique where the current is controlled and the voltage is measured (voltage vs. current), therefore  $V-I$  should be used, but the standard nomenclature used by electrical engineers is  $I-V$  and will be used for consistency with the literature. A basic four-probe voltage measurement is the basis of all the different measurements, as will now be described in detail.

The entire system is computer controlled through a Macintosh Plus computer using a QuickBasic program we developed. After the appropriate parameters are put in the program, the temperature of the system is measured using a LakeShore 330 Temperature Controller. The temperature between the top and the bottom of the copper stage must lie in a given DT from the assigned temperature. If the temperature is not in this range, the controller waits until it cools to the given temperature (this can be accelerated by regulating the helium flow to the system), or it heats the copper block if the temperature is too low. Once the appropriate temperature is attained, a current is driven through the system using a Keithley 224 Programmable Current Source (with a maximum output of 100 mA). The current first passes through a 100 Ohm standard resistor with a Keithley 197A Digital Voltmeter attached in parallel to measure the voltage drop across the resistor. The measured voltage across the standard resistor is a more accurate reading of the current than the readout on the current source and is used as the "measured current" ( $I_m$ ). The current then

passes through the sample, and the voltage drop across each individual channel is measured using a Keithley 182 Sensitive Voltmeter through a Hewlett-Packard 3495A Scanner, which scans the given channels. The information is all transferred through a Mac 488B Bus Controller and stored as an ASCII file. All of the electrical equipment is grounded to a common ground to prevent stray ground loops. For a standard I-V measurement, the current starts at zero and is incrementally decreased to the minimum voltage requested and then increased (through zero) to the maximum voltage and then dropped back to zero (this checks for hysteresis in the measurement). There is also an option in the program to use different current increments at various points of the measurement. This allows more detailed measurement of specific areas of the curve.

There are many permutations of these measurements depending on the specific conditions needed. Several variables can be altered to improve the measurement. For example, the wait time between turning on the current supply and taking a measurement can be varied, either to stabilize the voltage reading, or to reduce the sample heating (by shortening the wait time). The current can be turned off after the measurement to allow any sample heating to dissipate prior to the subsequent reading. Also the integration time for the voltage measurement can be varied. Typically ten readings are averaged to get a measurement, and a standard deviation is determined to verify that no major fluctuations occurred during the measurement (eq. 3.1).

$$V = \frac{\sum_{n=1}^{10} V_n}{n} \quad (3.1)$$

For the R-T measurement it is necessary to remove any thermal voltages to verify superconductivity. This is done by measuring a voltage drop with a positive current bias, then measuring a voltage drop with a negative current bias, subtracting the two values and dividing by two (eq. 3.2). Using this technique removes a thermal voltage from the measurement, if one is present in the sample. The resistance is then determined by dividing the voltage with the measured current (eq. 3.3).

$$V = \frac{V_+ - V_-}{2} \quad (3.2)$$

$$R = \frac{V}{I_m} \quad (3.3)$$

The resistivity can be calculated by equation 3.4,

$$\rho = \frac{RA}{L} \quad (3.4)$$

where A is the cross-sectional area of the sample (defined in this work by the microbridge dimensions), and L is the length of the material between contacts. For the grain boundary junctions the intrinsic junction resistivity is particularly difficult to determine accurately due to the large variations in both the cross-sectional area (see discussion on meandering) and due to the lack of a length scale along the boundary. However, the value from eq. 3.4 will be used in some specific instances with clearly stated assumptions for the dimensions used.

The system can be used for I-V measurements in an applied magnetic field. The magnetic field is measured in close proximity to the sample using a Magnos 1600 Gaussmeter. The strength of the field is controlled with two different current sources, depending on the strength of field and the sensitivity required. The field can be varied from 0 to 5000 Gauss (0.5 Tesla) with a control of 0.02 Gauss up to approximately 20 Gauss. The field can also be reversed to go negative.

One final comment is necessary with specific regard to measuring a grain boundary junction. The junctions are extremely sensitive to both magnetic fields and radio-frequency (R-F) radiation, therefore special precautions are necessary to insure valid measurements. Mu metal is used for measurements without a field to insure a zero-field environment (within 0.01 G). The r-f radiation can be screened out by using a screen room with a mesh size smaller than the radiation wavelength (1 mm<sup>2</sup> mesh should be more than enough) and shielded cable. The system used has shielded cable, and an additional 100 Ohm resistor in series with every line that goes into the cryostat. This effectively increases the damping of the lines and prevents R-F interference.

### III.2. Experimental Method

The goal of this study is to correlate grain boundary transport properties to microstructural features of the junctions in bi-epitaxial and sputter-induced epitaxy junctions. The basic methodology was to first form grain boundaries in thin film YBa<sub>2</sub>Cu<sub>3</sub>O<sub>7-x</sub> samples. These grain boundaries were subsequently electrically isolated for cryogenic transport characterization. Then the boundaries were thinned to electron transparency for further microstructural

characterization using transmission electron microscopy. This section details the procedures used in these experiments.

### III.2.1. Grain Boundary Formation

There are numerous types of grain boundary junctions that can be formed in  $\text{YBa}_2\text{Cu}_3\text{O}_{7-x}$  thin films (see chapter II,  $\text{YBa}_2\text{Cu}_3\text{O}_{7-x}$  Junctions). For this experiment the grain boundaries needed to be relatively easy to make in different configurations. Single grain boundaries were also necessary to provide straight forward correlation between the transport properties and microstructure. These criteria eliminated both the step-edge junctions (with two grain boundaries and difficult to image using transmission electron microscopy) and the bicrystal junction which only allows one grain boundary configuration. The two types of grain boundaries selected were the bi-epitaxial grain boundary junctions, and a technique developed for this thesis called sputter-induced epitaxial junctions. The added benefit of these junctions is that they are both  $45^\circ$  [001] tilt boundaries so they could be directly compared to each other in terms of transport and microstructure, with the caveat that the different substrates and deposition techniques could affect grain boundary structure and properties.

A set of grain boundaries were made using a technique called sputter-induced epitaxy (see figure 3.9). The basic method is to sputter a portion of a (100) MgO substrate prior to thin film growth using a low voltage argon ion beam (described in section III.1-1). Upon growth of the thin film, the thin film on the pre-irradiated portion of the substrate grows with a  $45^\circ$  modified epitaxy about the [001] relative to the unspattered part of the substrate. This creates a  $45^\circ$  [001] tilt grain boundary at the point where the two grains join. The details

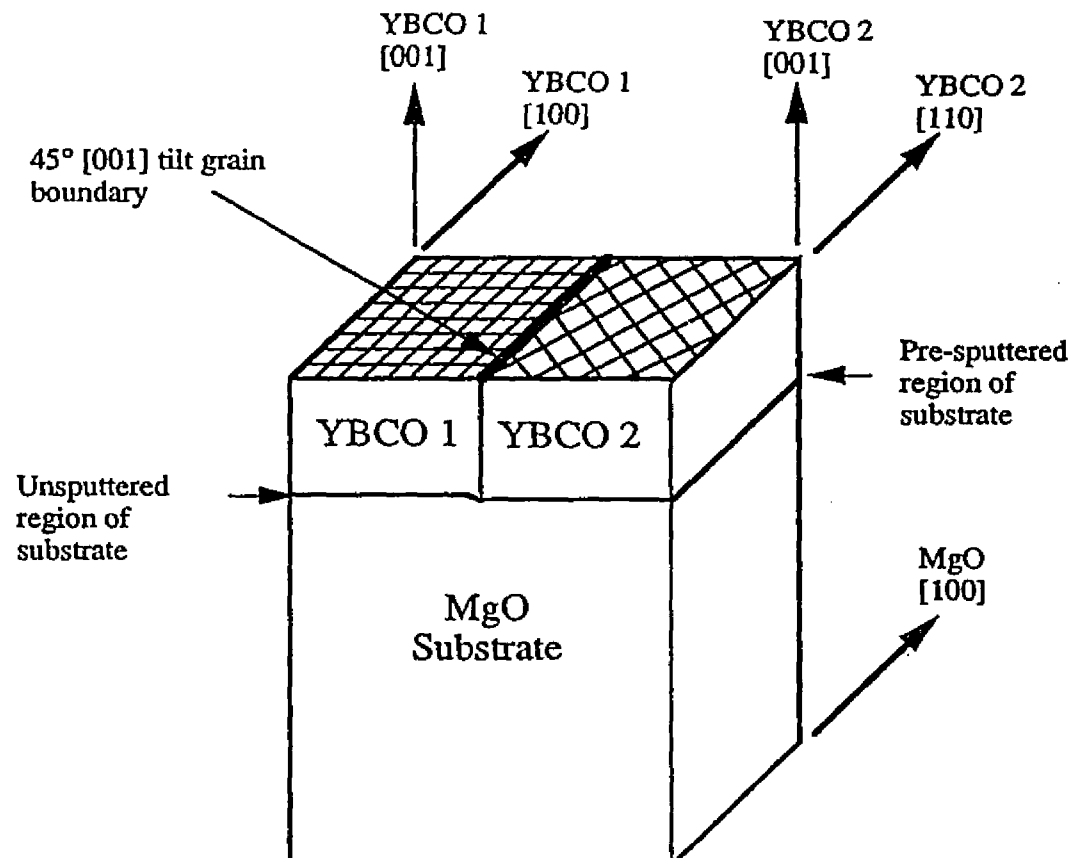


Figure 3.9. Sputter-induced epitaxy 45° [001] tilt grain boundary junction.

of the modified epitaxy and specific conditions necessary to produce grain boundaries will be discussed in the following chapter, but the substrate patterning technique is described below.

Epitaxially polished (100) MgO bulk single crystals (with nominal dimensions 1 cm x 1 cm x 0.5 mm) from Coatings and Crystals Technology (Kittanning, PA) are used. Due to the hygroscopic nature of the MgO, it is essential to keep the substrates in a dry atmosphere (in a desiccant environment) to prevent hydroxide formation on the crystal surface (a cloudy layer can be seen optically when the hydroxide forms). The crystals are often cleaved to smaller dimensions, or cut to 3 mm diameter disks (these samples can be directly prepared for standard TEM usage) using an ultrasonic disk cutter. A standard contact photolithographic procedure is used to pattern the substrates prior to ion irradiation. The samples are typically cleaned using acetone and methanol. Shipley Type S-1813 positive photoresist is spun onto the sample at 3000 rpm leaving a 1.25-1.5  $\mu\text{m}$  thick layer of photoresist on the entire substrate. The sample is then soft-baked at 80-100 °C for 20 minutes. A chromium metal mask with several different configurations is then placed on top of the substrate with the metal coated side in direct contact with the photoresist. The sample is then exposed to a mercury lamp for the optimal exposure time (approximately 25-30 seconds). Longer or shorter exposure times destroy the quality of the photoresist edge, which is crucial for a sharp delineation between the irradiated and unirradiated parts of the sample. The mask is removed and the photoresist is developed for 20-30 seconds in Microposit MF-319 developer and then rinsed in deionized water. The sample is then hard baked at 120-130°C for 20 minutes. The photolithography was done in a regular lab under yellow light without

clean room facilities and 5  $\mu\text{m}$  parallel lines were readily achieved (courtesy of the Emerging Materials Group and Dr. David Steel). With higher quality equipment (e.g. better control of mask placement and more uniform illumination) higher resolution lines could be produced.

The samples are then irradiated in the low voltage ion mill. The substrates are attached to the copper stub using silver paint and then irradiated for the appropriate time (this will be detailed in the following chapter). The irradiation time for the substrates is typically less than 5 minutes so beam heating has not been a major issue. After irradiation the photoresist is removed using acetone and the sample is then further cleaned with methanol. The sample is then placed in a dessicator and stored until the deposition is made (this time frame has been on the order of months, which is important to demonstrate the independence of the technique on storage, of particular concern for MgO substrates). The thin films were grown by K.A. Dean, D.B. Buchholz and S. Duray, under the supervision of Professor R.P.H. Chang.

The first group of samples made using sputter induced epitaxy were sputtered with a physical mask instead of photoresist. The mask was made of tantalum or stainless steel and affixed to the stub using small screws. The problem with these masks was that it was difficult to make direct contact at the mask edge across the entire sample, and the edge was not very sharp or straight. As is discussed later, the samples using this masking technique did not make as reproducible high-quality junctions as the photoresist covered samples.

The grain boundaries were made in a variety of configurations for different experiments. For basic transport measurements, 3 mm diameter disks were patterned with one grain boundary bisecting the substrate. Other samples

## Bi-epitaxial Grain Boundary Junction

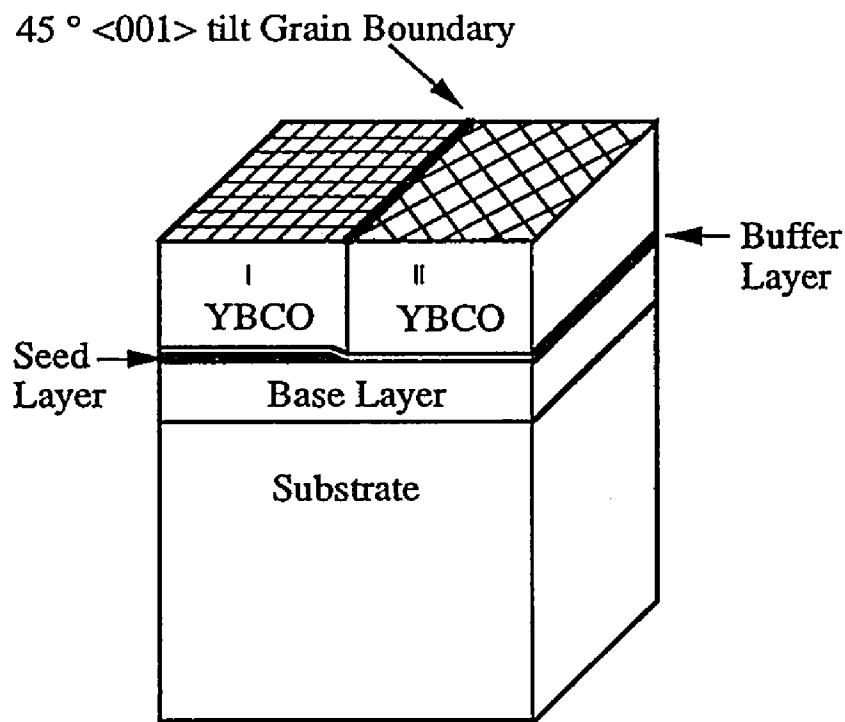


Figure 3.10 Bi-epitaxial substrate forming [001] 45° tilt grain boundary junction.

were made for TEM analysis using 5  $\mu\text{m}$  wide parallel lines to allow easy location of the grain boundaries. Several other experiments required different configurations including 20  $\mu\text{m}$  diameter circles for magneto-optic measurements and 100  $\mu\text{m}$  wide parallel lines for noise measurements.

The second set of grain boundaries was grown on bi-epitaxial substrates made by Conductus (see figure 3.10). The rotated epitaxy is controlled using a multilayer process to modify the epitaxial relation in two regions of the thin film. More details of the layers and the specific orientation relations are discussed in section II. The bulk substrates used were either YSZ or LaAlO<sub>3</sub> and then layers of CeO<sub>2</sub>, PrBa<sub>2</sub>Cu<sub>3</sub>O<sub>7-d</sub>, SrTiO<sub>3</sub>, MgO and CeO<sub>2</sub> are deposited. The final MgO and CeO<sub>2</sub> layers are between 100 and 200 Å thick and are etched away to produce the bi-epitaxial substrate. The substrates were made by Conductus using pulsed laser deposition and were patterned to form parallel 100  $\mu\text{m}$  grain boundary junctions. This configuration was used to allow two grain boundary junctions on the same sample to be measured, and increase the probability of successfully performing TEM microstructural characterization.

### III.2.2. Thin Film Growth

The YBa<sub>2</sub>Cu<sub>3</sub>O<sub>7-x</sub> thin film growth was done using POMBE and pulsed laser deposition. For the pre-sputtered MgO substrates, only the POMBE technique has been used. After the pre-growth sputter treatment and the removal of the photoresist mask, the sample is placed on the sample mount in the POMBE system using silver paint. The sample is then heated to the growth temperature (650-750°C depending on the specific run) and held at the temperature in a microwave assisted oxygen plasma for approximately 30

minutes. This should clean the substrate surface by removing a possible contamination layer and thus could be an integral part to reproducibly forming the modified epitaxy. The details of the thin film growth are in section II.2-4.a. The actual depositions were done by D. Bruce Buchholz and Ken A. Dean under the direction of Professor R.P.H. Chang at Northwestern University. The bi-epitaxial junctions were formed using both the POMBE system and pulsed laser deposition. The differences in the resulting grain boundaries will be discussed in chapter VI.

### III.2.3. Grain Boundary Isolation

Low-temperature transport measurements of individual grain boundaries require electrical isolation of the boundary. The transport characterization also requires a defined cross-sectional area to determine various properties (e.g.  $J_c$  and  $r$ ). In order to achieve these criteria, a microbridge was designed to measure four separate channels along a 400  $\mu\text{m}$  long strip with a 35-40  $\mu\text{m}$  wide crossection (see Figs. 3.11 and 3.12). The current is driven across the entire microbridge (it is a current-biased technique) and voltage drops are taken across the separate channels (which can be connected in different ways across the grain boundaries). If one grain boundary is measured it is placed across the central segment of the microbridge. At room temperature the voltage drop across the grain boundary segment is the sum of the voltage drop of the two grains and the grain boundary. As the sample becomes superconducting, the grains go superconducting prior to the grain boundary, therefore the grain boundary characteristics can be separated from

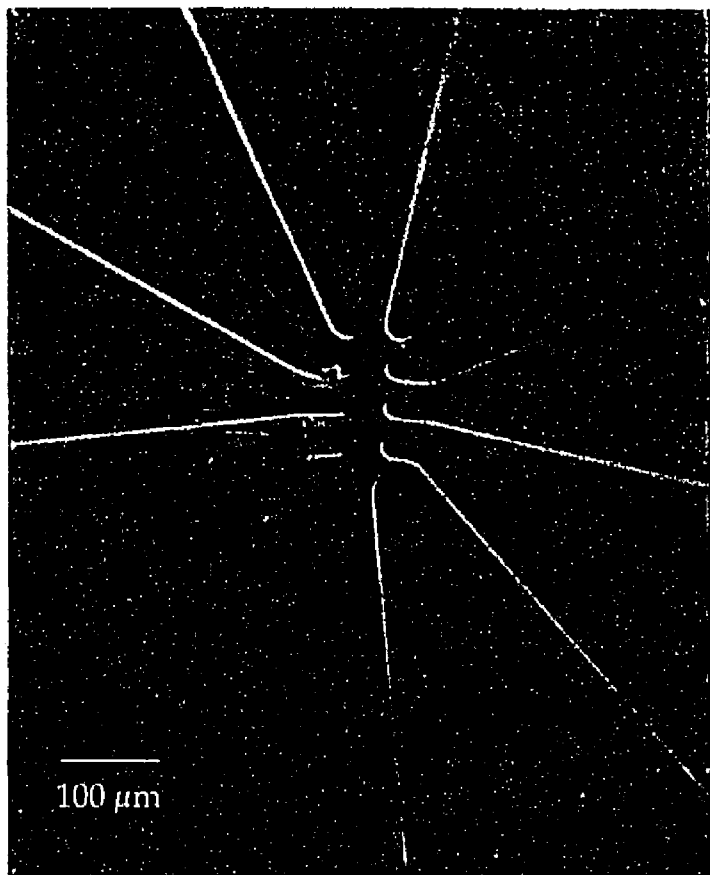


Figure 3.11. An optical micrograph of a patterned microbridge with  $100 \mu\text{m}$  spaced parallel bi-epitaxial grain boundary juncitons.

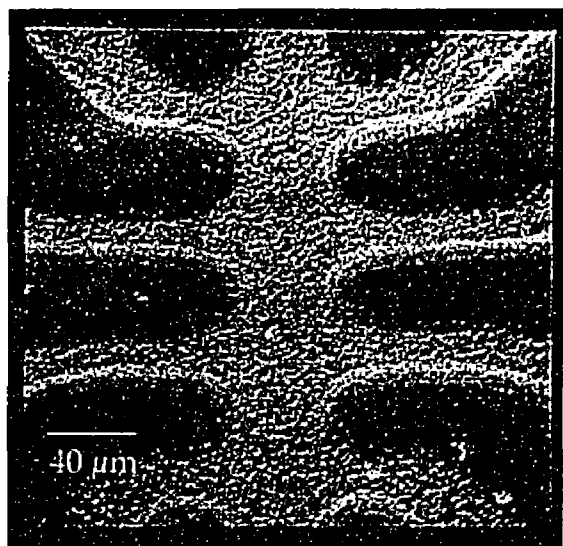


Figure 3.12. Secondary electron image of a  $40 \mu\text{m}$  wide microbridge patterned into a YBCO thin film on MgO.

the grains. The microbridge is also wide enough to make a TEM sample of the grain boundary measured.

The microbridge pattern was made from a molybdenum mask. Molybdenum was used because it has a low sputter yield, so contamination from the mask and mask deterioration over multiple uses was minimized. The thin film sample is affixed to a copper stub using silver paint for maximum thermal contact, and then the mask is placed on top using four 0-80 screws. It was always important to insure good contact between the mask and the sample to avoid shadowing effects. The sample was then milled in the low-voltage ion mill to sputter away the exposed regions of the thin film. The ion beam was perpendicular to the sample surface to minimize shadowing effects, and the sample was cooled using a liquid nitrogen cold finger to avoid heating effects. Sample heating was observed if the cold finger was not used, and this could destroy the superconducting properties of the thin film. The sputter conditions varied somewhat depending on the filament age, but generally a beam voltage of 500 V was used with an approximate beam current density of  $1 \text{ mA/cm}^2$ . The sputter rate of the YBCO thin film under these conditions was approximately  $100\text{-}125 \text{ \AA/min.}$ , so the duration of the sputtering was typically 20-25 minutes.

After patterning the film, a second mask (see figure 3.13) was used for silver evaporation for the contact pads. This mask protected the central microbridge, and allowed evaporation on the contact pads (figure 3.14 is a sample with evaporated silver contact pads). Another system, with two electron beam evaporators and a large (8 cm diameter) ion source was used for the silver evaporation (designed and maintained by Robert Erck). The exposed contact

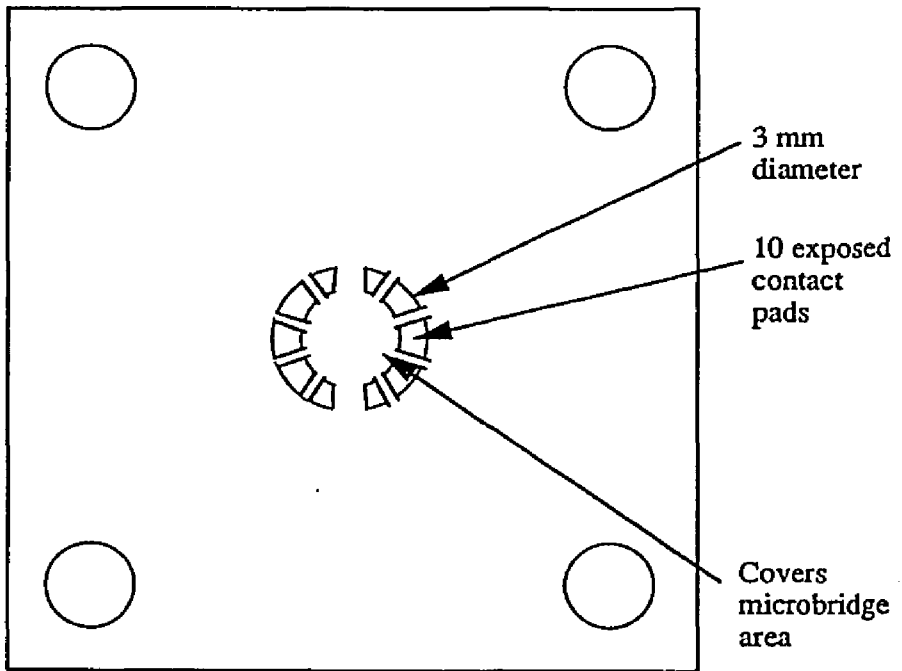


Figure 3.13. Mask design for silver evaporation of contact pads.

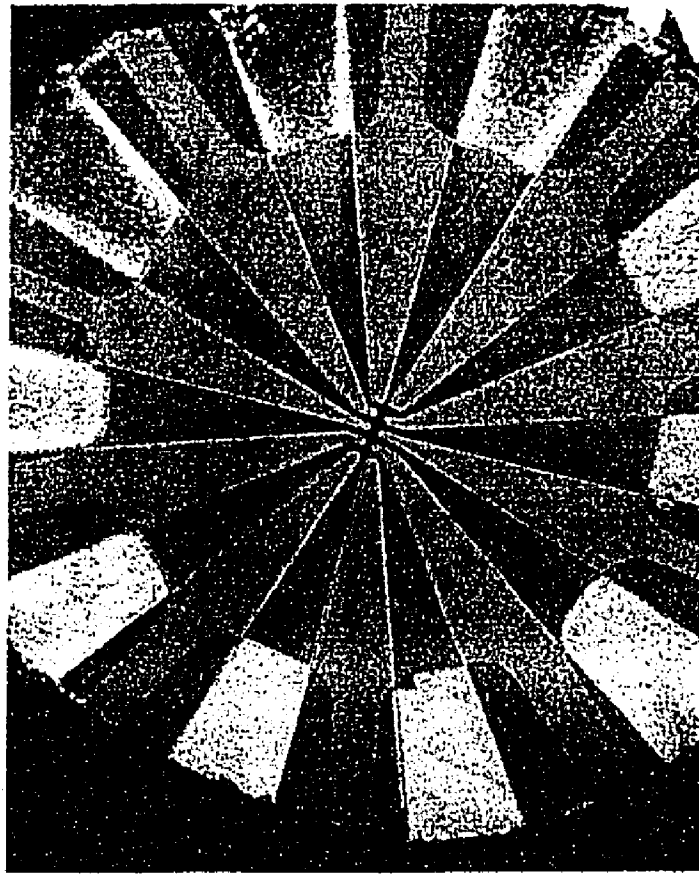


Figure 3.14. An optical micrograph of a patterned YBCO thin film with evaporated silver contact pads (substrate diameter is 3 mm).

pads were first sputtered for 15-30 seconds to remove the top layer of YBCO and any contamination on the surface. Then 2000-3000 Å of silver were evaporated. The sample was then removed and annealed in flowing ultra high purity oxygen at 450°C for 4 hours with a ramp up of 60°C/hr and a furnace cool. The anneal made the silver adhere better to the film and made low resistance contact pads. Gold wire leads were attached to the contact pads using silver paint. This was a tedious process, requiring significant dexterity to place 10 leads on the edge of a 3 mm disk without touching each other, or getting silver paint on the microbridge (see figure 3.15). The gold leads, either 50 or 100 µm in diameter, were straightened and placed in direct contact with the silver on the pad. The lead was then touched by a very small amount of silver paint to affix it to the thin film, followed by a slightly larger drop of silver paint to cover the entire wire on the pad. The sample was then placed into the cryostat after the silver paint was dried, and the contacts were checked for electrical shorts. The leads were then attached to the pins using Indium solder.

#### **III.2.4. Low Temperature Transport Measurements**

All samples were first measured at room temperature to determine the room temperature resistance, and to insure that all the contacts were isolated from each other. The room temperature resistance was used as a test on subsequent days to verify that the sample had not changed due to thermal cycling. The sample was slowly cooled in zero field, while measuring resistance to establish approximately the value of  $T_C$ . Careful R-T measurements were performed, usually starting at low temperature and increasing (because of better temperature control). Reproducible R-T measurements were made with

temperature resolution of 0.1 K, but typically 0.25 K increments were used. The constant current in the measurement essentially controlled the sensitivity to the resistance. Usually 1  $\mu$ A was used, but occasionally other values were used to determine the sensitivity to this parameter. Some R-T measurements were also made under applied magnetic field to decrease the transition temperature and observe the transition.

Current-voltage measurements were taken as a function of temperature to determine the critical current density of the grain boundary. A 1  $\mu$ V criterion was used to determine the critical current. These values were used to compare to the predicted values of S-N-S and S-I-S junctions. The grain critical current density was usually not determined because very high current values were necessary and this could destroy the grain boundary (due to resistive heating above the critical current).

A method was devised to determine the critical current as a function of applied magnetic field. This was done by biasing the sample with a current just below the maximum critical current value with a constant current. The voltage drop across the grain boundary was then measured as the applied magnetic field changed. The voltage measurement was therefore inversely proportional to the critical current (as the critical current value decreased, the voltage increased for a constant current bias). This measurement was typically taken at different temperatures (to see the effect of the change in the Josephson penetration depth). The magnetic field was always applied perpendicular to the thin film surface, except in one case which is described in the chapter on the results of the multi-layer sputter induced grain boundary.

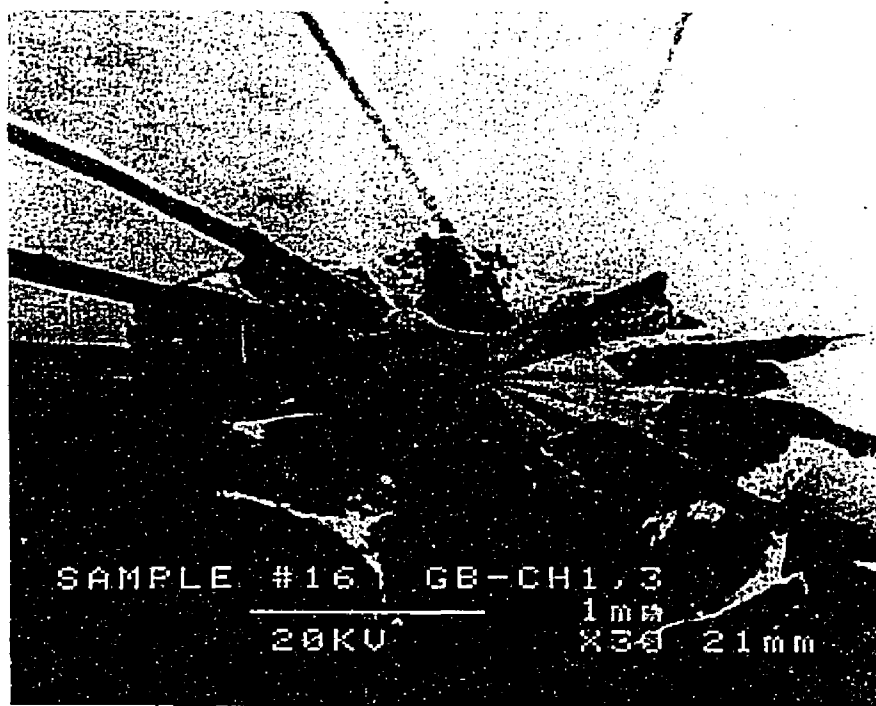


Figure 3.15. Secondary electron micrograph of patterned microbridge on a YBCO thin film with 10 gold wire leads attached.

A series of low-frequency voltage noise measurements (0.03-200 Hz) were performed, by Li Liu at the University of Chicago Physics Department, on a set of the bi-epitaxial junctions in a temperature range of 2-300 K. The microbridge pattern described previously was used in a 5-probe a.c. technique. Two grain boundaries in the sample made two arms of a Wheatstone bridge. The samples were biased with current densities from  $10^4$ - $10^5$  A/cm<sup>2</sup> so the grain boundaries were in the normal-state, and to ensure no resistive heating occurred. The details of the experiment are described elsewhere (Liu *et al.* 1995).

### III.2.5. Grain boundary TEM Sample Preparation

In order to observe the same grain boundary that was measured with minimal damage to the sample, a technique was developed to produce an electron transparent region at the position of the grain boundary. YBCO is very sensitive to water and acetone, which have been shown to destroy superconducting properties. Therefore, in every step of this process both water and acetone were eliminated from the procedure to minimize modification of the boundary characteristics. The first step in the procedure is to place the sample film side down on a glass slide (using a low melting point wax,  $T_m = 100^\circ\text{C}$ ) and grind the 0.5-0.75 mm thick substrate to 110-130  $\mu\text{m}$  thick using a 15  $\mu\text{m}$  grit diamond embedded polishing wheel. The sample is then removed and placed on a sapphire disk used as the stage for a VCR dimpler. A flattening wheel and 3  $\mu\text{m}$  paste are used to flatten the sample (in case of uneven grinding) and to identify where the center of rotation (and locate where the dimple will form). If the center is not above the grain boundary (this is determined using a transmission light optical microscope), the sample is moved to compensate. The

last two steps are performed iteratively until the grain boundary is successfully located at the center of the dimple. This step is crucial in carefully locating the point of perforation adjacent to the grain boundary.

There are a couple of precautions necessary to ensure successful dimpling of the sample. First all the pastes are combined with oil-based solutions to avoid water contamination. Sufficient wax is used to prevent any of the paste/solution from contacting the film, but no bubbles can be formed in the wax (or the sample can crack during the process). Also the dimpling wheels must be smooth to prevent non-uniform dimpling. Dimpling wheels from the manufacturer typically are uneven and are smoothed using a polishing wheel.

The dimple is then formed in the substrate, using 3  $\mu\text{m}$  diamond paste and 15 g of force at low speed, until the total sample thickness is approximately 30  $\mu\text{m}$  as measured optically. A final polish using a felt covered wheel is done using 1  $\mu\text{m}$  diamond paste until all visible scratches are removed. The final thickness is about 25-30  $\mu\text{m}$ , and it is critical that all the scratches are removed for even ion milling. A molybdenum ring is affixed to the film side of the sample using M-bond epoxy. This ring provides structural support for the sample, prevents the sample center from direct contact with a surface and gives good electrical contact to the film. The sample is then placed in a low-temperature ion mill holder. The sample is milled from the back side, and the thin film side is covered using a glass cover slide to prevent contamination during milling. The sample is cooled using liquid nitrogen for 30 minutes prior to milling and then 4 kV argon ions with a total beam current of 0.25-0.5 mA are used with an incident angle of 17-18°. As the sample approaches perforation (this can be determined using a monochromatic sodium light source and

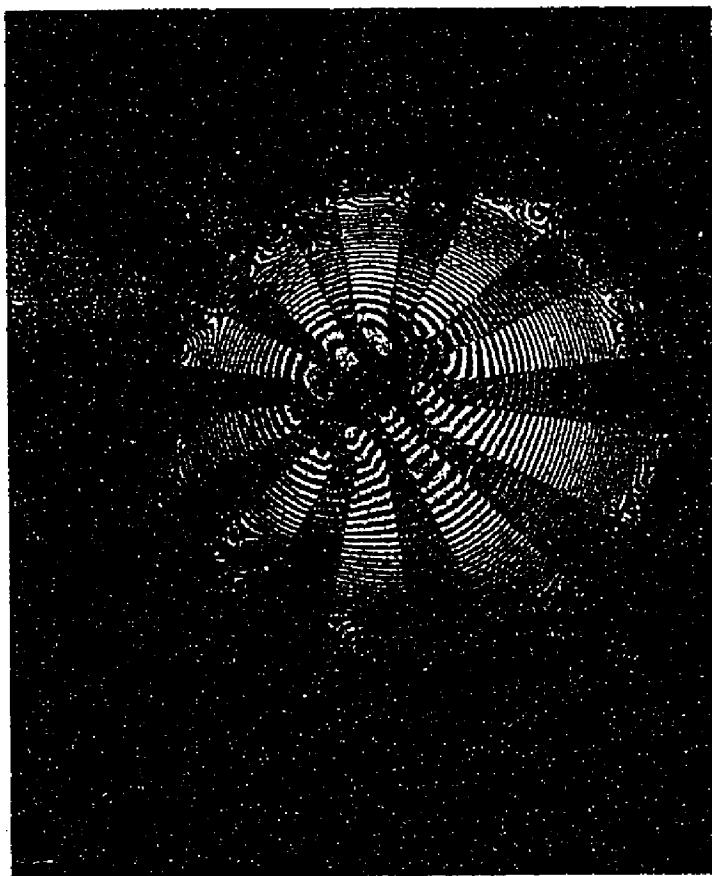


Figure 3.16. An optical micrograph of a TEM sample using monochromatic sodium light. The thickness fringes are due to interference contrast from the top and bottom sample surfaces. The microbridge width is  $40 \mu\text{m}$ .

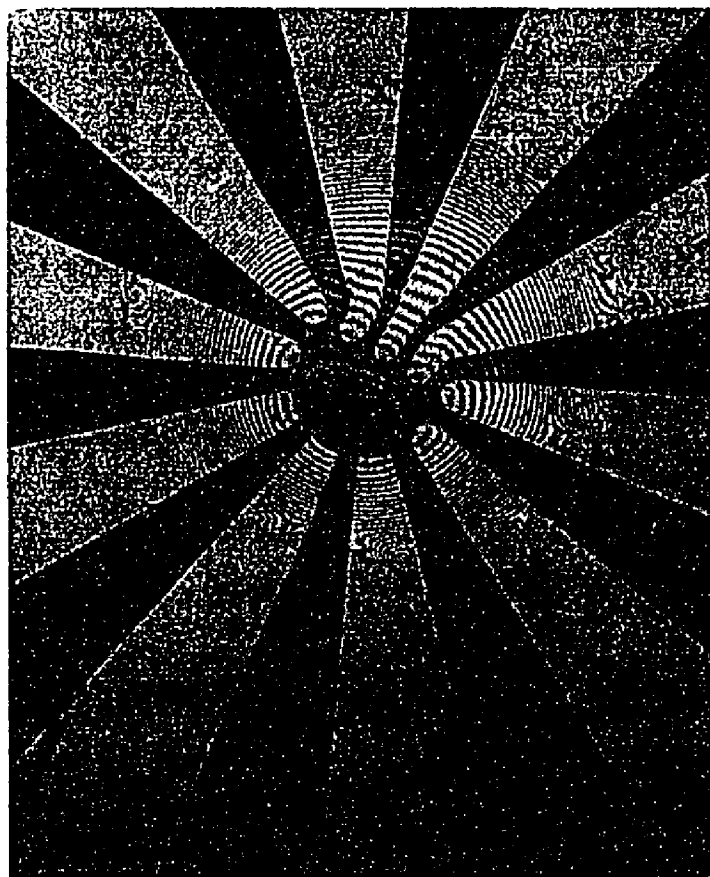


Figure 3.17. An optical micrograph, using monochromatic light, showing perforation of a TEM sample at the microbridge. The microbridge width is  $40 \mu\text{m}$ .

observing the fringe number and spacing (see Figs. 3.16 and 3.17), the incident angle is dropped to 12°. Figure 3.16 has large interference fringe spacings using monochromatic light, where the sample is about to form a hole, and figure 3.17 shows the hole formed. After perforation a final mill is done from both sides at 2.5 kV for a 5 minutes. The ion milling is in a Gatan duo-mill with a diffusion pump until near perforation. The final mill is performed in a turbo-pumped ion mill for cleanliness. The sample is then observed in the TEM and potentially milled further as is necessary.

### III.2.6. Electron Microscopy

Conventional bright field and dark field techniques were used to analyze the grain boundary structure. The grain boundaries were identified using standard electron diffraction. Dark field imaging was used to highlight the grain boundary path (which typically meandered significantly) and any precipitates located at the boundary. The samples were analyzed using standard plan view imaging. Both a Phillips EM 420 and CM30 were used at 100 kV to minimize beam damage and oxygen loss in the sample. Energy dispersive x-ray spectroscopy was used to identify precipitates in the film.

High resolution electron microscopy (HREM) was performed to study the detailed atomic structure at the grain boundary. The grains on either side of the boundary were [001] oriented it was possible to image both simultaneously with good resolution. It is important to note that variations in the film thickness (from thinning) and damage during the milling process would alter the local image conditions. A JEOL 4000 EXII was used at 200 kV (to minimize beam damage and maintain sufficient resolution). The effect of the electron beam on

the sample has been demonstrated by different groups (Rickards *et al.* 1989; McKernan *et al.* 1992). At 400 kV accelerating voltage there is significant disordering of the grain boundary structure after 10 minutes, which does not occur at 200 kV. In the samples analyzed for this study, beam damage was apparent after extended periods of exposure (> 1 hour), however, the damage was uniform across the sample, and did not appear to preferentially modify the boundary structure. Through focal series of grain boundaries were used to match image simulations. HREM image simulations of the grain boundary were made using NUMIS software at Northwestern University.

High resolution analytical electron microscopy was used on some grain boundaries for compositional analysis. The microscope was a Hitachi HF-2000 with a cold field emission gun for high brightness and a small probe size (1 nm). EDS and PEELS analysis was performed with a Link EDS unit and a Gatan 666 PEELS detector. Image-coupling mode was used by forming a diffraction pattern on the image screen to acquire the spectrum. More details will be described with the data in chapter IV.

## **Chapter IV. Sputter-Induced Epitaxy**

Many different types of grain boundary junctions in high-T<sub>C</sub> materials have been developed to utilize the Josephson-like properties in microelectronic devices. The junctions were made using numerous techniques to modify the epitaxial condition between the thin film and the substrate as mentioned in II.2.4. This chapter describes the development and study of a method that we call sputter-induced epitaxy, that is used to form 45° grain boundary junctions on MgO substrates (see figure 4.1) (Chew *et al.* 1992b; Vuchic *et al.* 1995a; Vuchic *et al.* 1995b). The first half of this chapter details the conditions necessary to achieve modified epitaxy on MgO, and experimental results studying the potential reasons for the modified epitaxy. The second half describes the structure-property relationship of the grain boundary junctions using low-temperature electrical transport measurements and structural characterization methods.

### **IV.1. Formation of Sputter Induced Epitaxy Grain Boundaries**

#### **IV.1.2. Thin Film Junctions on MgO**

MgO has been commonly used as a substrate for YBCO thin films for several reasons including favorable dielectric properties, minimized interdiffusion with the YBCO film, cost and reasonable lattice match. Thin films with high epitaxial quality and excellent transport properties were formed on MgO by several groups (see section II.3.2.). More recently several types of junctions have been made specifically using MgO substrates, including

bicrystal,(Lu *et al.* 1993) bi-epitaxial,(IJsselsteijn *et al.* 1993) focused ion beam (FIB),(Neumann *et al.* 1993a; Neumann *et al.* 1993b) step-edge,(Edwards *et al.* 1992) and directional ion beam etching (Ramos *et al.* 1993). The advantages and disadvantages of the bi-epitaxial, bicrystal and step edge junctions were mentioned earlier in section II.4. FIB and directional ion beam etching were developed using different ion beam processes on MgO substrates and will be detailed here.

Both FIB and directional ion beam etching employ two junctions in series to create a weak link (see figures 1c-d). The FIB technique uses a 30 keV Ga<sup>+</sup> ion beam, 50 nm in diameter, in two ways to form junctions (Neumann *et al.* 1993a; Neumann *et al.* 1993b). In the first method low doses of Ga<sup>+</sup> are implanted locally at the substrate surface, and subsequently diffuse into the deposited YBCO film and form a weak-link region. The second method uses the focused ion beam to etch a groove in the substrate. The thin film then grows polycrystalline in this region, forming a weak link. The FIB techniques depend on at least two interfaces (either uncontrolled grain boundaries or diffusion barriers) to form the weak links, reducing the reproducibility of the process (analogous to the step edge with two grain boundaries in series).

The directionally ion beam etched MgO substrates have two 45° grain boundaries in series to form a weak link (Ramos *et al.* 1993; Olsson 1994). This technique employs a 300 eV Ar ion beam at a 30° angle of incidence to etch a (100) MgO substrate. The resulting film forms a 45° rotated grain (about [001]) in the step region adjacent to where the mask was placed. The reason for this rotation was ultimately determined to be the sputtering of the photoresist mask onto the substrate (Olsson 1994). The junctions show significant scatter in the

critical current densities on the same chip and from chip to chip. This effect is due to the formation of two grain boundaries in series, making reproducibility a significant issue. Note that sputter-induced epitaxy is completely different from the directional ion beam etching in that it induces a modified epitaxy across the entire pre-sputtered region. The directional ion beam etching only produces a rotated grain in the immediate vicinity of the mask using a completely different mechanism than the sputter-induced epitaxy (see RBS results below). It should also be noted that studies have shown that on vicinal MgO with small miscut angles, YBCO films grow with [001] parallel to the substrate normal, and not MgO [001] (Norton *et al.* 1994). This type of epitaxy is termed graphoepitaxy and has been seen in other materials systems as well (Norton *et al.* 1994). The implication of graphoepitaxy is that on a shallow step edge, the film will form [100] tilt grain boundaries at the top and bottom of the step. The YBCO will grow with the c-axis perpendicular to the substrate surface along the step edge between the boundaries.

#### IV.1.2. Sputter Induced Epitaxy Junctions

Sputter induced epitaxy is a technique developed to modify the epitaxial relationship between a YBCO thin film and a MgO substrate. By controlling this relationship, grain boundaries can be formed in predetermined areas of the substrate to make high quality grain boundary junctions. As discussed previously (see section II.3.2), YBCO thin films can grow with different epitaxial relations relative to the MgO. The most common epitaxial orientation relationship observed is  $\text{YBa}_2\text{Cu}_3\text{O}_{7-x}$  [001] || MgO [001] and  $\text{YBa}_2\text{Cu}_3\text{O}_{7-x}$

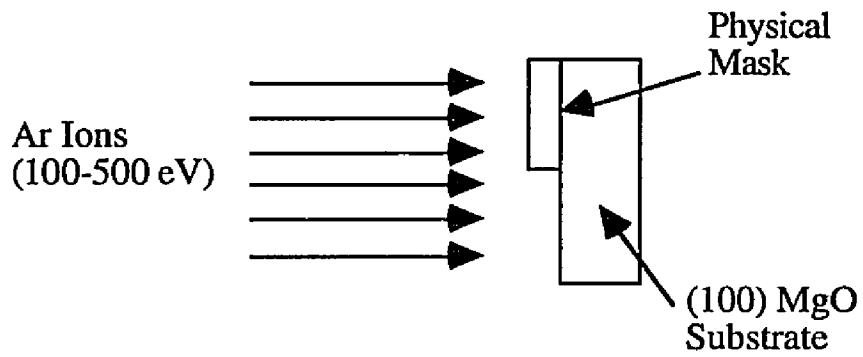


Figure 4.1a. Pre-growth sputter treatment for sputter-induced epitaxy samples.

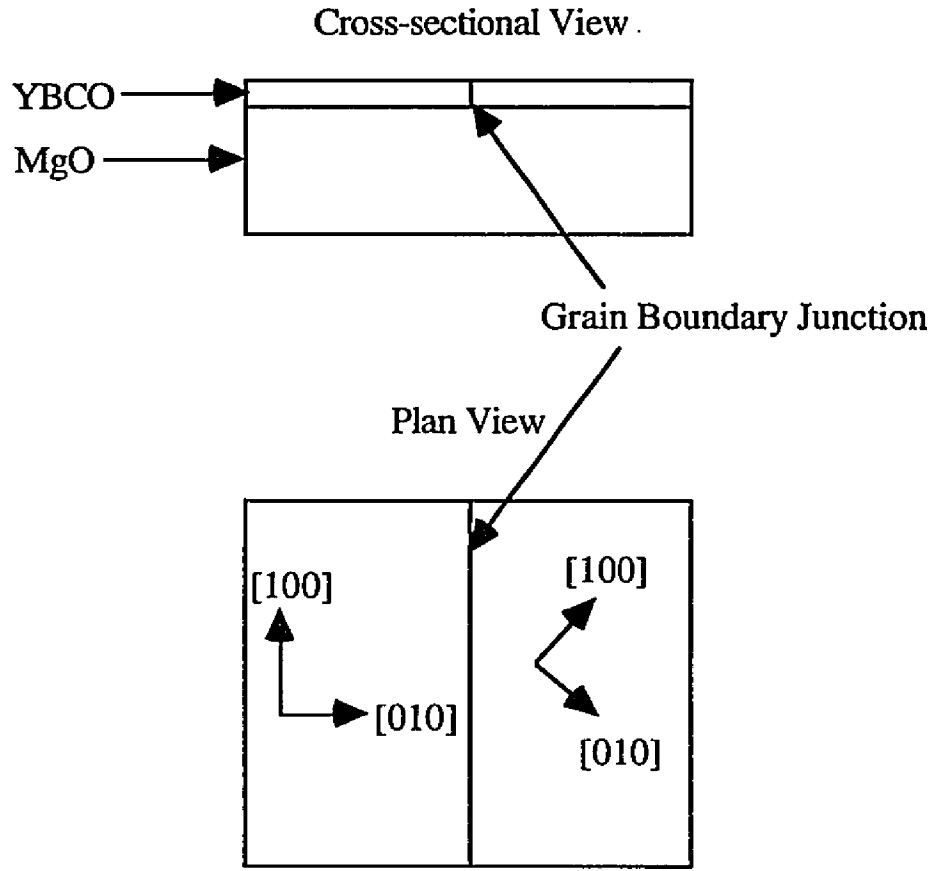
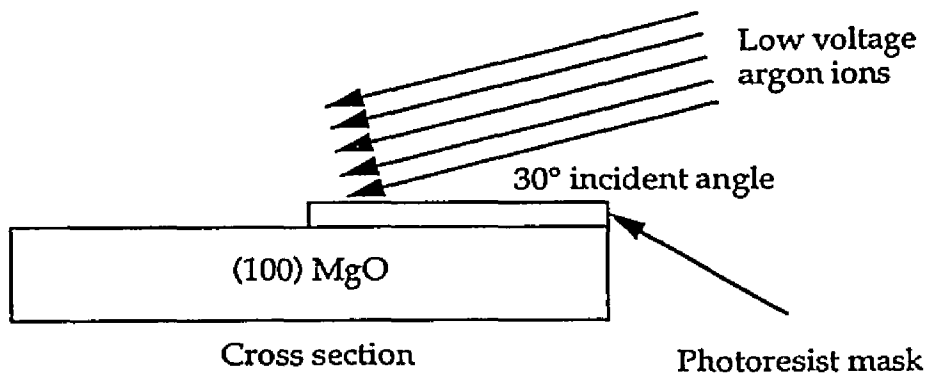


Figure. 4.1b. Schematic of YBCO thin film orientation after deposition.



Both sputtered and unsputtered regions grow cube-on-cube.

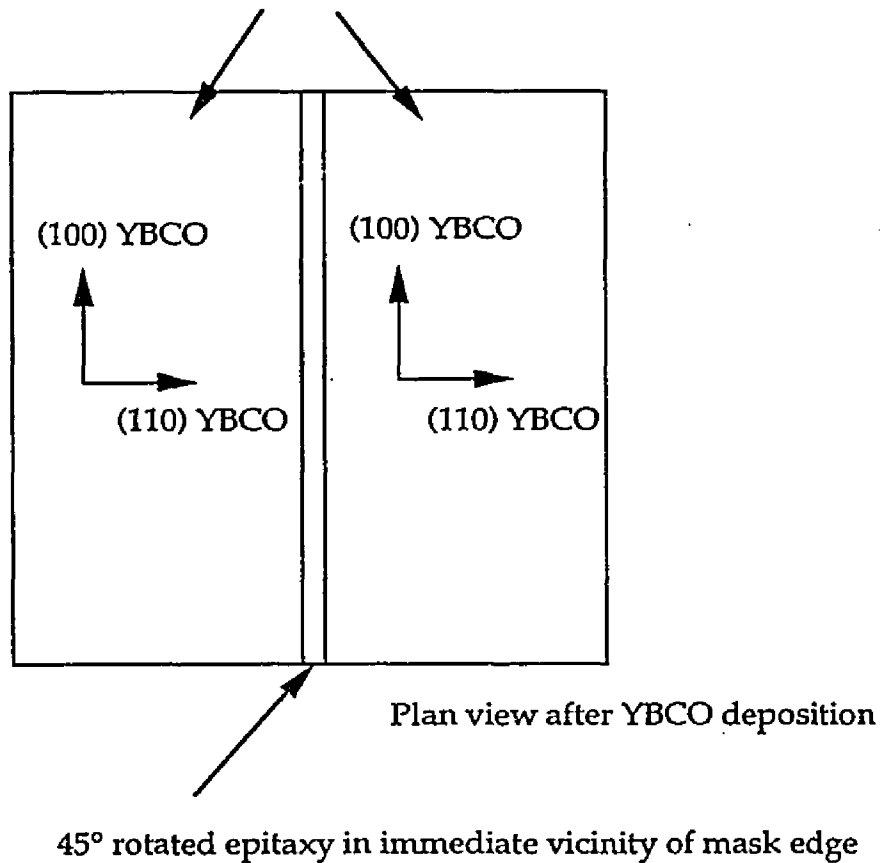


Figure 4.1c. Directional ion beam etching forms a narrow region of modified epitaxy due to contamination from redeposition of the photoresist mask.

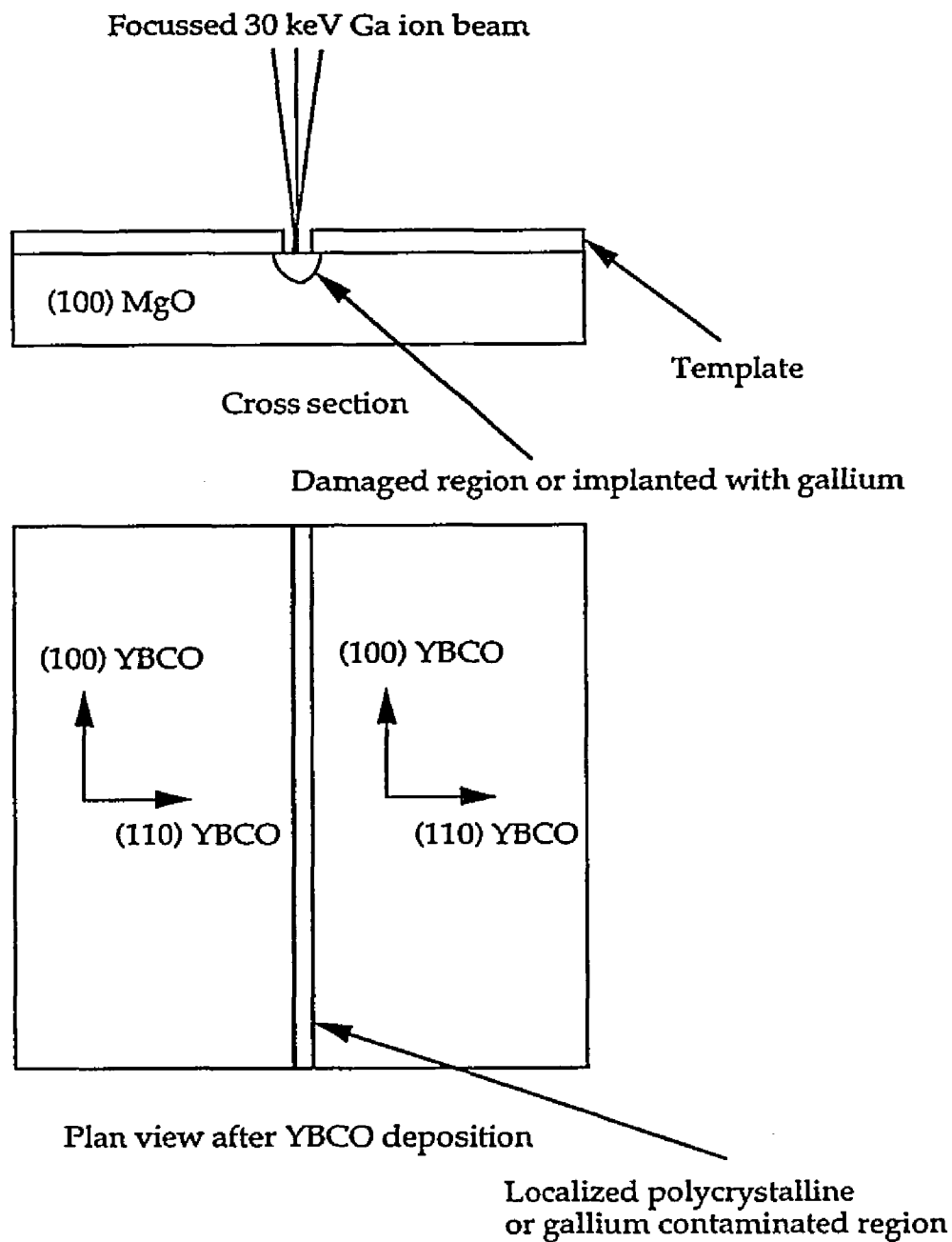


Figure 4.1c. Schematic diagram of focused ion beam technique that uses medium energy gallium ions to create a narrow damaged region in the substrate. The YBCO film is subsequently either polycrystalline in the region or contaminated with diffused gallium.

[110] || MgO [110], otherwise referred to as cube-on-cube orientation. Another type of orientation relation often seen is YBa<sub>2</sub>Cu<sub>3</sub>O<sub>7-x</sub> [001] || MgO [001] and YBa<sub>2</sub>Cu<sub>3</sub>O<sub>7-x</sub> [100] || MgO [110] where the YBCO unit cell is rotated 45° about [001] relative to the cube-on-cube scenario. The 45° misorientation forms due to a low lattice mismatch in that configuration (only 2.8%), making it a favorable secondary orientation. This second type of orientation will be referred to as modified epitaxy throughout the text. Recently groups have grown single crystal epitaxial YBCO thin films on MgO with the cube-on-cube orientation (see section II.2.4 and Dean *et al.*(Dean *et al.* submitted)). Previous work has suggested that under suitable conditions, ion beam modification of the substrate could induce a modified epitaxy,(Chew *et al.* 1992b) however this result was not reproduced due to variations in the growth conditions and chambers (Chew 1992a).

This work demonstrates a technique developed to control the epitaxial relationship between a YBCO thin film and a MgO substrate using a simple pre-growth substrate treatment. A commercially acquired (100) MgO substrate is partially covered with a physical mask (either hard baked photoresist or a metal contact mask) and then irradiated with low-voltage argon ions prior to growth (see chapter III. for more experimental details). After irradiation at room temperature for more than 2 minutes with a beam current density of approximately 1 mA/cm<sup>2</sup>, the sample is removed from the ion mill and the mask is taken off of the sample. A thin film of YBCO, usually 2000 - 3000 Å thick, is deposited on both the pre-sputtered and unsputtered regions of the substrate using POMBE. The resultant epitaxial relationship of the film to the substrate is cube-on-cube on the unsputtered region of the substrate, and

rotated by 45° about [001] on the presputtered region. Therefore, a 45° [001] tilt grain boundary is formed where the two grains meet. The rotation in the thin film occurred consistently using various ion beam energies, incident angles and irradiation times as described in the following section.

Sputter-induced epitaxy offers several distinct advantages over other junction techniques. The technique is extremely simple in implementation and uses current technology that is easily scalable. All of the other current junction technologies require more complex processing steps (except step-edge junctions, which are currently pursued for their simplicity). Industry uses both OMCVD growth systems and low voltage ion beams (the basic equipment necessary for sputter-induced epitaxy) on a large scale for semiconductor technology. Therefore implementation and scale-up of this technology would be relatively straightforward.

The junctions can be formed in virtually any configuration, currently only limited by the resolution of the mask. This is important for use in multi-device applications where junctions need to be formed in numerous geometries. Ultimately grain growth could be the limiting factor if sufficiently small size features can be patterned onto the substrate (e.g. using a focused ion source). Since the junction is based on a single grain boundary as opposed to multiple grain boundaries formed with step-edges and other methods, the transport properties are in principle more reproducible. The technique is planar, allowing vias and crossovers to be made without the problem of steps in the substrate. Also the grains are deposited on MgO across the entire substrate, so the grains have similar properties. In comparison, bi-epitaxial junctions are formed on different substrate materials and the grains can have very different properties

(see chapter VI). Other advantages will be discussed as the experimental data is presented.

There are two major disadvantages of sputter-induced epitaxy, the current limitation of using only a 45° misorientation geometry and having to use bulk MgO substrates. The 45° misorientation limits the ultimate critical current that can be passed through the sample. The relevance of the 45° misorientation on the transport data will be discussed in the following sections. The disadvantage of only using bulk MgO substrates can be circumvented using multilayers, which are discussed in chapter V.

#### **IV.1.2.1. Pre-growth Sputter Conditions**

##### **IV.1.2.1.1. Masking Techniques**

The basic pre-sputter conditions that were initially attempted to achieve the rotation were 300 eV argon ions at normal incidence to the substrate. The beam current density was approximately 1 mA/cm<sup>2</sup> during the irradiation. A tantalum metal mask covered part of the substrate, which was mounted with good thermal contact to a copper stub using silver paint. The irradiation was done at room temperature with minimal beam heating due to short irradiation times (typically 3 minutes). An optical image and a SEM micrograph of some of the first samples are represented in figure 4.2.

The samples were examined using EBSP to quickly and non-destructively determine the crystallographic orientation of the thin film. The first samples made with the metal mask had a modified epitaxy across the entire pre-sputtered region, except for an "interface" region that was polycrystalline. Such polycrystalline regions do not allow for simple isolation of an individual grain

boundary and lead to non-reproducible weak-link type behavior (see section IV.2.2). Therefore several modifications were necessary to develop high-quality grain boundaries, by controlling the interface region between the adjacent grains.

In order to improve the sample to form only one grain boundary, it was realized that the proximity of the mask to the substrate was important in determining the size of the polycrystalline region. The location of the polycrystalline region on the first sputter-induced epitaxy samples was found to correspond to regions along the edge of the mask that were not in direct contact with the substrate. Furthermore, the width of the polycrystalline region was larger the farther the mask was from the substrate during irradiation (see figure 4.2a). There are two possibilities for this effect. First, the mask would only partially shield the beam so some regions would receive a lower ion density bombardment, which creates a polycrystalline region. Second, the mask material could be sputtered and contaminate the substrate surface and affect the film growth. The inherent problem with the metal masks was that they could not be held in direct contact with the substrate across the entire length of the sample. Therefore, hard baked photoresist was used to form a mask that covered the desired regions, and was in direct contact with the substrate.

The samples made using the photoresist formed one grain boundary junction. The grain boundary was often indistinguishable from the film (see figure 4.2b), and could only be detected using EBSP diffraction (see IV.3.1). The photoresist is a standard patterning procedure, further simplifying the process of making the junctions. The added advantage of the photoresist is the easy ability to form junctions in a wide variety of geometries with relatively small

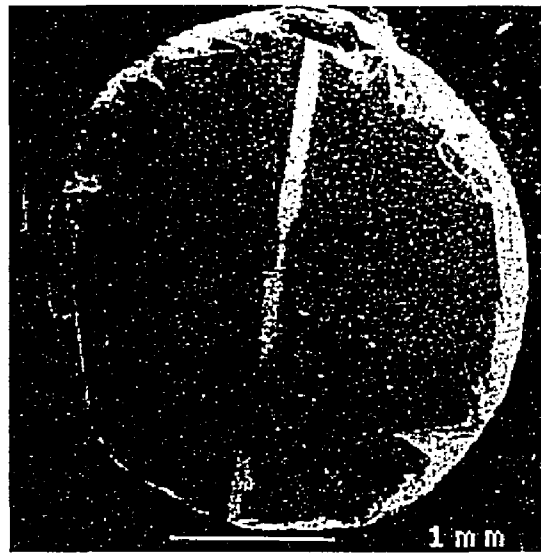


Figure 4.2a. A secondary electron micrograph of a sputter-induced epitaxy grain boundary junction with a polycrystalline "interface" region.

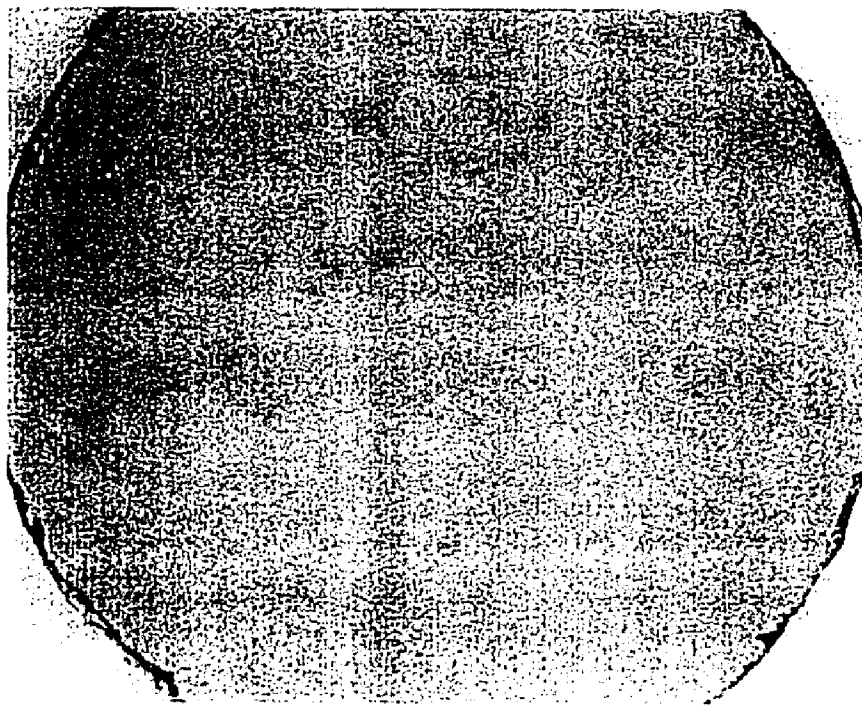


Figure 4.2b. An optical image of a high quality sputter-induced grain boundary junction. The junction is centered in the 3 mm diameter disk, and is barely discernible.

spacings (on the order of microns). All the subsequent junctions were then made using photoresist masks.

#### IV.1.2.1.2. Sputtering Conditions

Numerous processes occur during low voltage ion bombardment of the surface (see Chapter II.). Of these, we consider three possible mechanisms for sputter-induced epitaxy, that are based on the effect of ion beam modification of the substrate and the implantation of ions. Firstly, the ions could be damaging the surface in such a way to create more favorable nucleation sites for the modified epitaxy. Potentially, the uniform exposing of specific facets due to sputtering could establish a more stable environment for a secondary epitaxial condition. The surface damage could also destroy step sites that are favorable for nucleation of the cube-on-cube orientation (Traeholt *et al.* 1994a; Norton *et al.* 1991; Norton *et al.* 1992). The surface could even be amorphized in the process. Second, the ions could be modifying the surface structure through implantation. The implanted ions could distort the surface lattice parameter, making a secondary orientation very favorable due to a closer lattice match. Implantation could also form a specific type of surface damage that serves as a nucleation site for the modified epitaxy. Third, there could be a chemical effect of the implanted ions.

The possibility of chemical effects is discounted due to the inert gas that is used. Argon is used extensively in thin film processing and has not been seen to have a chemical effect in other systems (Baglin 1994). The role of surface damage versus ion implantation was studied by varying the conditions of the sputter and analyzing the results. Atomic force microscopy (AFM) was used to determine the type of damage done on the surface. The role of implantation

was studied using Rutherford Backscattering Spectroscopy (RBS) on substrates prepared using different pretreatments.

To gain a better understanding of the mechanism for the modified epitaxy, a variety of conditions were used to test the range available in the parameters of the pre-sputter treatment. The first test was simply whether or not modified epitaxy resulted on the pre-sputtered substrate region. Then, a set of samples was made using these conditions without depositing a film, and they were analyzed with RBS to gain insight into the surface chemistry of the MgO prior to deposition (see section IV.1.3).

A standard was adopted to confirm the rotation during specific growth runs. The conditions for the standard were 250 eV argon ions at normal incidence with approximately  $1 \text{ mA/cm}^2$  beam current for 3 minutes. These values consistently resulted in the modified epitaxy and were therefore used as a comparison value for other pre-sputter treatments.

There are many parameters in this process that could be explored. The three major variables that were investigated are incident ion beam energy, angle of ion incidence (relative to the substrate surface) and duration of sputter. Table 4.1 has a list of the various parameters attempted and whether the technique successfully produced a modified epitaxy.

The first set of experiments analyzed were the variation of the incident ion energy. The pre-growth sputter treatment caused a modified epitaxy for all incident ion energies for 100 eV and higher. At 50 eV some regions of the pre-sputtered substrate had a modified epitaxy, but other areas did not rotate. The growth run for the 50 eV sample, however, did not provide high quality films so it is still unclear whether the technique would work at this ion energy. The

Substrate Material	Incident Ion Energy (eV)	Angle of Ion Incidence	Duration of Sputter	Modified Epitaxy (Y/N)
<b>Standard</b>				
(100) MgO	250	90°	3 min.	Y
<b>Varying incident ion energy</b>				
(100) MgO	50	90°	3 min.	Partial
(100) MgO	100	90°	3 min.	Y
(100) MgO	200	90°	3 min.	Y
(100) MgO	250	90°	3 min.	Y
(100) MgO	300	90°	3 min.	Y
(100) MgO	400	90°	3 min.	Y
(100) MgO	500	90°	3 min.	Y
<b>Varying angle of incidence</b>				
(100) MgO	250	90°	3 min.	Y
(100) MgO	250	75°	3 min.	Y
(100) MgO	250	60°	3 min.	Y
(100) MgO	250	45°	3 min.	N
(100) MgO	250	30°	3 min.	N
(100) MgO	250	10°	3 min.	N
<b>Varying irradiation time</b>				
(100) MgO	300	90°	1 min.	N
(100) MgO	300	90°	2 min.	
(100) MgO	300	90°	3 min.	Y
(100) MgO	300	90°	4 min.	Y
(100) MgO	300	90°	5 min.	Y
(100) MgO	300	90°	6 min.	Y
(100) MgO	300	90°	9 min.	Y
(100) MgO	300	90°	12 min.	Y

Table 4.1. Results of YBCO thin film growth for different pre-sputter conditions.

advantages of lower beam energies is that the damage on the substrate can be minimized, as well as any step heights between the two grains. There must be a threshold energy to induce the modified epitaxy, and it is clear that the energy is below 100 eV.

The angle of ion incidence was varied to see the role of implantation vs. other surface damage. As the angle of the incident beam is decreased, there will be significantly less ion implantation, but increased sputtering of the surface, indicating which process is more significant (see figure 2.5b). Also if there is a preferred angle for which the rotation occurs, the role of preferential faceting could be determined. The modified epitaxy occurred for all incident angles greater than 45°. These results are correlated with RBS data on irradiated substrates to better understand the mechanism causing the modified epitaxy, and will be detailed in the following section.

The duration of the pre-sputter, which is proportional to the total number of ions for a constant current density, was also varied from 1 to 12 minutes. The modified epitaxy occurred for all times two minutes or greater. There is a threshold number of ions needed to induce the rotation. The total number of ions for a  $1 \text{ mA/cm}^2$  beam for 2 minutes is  $7.5 \times 10^{17} \text{ ions/cm}^2$  can be used as an approximation of the number of ions necessary. As with the lower ion energies, minimization of the duration of the pre-sputter will decrease the step height formed in the MgO, which is better for multilayer processing. As a general comment, the pre-sputter treatment is relatively robust to varying conditions, and the process is done in a separate chamber from the growth chamber indicating that it is not affected by the intermittent exposure to

Substrate Material	Incident Ion Energy (eV)	Angle of Ion Incidence	Duration of Sputter	Modified Epitaxy (Y/N)
Different substrates				
(100) MgO	100-500	60°-90°	>2 min.	Y
(100) SrTiO <sub>3</sub>	500	90°	5 min.	N
(100) LaAlO <sub>3</sub>	500	90°	5 min.	N
(100) YSZ	500	90°	5 min.	N
(100) Si	500	90°	5 min.	N
(1120) Al <sub>2</sub> O <sub>3</sub>	500	90°	5 min.	N
(110) MgO	500	90°	5 min.	N
(100) NiO	250	90°	3 min.	NA
(100) MgO/ (100) LaAlO <sub>3</sub>	250	90°	3 min.	Y (see Ch. V.)

Table 4.2. Different substrates attempted for sputter-induced epitaxy.

atmosphere (predominantly in desiccant) or by the amount of time between the irradiation and the growth.

The pre-sputter treatment was tried on numerous substrate materials to see if the modified epitaxy occurred. Table 4.2 has the results from these experiments showing that the technique did not produce a modified epitaxy on any other substrate material except for multilayers. The multilayers will be discussed in the next chapter. NiO and Mg<sub>2</sub>TiO<sub>4</sub> were identified as two substrates that could potentially work due to the similar lattice parameter and crystal structure to MgO, but have not yet been tried.

#### **IV.1.3. Rutherford Backscattering Spectrometry**

##### **IV.1.3.1. Background**

A group of substrates were analyzed using RBS to probe the surface chemistry (with a 40 Å depth resolution). RBS uses a beam of monoenergetic and highly collimated alpha particles (<sup>4</sup>He nuclei) to probe the sample (for more details see Chu *et al.*(Chu *et al.* 1978)). Some of the particles are backscattered due to close interaction with the nucleus of an atom and the strong Coulombic force involved. These backscattered particles are counted by a detector that also measures the energy loss. The understanding of the spectra is based on elastic collisions between two hard spheres and the energy loss during the process. Helium is a light element, which will therefore be sensitive to heavier masses. In order to determine the energy of the backscattered particle after the collision, a kinematic factor, K, is used. The kinematic factor is the ratio of the projectile energy after the collision to the energy prior to the collision, and depends on the scattering angle, and the atomic masses of the incident particle and the target

atom. From the energy loss of the detected particle and the mass of the target, the depth into the sample of the detected mass can also be determined. The depth profile is determined by the additional loss of energy as the alpha particle travels through a dense medium. Therefore this technique can be used to determine the mass and depth of elements in the sample with great sensitivity (note that due to the dependence of the kinematic factor on mass, heavier elements are significantly easier to detect than lighter elements).

Several (100) MgO samples were prepared with a variety of substrate pre-treatments and analyzed with RBS to determine the chemistry of the sample surface region. The experimental configuration was identical for all the runs. The beam incident on the sample was a highly collimated beam of 1.6 MeV  ${}^4\text{He}$  particles. The sample was tilted 10° off the sample normal and away from the detector to avoid channeling conditions that decrease depth resolution, and increase the detector counts. The detector was at a 45° angle to the sample. The energy loss of the particles was calibrated with a Cu-1%Au standard and an Al standard. The counts were normalized to 100,000 for channels 451-500 for the Mg peak. The actual measurements were performed by Pete Baldo at Argonne National Laboratory.

#### **IV.1.3.2. RBS on Pre-Sputtered Substrates**

##### **IV.1.3.2.1. Standard Pre-Sputter Conditions**

A RBS spectrum of a MgO substrate sputtered for 3 minutes at 250 eV (90° incident angle) is shown in figures 4.3a-b. Two large edges are due to the Mg and O that are present in the bulk, but if the higher end of the energy loss spectrum is magnified (figure 4.3b.), two other peaks are clearly present. The

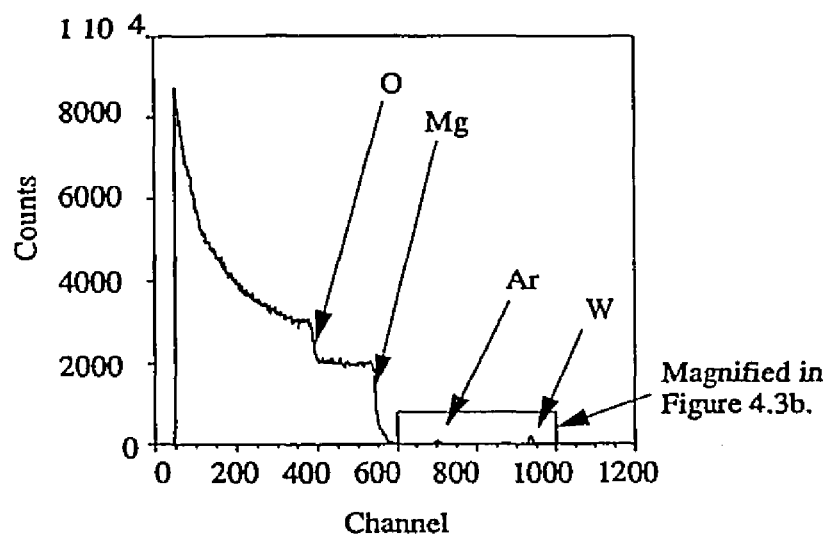


Figure 4.3a. RBS spectrum for a MgO substrate irradiated for 3 minutes with 250 eV ions and a beam current density of  $1 \text{ mA/cm}^2$ .

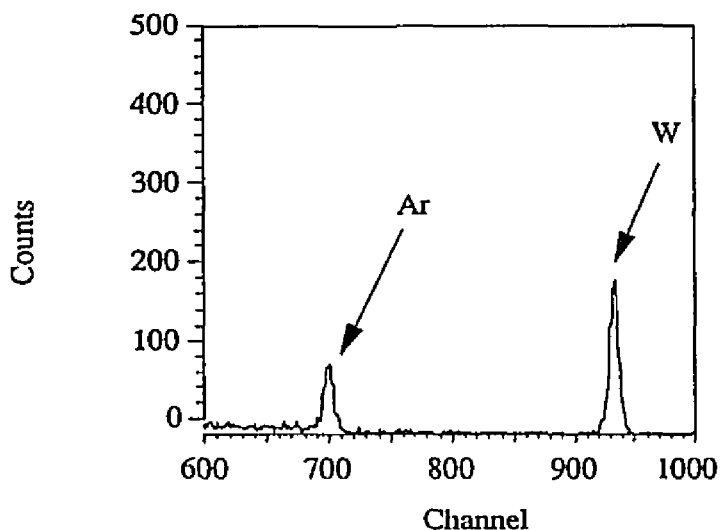
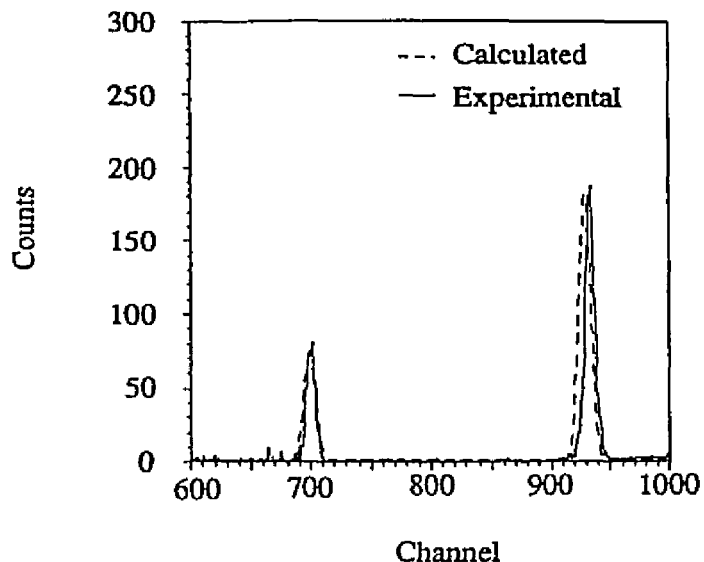
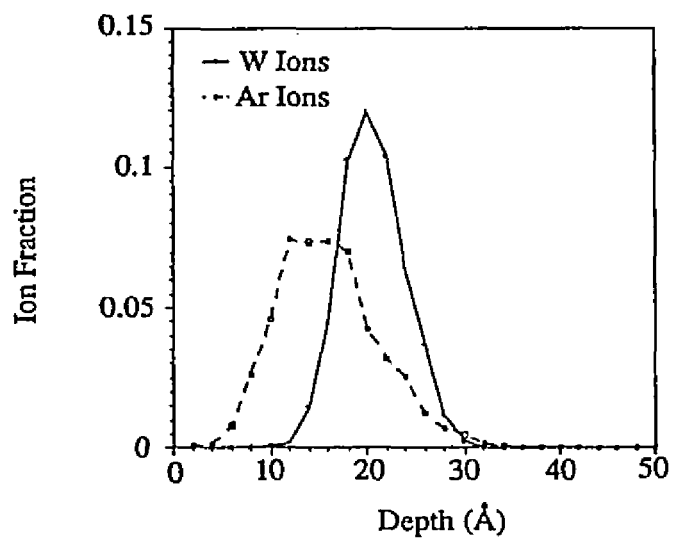


Figure 4.3b. Magnified image of high energy loss regime from inset in figure 4.3a.



**Figure 4.4.** Experimental and calculated RBS spectra. The simulation of the RBS spectrum is done using 1 monolayer of argon and 0.1 monolayer of tungsten in the top 10 Å of the substrate.



**Figure 4.5.** TRIM calculation of argon and tungsten ion penetration into a MgO substrate.

first peak at channels 691-715 is due to argon, indicating that there is argon in the top layer (within 40 Å of the surface, the depth resolution of the experiment). Note that the integrated counts are taken after a linear background is subtracted. The second peak at channels 911-950 is due to tungsten also in the top 40 Å of the surface. It was determined that the tungsten could only come from the filament in the low voltage ion mill.

A simulation of the spectrum, shown in figure 4.4, verifies that the argon and tungsten remain in the top surface layer. The ratio of argon to tungsten is determined from the simulation to be approximately 10:1, Ar:W. In the unmodified spectrum, the tungsten peak is larger due to the higher sensitivity to heavier masses. The slight offset between the tungsten peak and the simulated peak is probably due to the non-linearity of the detector response. In this simulation the first ten layers of the sample were considered to have 0.1 layer of argon and 0.01 layer of tungsten. This amount provided the most accurate match with the data. Quantitatively the amount of argon is equivalent to one monolayer and the tungsten a tenth of a monolayer total. For a 3 minute sputter with  $1 \text{ mA/cm}^2$  beam current density, the total number of ions is  $1.125 \times 10^{18} \text{ ions/cm}^2$ . The total number of atoms in a monolayer of MgO is  $9.52 \times 10^{15} \text{ atoms/cm}^2$ . Therefore approximately 1% of the ions impinging on the surface are implanted, which is reasonable.

A TRIM code Monte Carlo simulation of low voltage argon and tungsten bombarding a MgO substrate was also performed. There are some limitations to the TRIM code particularly in the low energy regime. First, the code treats the target as an amorphous solid, therefore it does not take into account channeling or crystallographic effects, which can be significant at low energies.

Also, TRIM does not account for material that is sputtered away. The calculation for 500 eV argon and tungsten ions into MgO is shown in figure 4.5. The results qualitatively confirm that the implanted ions all sit in the top 20 Å of the sample surface, with the tungsten atoms lying slightly deeper in the target. Sputtering of the substrate, that is not accounted for using TRIM, would make the argon and tungsten even closer to the surface. This agrees with the RBS data and simulation.

#### IV.1.3.2.2. Modified Pre-Sputter Conditions

A list of the RBS results for substrates given different pre-treatments is compiled in Table 4.3. A standard MgO sample was run without any sputter treatment and did not have any Ar or W present, however there was a slight peak at approximately channel 800 that disappeared after any type of sputter pre-treatment. This peak could be due to some surface contamination, or residual material from the commercial polish used to obtain the epitaxial finish. Using the same ion beam density and irradiation time, the Ar counts increase rapidly, as a function of incident ion beam energy, from 50 eV to 100 eV and then appear to saturate at around 250 eV. The W counts increase significantly between 50 eV to 100 eV, then increasing minimally above 250 eV. With respect to the growth conditions that successfully produced a modified epitaxy in the YBCO film, only 50 eV did not form a modified epitaxy. This indicates that a potential threshold energy is necessary to imbed sufficient argon or tungsten into the sample to cause the rotation.

As the incident angle is varied from 90°, there is a marked decrease in the ion implantation. Table 4.4 shows the normalized ratio of the implanted ions at

Ion Energy (eV)	Angle of Incidence	Time (sec.)	Ar (counts)	W(counts)	Ar/W (counts)
50	90°	180	421	847	0.497
100	90°	180	666	1397	0.477
200	90°	180	678	1409	0.481
250	90°	180	780	1735	0.450
300	90°	180	754	1758	0.430
250	90°	180	780	1735	0.450
250	45° (aligned)	180	108	626	0.173
250	45°(not aligned)	180	0	93	0
250	30°	180	0	66	0
250	90°	2	0	50	0
250	90°	5	393	93	4.226
250	90°	30	758	249	3.044
250	90°	60	777	463	1.678
250	90°	120	733	819	0.895
250	90°	180	780	1735	0.450
250	90°	600	525	2872	0.183
300/250	90°/30°	180/180	754/115	1758/364	0.429/ 0.316

Table 4.3. RBS data for pre-sputtered MgO substrates under different conditions. Ar and W counts are the integrated counts over the entire peak after a modeled background is removed.

Ion Energy (eV)	Angle of Incidence	Time (sec.)	Ar:Ar(90°)	W:W(90°)
250	90	180	1.00	1.00
250	75	180	0.29	0.89
250	60	180	0.29	0.32
250	45	180	0.11	0.08
250	30	180	0.00	0.04

Table 4.4. RBS results for a series of incident angles. Ar and W counts as a percentage of the counts at 90°.

a given incident angle to the implanted ions at 90°. The results for samples irradiated at 45° and lower indicate that the argon and tungsten are removed from the sample. The data show that at 45° the rate of implantation is lower than the sputter removal rate, so any ions implanted are removed. There were two samples sputtered at 45°, one in a channeling (110) condition and one in a non-channeling condition. The argon and tungsten are virtually absent in the non-channeled sample, but there is still significant argon and tungsten left in the channeled sample indicating a clear crystallographic effect. At 30° there was virtually no argon or tungsten present. Thin films grown on substrates pre-irradiated at 45° or less did not have a modified epitaxy on the pre-irradiated regions.

The implications of the results from the angular dependence of the Ar and W content are two-fold. First the implanted argon and tungsten potentially play a role in the surface modification, possibly by inducing a lattice strain that would favor the 45° rotated condition. Both argon and tungsten are larger than the Mg and O and would expand the lattice as an interstitial. By expanding the lattice, the mismatch between the substrate and film for the cube-on-cube orientation would increase above the already large 8.8%. For the 45° modified epitaxy, however, it would reduce the misfit from 2.8%, therefore making it more favorable.

The other possible implication is that the type of damage on the surface done at 45° is different from the damage at 90°. One possibility is that a faceted surface favoring the growth of the 45° modified epitaxy is created at the higher incident angles. This is doubtful since the epitaxy is modified using both 60° and 75° incident angles. Preferential faceting would be expected if the

technique only produced the modified epitaxy for a given angle, and a relatively small tolerance (approximately 5°) about that angle.

Another type of surface damage could be destruction of the step structure. The surface step structure is heavily modified by ions at all incident angles, especially at the lower angles where the sputter yield is higher. Therefore, this is probably not the mechanism responsible for the modified epitaxy. The ions could also locally amorphize the surface of the substrate. If the surface was amorphized then sputter induced epitaxy in principle should modify the epitaxy of YBCO on MgO with a different substrate orientation. [110] MgO was attempted, but did not show any favored epitaxy indicating that this is not a factor. This is also confirmed by Traeholt *et al.* (Traeholt *et al.* 1994a) who showed that YBCO can grow with the cube-on-cube orientation with a small amorphous layer at the substrate surface.

The final type of possible surface damage is the creation of a defect structure directly associated with the ion implantation. The modified epitaxy occurs only for conditions where argon and tungsten are implanted. Thus, a type of damage site could be produced by the implantation, such as ions that coalesce at the surface, or regions with a modified lattice parameter associated with a defect. AFM results on the irradiated surface structure are discussed in the following section.

The ion implantation as a function of time provides more insight into the mechanism for the modified epitaxy. Figure 4.6 is a plot of the argon and tungsten counts as a function of irradiation time. Note that the counts are not normalized, and the ratio is approximately 10:1 of Ar:W at 180 seconds (determined from simulation of the spectra). It is apparent that the argon

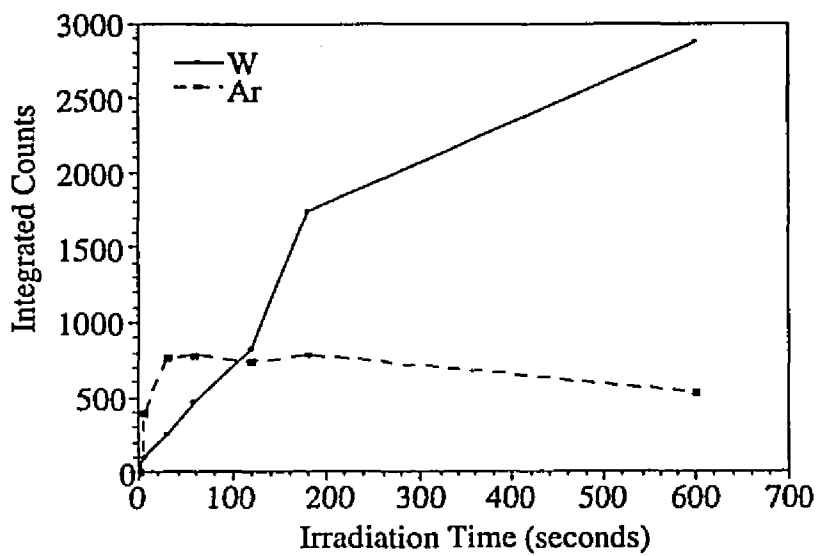


Figure 4.6a. Integrated counts of argon and tungsten as a function of irradiation time.

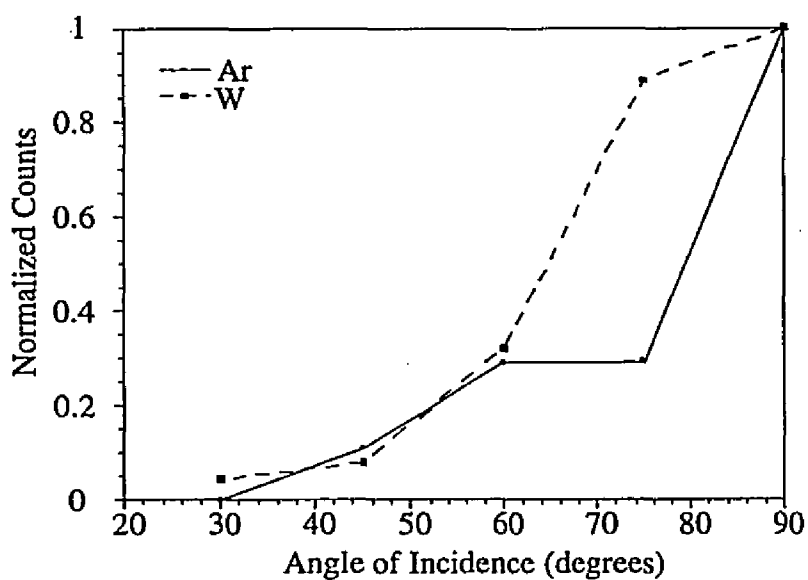


Figure 4.6b. Normalized counts of argon and tungsten as a function of angle of incidence. Counts are normalized to values for 90° incidence.

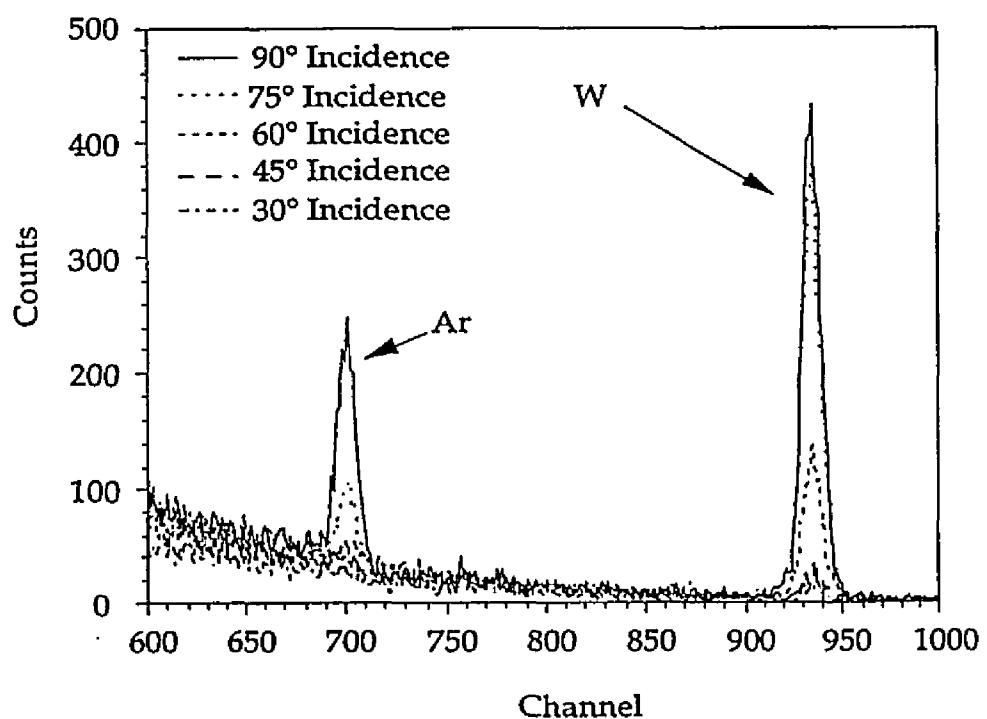


Figure 4.6c. RBS spectra from varying ion incidence angle.

reaches an equilibrium point after approximately 30 seconds. At that point the amount of argon being implanted is equivalent to the amount that is removed due to sputtering. The tungsten content, however, increases linearly with the duration of irradiation up to at least 10 minutes. The modified epitaxy occurred for irradiation times of 2 minutes or greater. This suggests that the tungsten may play an integral role in the process of forming the modified substrate. The tungsten can play two roles during irradiation. First the tungsten is implanted, which as previously mentioned distorts the lattice. Tungsten is significantly larger than argon, therefore it creates a larger lattice strain on the surface when it is implanted. The second effect is the damage on the surface. The tungsten will damage the surface more during bombardment due to its size.

There is the possibility that the substrate treatment in the growth chamber could remove some of the implanted ions. Several of the samples measured initially were subsequently given the standard pre-treatment in the POMBE system. There was no marked difference in the spectra after the ozone anneal. This indicates that both the argon and tungsten remain in the substrate during the deposition.

The combination of the RBS data, growth data and simulations gives a good understanding of the mechanism for the sputter-induced epitaxy. It appears that the implanted ions, including the tungsten play an integral role in the process. If only generic surface damage or roughening is responsible for the rotated epitaxy, then even low angle sputtering would be effective, however this is not the case. For incident angles of 45° or less the modified epitaxy did not occur, so the implanted ions play some role in the resulting film orientation. This result also indicates that a given number of ions implanted/cm<sup>2</sup> are

necessary to see the effect, not just the total number of ions impinging on the surface. It appears consistent to suggest a locally modified lattice parameter that would effect the growth since the results indicate that all the ions are at the substrate surface (probably within the top 10 Å). The lattice parameter change could also be associated with a specific type of defect site that facilitates nucleation of the modified epitaxy.

These results also suggests why other groups using ion beams on MgO do not see the effect. The FIB technique uses much higher energy ions (5-50 keV), which implants the ions deeper in the surface. The directionally ion milled substrates uses lower incident angles that would not be expected to give a modified epitaxy. Comments on further potential studies are made in the conclusion (chapter VIII).

#### IV.1.3. Surface Profile

Atomic force microscopy (AFM) was used to analyze the MgO pre-sputtered and unspattered surfaces. In these measurements, the tip radius was on the order of 200 Å. The images therefore were a convolution of the tip shape and the substrate surface. Deconvolution was not performed on the images, and they are only used comparatively. Figures 4.7a-b. are AFM images from unspattered and sputtered commercially polished MgO substrates. It is immediately apparent that the surface is not very smooth on a nanometer scale. There is significant surface roughness and some deep craters on the surface. The craters are probably etch pits due to the commercial substrate preparation that includes a chemical etch. The image of this surface gives an obvious indication as to why MgO is not always a favored substrate for thin film growth.

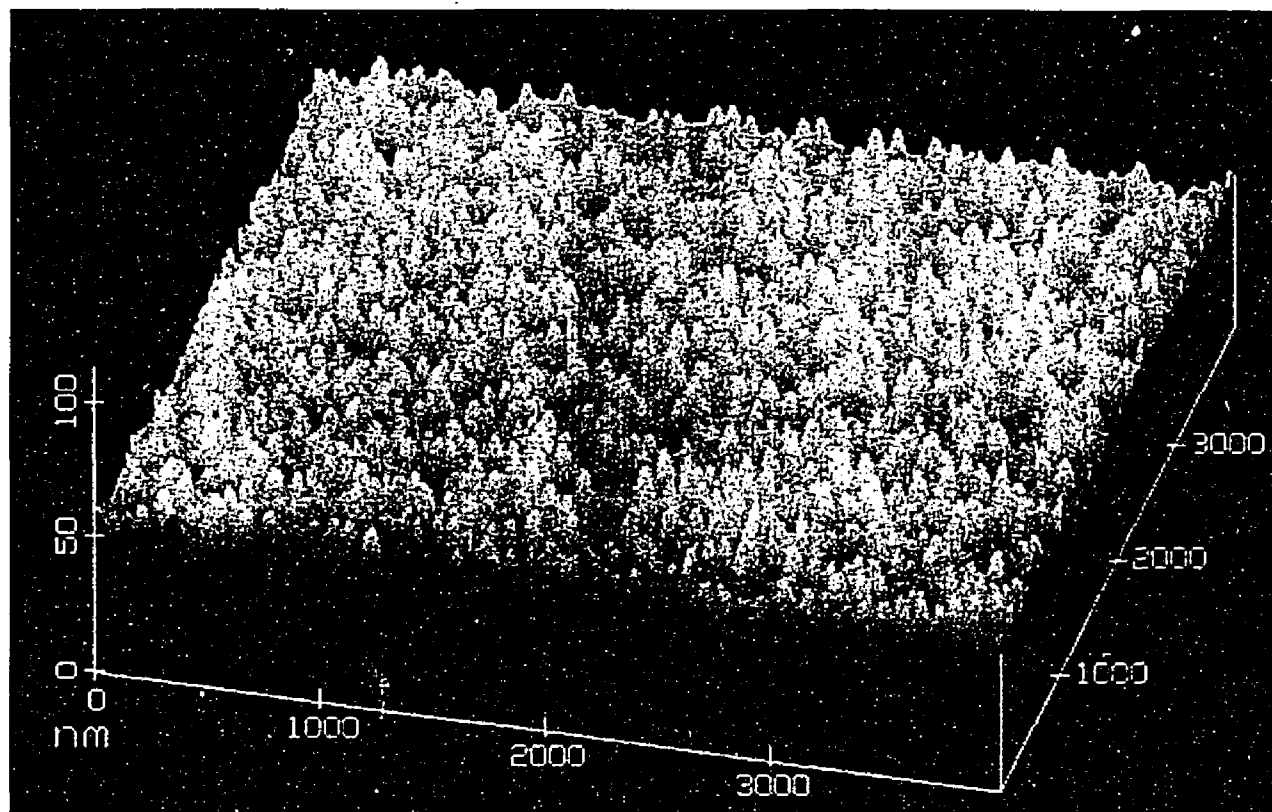


Figure 4.7a. AFM image of an unspattered region on a (100) substrate prior to annealing.

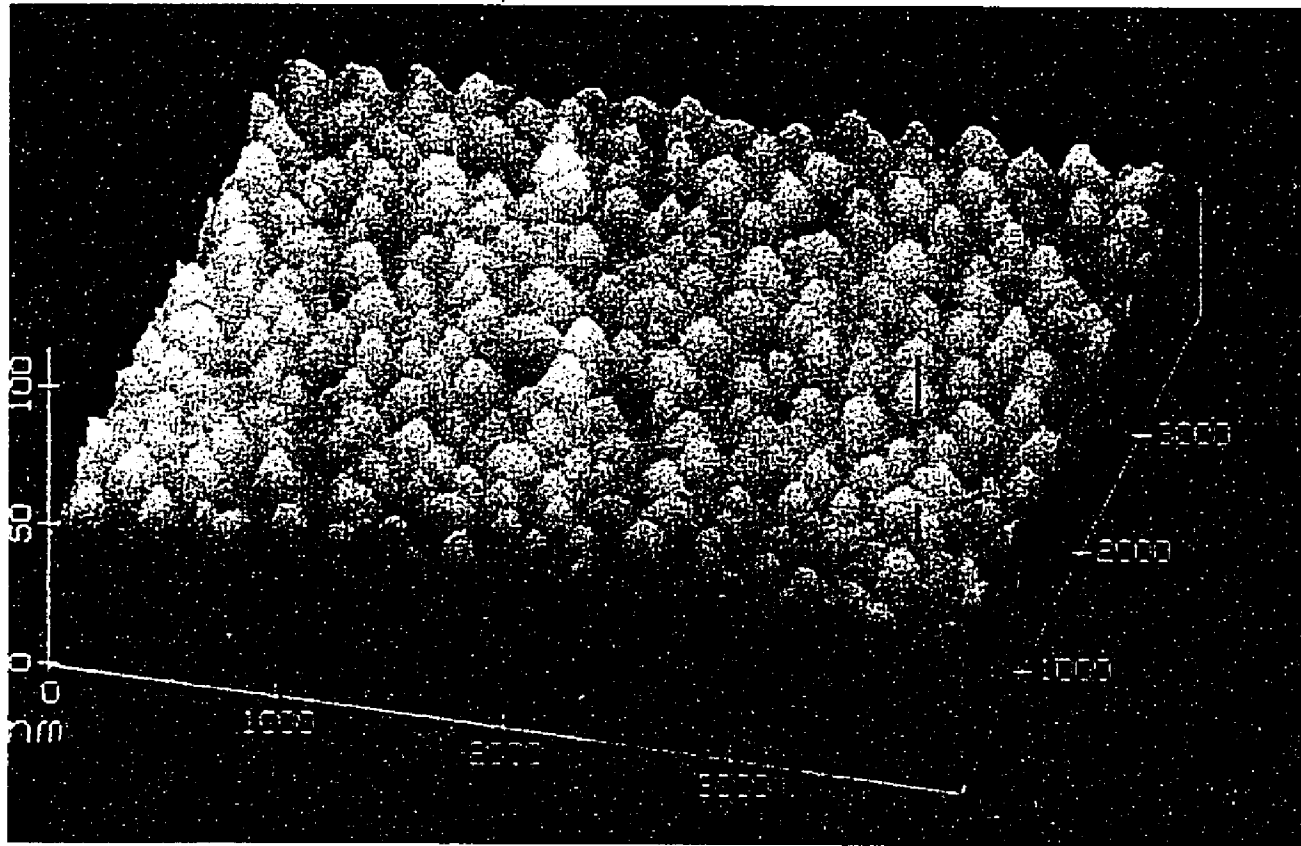


Figure 4.7b. AFM image of a pre-sputtered substrate (300 eV argon for 3 minutes) prior to annealing.

In order to get an accurate surface image of the substrate during deposition, a set of samples was preirradiated and then given the standard substrate pre-treatment used before a POMBE growth. The pretreatment included an anneal at 680°C in an oxygenated plasma for 30 minutes and then a slow cool in the plasma to 400°C. The sample was removed at approximately 330°C and was air cooled. The samples were irradiated for 3 minutes at 300 eV with hard baked photoresist masks covering part of the sample. The image of a step, which delimits the sputtered and unspattered regions, is shown in figure 4.8a. The step is relatively sharp and approximately 160 nm wide, not accounting for the deconvolution of the probe (which would make it narrower). The height of the step is 12 nm indicating a sputter rate of approximately 4 nm/min.

The oxygen plasma definitely removes contaminants from the surface of the substrate. The images taken prior to the anneal and after the anneal clearly show a large decrease in the magnitude of the surface roughness. In the annealed samples, the major difference between the sputtered and unspattered regions is the roughness of the surface. At first glance this is not apparent, but a higher magnification scan (see figure 4.8c-d) shows that the unspattered region is very smooth with only a few surface defects probably from the polishing procedure. The presputtered region has some coarse roughness (and the edge of an etch pit can be seen). The roughness has the characteristic appearance of small rounded lumps on the order of 25-100 nm in size. This type of defect appears to be associated with the bombardment and could be a favorable nucleation site for the modified epitaxy. Average roughness from the sputtered and unspattered regions also proves an increased roughness on the pre-

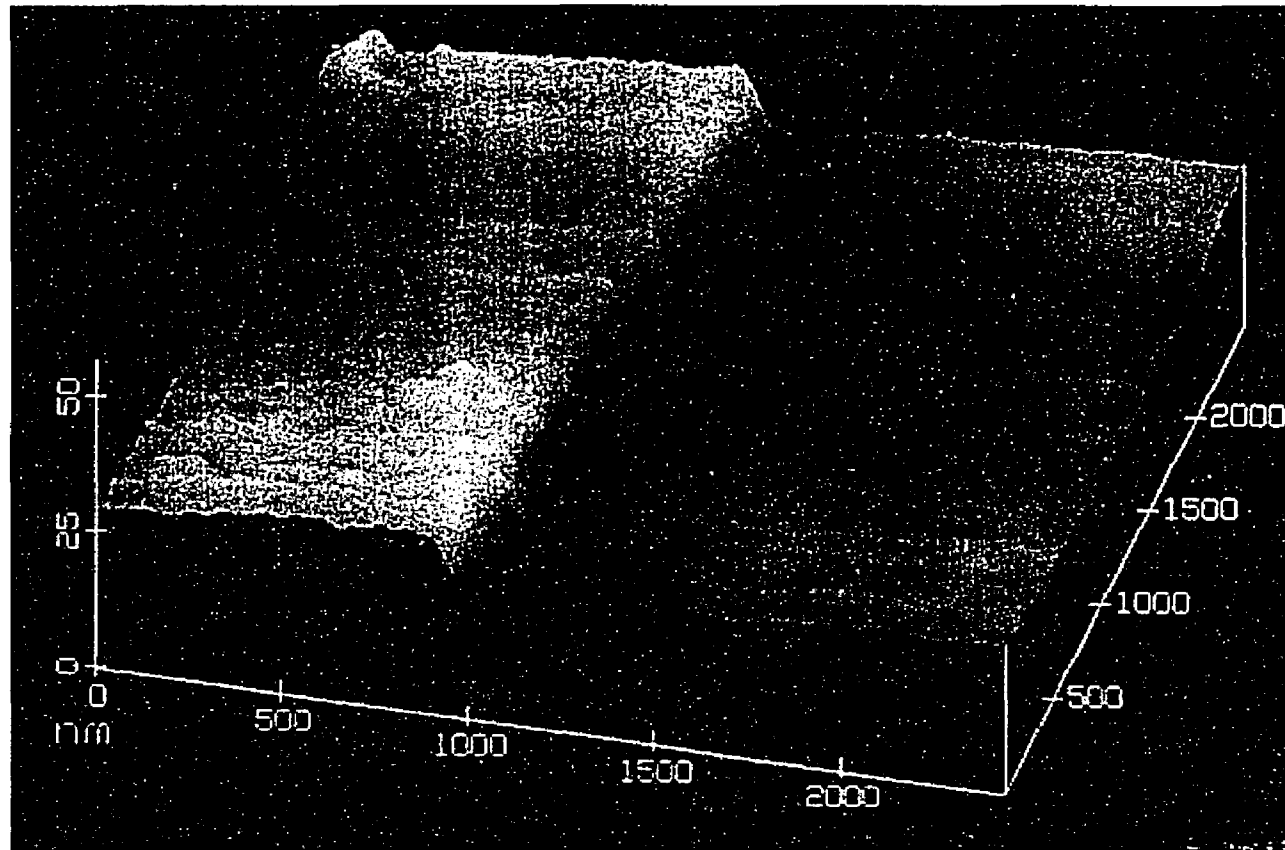


Figure 4.8a. AFM image of the edge delineating the pre-sputtered and unspattered regions of the substrate after an oxygen plasma anneal.

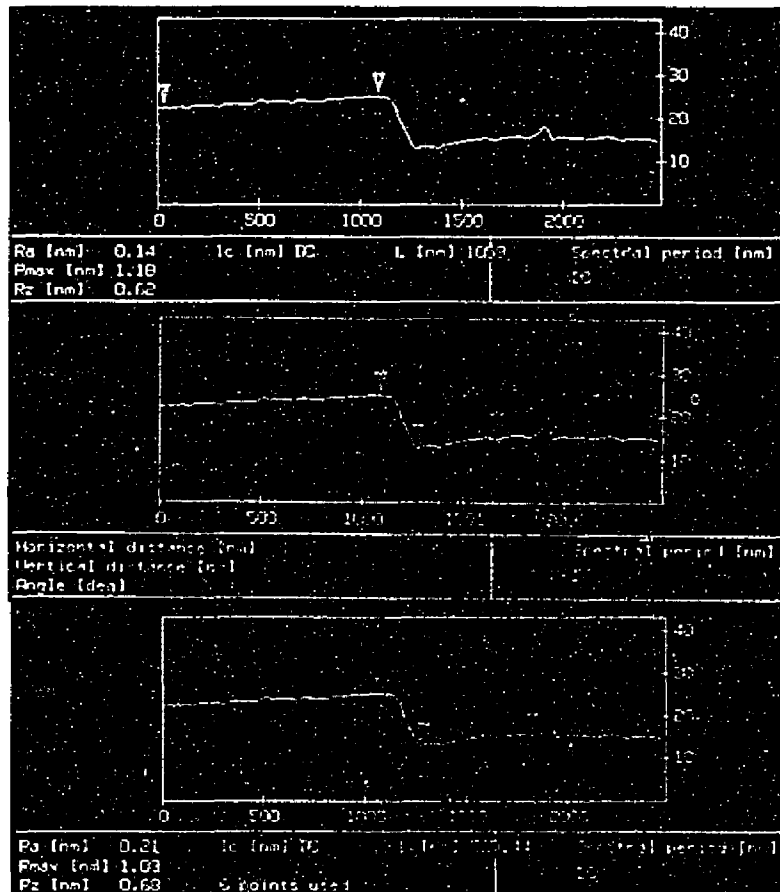


Figure 4.8b. Line scans of step region in figure 4.8a. showing roughness values for the unsputtered region (top scan) and sputtered region (bottom scan). The middle scan shows the step edge height.

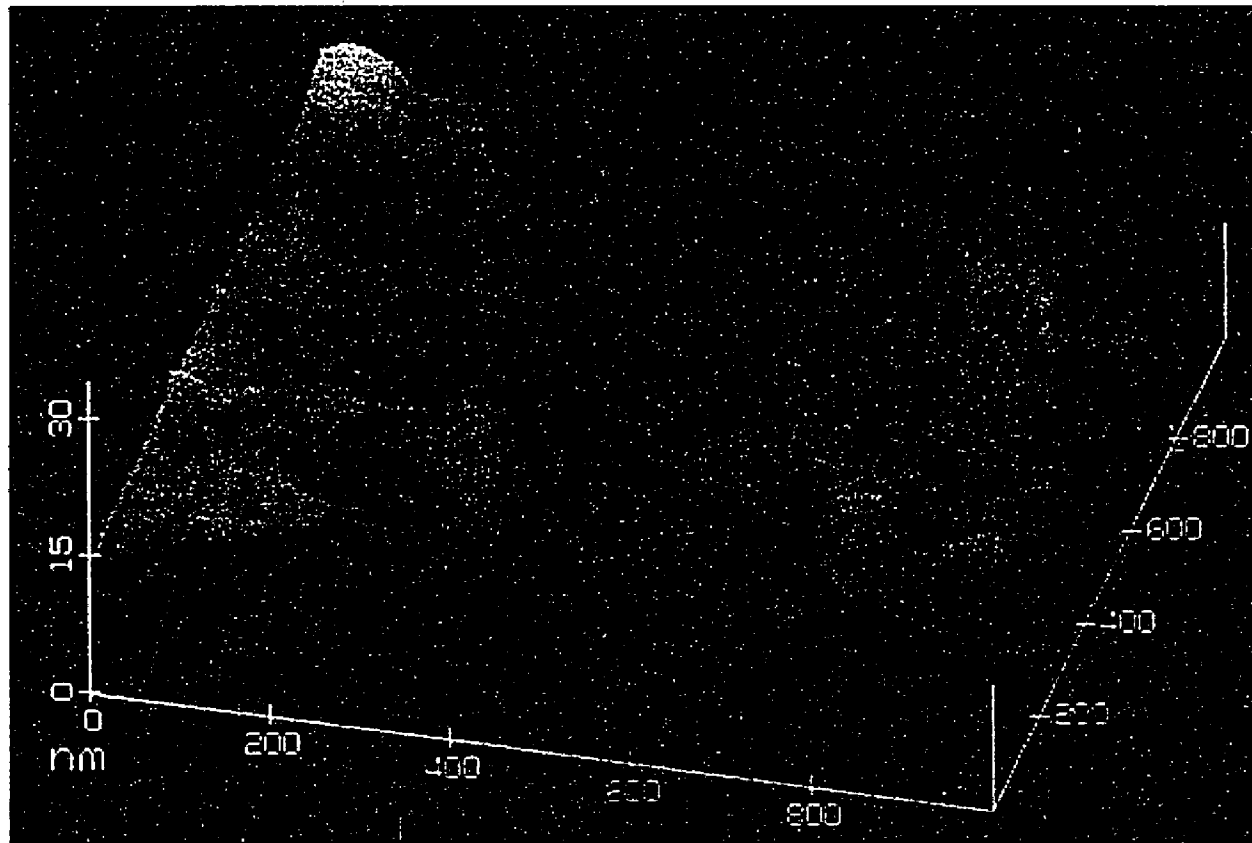


Figure 4.8c. AFM image of unspattered region after anneal in an oxygenated plasma.

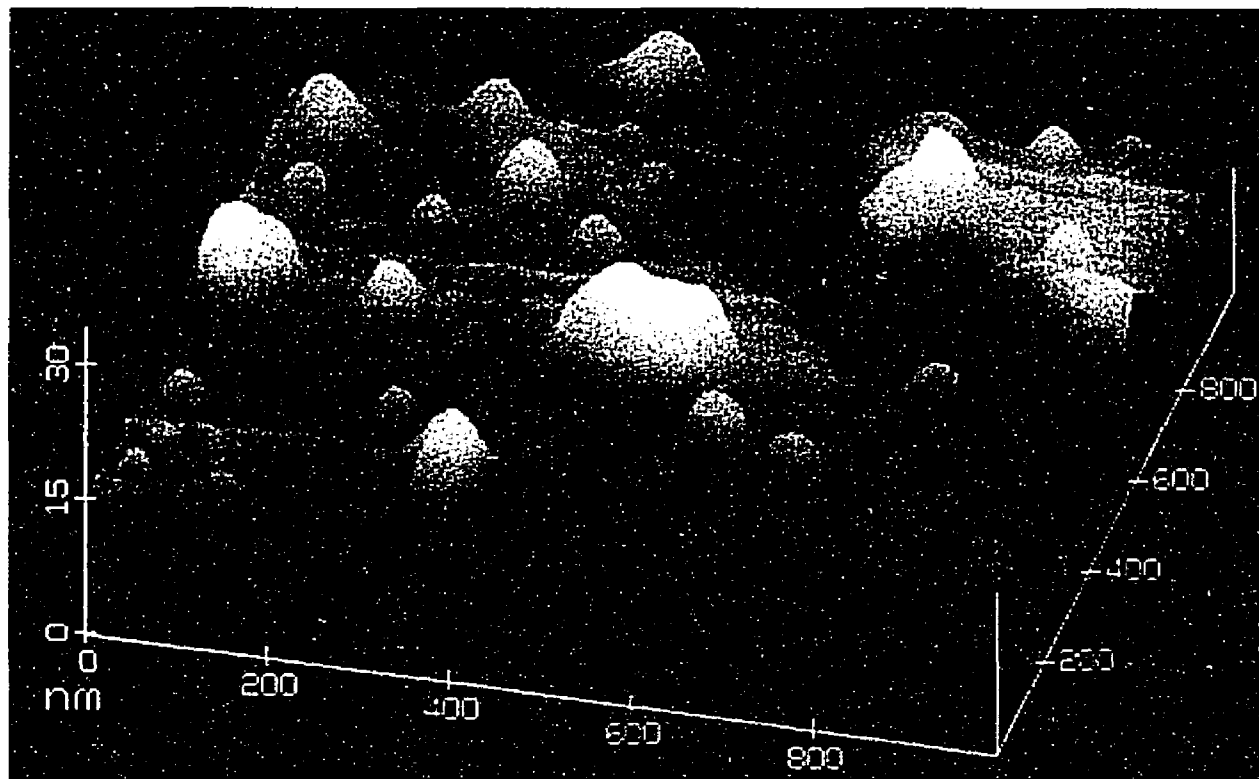


Figure 4.8d. AFM image of a pre-sputtered region (300 eV argon ions for 3 minutes) after anneal in fully oxygenated plasma.

sputtered region of about 50%. The increased roughness, however, would still be expected from sputtering at different angles. Therefore to consistently explain the results, the type of surface damage is uniquely associated with the ion implantation. It was not possible to get an atomic resolution image to determine the local structure of the sample. The implanted ions remain in the substrate even after the anneal, but the surface topology is significantly improved and exhibits a characteristic damaged structure.

## IV.2. Transport Properties

Individual grain boundaries were patterned for low temperature measurements as described previously (see Chapter III.). The first grain boundaries measured were formed using a metal mask. These samples had a polycrystalline interface region between the rotated and unrotated parts of the thin film. After improving the masking techniques, samples were measured with just one grain boundary junction. The samples measured were prepared under generally standard pre-growth conditions due to the large preparation time to make a measurement sample. The grain boundary junctions were not compared for significantly varying pre-sputter treatments, other than the change in type of physical mask. The various transport properties of these junctions are discussed in this section.

### IV.2.1. Resistance-Temperature

The R-T characteristics are intimately connected to the structure of the boundary region as is shown by comparing the resistance vs. temperature measurements for three different sputter-induced samples (see figures 4.9-4.11).

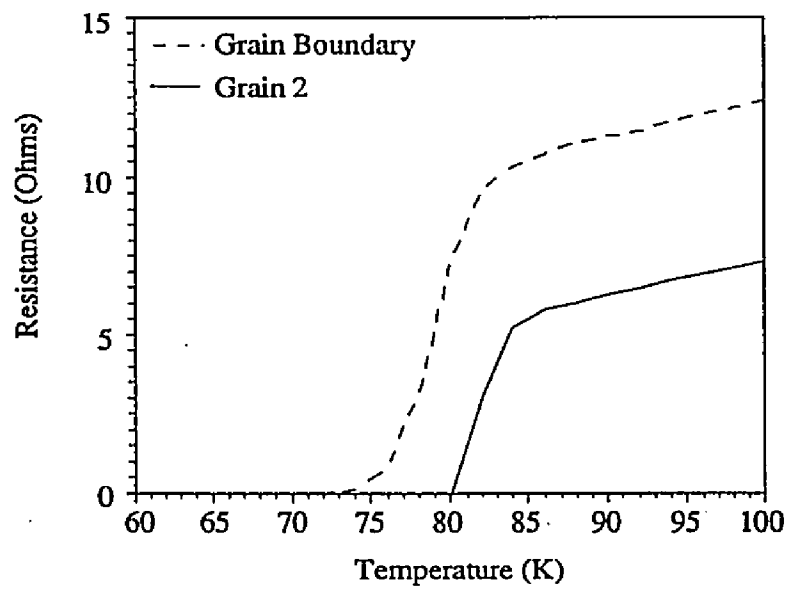


Figure 4.9. Resistance vs. temperature curve for a polycrystalline grain boundary region.

Figure 4.9 is from one of the first sputter-induced samples that was made with a metal contact mask in poor contact with the substrate. The normal state resistance of the grains and the grain boundary channels exhibit a linear decrease in resistance as a function of temperature above  $T_c$  (note that "grain boundary" is a misnomer in this case because the region was polycrystalline and the term is only used for convenience). They both have the same slope  $dR/dT$ , but not the same magnitude of resistance (note that all the resistances are across the same width microbridge, 40  $\mu\text{m}$ , so they can be directly compared). The grain has a relatively abrupt transition at 80 K, but the grain boundary region has a broadened transition with a positive curvature at the base. The curvature is indicative of a polycrystalline sample where the path of least resistance goes through a series of grain boundaries with different transition temperatures. The abrupt transition of the grain is indicative of the material having predominantly a single  $T_c$ . Figure 4.12 illustrates the cause of the broadened base of the resistance curve for a polycrystalline region and the more abrupt transition for a single grain boundary. The current path crosses many grain boundaries with varying critical temperatures that go superconducting one at a time until a whole superconducting path is created. This is distinguished from a single grain boundary where in spite of variations in  $T_c$  along the grain boundary a more abrupt transition exists. The variations of  $T_c$  along the grain boundary are less significant because it is a parallel connection as opposed to a serial connection of the different regions.

The R-T curve in figure 4.10 is from a sample with a metal mask that had better contact than the sample in figure 4.9. The normal state resistance of the grains and the grain boundary were virtually identical in this sample, and the

transitions were very abrupt with  $T_C = 85$  K. There is no rounding of the transition at the base. Using a larger measuring current, an extended hump is formed at the base of the transition. This is the resistance from the grain boundary (the grain goes superconducting at 84 K), and can be attributed to thermally activated transport channels that are in parallel with superconducting channels across the boundary. The curve is fit well with a model of parallel conduction channels based on eq. 4.5 (see figure 4.10c.), which is discussed in the following section.

Figure 4.11 is the R-T curve for a sample prepared using a photoresist mask for the pre-sputter treatment. The grain has a critical temperature of 86 K, but the grain boundary region clearly exhibits a foot-like structure. This is indicative of a high-quality grain boundary junction, clearly different from the polycrystalline example in figure 4.9. After the grain onset, which is closely followed by the grain boundary because it has the grain adjacent to it, the foot structure has a slight linear decay until there is an abrupt transition to the superconducting state at 81.25 K. The foot-like structure can be attributed to thermally activated phase slippage (TAPS) as shown in the following section. Essentially, the Josephson coupling energy,  $E_J$ , is diminished at the grain boundary due to the small critical current, and allows thermally activated phase slippage to create a finite resistance. The linear decrease and abrupt transition are due to the resistance of one boundary, unlike the polycrystalline samples that exhibited a curvature. The variation in the normal state is due to the two grains on either side of the boundary having different  $T_C$ 's. The grain boundary only provides a small addition to the normal state resistance above  $T_C$  and is dominated by the resistance of the grains on either side. The difference in the

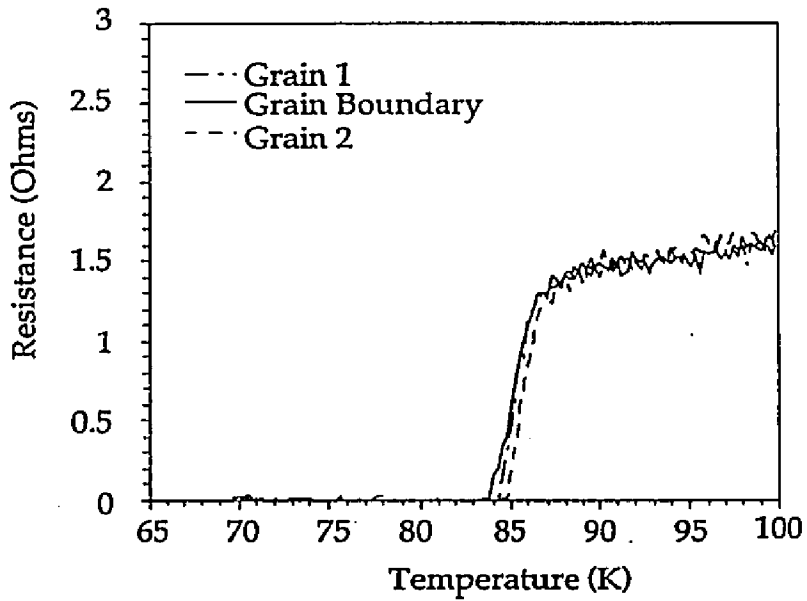


Figure 4.10a. Resistance vs. temperature characteristics for a grain boundary junction formed with a metal mask.

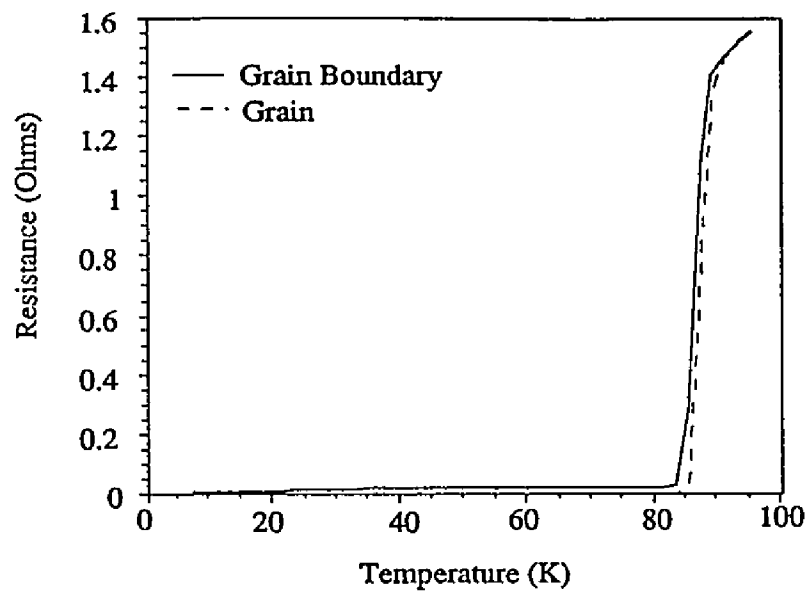


Figure 4.10b. Resistance vs. temperature for sample in figure 4.10a using 1 mA measuring current.

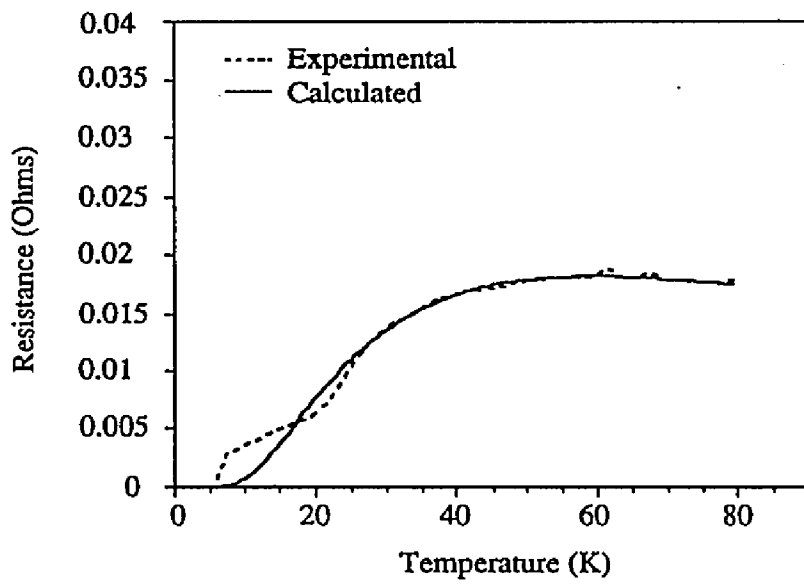


Figure 4.10c. Magnified foot-like structure from (b.), with calculated fit to a set of parallel thermally activated transport passages.

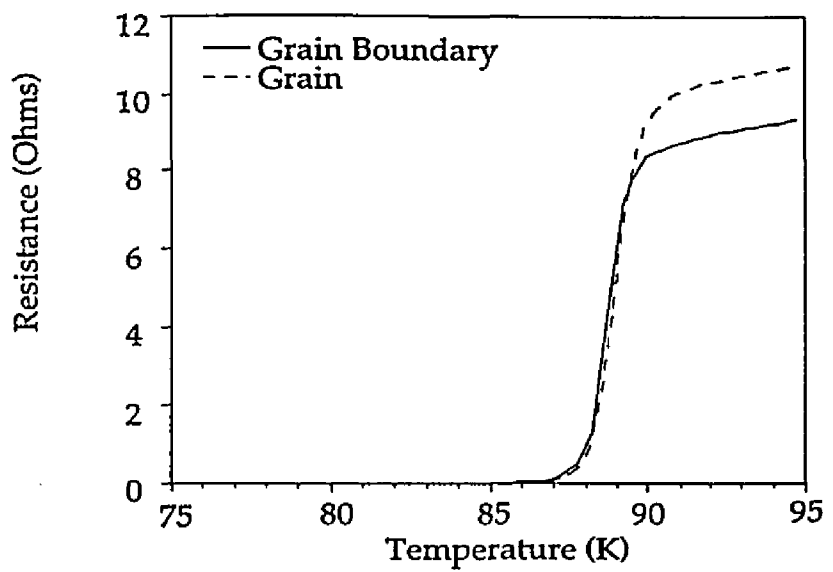


Figure 4.11a. Resistance vs. temperature for photoresist masked sample.

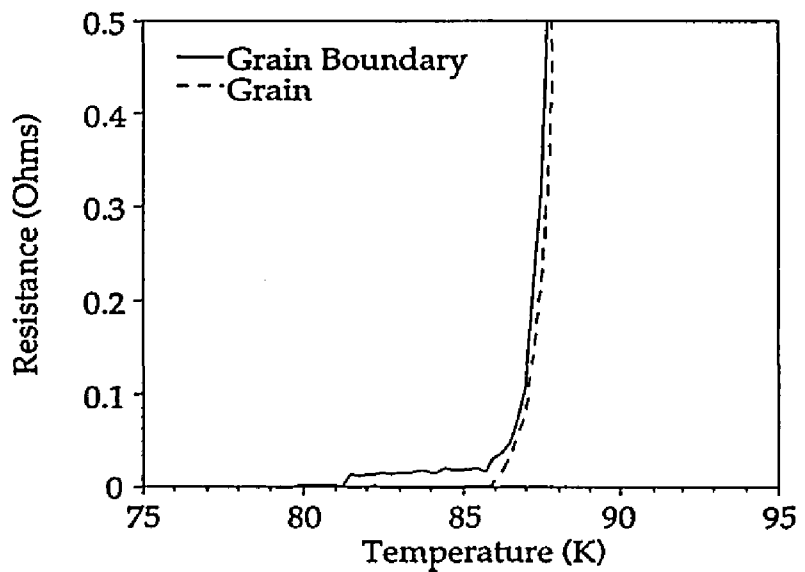


Figure 4.11b. Magnified foot region for resistance vs. temperature.

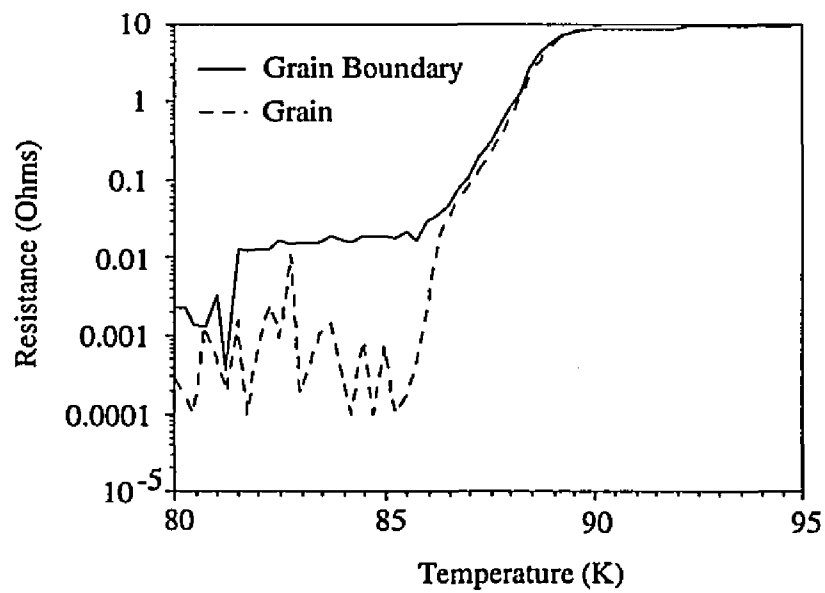
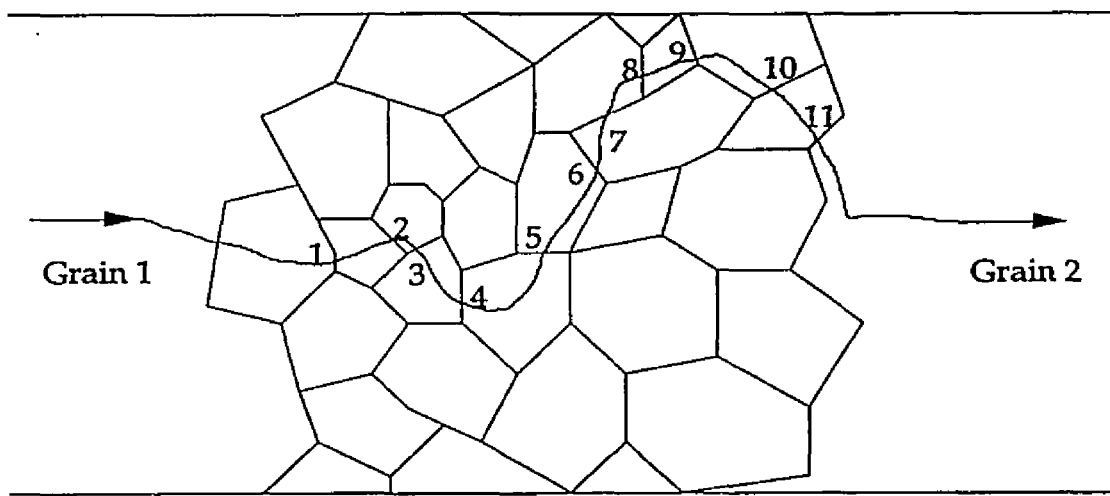


Figure 4.11c. R-T log plot demonstrating the grain boundary resistance is above the noise level of the measuring instruments



for example:

$$T_{c\text{grain}1} = T_{c\text{grain}2} > T_{c3} = T_{c7} = T_{c10} > T_{c11} = T_{c4} = T_{c2} > T_{c1} = T_{c10} > T_{c5} = T_{c8} > T_{c6} > T_{c9}$$

Figure 4.12a. Schematic diagram of a polycrystalline region showing a percolative current path. The path of least resistance crosses grain boundaries with different transition temperatures as indicated. All of the regions along the path must be superconducting before a continuous path across the polycrystalline area is fully superconducting.

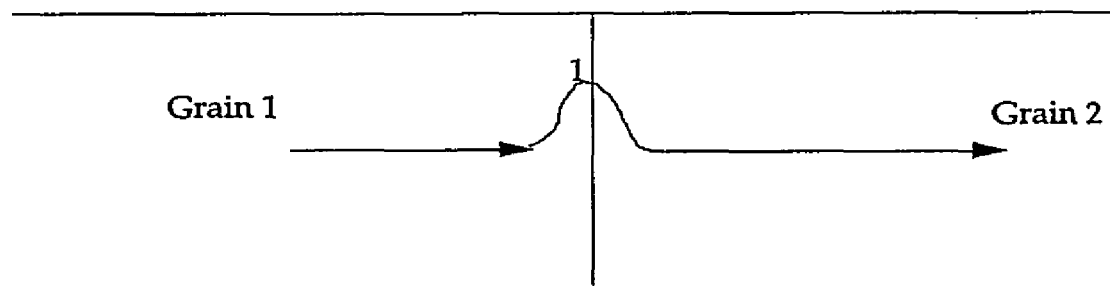


Figure 4.12b. Schematic diagram of a single grain boundary region. The first region that has a detectable transition will provide a continuous superconducting path across the grain boundary.

grain resistance could be from a different quality of epitaxy in the portion that grew 45° rotated relative to the substrate, but this has not been confirmed. The foot-like structure can be changed by varying the applied current, as is expected because this varies the sensitivity of the measurement (as was shown in figure 4.10). The R-T curve of figure 4.11a-b. on a log scale is shown in figure 4.11c. The curve clearly indicates that the foot-like structure is real and lies above the noise of the measuring instruments.

Measuring the resistance of a superconducting sample gives the path of least resistance for a given applied current. If a sample has only one region that is superconducting, then when the measuring current is less than the critical current, the resistance will be zero. The implication is that the R-T curve only measures the resistance of the best connected region. In contrast, the critical current of the sample is the sum of the total number of superconducting paths across the region. An R-T curve can show a difference between a polycrystalline sample and a sample with just one grain boundary. The resistance of a polycrystalline sample will be from a percolation path across the region. For a single grain boundary, however, an extended foot-like structure due to TAPS for low  $I_c$  grain boundaries or from the normal state resistance of the boundary is expected as is seen in figures 4.10 and 4.11 and explained below.

The sputter-induced grain boundary junctions have high transition temperatures. The R-T behavior exhibits characteristics of a single junction. The foot-like structure at the base of the transition is attributed to TAPS across the grain boundary junction, and has an abrupt transition into the superconducting state.

#### IV.2.1.1. TAPS and Thermally Activated Conduction Paths

The R-T curve gives information about the transition temperature and the normal state resistance of the sample. A high quality single crystal grain will have an abrupt transition to the superconducting state. The weak linked high-angle grain boundaries have markedly different behavior. The onset can have a foot like structure, which can be extended using different measuring currents. By varying the measuring current, two separate effects can be studied, thermally activated phase slippage (TAPS) and the grain boundary normal state resistance.

The R-T curve is measured using a constant current. A typical I-V curve is shown in figure 4.14a. The amount of current dictates where along the I-V curve the resistance is being measured. If the current is below  $I_c$  then there is no resistance (unless a small resistance is caused by TAPS, see below), if it is greater than  $I_c$  a resistance is seen. By using varying measuring currents, different regimes of the I-V curve can be studied. The two predominant effects that can alter the R-T characteristics of a single grain boundary will now be described to understand the normal state resistance behavior of the grain boundaries.

TAPS is due to thermally activated phase changes across the grain boundary that cause a small finite resistance. There is a barrier height associated with the onset of TAPS. The normalized barrier height for TAPS is the ratio of twice the maximum Josephson coupling energy,  $E_J$ , to the thermal energy,  $E_{Th}=k_B T$ , (eq. 4.1)(Gross 1992)

$$\gamma(T) = \frac{2E_J}{k_B T} = \frac{\hbar I_c(T)}{2\pi e k_B T} = \frac{\Phi_0 I_c(T)}{\pi k_B T} \quad (4.1)$$

The barrier height is inversely proportional to the temperature. As the temperature decreases both the thermal energy decreases and the critical current of the junction increases. It is important to realize the barrier height is proportional to the critical current, not the critical current density. Therefore for samples with a high-angle grain boundary, the critical currents are low and TAPS would be expected even with a relatively wide junction. The high critical currents of grains and physically large junctions are the reason no foot-structure is seen in their respective transition curves. TAPS is manifested as a rounding of the I-V characteristics with a small slope at relatively high temperatures, which is seen as a finite resistance foot in the R-T curve. Specific numbers show that a junction with a critical current of 1  $\mu\text{A}$  (used as the measuring current in the measurement of fig. 4.11,  $E_J=3.3\times 10^{-22}\text{J}$ ) could exhibit TAPS down to 40 K. The Josephson coupling energy for the sample in figure 4.10 increases above the thermal energy at approximately 80.25 K and therefore the junction does not exhibit TAPS below that temperature. An example of this behavior will be shown in the bi-epitaxial samples in chapter VI.

The second effect that can be studied using the R-T curve is the normal state resistance. Based on work on bi-epitaxial samples described later, the normal state resistance of the grain boundary can be modeled as a sum of the temperature independent resistance and a set of parallel thermally activated conductance channels (Liu *et al.* 1995). Following Liu *et al.*,(Liu *et al.* 1995):

$$G_{gb} = G_0 + \sum_i G_i \quad (4.2)$$

The temperature independent conductance is equal to  $1/R_0$ , and the temperature dependent channels can be expressed as (eq. 4.3):

$$G_i = g \exp\left(\frac{-E_i}{k_B T}\right) \quad (4.3)$$

By assuming a simple distribution of the activation energies  $N(E)=N_0$  from  $E_{\min}$  to  $E_{\max}$  (also assuming  $E_{\max} \gg k_B T$ ) and integrating over this energy range eq. 4.4 is obtained. This represents the contribution to the conductance from the thermally activated channels.

$$gk_B T \exp\left(\frac{-E_{\min}}{k_B T}\right) \quad (4.4)$$

Putting this expression back into eq. 4.2 and solving for  $R_{gb}$  results in eq. 4.5:

$$R_{gb} = \frac{R_0}{1 + \beta T \exp\left(\frac{-E_{\min}}{k_B T}\right)} \quad (4.5)$$

where  $\beta=N_0(g/G_0)k_B$  is the number of conduction paths that open per increase in temperature. This resistance is manifested in the normal state regime of the I-V characteristic.

The difference between TAPS and the thermally activated conduction paths can be detected in the R-T curves. If a small enough measuring current is used, and TAPS is present it will be detected as a small foot-like structure as is seen in figure 4.11. This resistance is from measuring below the "critical current" where there is still a small finite resistance due to TAPS. For a critical current on

the order of 1  $\mu\text{A}$  this is expected to show TAPS down to the temperatures observed ( $E_{\text{Th}} > E_J$ ), and is consistent with the measurement. If a high enough current is used, the true normal state resistance of the boundary is measured. Figure 4.10 shows a larger hump that extends well below where TAPS is expected. The shape of this curve has an excellent fit with eq. 4.5 indicating that the critical current of the junctions is exceeded and the parallel thermally activated conduction paths are now being measured. It will later be shown that the number of conduction paths appears to be inversely proportional to the critical current.

#### IV.2.2. Current-Voltage Characteristics

The two important aspects of the I-V curve are the shape of the normal state response and the magnitude of the critical current. The shape indicates whether the weak link region is flux-flow type, modeled by a resistively-shunted-junction (RSJ) or a modified RSJ with TAPS. Therefore, the curvature of the I-V characteristics indicates the type of coupling across the junction. The magnitude of the critical current is important as the total amount of current across the junction. Essentially it is the sum of all the varying critical currents (eq. 4.6)

$$I_{c, \text{tot}} = \int_0^w I_c(x) dx \quad (4.6)$$

If there is a variation of the magnitude of the critical current along the grain boundary it will all be integrated into the total critical current. Spatially varying

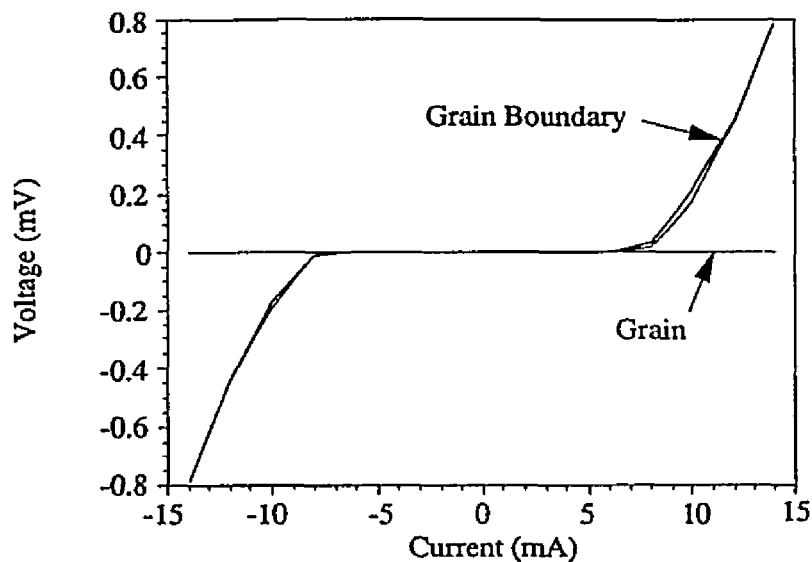


Figure 4.13a. I-V curve for a polycrystalline grain boundary region at  $T=35\text{ K}$ .

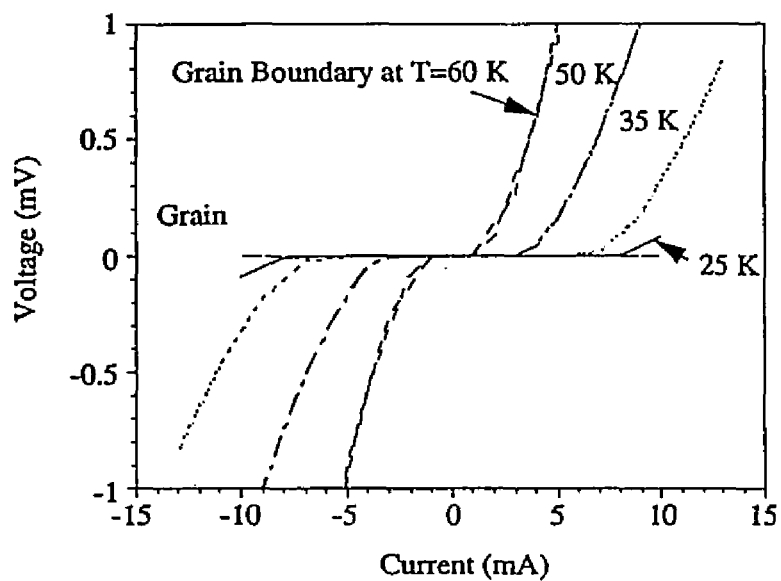


Figure 4.13b. I-V curves for a polycrystalline grain boundary region at different temperatures.

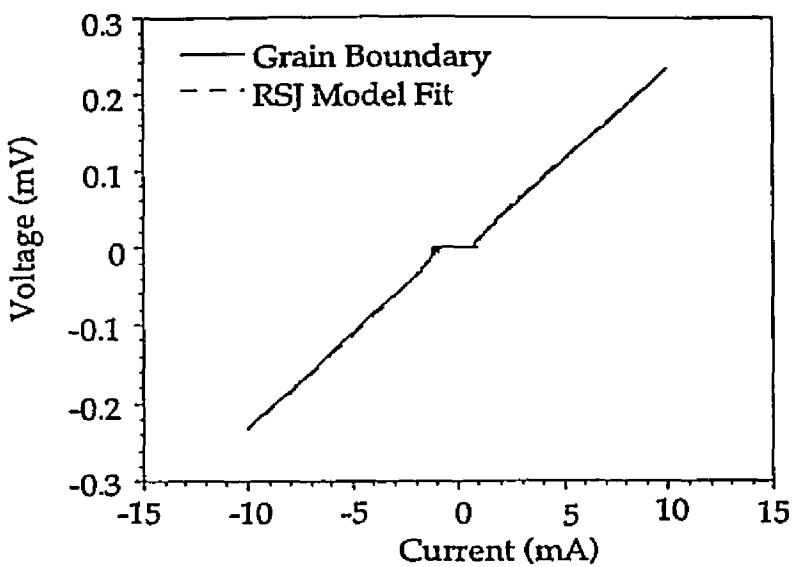


Figure 4.14a. I-V characteristic for sputter-induced grain boundary junction with RSJ model fit ( $\beta_c=0$ ).

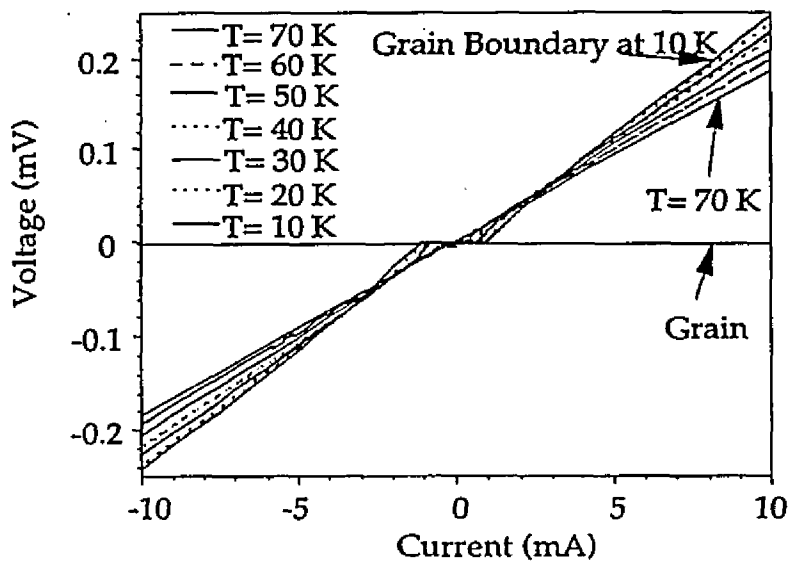


Figure 4.14b. I-V characteristics for temperatures from 10 K to 70 K for a sputter induced grain boundary junction.

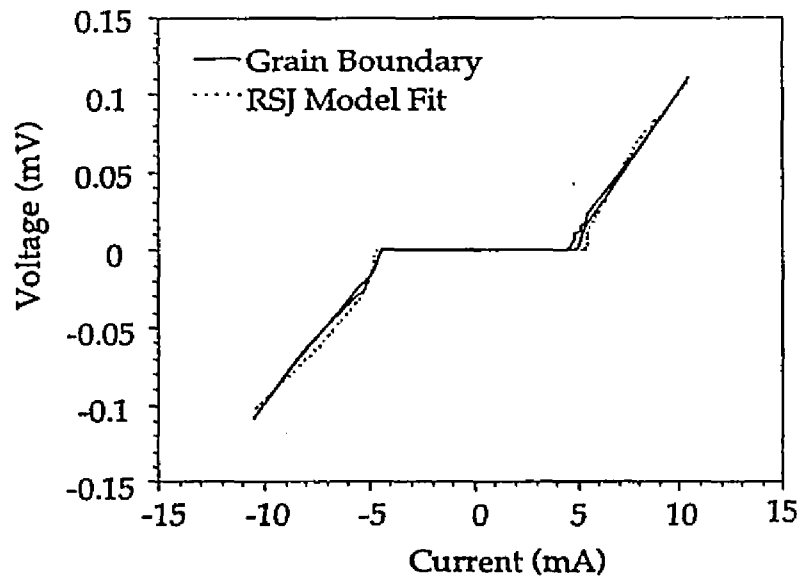


Figure 4.15. I-V characteristics and RSJ fit for sputter-induced grain boundary junction at 4.2 K.

changes in the critical current are not discernible using the I-V measurement, only the absolute magnitude of current crossing the region.

The current-voltage characteristics of these grain boundaries exhibited weak-link behavior. The samples with polycrystalline regions had rounded I-V curves even at low temperatures, indicative of a flux-flow type mechanism (see figures 4.13a-b). The I-V plot maintains a positive curvature even at relatively high current biases. The flux flow behavior at low temperature is expected for a path of strongly coupled junctions, therefore implying that there could be a "short" across this region of lower angle grain boundaries supporting a high critical current.

The I-V characteristics for two different sputter-induced junctions are in figures 4.14 and 4.15. Both of these junctions have RSJ-like behavior, which is modeled in the figures. By solving equation 2.8 for the case of the Stewart-McCumber parameter(Stewart 1968; McCumber 1968),  $B_C=0$ , equation 4.7 is obtained:

$$\begin{aligned} V &= 0 && \text{for } I < I_c \\ V &= I_c R_n \sqrt{\left(\frac{I}{I_c}\right)^2 - 1} && \text{for } I > I_c \end{aligned} \quad (4.7)$$

A good fit is made using this solution where the capacitance of the junction is set to zero. Therefore the junction is modeled by a Josephson element in parallel with a resistance.

The highest critical current density values obtained for these junctions was  $5 \times 10^4 \text{ A/cm}^2$  at 4.2 K, and  $1.6 \times 10^3 \text{ A/cm}^2$  at 77 K, with an  $I_c R_n$  product of  $125 \mu\text{V}$  at 4.2 K. This is the largest critical current density published for a

[001] 45° tilt grain boundary junction, including asymmetric bicrystal junctions on YSZ (Ivanov *et al.* 1991a), symmetric bicrystal (values published for 35.5°, which in principle should be larger)(Dimos *et al.* 1988) and bi-epitaxial junctions(Char *et al.* 1991a; Char *et al.* 1991b; Early *et al.* 1994). One potential reason for the high values is that the sputter-induced grain boundaries are "naturally" formed grain boundaries. The thin film is grown on MgO on both sides of the boundary (unlike a bi-epitaxial junction), with no misalignment of the substrate (as in a bicrystal) allowing lower energy formations of the grain boundary. This will be discussed in more detail with respect to the microstructure later. The relatively low  $I_c R_n$  product is due to relatively low  $R_n$  values as opposed to low  $I_c$  values.

The I-V characteristics tend to show some hysteresis at the lower temperatures, which is typical of many junctions. At higher temperatures the curves show increasing resistance with increasing temperature (a positive curvature in the I-V behavior) from flux flow along the boundary. The lower critical current at higher temperatures cannot prevent Josephson flux motion along the grain boundary. Also a small finite resistance at small currents is present due to TAPS.

Figure 4.16a-f. are the I-V characteristics of a junction for six different temperatures to show the different shapes of curvature and magnitude at the different temperatures. These are all condensed onto one plot in figure 4.17. The change in the critical current is an order of magnitude over the 80 K temperature range. The critical current as a function of temperature can be modeled with eq.4.3:

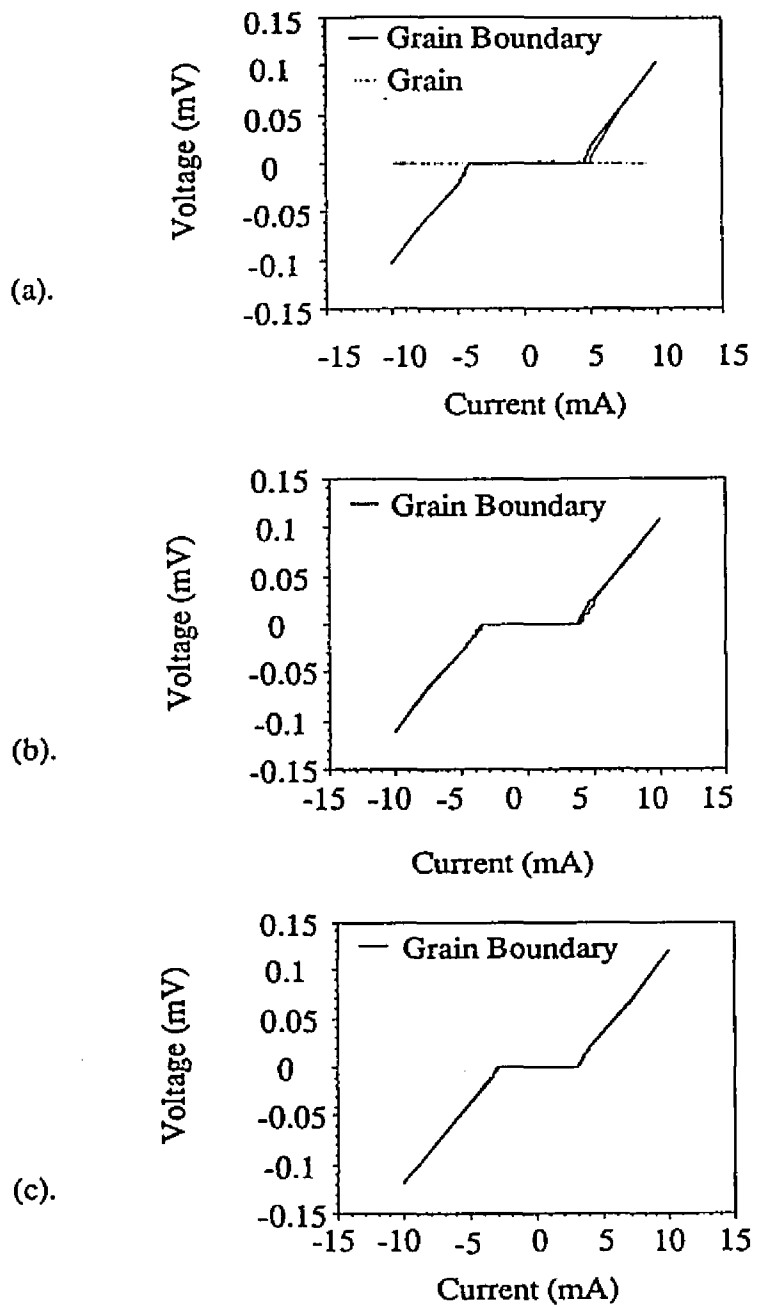
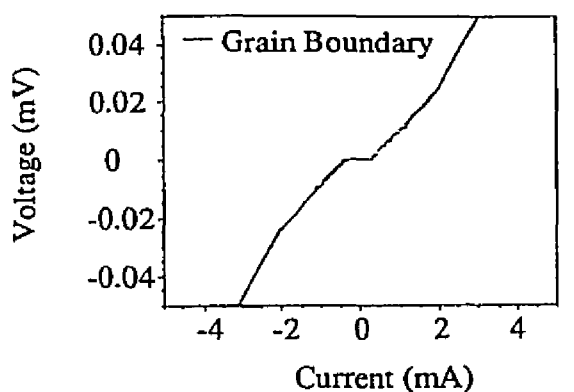
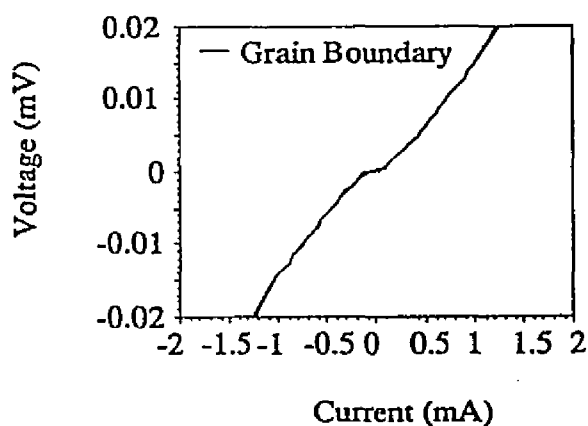


Figure 4.16a-c. I-V characteristics for (a).  $T=10\text{ K}$ , (b).  $T=20\text{ K}$ , and (c).  $T=30\text{ K}$ .

(d).



(e).



(f).

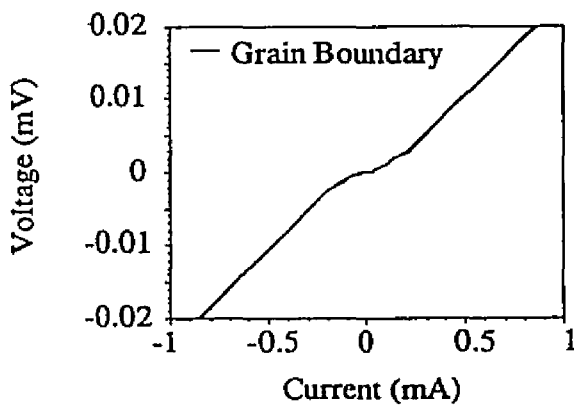


Figure 4.16d-f. I-V characteristics for a grain boundary at (d).  $T=70\text{ K}$ , (e).  $T=77\text{ K}$ , and (f).  $T=80\text{ K}$ .

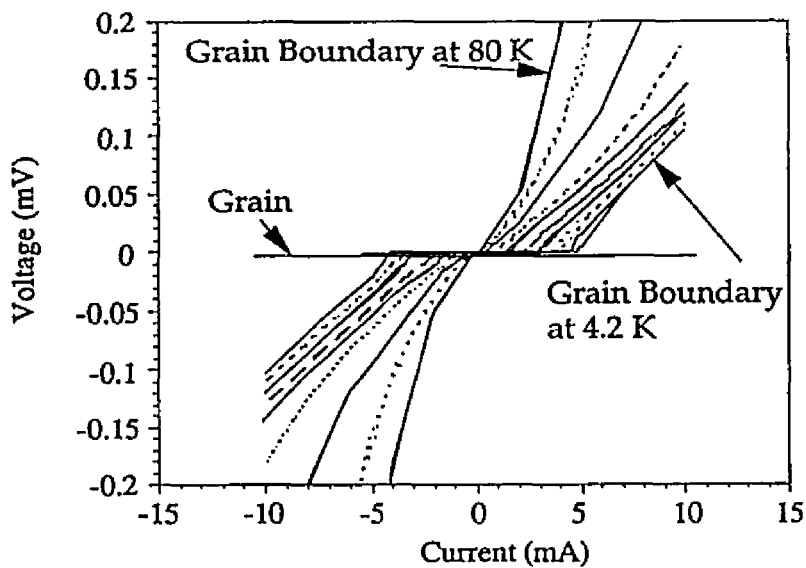


Figure 4.17. I-V characteristics at 4.2 K, 20 K, 30 K, 40 K, 50 K, 60 K, 70 K, 77 K and 80 K showing transition from RSJ type behavior to flux-flow behavior.

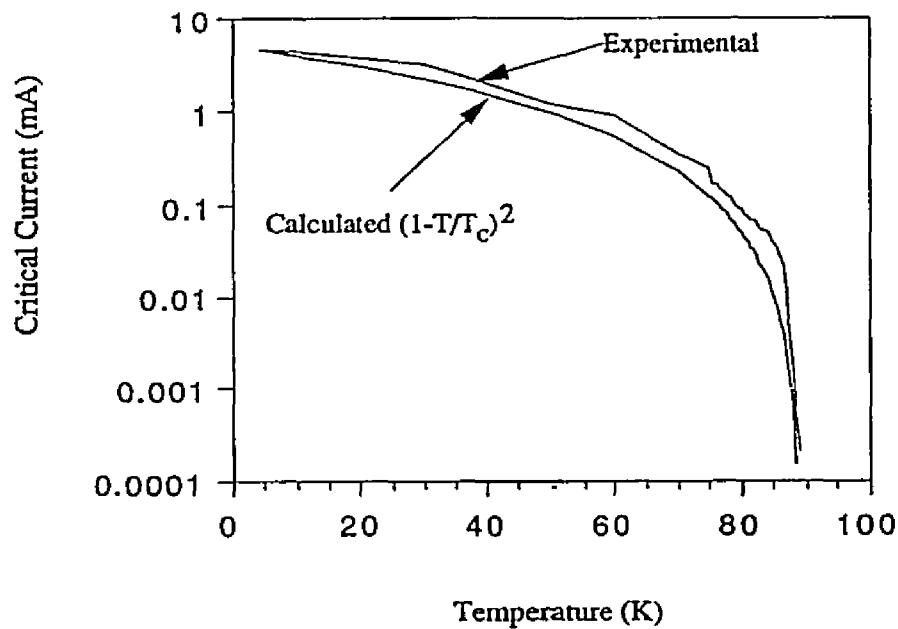


Figure 4.18. Critical current as a function of temperature.  
The calculated curve follows  $I = I_c(1 - T/T_c)^2$ .

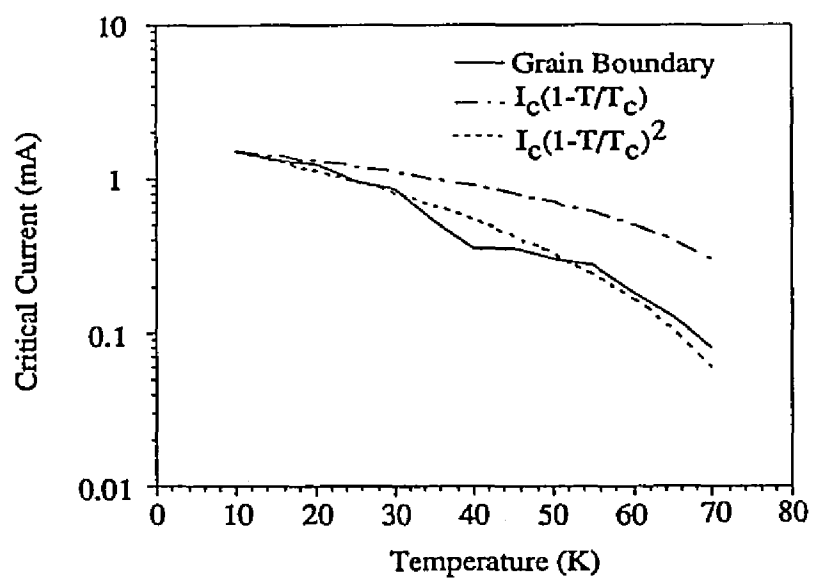


Fig. 4.18b. Critical current as a function of temperature for a second sputter-induced epitaxy grain boundary.

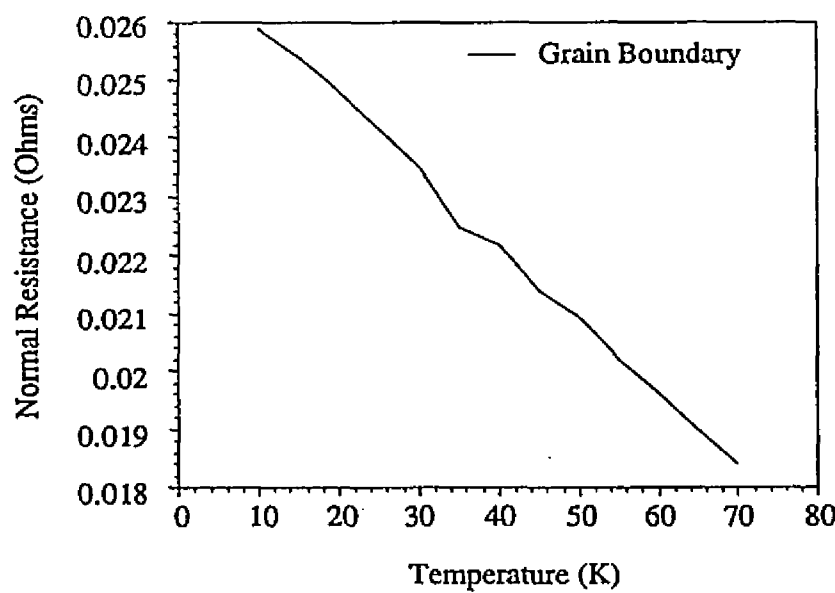


Figure 4.19. Grain boundary normal state resistance as a function of temperature.

$$I_c = I_{c0} \left(1 - \frac{T}{T_c}\right)^2 \quad (4.8)$$

This behavior is predicted for a superconductor-normal-superconductor type junction. The relationship is different than the  $(1-T/T_c)$  behavior expected for a superconductor-insulator-superconductor (Ambegaokar *et al.* 1963). Therefore the grain boundary does have similar characteristics to a normal metal region between two superconductors.

The normal state resistance is determined from the I-V characteristics at currents greater than  $I_c$ . The temperature dependence of the normal state resistance varies depending on the sample quality. There is an inverse relationship between the junction critical current and the normal state resistance. For lower critical currents it appears that the normal state resistance is decreasing with increasing temperature (see figure 4.19). The resistance due to the grain boundary exhibits semiconducting type behavior. This is consistent with a picture where parallel conduction paths along the grain boundary of superconducting elements with thermally activated transport elements. The thermally activated elements appear to be unique to the grain boundaries because this effect is not seen in bulk samples, which exhibit strictly metallic type behavior. This is discussed in more detail in chapter VII and appendix I.

#### **IV.2.3. Magnetic Field Behavior**

For the sample with the highest critical current value, the variation of the voltage as a function of applied magnetic field (the sample is d.c. current biased) is shown in figures 4.20 and 4.21. Measurements were made with an applied magnetic field normal to the substrate surface. The voltage is proportional to

the critical current of the boundary. There is clearly a strong dependence of the critical current on the applied field perpendicular to the thin film surface indicating a d.c. Josephson-like effect due to the phase interference of the wavefunctions from either grain across the junction. The response, however, is not a clean Fraunhofer pattern as is expected for a junction with a perfectly uniform current distribution (see chapter II). There is a maximum peak close to zero, and then changes in critical current as a function of small incremental steps in the magnetic field on the order of 0.02 G. The Josephson current never goes to zero, unlike a perfect junction, which has total cancellation of the Josephson current at integral flux values.

Typically wide junctions ( $w > 4\lambda_j$ ) do not exhibit a perfect Fraunhofer interference pattern due to the current distribution (see chapter II). The current is mostly carried within a penetration depth of the edge of the junction and self-field effects becomes important. This is not the effect observed in these measurements. Due to the inhomogeneity of the current transport along the junction length, the current is not maintained in the edges of the junction. The current traverses the boundary even in the center of the junction. This is confirmed by studies of the critical current as a function of the junction width. These experiments showed that the critical current does not saturate at a given width as would be expected if the supercurrent was only at the edges of the junction (Rosenthal *et al.* 1991; Early *et al.* 1993; Mayer *et al.* 1993). In the high- $T_c$  samples there are parallel conduction paths across the boundary separated by normal regions, which prevent large scale self-field effects from being significant. In this case the junction can be treated as a narrow junction.

These junctions do not exhibit a perfect interference pattern because of inhomogeneous flow along the boundary, however there is some indication of periodicity in the measurement. If the phase difference ( $\phi_1 - \phi_2$ ) is constant along the grain boundary, the  $I_c(H)$  measurement is the absolute value of the Fourier transform of the critical current density along the grain boundary (as in eq. 2.4):

$$J_c(H) = \left| \int_{-\infty}^{+\infty} J_c(x) e^{i\beta x} dx \right|$$

where,  $\beta = (2\lambda + d) \frac{2\pi H}{\phi_0}$  (2.4)

Since the modulus is measured, the phase information is lost and it is not possible to determine the actual distribution of the current along the grain boundary. Extensive simulations of various critical current distributions along the boundary were performed to simulate the low applied magnetic field response. The current distributions modeled varied from uniform distribution along the boundary length to a filamentary model of 1 nm sized superconducting regions randomly distributed along the boundary length. None of these models even remotely agreed with the measured data. The reason for the lack of concurrence with the simulations is due to a change in the phase difference along the boundary.

The phase difference is assumed to be constant in the traditional analysis. The manifestation of this is that a given current profile will not respond in a uniform fashion to an applied magnetic field. Certain regions will decrease in critical current while others can increase depending on the flux penetration at the boundary. Note that there is no direct analogy in optics to this difference in

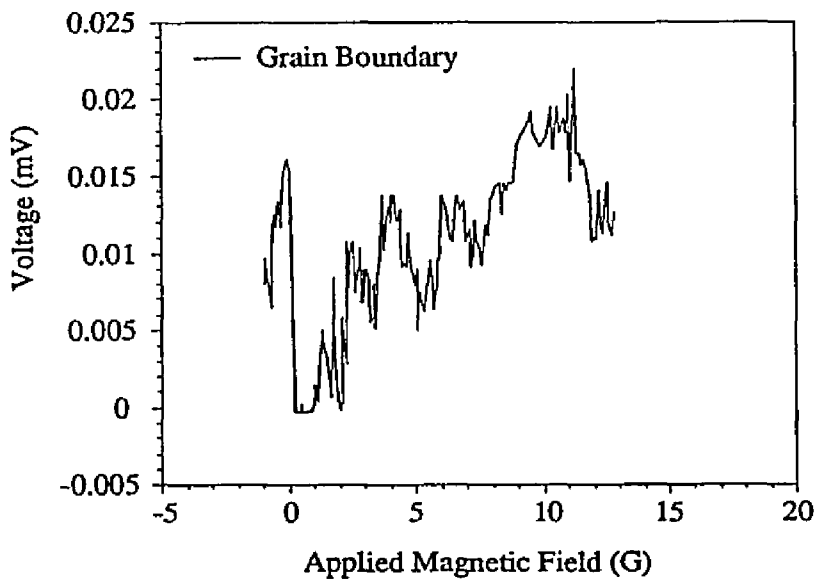


Figure 4.20. Low magnetic field behavior of a sputter-induced grain boundary junction.

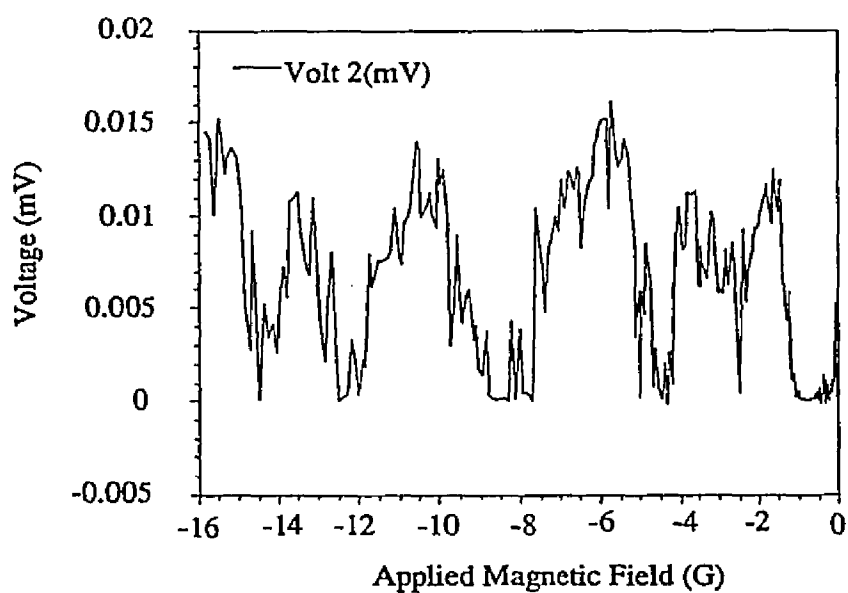


Figure 4.21. Low magnetic field behavior for a sputter induced grain boundary junction.

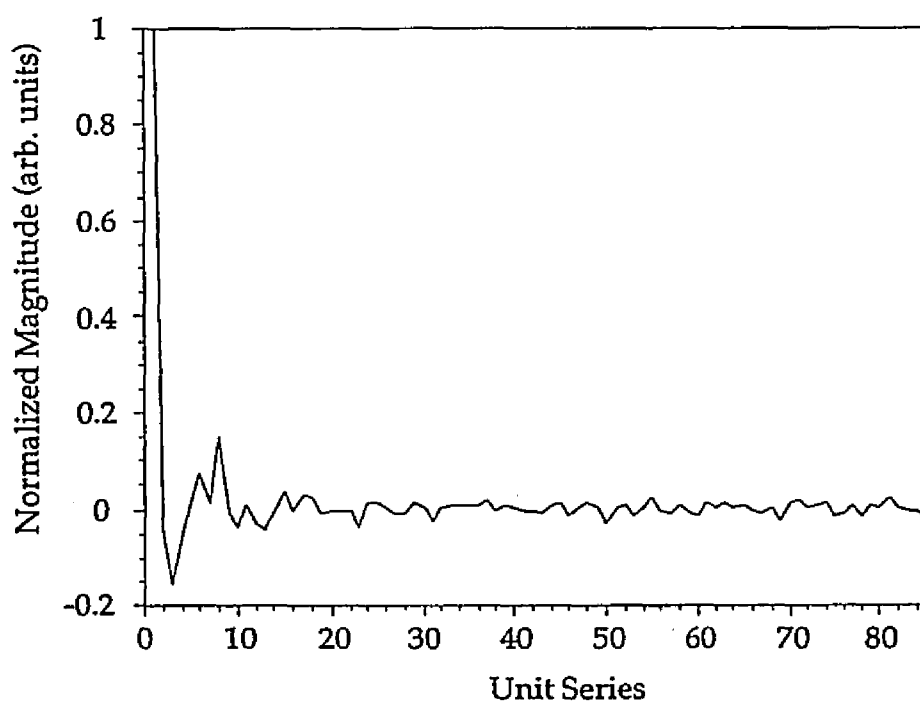


Figure 4.22. Patterson function of magnetic field data from figure 4.20.

phase shift along the boundary because self-inductance can not be modeled. This is discussed in more detail in chapter VII and appendix I.

A Patterson function of the data determines any frequencies present. The one predominant peak is a 2.2 G periodicity, which will be compared to the bi-epitaxial junctions later. The periodicity does suggest a certain degree of homogeneity along regions of the boundary.

Three studies (Froehlich *et al.* 1995; Sarnelli *et al.* 1993c; Daumling *et al.* 1992) have looked at high field measurements of different types of grain boundary junctions. There is a residual critical current across the grain boundary up to 12T (the highest field measured). The authors claim that this indicates the size scale of the current distributions is on the level of down to 1 nm or less (Froehlich *et al.* 1995). The problem is that this analysis assumed a constant phase difference along the junction. This is incorrect and explains the lack of a good match to the data at low fields. The fact that the critical current never fully disappears can be explained by the asymmetric parallel junction model described in chapter VII and appendix I.

The model of asymmetric parallel junctions is extremely difficult to simulate due to the lack of data of the current distribution along the boundary. Analogies to an interferometer can be made, which has been simulated under limited conditions. One calculation of ten Josephson junctions in parallel showed that the mutual and self inductance of neighboring junctions plays a key role in the response to a magnetic field (Miller *et al.* 1991). Two variables were analyzed, the self inductance of a loop formed by two Josephson junctions and the non-uniformity of the critical current. By increasing the self-inductance, the modulations peak to valley ratio decreased and did not have an obvious

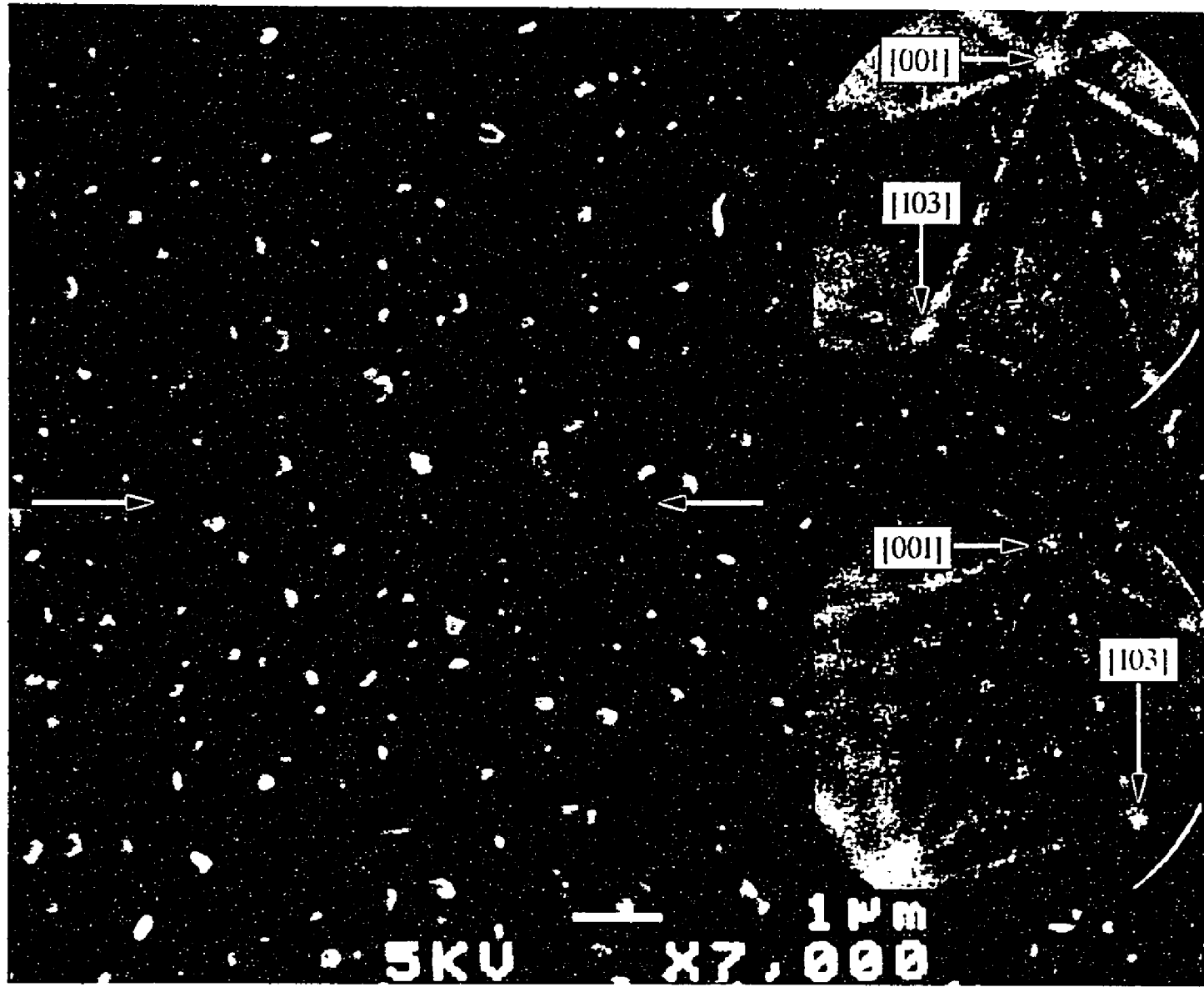
periodicity. The critical current also never went to zero as it did when the self-inductance increased. A variation in the critical current further modified the behavior. Clearly both the self-inductance and the change in critical currents are strong effects, which contribute to the measurement. The modulations in the magnetic field data suggest a non-uniform current distribution along the boundary. In order to gain a greater understanding of the weak-link behavior microstructural analysis was performed using SEM and TEM. The modulation of the critical current must be related to the microstructure (as discussed in the next section).

#### **IV. 3. Microstructure**

##### **IV.3.1. Scanning electron microscopy**

The sputter induced epitaxy samples were always initially examined optically. The higher quality films were highly reflective, but scanning electron microscopy (SEM) was necessary for better analysis. The SEM in combination with the EBSP described earlier was used as the first test in determining whether the film grew with a modified epitaxy over the presputtered region, and to analyze the general microstructure. Figure 4.23 is a secondary electron image of the grain boundary in a sputter-induced sample. The insets are the EBSP patterns for each grain. The [001] zone axis lies, as expected, normal to the film surface ( $20^\circ$  above the pattern center). Even the polycrystalline samples were predominantly oriented with the [001] zone axis perpendicular to the sample surface. In figure 4.23 the [103] axis clearly rotates by  $45^\circ$  about the [001] axis from the pre-sputtered region to the unsputtered region. This is direct evidence that, within the resolution of the EBSP technique, a  $45^\circ$  grain boundary

Figure 4.23. A SEM image of a sputter-induced epitaxy grain boundary junction. The insets are the corresponding backscattered electron Kikuchi patterns for the grains indicating a 45° rotation about the [001] axis.



forms in the film at the interface of the two grain regions. The result is later confirmed with TEM to show that there are not any other grains in the region. The film was found to be rotated by 45° across the entire pre-sputtered region of the substrate. The advantage of EBSP is that spatially localized diffraction can be obtained from the thin film. In contrast, four-circle x-ray diffraction can only get spatially-averaged information from the entire film. For grain boundary junctions, it is important to insure that only one grain boundary exists across the microbridge, so EBSP was the relevant technique for this purpose.

The number, size and concentration of precipitates across the thin film would vary significantly depending on the specific deposition conditions used. For copper rich growths, copper-oxide precipitates (determined by EDS analysis) would be seen as boulders across the surface. Barium rich samples would also form precipitates. Variation in the yttrium concentration would typically change the morphology of the film, often making the surface rougher, with voids, if there was an increased concentration of yttrium. The growth temperature also played an important role with the lower temperatures resulting in a surface with a higher concentration of precipitates. More detailed studies of the effect of stoichiometry and growth temperature on the surface morphology are in Buchholz *et al.* (Buchholz *et al.* 1994).

The morphology of the film did not vary from the pre-sputtered region to the unsputtered region. The grain boundary was typically not distinguishable unless EBSP diffraction was used to determine where the rotation occurred (this was an experimental difficulty in isolating junctions for measurement). This indicates that despite the modified epitaxy and the pre-sputter treatment, there are no significant differences in the thin film growth that can be seen on this

scale. The effect of the sputtering damage on the substrate, does not appear to propagate through the film. The ability to form a grain boundary junction without a difference in morphology across the boundary is a distinct advantage of this technique. Other junctions, such as bi-epitaxial junctions, have the problem of different morphologies on the films on either side of the junction. This becomes an important issue for optimizing the thin film growth as well as for multilayer situations.

In general, the pre-sputtered region would have <1% unrotated grains. Some of the initial samples formed with a metal mask had polycrystalline region adjacent at the interface of the sputter-induced region and the non-sputtered area. A variety of EBSP patterns could be observed in these areas, with most being [001] epitaxial, but having different in-plane orientations. These films were rotated either due to the sputtering of the mask onto the substrate prior to growth, or a reduced dose of ions from only partial shielding of the mask. Thin films formed using photoresist masks had higher quality grain boundary regions. The two grains of the film would meet at the grain boundary with virtually no rotated or unrotated grains. The grain boundary would appear straight to within the 0.5  $\mu\text{m}$  resolution of the EBSP method. Generally the grain boundaries did not show any preferential formation of precipitates, but they would sometimes have porosity. Again, the specific appearance of the grain boundary region was dependent on the growth conditions.

Figure 4.23 is a SEM image of a grain boundary formed with a photoresist mask. The boundary does show localized porosity (dark voids between the arrows). There usually was not any porosity along the boundary, however this helps identify the grain boundary in the image. The white

precipitates are copper oxide formed from excess copper during deposition. The variation in the surface structure suggests that perhaps the largest obstacle to obtaining uniform critical current densities and junction behavior, is consistent reproducible thin film deposition.

Grain boundaries were formed in numerous configurations for different experimental requirements, and to prove the abilities of the technique. The finest resolution was 5  $\mu\text{m}$  spaced parallel grain boundaries (see Chapter V). This indicates that the technique is potentially limited only by the mask resolution, and the grain growth across the grain boundary region. Current photolithographic techniques can form submicron features, and could be used for very fine patterning. Both circular and square grain boundaries were formed as small as a 20  $\mu\text{m}$  diameter for the circular boundaries. There were no observable structural effects from the various geometries used.

#### IV.3.2. Transmission Electron Microscopy

Electron transparent samples were made to analyze the grain boundary structure. The samples with the polycrystalline regions had multiple grains with numerous orientations at the grain boundary interface. Most of them were [001] oriented relative to the substrate, so the diffraction patterns showed distinct spots along the (100) and the (110) rings (see figure 4.25). The highest quality samples appeared to only have one grain boundary along the interface of the two regions (see figures 4.24a-b.). The selected area diffraction patterns showed a distinct 45° rotation about the [001] axis, corroborating the result of the EBSP analysis.

Figure 4.24a. Bright field TEM image of a sputter-induced grain boundary junction. The grain boundary (indicated by the arrows) meanders significantly.



Figure 4.24b. Corresponding dark field TEM image to figure 4.24a. The image highlights how much boundary meanders (the arrows are the same locations in the boundary as in figure 4.24a).



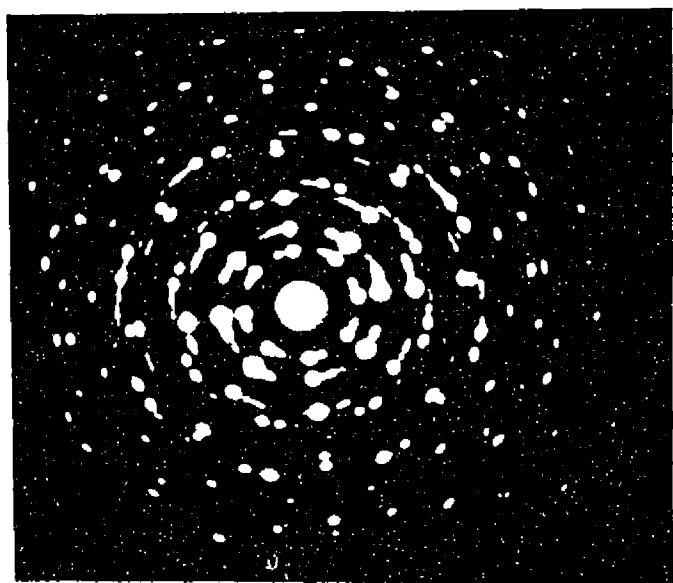


Figure 4.25. Diffraction pattern of a polycrystalline "interface" region observed in samples made with a poorly contacting metal mask.

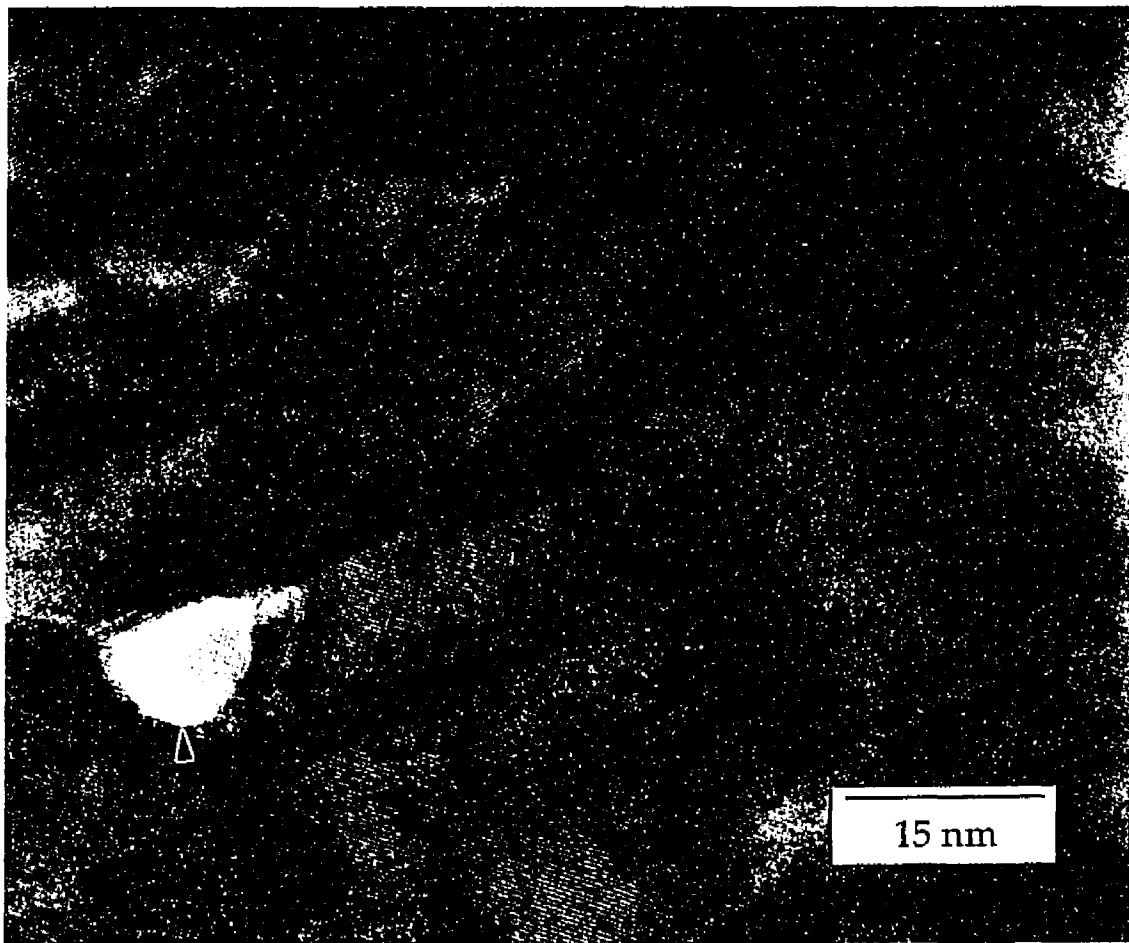


Figure 4.26. TEM image of a sputter-induced grain boundary with a  $\text{Y}_2\text{O}_3$  particle at the boundary. The boundary is asymmetrically faceted.

The most obvious feature of the boundary is that it meanders, and does not follow a straight line across the substrate (see figures 4.24a-b, 4.26). The grain boundary deviates from a hypothetical straight line defined, by the photolithography, by hundreds of nanometers. This behavior has also been observed in bicrystal samples, where the grain boundary does not follow the path of the bicrystal substrate (Miller *et al.* 1995; Traeholt *et al.* 1994b). Meandering is also seen in bi-epitaxial grain boundaries (see chapter VI.) and in polycrystalline thin film samples (McKernan *et al.* 1992). For the sputter-induced grain boundaries, it is not possible to tell from these images where exactly the pre-sputtered region of the substrate lies. Since a photoresist mask is not atomically abrupt, the sputtered region and the unsputtered regions will not be delineated by a straight line. Knowing that the grains grow significantly faster in the a-b direction than in the c-direction, it can be assumed that there will be some interpenetration of grains across the pre-sputtered/non-sputtered separation. Therefore the meandering results from a combination of both the mask resolution and the grain growth. The two effects combined will enhance the magnitude of meandering relative to a bicrystal substrate, which provides a straight template for the boundary. This is consistent with the results from other references where the meandering is on the order of tens of nanometers deviation from the bicrystal grain boundary(Miller *et al.* 1995; Traeholt *et al.* 1994b) . Similar effects are evidenced in the bi-epitaxial grain boundaries, which also uses a photoresist mask to define the substrate (see Chapter VI). Slower growth rates of the film should minimize the effect by reducing the amount of interpenetration of the grains.

Figure 4.27a. An image of a 100 nm long asymmetric facet at the grain boundary. The (100) planes of the left grains are parallel to the (110) planes of the adjacent grain.

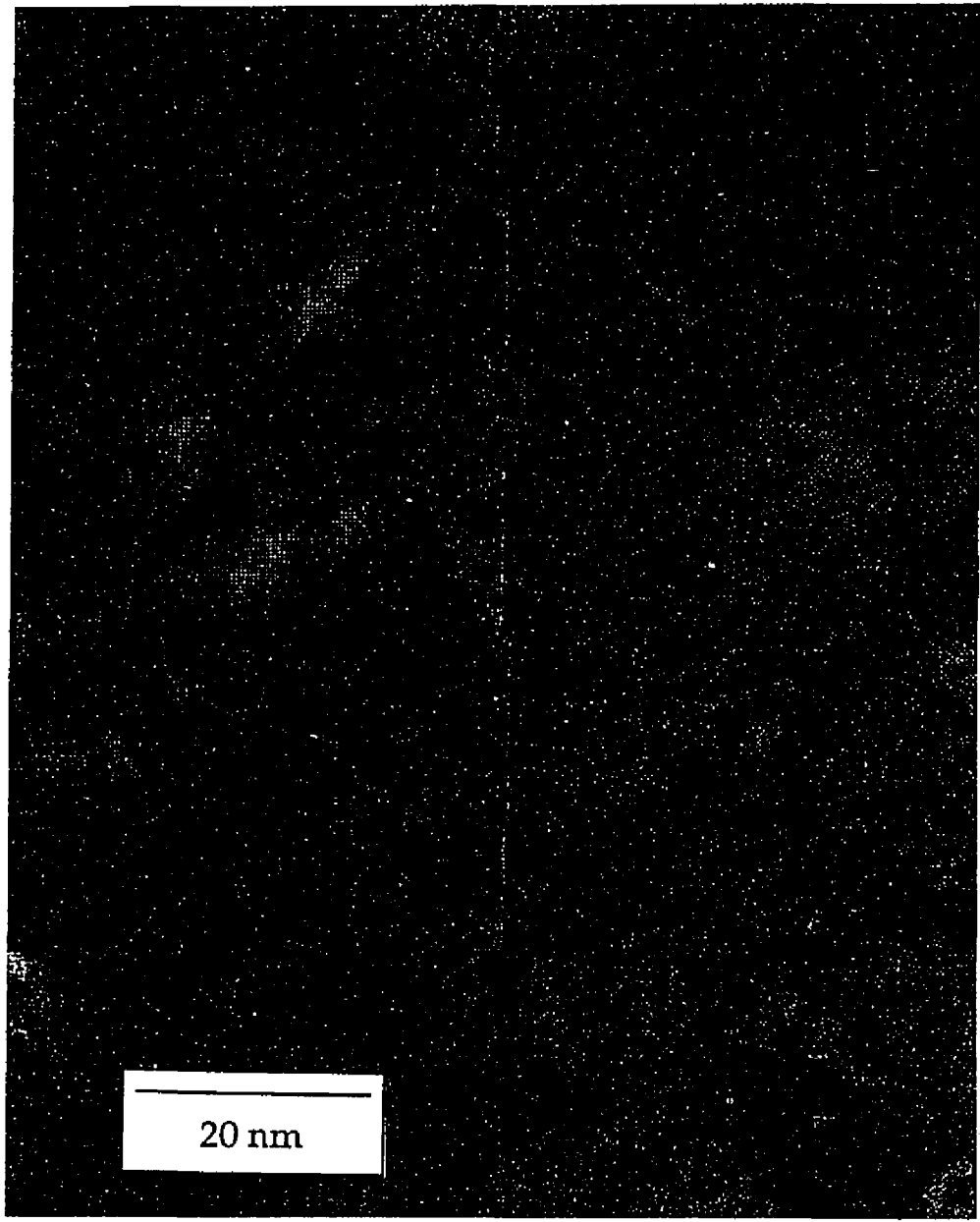
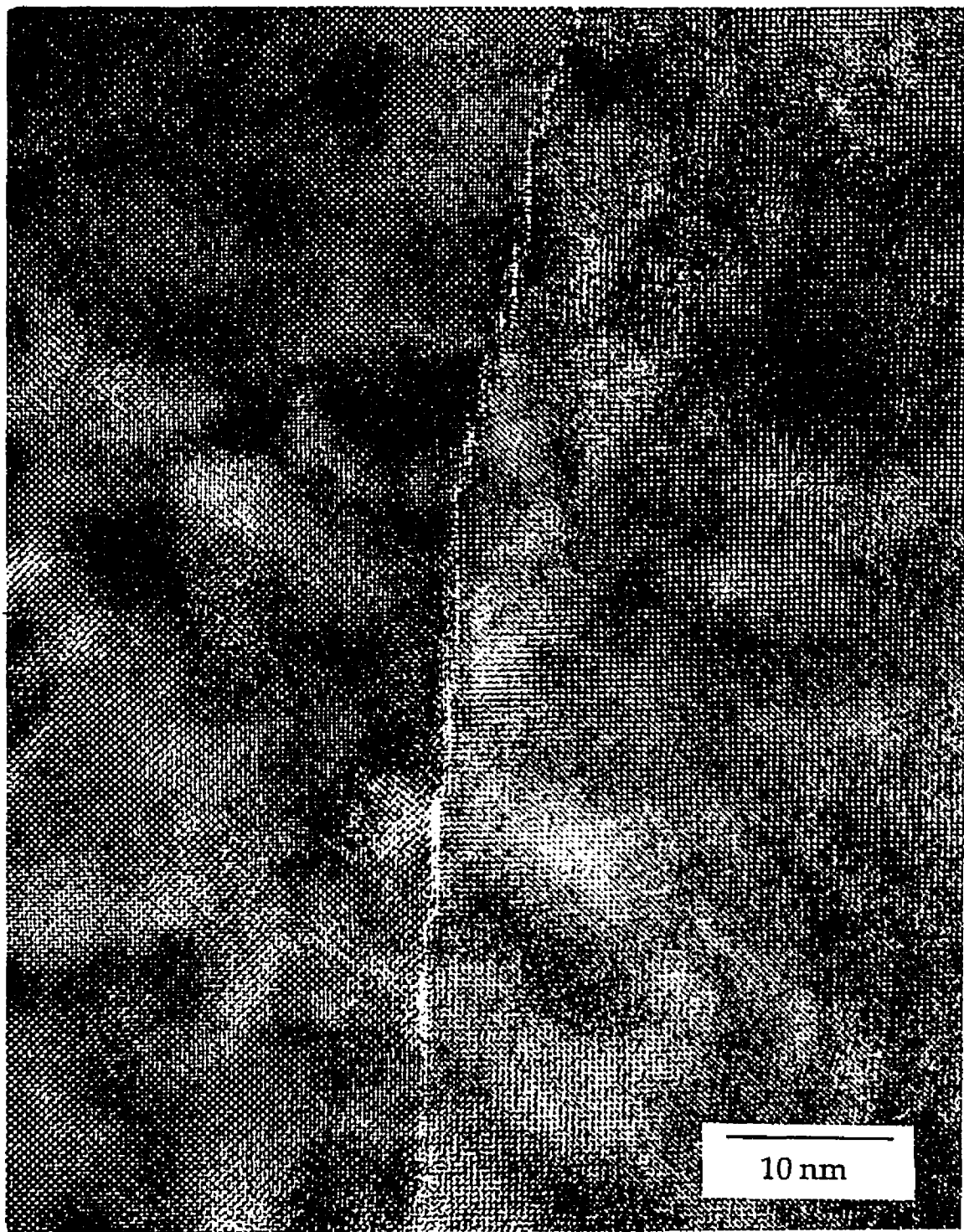


Figure 4.27b. Asymmetric facets along a length of a sputter-induced epitaxy grain boundary.



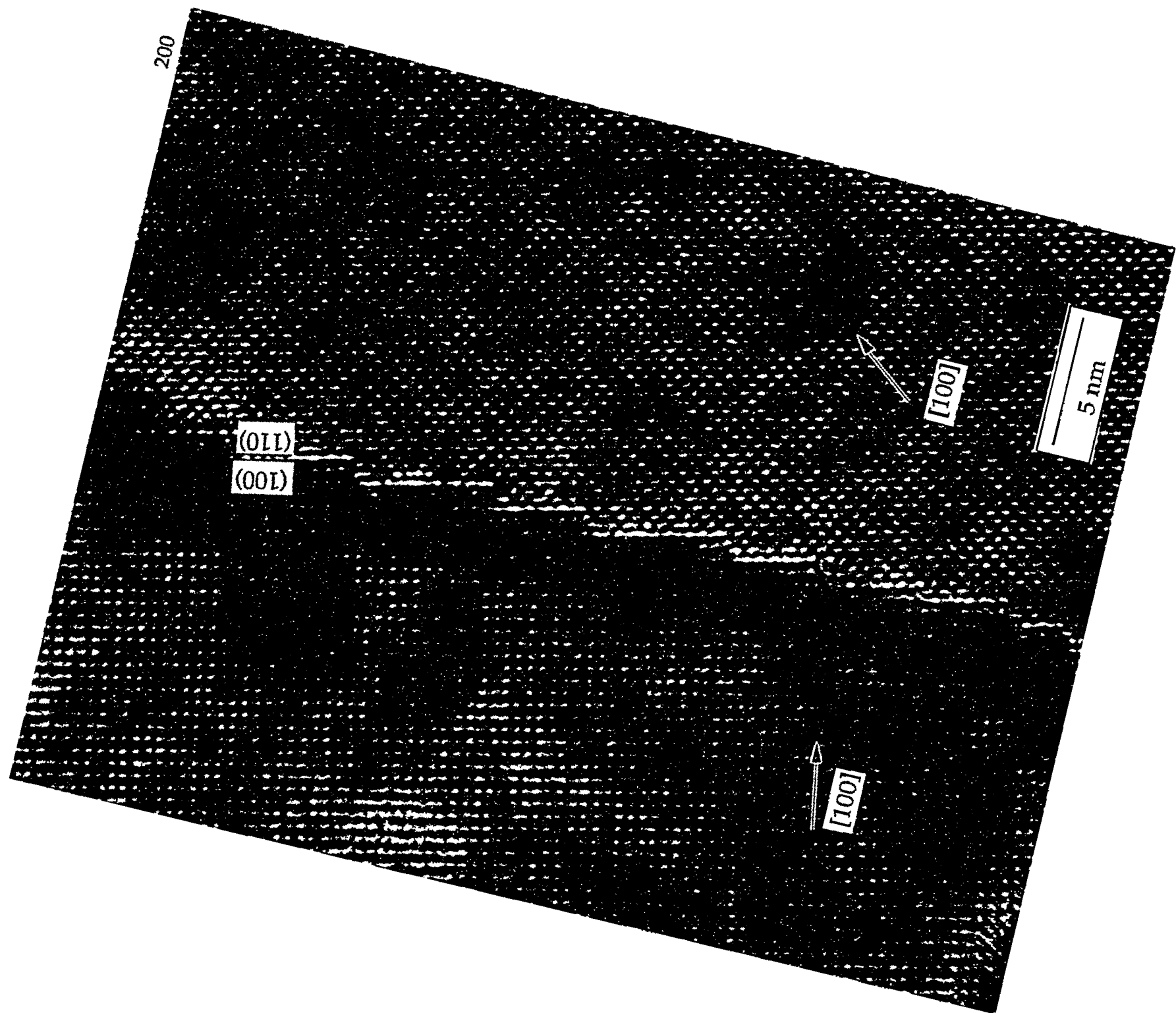
The grain boundaries appear free of second phases along their length. There is occasional precipitation (see figure 4.26), however the concentration of precipitates at the boundary is on the same order of precipitates in the grains. The precipitate in figure 4.26a. is  $\text{Y}_2\text{O}_3$  that forms during yttria rich growths and do not form preferentially at the boundary. Often no precipitates are seen along the boundaries, but even when there are precipitates, they constitute much less than 5% of the boundary length. Many other types of grain boundaries show favorable formation of precipitates or phases at the boundary (such as bulk melt-textured samples and biepitaxial, see Ch.VI). The minimization of precipitation and lack of second phases at the boundary indicates that there are no significant interruptions at the junction, which is beneficial for the transport properties.

The dominant feature of the grain boundary structure is the preferential asymmetric faceting along the majority of the boundary (see figures 4.26, 4.27 a-b.). The faceting forms such that the (100) plane of one grain lies parallel to the (110) plane of the adjacent grain. Note the a- and b-axes are not differentiated due to their close lattice parameters. The facets extended for relatively long lengths observed up to over 100 nm along the boundary (see figure 4.27a). To accommodate for the meandering of the boundary, the boundary must curve, but this is also often accommodated with asymmetric microfacets even as small as one unit cell in dimension. Figures 4.28a-b. show a region of the boundary that curves 90°, but it maintains asymmetric microfacets along the entire length. The one region (figure 4.28b.) has a stepped boundary with alternating microfacets. The microfacets have a reversal in structure with the (100) of the

Figure 4.28a. A region of a grain boundary that curves 90°, but maintains the asymmetric facets along the entire length. The region indicated by the arrow is magnified in figure 4.28b.



Figure 4.28b. Magnified region of the grain boundary in figure 4.28a. The boundary is stepped with asymmetric microfacets maintaining the local asymmetry. The "step" regions have reversed symmetry of the "ledge" regions.



top grain parallel to the (110) of the bottom grain on the "flat" region, and then the (110) of the top grain parallel to the (100) of the bottom grain on the "step".

There are different possibilities for the formation of the asymmetric facets. The preferred formation of the facets could be either kinetically or thermodynamically driven. Kinetically, the growth fronts could be (100) and (110), which are then forced together during growth. The other possibility is that the asymmetric boundaries have a lower energy than the symmetric boundaries at thermodynamic equilibrium and would preferentially form. Calculations of the grain boundary energy in other materials have shown that there are certain configurations where asymmetric facets have lower energy than symmetric facets (Wolf *et al.* 1992). Moreover, grain boundaries that combine two dense-packed planes (low-index) tend to have low energies. The YBCO films are grown under conditions that are very close to thermodynamic equilibrium, at relatively slow growth rates in a fully oxygenated environment (see chapter III). This suggests that these asymmetric facets could be the thermodynamically favored orientation.

The grain boundary plane maintained the asymmetric faceting even when the macroscopic symmetry was changed. There were some regions where the boundary did not microfacet (see figure 4.29). In figure 4.29 two asymmetric (100)(110) facets are connected with a region that is not completely microfaceted (even though it does contain some microfacets). Approximately 70% ( $\pm 10\%$ ) of the grain boundary appeared to be faceted. This estimate is from extended regions where the faceting could be determined in a photoresist prepared sample. Therefore the asymmetric facets are expected to dominate the transport properties of these samples.

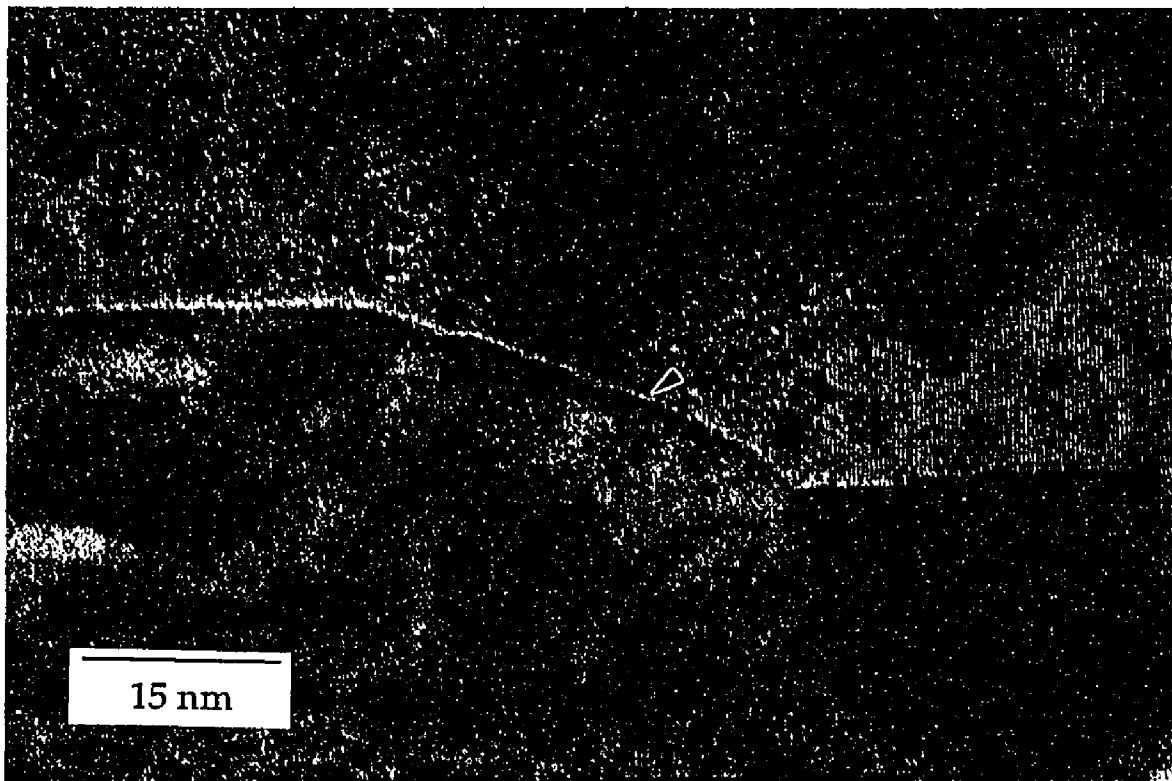


Figure 4.29. Two asymmetrically faceted regions of the grain boundary connected by an unfaceted region.

Figure 4.30a. A HREM image of an asymmetric facet. There is a small step in the boundary accommodated by a reversal in symmetry.

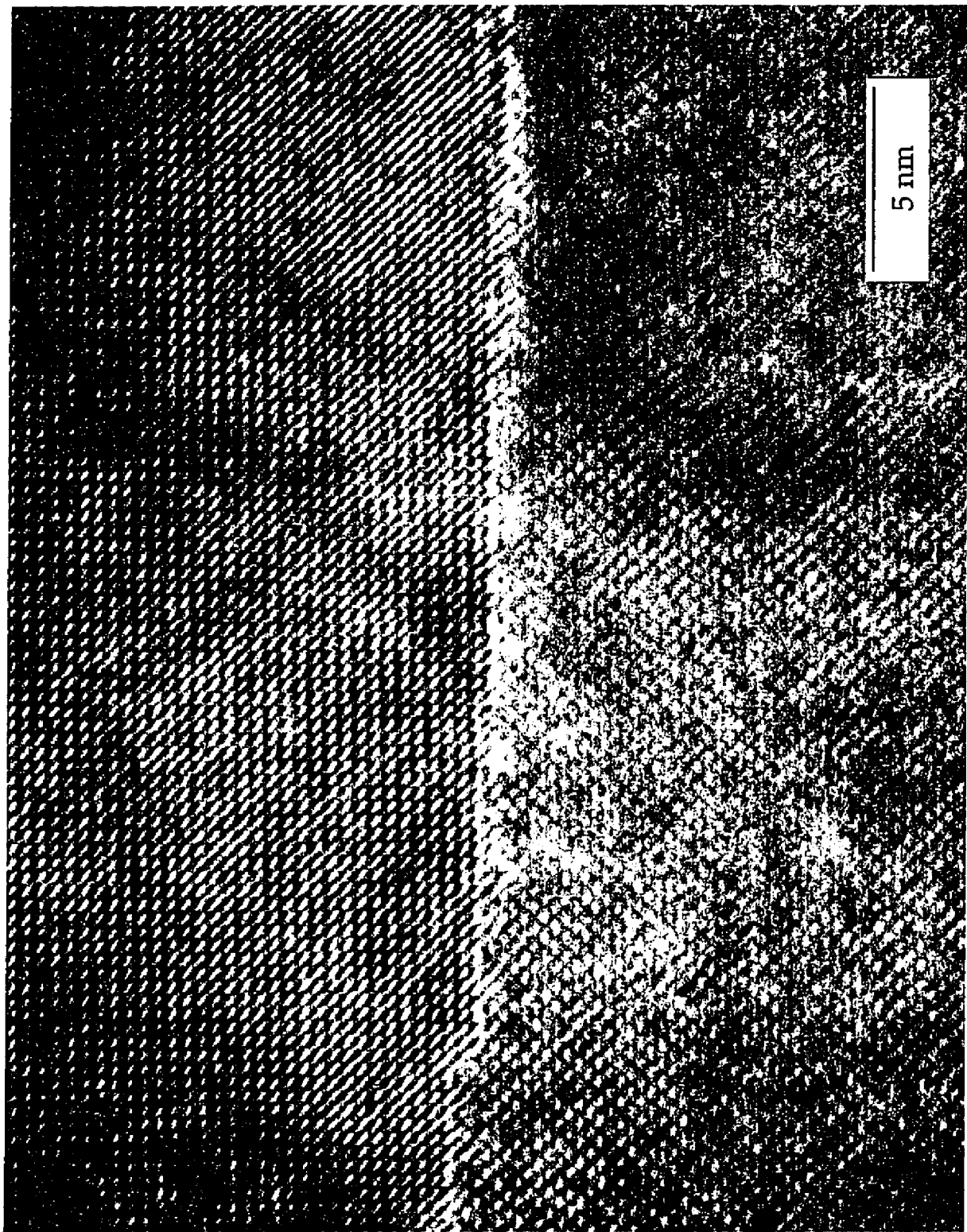
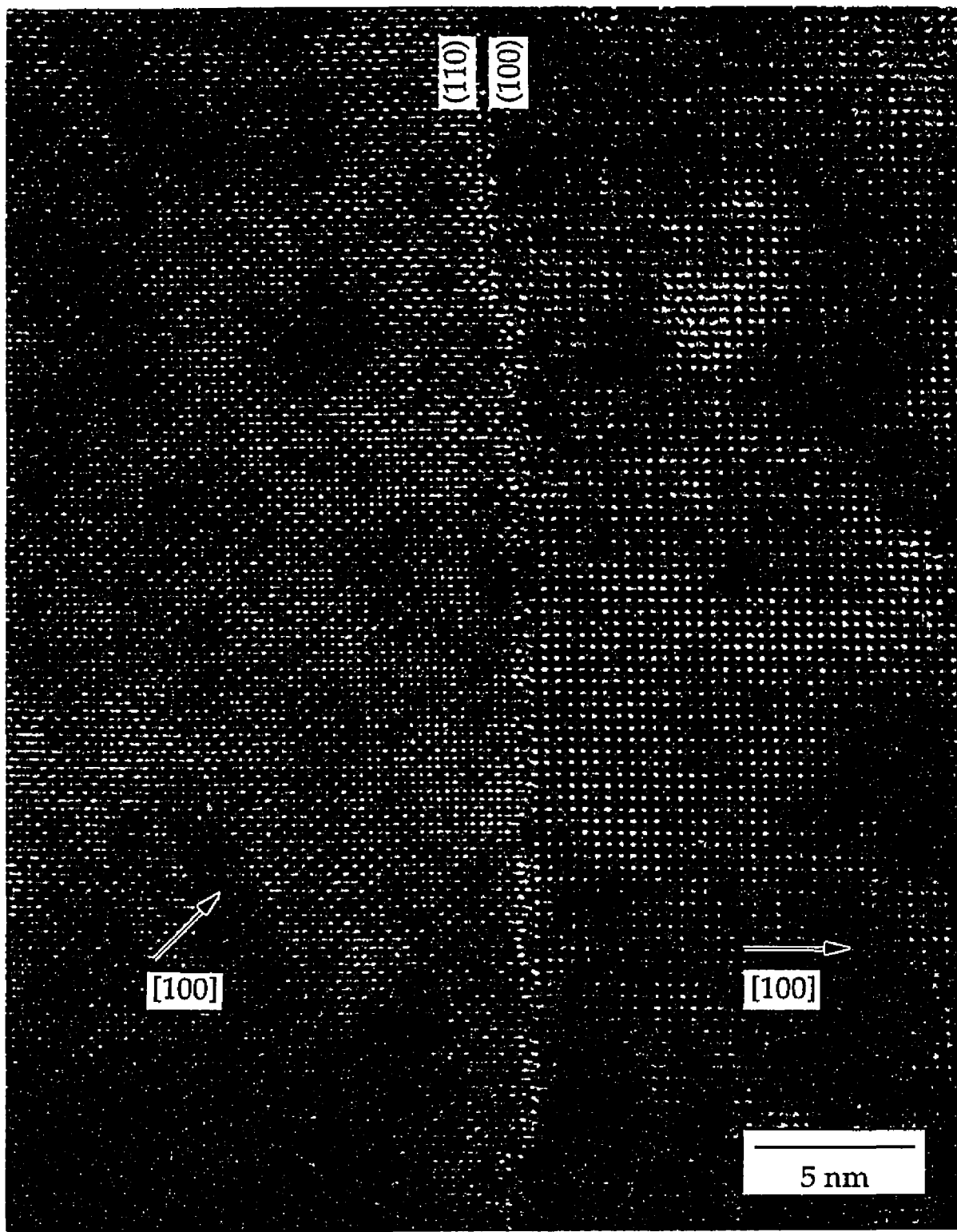


Figure 4.30b. A 40 nm long asymmetric facet along a grain boundary. The boundary maintains the grain structure to within one plane of the grain boundary plane.



The grain boundaries appear to be very well structured (see figures 4.30a-b). Any distortion from strain appears to be localized at the grain boundary plane, and one lattice dimension in either direction. High resolution simulations of the boundary were made using a simple rigid model of two grains and reordering the grain boundary plane to insure that the atoms were spaced sufficiently apart. A through focal series for a thickness of 114 Å for one of the simulations is shown in figure 4.31. The simulation is matched to two images of a series shown in figure 4.32. The experimental image of the grain boundary structure is aperiodic, and has variations in the local structure. A perfect match between the simulation and the image is difficult because of the complexity of the grain boundary structure and the variation along the boundary. Therefore this model only attempts to highlight a few basic points. The boundary has the lightened contrast and streaks seen in the simulation. This contrast was highly dependent on the oxygen placement at the grain boundary. The oxygen cannot be observed directly, but the effect of the oxygen arrangement can be seen. The slight bending of the lattice plane immediately adjacent to the boundary plane is also visible. The dark holes along the boundary are matched by the simulation. From the model used in the simulation, the boundary appears to be disordered in a region with a total width of 4 Å about the grain boundary plane. The image simulations were performed with the considerable assistance of Dr. Hong Zhang.

The uniform asymmetric facets at the boundary and the lack of second phases indicate a cleaner boundary than others analyzed such as the bi-epitaxial boundaries. Theoretical calculations of the critical currents across symmetric vs. asymmetric suggest that asymmetric grain boundaries can

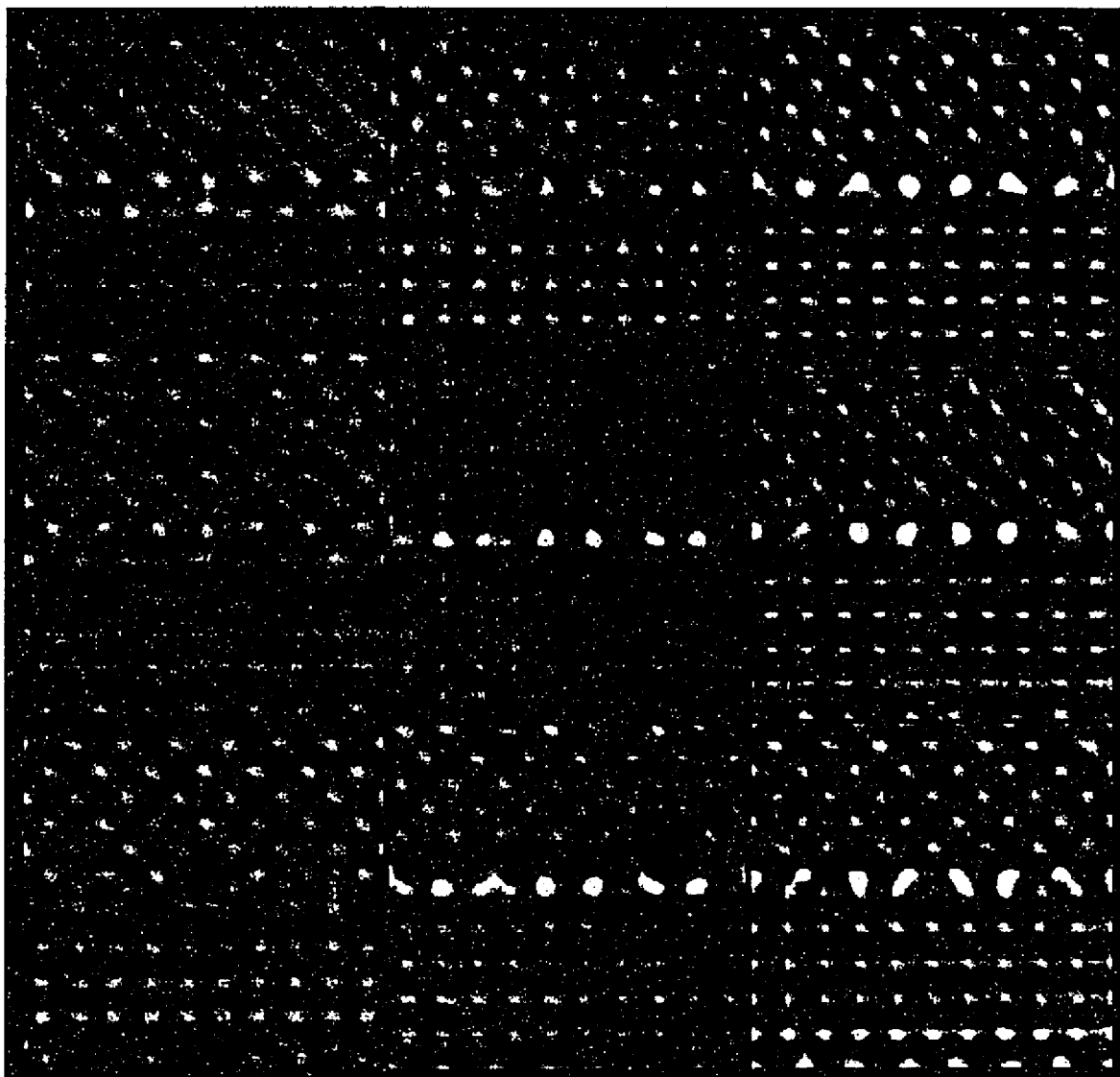


Figure 4.31. HREM through focal series simulation from 0 defocus in -100 Å steps (upper right to lower left going down the columns). The thickness is 114 Å.

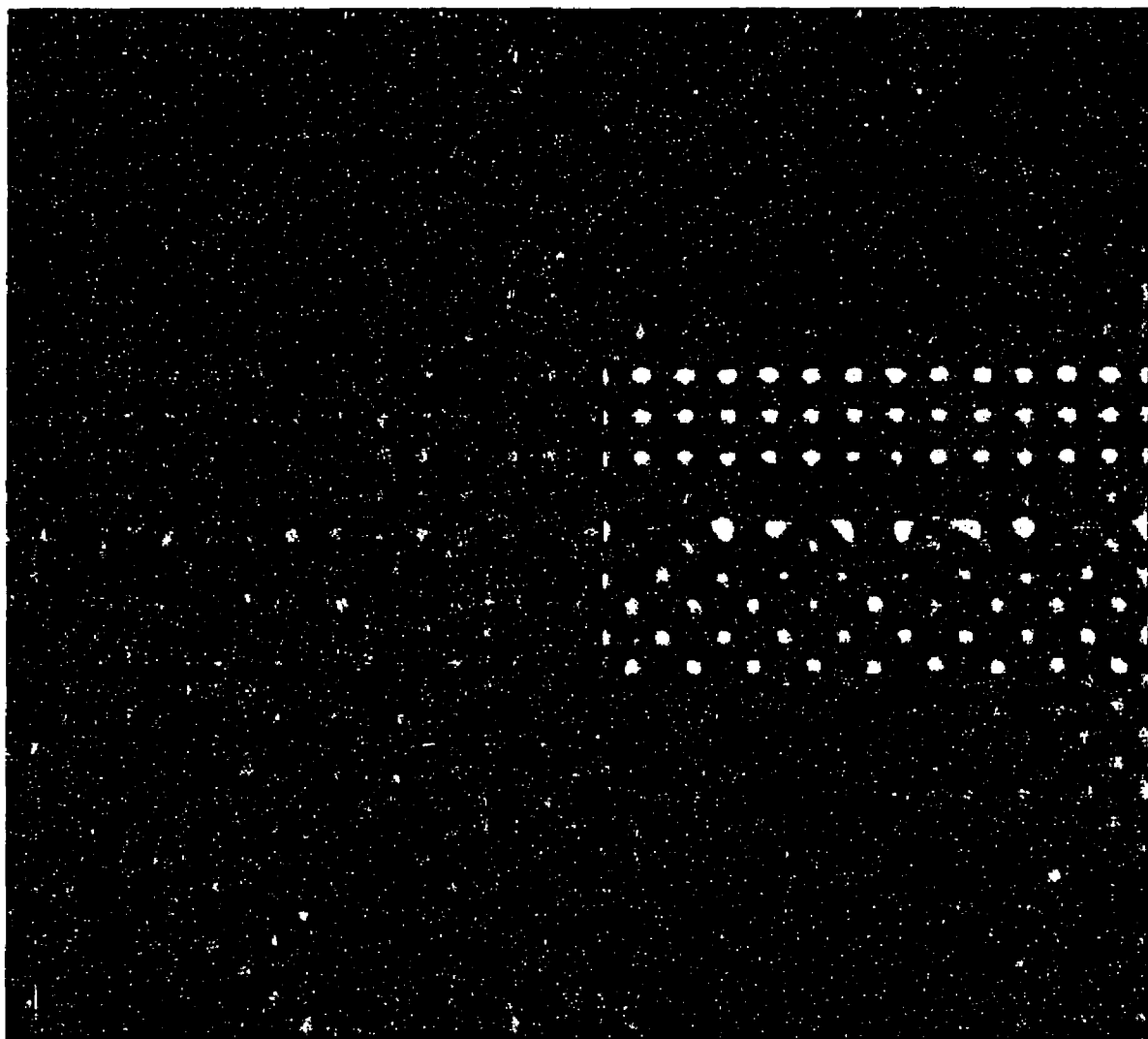


Figure 4.32a. HREM image and simulation of a sputter-induced epitaxy grain boundary. The simulation is at 400 Å defocus and a sample thickness of 114 Å.

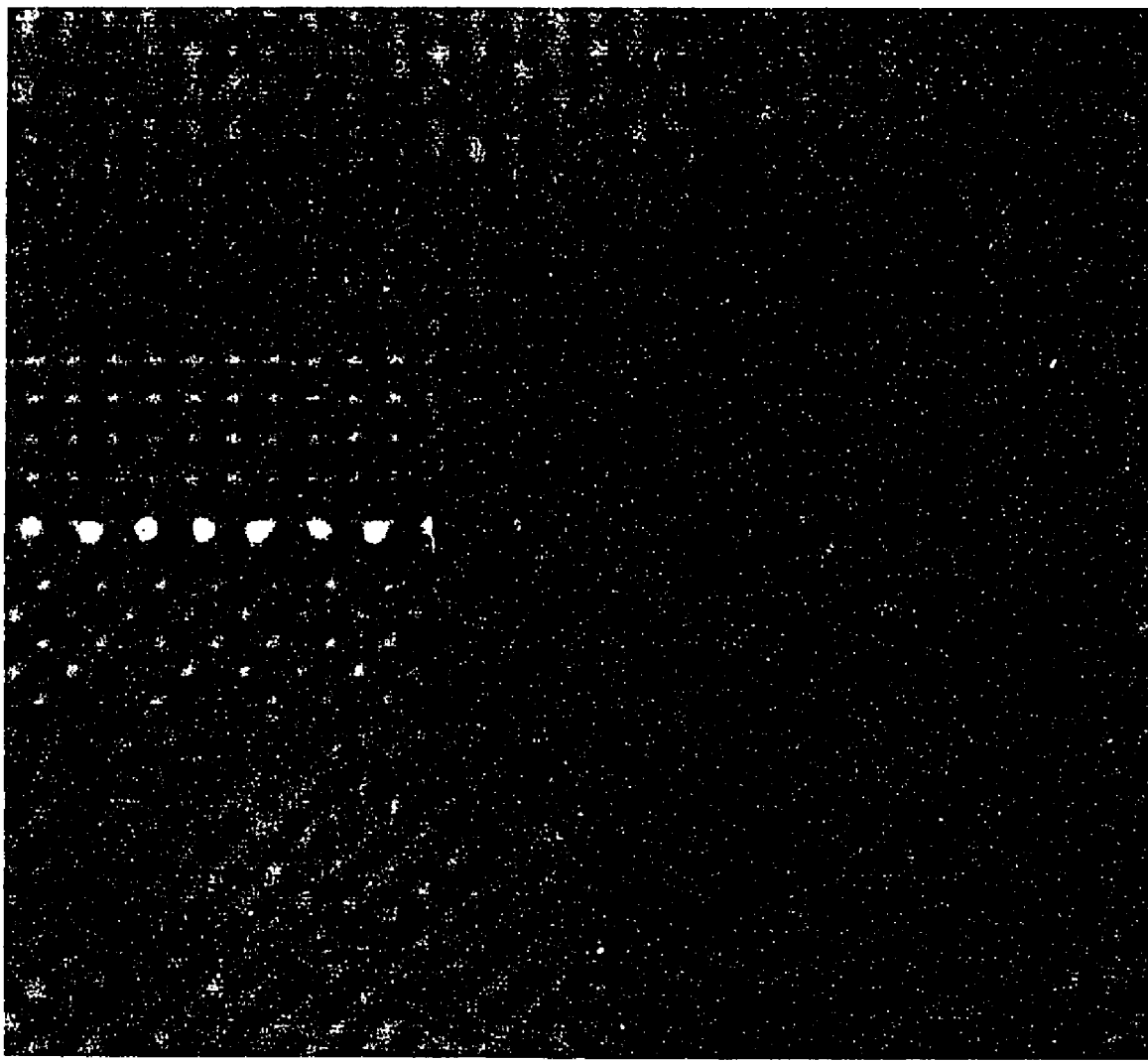


Figure 4.32b. HREM image and simulation of grain boundary junction. The simulation is for a defocus of  $-700 \text{ \AA}$  and a sample thickness of  $114 \text{ \AA}$ .

support higher critical currents. (Meilikhov 1994) This is consistent with the large critical currents supported by the boundary relative to the bi-epitaxial samples (discussed in detail in chapter VII and appendix I). Also the periodicity in the magnetic field measurements suggest length scales of uniform critical current densities. The microstructure supports this property relation and will be discussed in detail in chapter VII and appendix I, which compares the sputter-induced junctions and the bi-epitaxial junctions.

#### IV.3.3. Parallel Electron Energy Loss Spectroscopy

One grain boundary was analyzed with parallel electron energy loss spectroscopy (PEELS) to study the hole carrier concentration along the boundary (see chapter II.). Superconductivity in YBCO has been attributed to 2p hole states. These hole states have been shown to cause a characteristic pre-edge structure on the oxygen K edge. Several groups have correlated the pre-edge structure in the electron energy loss oxygen peak to the 2p hole carrier concentration (Nücker *et al.* 1988; Nücker *et al.* 1989; Browning *et al.* 1992; Browning *et al.* 1993; Dravid *et al.* 1993). The ratio of the pre-edge intensity to the main edge intensity has been related to the transition temperature of the material. In this experiment the absolute relation to  $T_c$  was not determined, so only relative comparisons are made. The measurements were made with the assistance of Dr. Yunyu Wang.

An electron transparent sample with several grain boundaries was made. The samples were prepared with specific attention to minimizing damage during preparation (see Chapter III.). The specimen was cooled to -90° C to minimize beam damage during the experiment, lower temperatures would

sometimes result in ice forming on the sample. A thin region with a grain boundary was found with a zero loss to low loss intensity ratio of 10:1. The cold field emission gun HF-2000 was used at 200 kV accelerating voltage with a Gatan 666 PEELS spectrometer. The smallest probe size was used, and measured by imaging the probe (found to be 2 nm maximum diameter). The minimum probe step size was used and calibrated using images of the probe. The step size was 2 nm in all the measurements. The measurements presented are from the same session to insure similar scope and sample conditions for comparison.

The PEELS spectra were taken in diffraction mode (called image-coupling) with a spectrometer collection angle of 10-15 mR. The sample was tilted slightly off the major zone axis to avoid channeling conditions that could modify the spectra. The diffraction pattern insured that the probe was at the grain boundary or in the grain. Consecutive spectra were measured 8 times for 0.8 seconds and analyzed to verify that there was no noticeable change in the spectrum over time from drift or beam damage. The 8 spectra were then summed to increase the counting statistics. Care was taken to note whether the beam drifted or not during each acquisition, and only the spectra taken without drift are used in these results. No noticeable beam damage was detected in the spectra during the session.

Two typical spectra are shown if figures 4.33a-b. The background was fitted using a power-law fit and then subtracted. The remaining peak was then smoothed and fitted using a two Gaussian fit. The error were determined using the maximum errors in the fit.

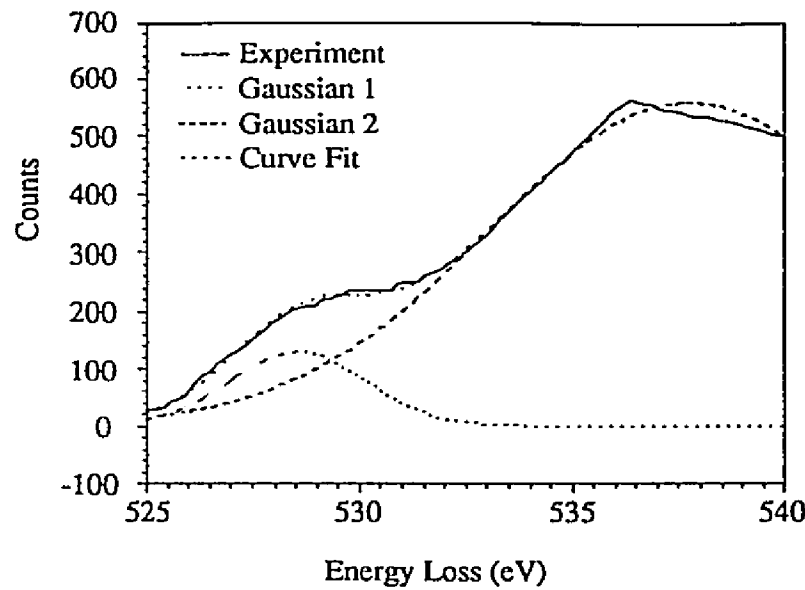


Figure 4.33a. PEELS spectrum of a grain region in the sample with the two gaussian fit.

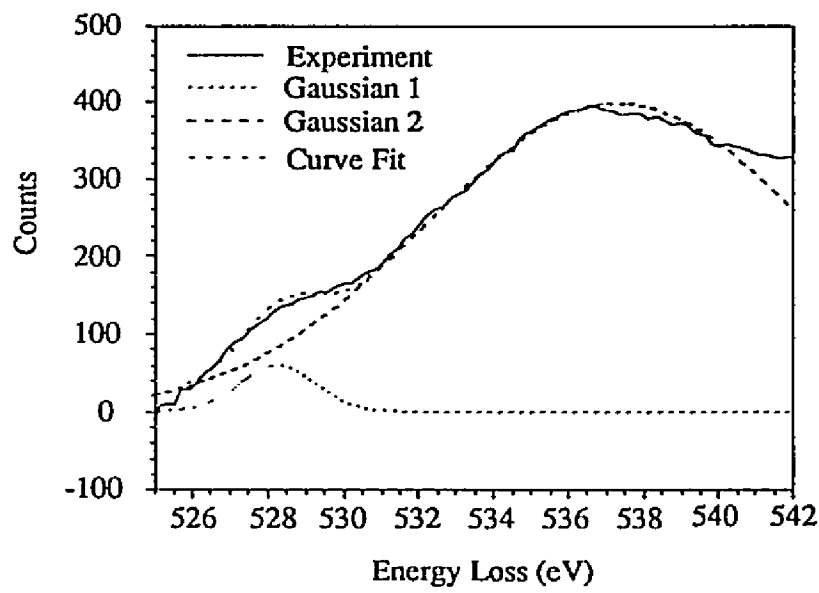


Figure 4.33b. PEELS spectrum of a grain boundary region in the sample with the two gaussian fit.

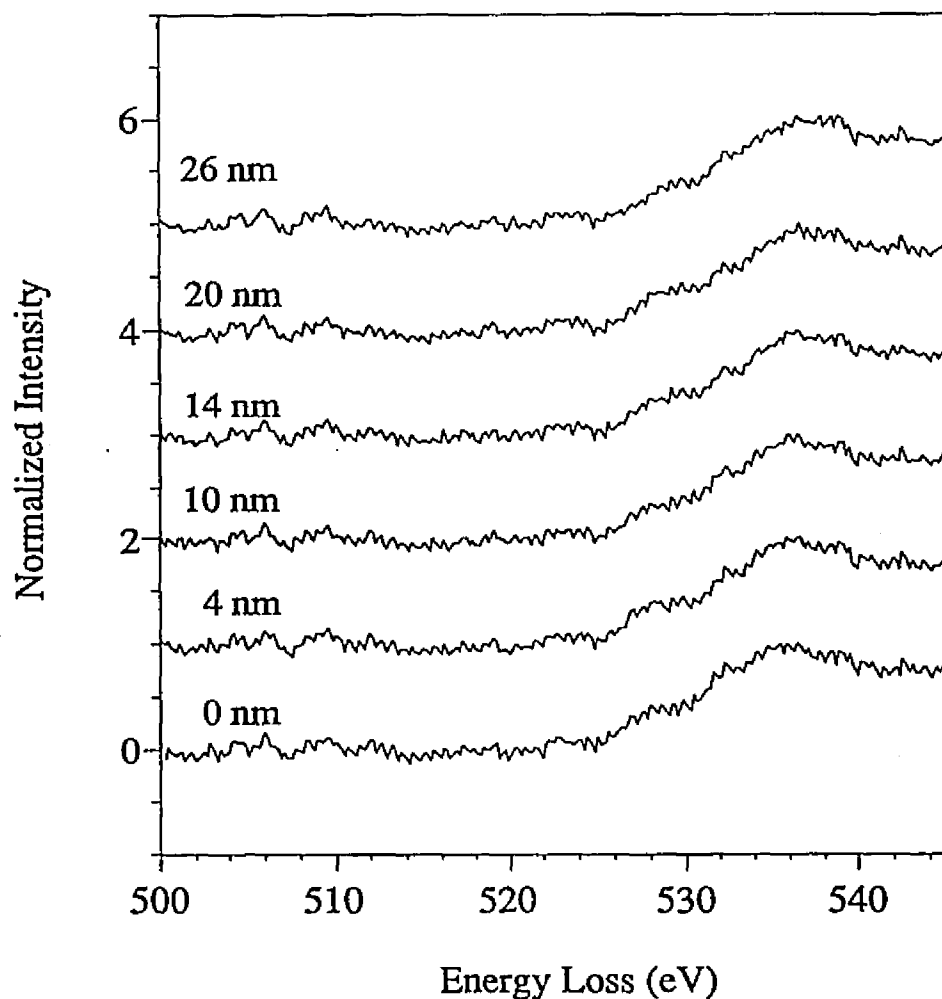


Figure 4.34. Seven spectra from along the grain boundary.

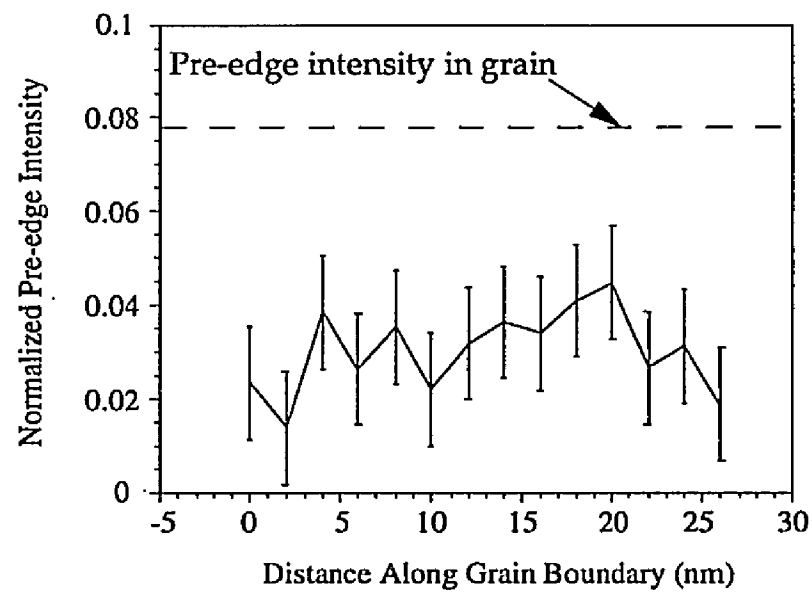


Figure 4.35. Normalized pre-edge intensity along the grain boundary in 2 nm steps. Grain pre-edge intensity is denoted by the dashed line, the error bars for the grain are as large as in the boundary.

A series of spectra along a grain boundary are shown in figure 4.34. These spectra are every third spectrum taken along the grain boundary. The spectra were taken in 2 nm steps along a grain boundary. They show remarkable similarity in the pre-edge structure and intensity. The results of the normalized pre-edge intensities from all the spectra along the grain boundary are in figure 4.35. There appears to be no variation along the boundary within statistical error. The maximum normalized intensity observed under these conditions in the grain was 0.0775, indicating that statistically the grain boundary is not depleted in hole carriers relative to the grain region. Absolute quantification was not made due to the lack of a characterized standard.

To within the resolution of the probe size, 2 nm, there was no variation in the hole carrier concentration along the boundary. The entire boundary did not have statistically significant variations in concentration along this region. This result suggests that regions of the boundary can have relatively consistent concentrations of hole carriers along their length to within the resolution of the technique.

#### IV.4. Conclusions

Sputter-induced epitaxy is a unique and simple method to form high quality grain boundary junctions. This is one of the first strictly pre-growth ion treatments that has modified the epitaxial relationship between the thin film and the substrate in any materials system. The overriding advantages of this technique are its simplicity and versatility. Grain boundary junctions with relatively large critical current densities can be formed using standard equipment including a low voltage ion mill and an OMCVD growth system.

This is completely compatible with modern industrial processes and can be scaled up for large scale production. The versatility is apparent in the ability to form junctions in virtually any configuration. The size limitation on patterning feature size is in the photolithographic resolution of the masks used. The sputter-induced epitaxy samples have been formed consistently and reproducibly with favorable transport characteristics. The technique is planar, which is an advantage for multilayer systems.

RBS and AFM were used in conjunction with a variety of pre-sputter conditions to study the mechanism causing the modified epitaxy. The results indicate that both implanted argon and tungsten could play an integral role in the process. The conditions for all the samples that had the modified epitaxy resulted in implanted argon and tungsten. These ions could create a distorted lattice parameter by their positions in the lattice, therefore favoring the 45° rotated epitaxy. There is the possibility of surface chemistry effects due to the ion implantation. The AFM results also suggest that a specific type of damage associated with the ion implantation could be necessary to control the film orientation. Therefore a combination of surface disorder and ion implantation play a role in the modified epitaxy.

The grain boundary structure has been shown to form relatively long (hundreds of nm) straight asymmetrically faceted grain boundaries. The boundaries are free of second phases. Since the film is grown on MgO on both sides of the boundary there is no preferential precipitation along the boundary unlike other types of samples. HREM images and simulations indicate that there is a localized disordered region, 4 Å wide, at the boundary. The grains maintain their structure up to the boundary. PEELS measurements indicate a

statistically constant hole carrier concentration at the grain boundary relative to the grain, which remains consistent along the boundary to within the 2 nm probe size.

There are some drawbacks to this technique. First it is limited to a bulk MgO substrate, which is not always favorable. Chapter V describes a technique to use other bulk substrates to overcome this disadvantage. The other drawback is the fixed misorientation of 45°, which has inherently lower critical current densities than lower angle boundaries. Other types of high-T<sub>C</sub> films with similar lattice parameters can be tried on MgO, but unfortunately high quality phase pure and epitaxial single crystal thin films in the bismuth and thallium systems have only recently been developed. The obvious advantages of other high-T<sub>C</sub> materials would be the higher critical currents of the junction.

A more complete understanding of the mechanism will allow translation of the technique to other materials systems. Of particular interest would be systems where grain boundaries play a crucial role in desired properties, e.g. ferroelectrics. By controlling epitaxy with a simple pre-growth treatment, grain boundaries can be placed in virtually any configuration.

## V. Multilayer Sputter-Induced Epitaxy

One of the major drawbacks of the sputter-induced epitaxy grain boundary junctions is that they are formed on bulk MgO substrates. Despite all the favorable aspects of MgO, there are many applications, such as integrating with semiconductors, where other substrates would be more desirable. The use of MgO is also not preferable simply due to the rough surface structure of the bulk substrates and hygroscopic properties (see figure 4.7). A method to form sputter-induced epitaxy grain boundary junctions on a bulk substrate other than MgO is discussed in this chapter.

### V.1. Grain Boundary Formation

There are two basic ways to circumvent the problem of using a bulk MgO substrate. The first method is to use sputter induced epitaxy with YBCO on other bulk substrates. In principle, if the mechanism to induce the modified epitaxy is not unique to MgO, other bulk substrates could be used. The pre-sputtering treatment of different material substrates has not yet produced a modified epitaxy in the thin film (see chapter IV).

The second method to form sputter-induced epitaxy junctions on a different bulk substrate is to use multilayers. The idea is to deposit an epitaxial thin film layer of (100) MgO on a bulk substrate other than MgO. The thin film is then patterned and sputtered with a pregrowth treatment of 200-300 eV low voltage ions. A YBCO thin film is then deposited on the MgO film. The resulting film has a cube-on-cube orientation on the unspattered region and an

epitaxy rotated 45° about [001] on the pre-sputtered region of the multilayer.

It is not obvious that the ion beam pretreatment on a MgO multilayer thin film would modify the YBCO epitaxy. Bulk MgO typically has a contaminated surface due to its hygroscopic properties. The mechanical and chemical processes in making an epitaxial polish on the substrate further damage the surface. The damage often results in a substrate that can be tilted as much as 1° from the desired [100] orientation. The final polish also leaves impurities and etch pits on the surface as illustrated using AFM in figure 4.7. It has been shown that even slight contamination of the substrate can cause the film to grow polycrystalline in an uncontrolled fashion (Olsson 1994; Ramos *et al.* 1993). The MgO thin film could potentially have a much smoother surface than the bulk. AFM images of the MgO multilayer (Dean *et al.* 1995) indicate that the surface is smoother than the bulk and is obviously more pristine since it does not go through any polishing steps. If the sputter-induced epitaxy is caused by the modification of a contaminated surface, then the technique should not modify the epitaxy of YBCO on a high quality epitaxial MgO thin film.

### V.1.1. Sputter Induced Epitaxy Conditions

Figure 5.1 represents a schematic of the multilayer sputter-induced epitaxy process. An MgO film is deposited on a (100) LaAlO<sub>3</sub> substrate using POMBE. In order to form a highly epitaxial (100) MgO film, a buffer layer was used to reduce the strain between the film and substrate (about 10% misfit between MgO (100) and LaAlO<sub>3</sub> (100)). Two different buffer layers were used, YBCO (approximately 120 Å) or 10-20 Å of CuO<sub>x</sub> (0 < x < 1). The buffer layer thickness was optimized by determining the thickness that minimized the full

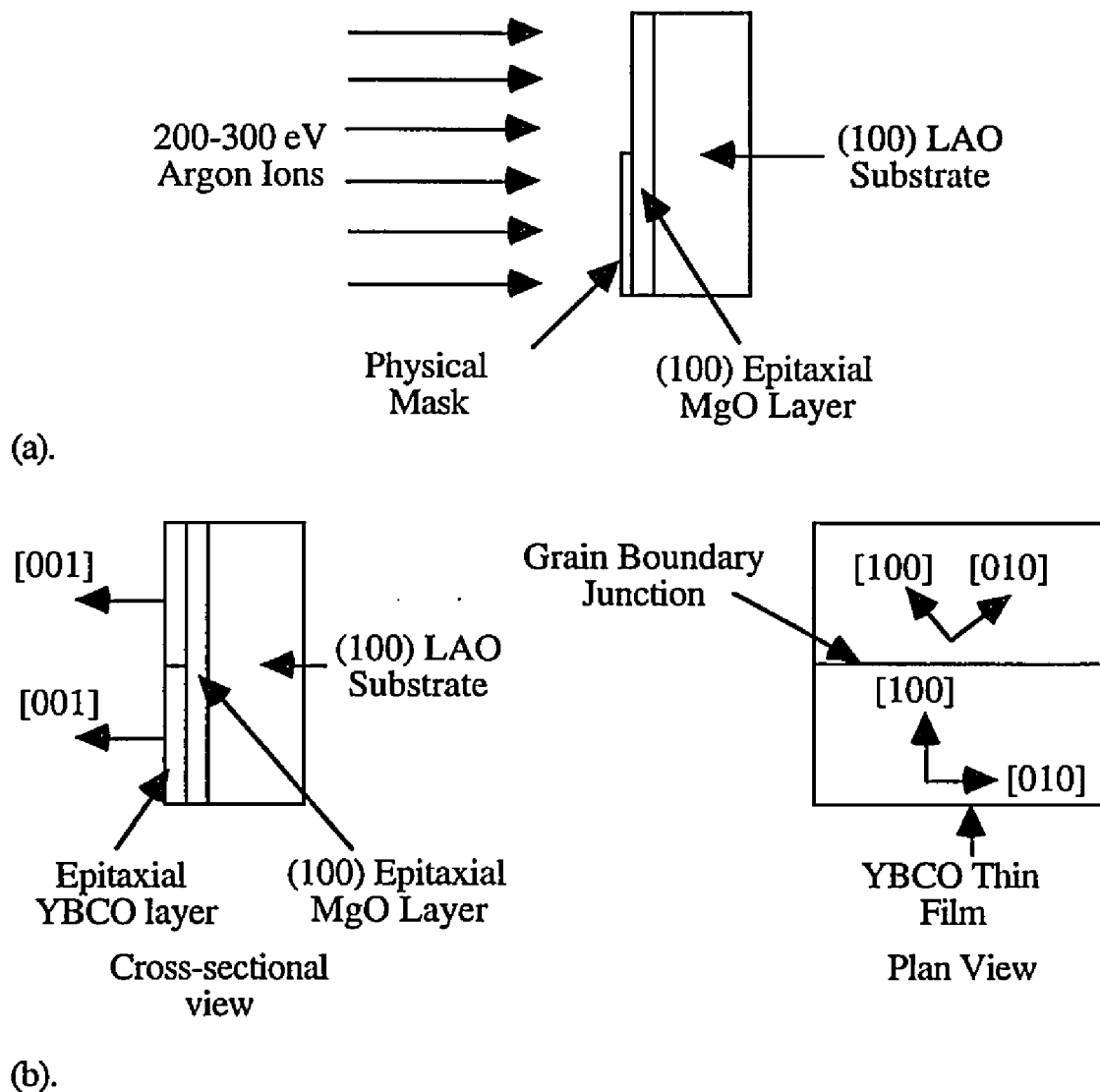


Figure 5.1a-b. Schematic diagram of the multilayer sputter-induced epitaxy process.

width at half maximum (FWHM) of the x-ray rocking curve of the MgO (200). The FWHM of the films used, varied between  $1.08^\circ$  and  $0.88^\circ$ , which are the highest epitaxial quality films reported grown using OMCVD. The film growth is described in detail elsewhere (see Dean *et al.*(Dean *et al.* submitted)).

After the film is grown, the sample is then partially covered with a hardbaked photoresist mask. The uncovered portions of the MgO layer is then irradiated using low voltage argon ions (200-300 eV) with  $1 \text{ mA/cm}^2$  ion current density for 3 minutes at  $90^\circ$  incidence to the sample surface. These conditions were not varied for the different samples.

A YBCO film is then deposited on the sample with a thickness between 2000 and 3000 Å. The film grew with a cube-on-cube orientation on the unsputtered areas of the substrate. On the pre-sputtered regions the orientation relation between the thin film and the substrate was  $\text{YBa}_2\text{Cu}_3\text{O}_{7-x}$  [001] || MgO [001] and  $\text{YBa}_2\text{Cu}_3\text{O}_{7-x}$  [100] || MgO [110]. Therefore the modified epitaxy matched the epitaxial conditions for YBCO films grown on bulk MgO. This implies that there is no connection between the modified epitaxy and the typically contaminated bulk surface. The technique modified the epitaxy successfully on several different multilayer thin films grown during different runs, indicating that the technique is reproducible.

### V.1.2. Surface Morphology

The MgO thin film was already shown to have a very smooth surface (Dean *et al.* 1995). The YBCO thin film quality was highly dependent on specific growth conditions. The films were usually optically reflective, but SEM analysis of the film surface showed largely varying surface morphologies. Often

copper oxide precipitates were formed on the sample due to excess copper during film growth. There was no preferential precipitate formation along the grain boundary, which is important for maximizing the contact area between the two grains along the boundary.

Figure 5.2 is an SEM image of a YBCO film grown on a multilayer substrate. The grain boundary was not discernible using normal secondary electron imaging techniques. Using EBSP it was identified and lies between the arrows in the image. The corresponding backscattered diffraction patterns are shown in the insets. There are some copper rich precipitates that are generally less than  $1 \mu\text{m}^2$  in size. The precipitation concentration on the surface is 6 per  $100 \mu\text{m}^2$ , which is extremely smooth. The precipitates clearly do not line up along the boundary. The good surface quality could indicate that better YBCO films can be grown on a multilayer substrate than a bulk MgO substrate, due to the smoother surface of the MgO film compared to the rougher surface of the bulk substrate.

Another SEM image of a YBCO film on a multilayer substrate is shown in figure 5.3. This image has a  $5 \mu\text{m}$  wide strip that was sputtered and had a modified epitaxy relative to the rest of the sample. This indicates that the technique can be used on this small scale for numerous junction applications (one example is a series of junctions to increase the voltage that can be applied across the chip). In principle, the ultimate resolution of the technique could depend on the photolithographic capabilities.

The modified epitaxy occurred across the entire pre-sputtered region of the substrate. In this particular sample (figure 5.2) there were no other epitaxial conditions detected. Depending on the growth conditions, there

Figure 5.2. An SEM image of a multilayer sputter-induced epitaxy grain boundary junction. The grain boundary lies between the two arrows. The corresponding backscattered electron Kikuchi patterns (insets) show a 45° rotation about the [001] axis. The sample is inclined relative to the beam to maximize grain boundary contrast.

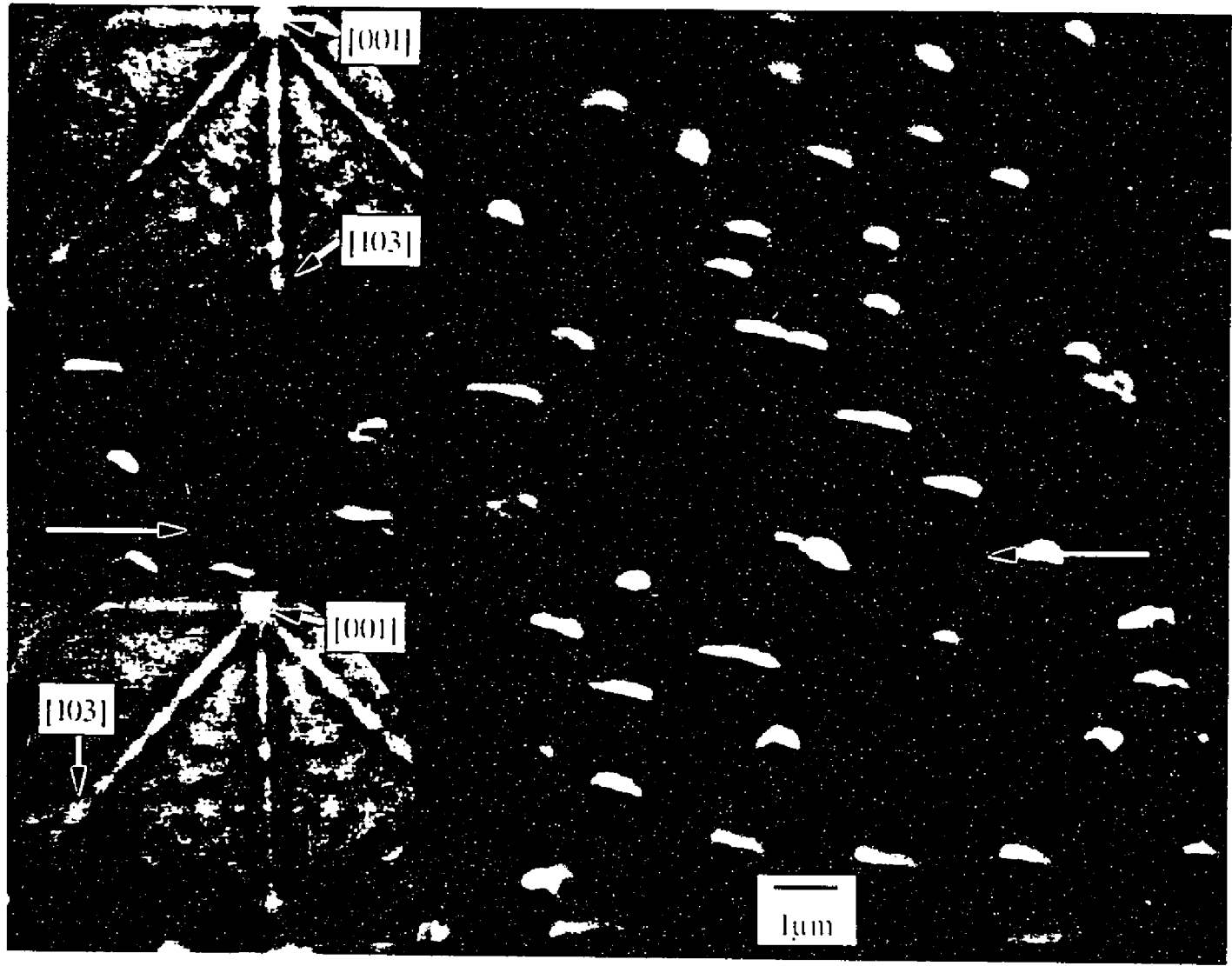
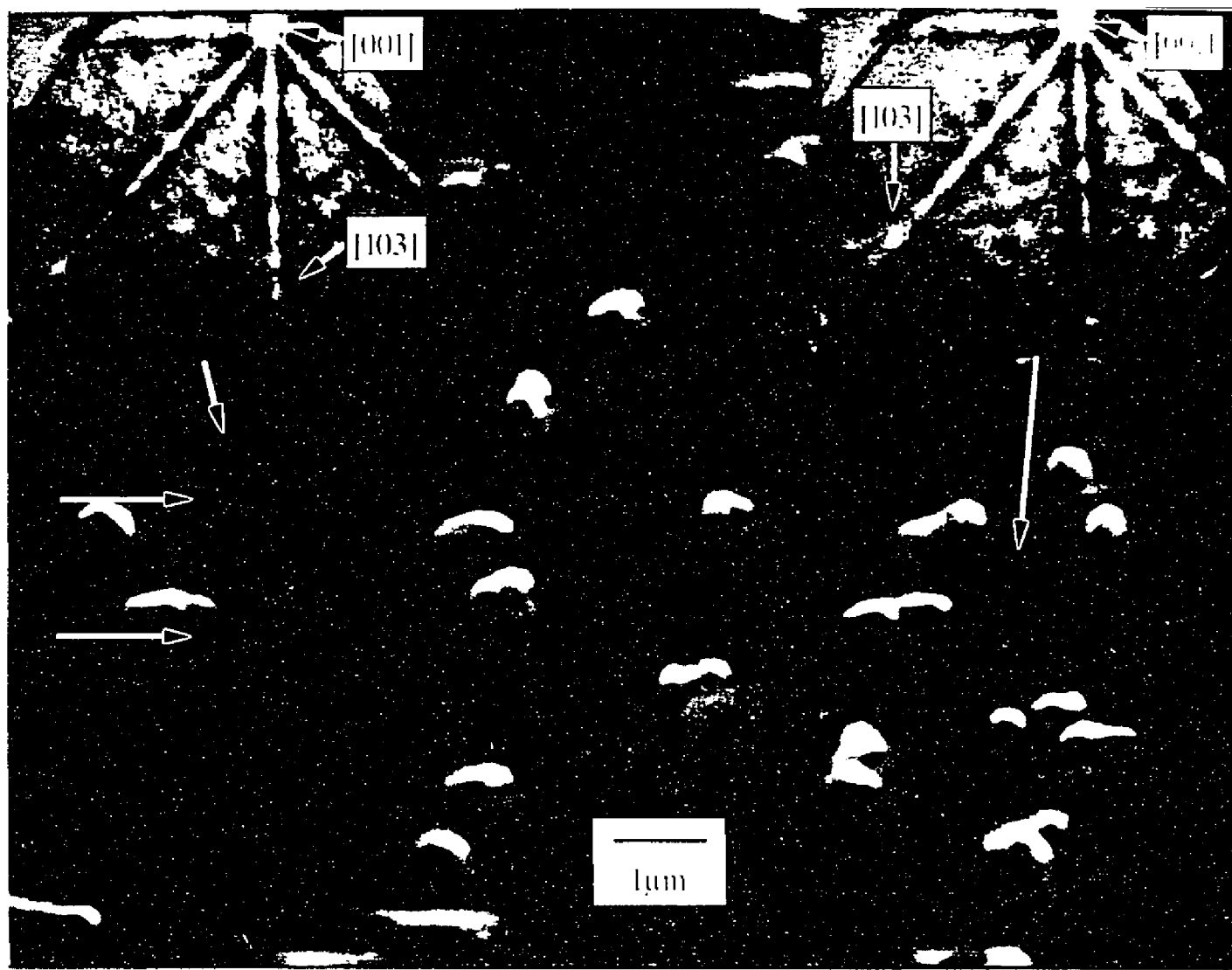


Figure 5.3. An SEM image of a  $5\text{ }\mu\text{m}$  wide strip of rotated grain forming two parallel junctions. The sample is inclined relative to the beam so the micron marker is only valid in the direction along the boundary.



would be an occasional unrotated grain on the pre-sputtered region (<1%). The grain boundary was very abrupt, and no meandering could be seen to within the resolution of the EBSP technique (< 1  $\mu\text{m}$ ).

## V.2. Transport Properties

An individual grain boundary from a YBCO thin film grown on a multilayer was isolated. A 35  $\mu\text{m}$  wide microbridge was formed as described previously in chapter III. The boundary had an isolated grain, and allowed independent low temperature measurement of both the grain and the boundary.

### V.2.1. Resistance-Temperature

The resistance vs. temperature behavior of the sample using a measuring current of 0.5  $\mu\text{A}$  is shown in figure 5.4. The grain has a relatively high  $T_c$  of 88 K indicating a good quality film. The grain boundary has a slightly broader transition than the grain, with an abrupt transition onset at 89 K and a distinct foot-like structure at the base that finally goes superconducting at 84 K. This indicates a weak link junction of a single grain boundary due to the shape of the foot structure (see chapter IV for comparison with a polycrystalline region). The resistance of the foot is from TAPS due to the lower critical current of the boundary particularly close to the transition temperature. With a 1  $\mu\text{A}$  measuring current the foot extends to about 74 K, which is still a valid regime for TAPS to occur. The normal state resistance above  $T_c$  has the usual linear metallic behavior. The grain boundary region has a slightly higher resistance compared to the grain, mostly from the resistance of the grain on the other side of the boundary.

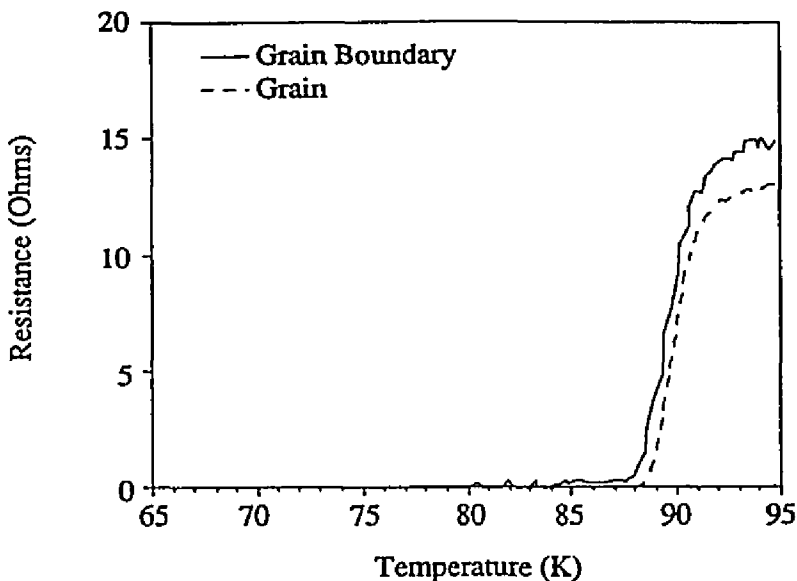


Figure 5.4a. Resistance vs. temperature for a grain and grain boundary in a multilayer sputter induced junction sample. Measuring current is  $0.5 \mu\text{A}$ .

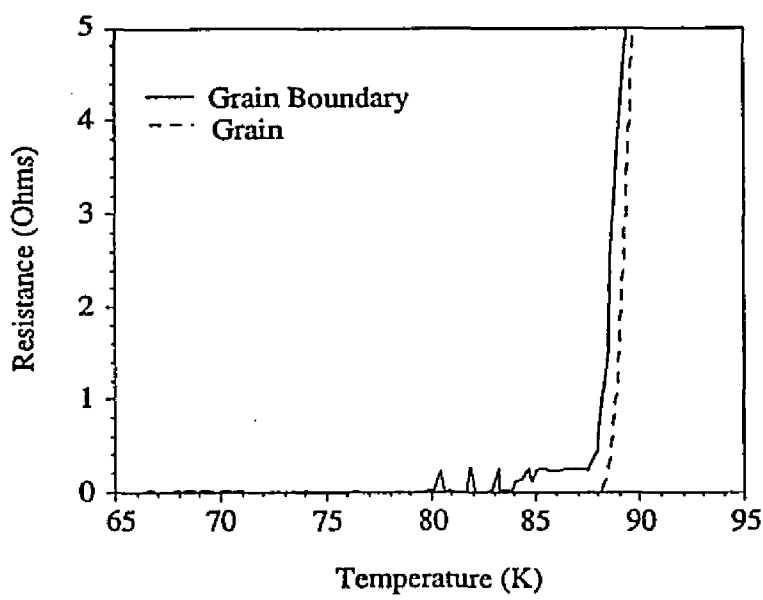


Figure 5.4b. Transition region of R-T curve showing the foot-like structure of grain boundary and sharp transition for grain.

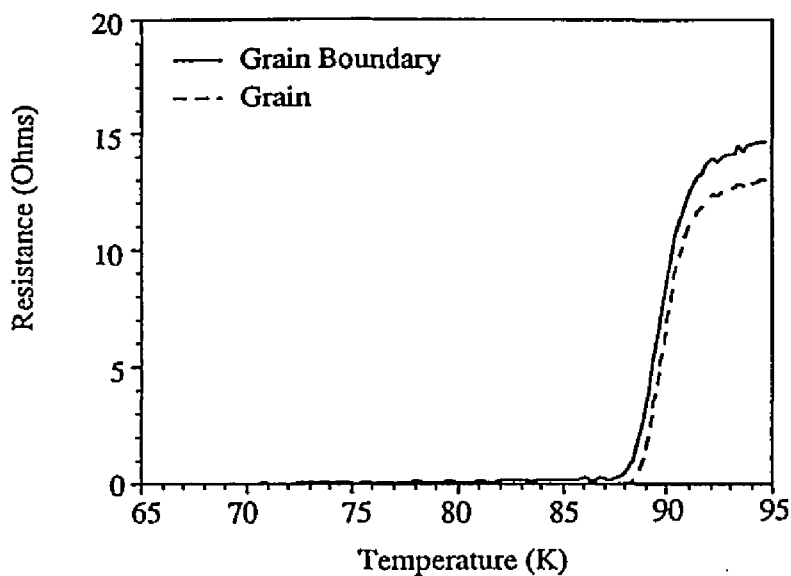


Figure 5.5a. Resistance vs. temperature curve for multilayer sputter induced grain boundary junction using a 1  $\mu\text{A}$  measuring current.

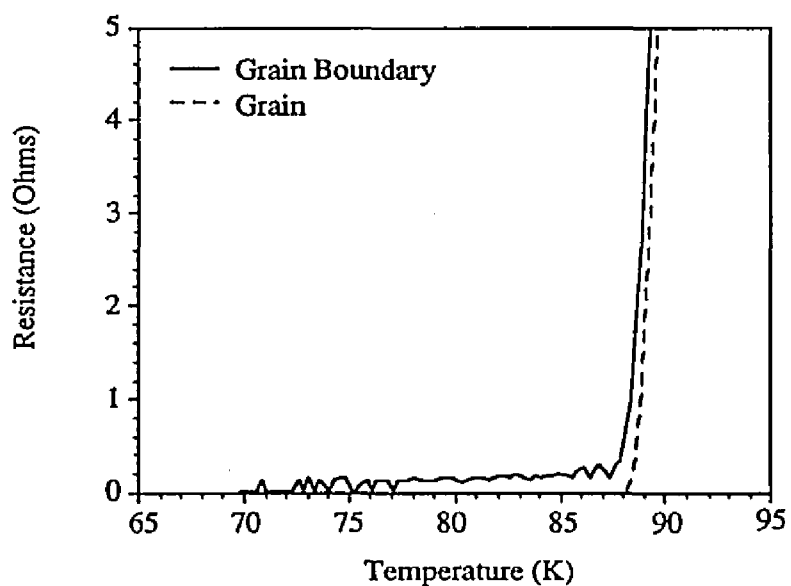


Figure 5.5b. R-T curve showing extended foot-like structure of grain boundary transition due to a larger measuring current (1  $\mu\text{A}$ ).

### V.2.2. Current-Voltage

The multilayer sputter induced grain boundary has typical weak-link current-voltage characteristics. Figures 5.6a-c. show the I-V characteristics of the grain boundary junction at different temperatures. The junction behavior can be modeled with the RSJ model using no capacitance ( $\beta_C=0$ ). Figure 5.6b. is the I-V characteristic at 40 K modeled using the RSJ model, exhibiting an excellent fit to the data. There is only a slight deviation near the transition due to the rounding of the experimental data due to noise effects. The RSJ fit allows accurate prediction of the junction behavior for microelectronic device applications.

The shape of the I-V curve indicates that there is only one high angle grain boundary along the junction, as described in chapter IV. The critical current density is  $5 \times 10^3 \text{ A/cm}^2$  at 5 K and  $7 \times 10^2 \text{ A/cm}^2$  at 60 K. The shape of the curve changes from RSJ-like at low temperatures to more of a flux-flow type of curve at higher temperatures as was also the case for the sputter-induced grain boundaries on bulk samples. The grain boundary critical current densities are about a factor of 10 less than the values for the boundaries on the bulk samples. The  $I_c R_n$  product is 52.5  $\mu\text{V}$  at 5 K and 8  $\mu\text{V}$  at 60 K, which again is relatively low compared to the values necessary for certain applications. This could be due to the quality of the MgO layer or YBCO layer being less than ideal. The entire process is still being optimized, and in principle there are no fundamental limitations that would prevent the grain boundary from having the same large critical current densities achieved on the bulk substrates.

The I-V characteristics for different temperatures are all plotted on a single graph in figure 5.7. This emphasizes the decreasing critical current and

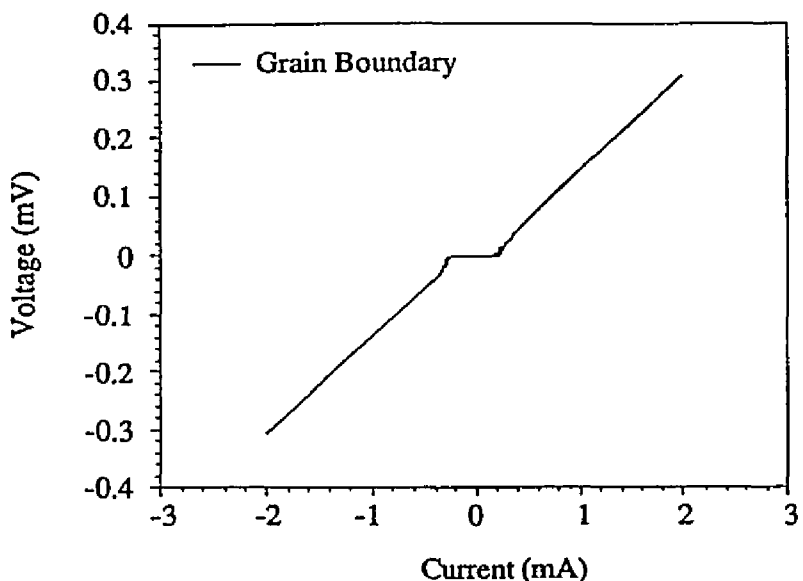


Figure 5.6a. I-V characteristics of multilayer sputter-induced grain boundary junction at 5 K.

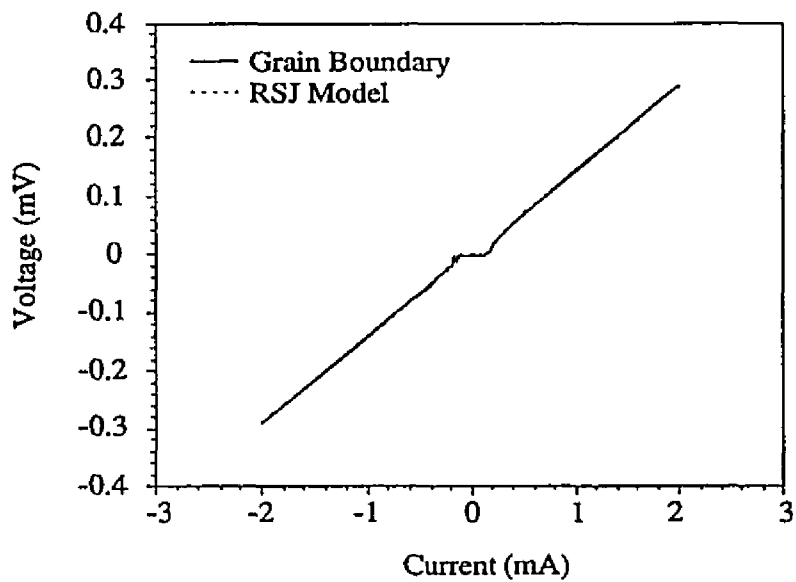


Figure 5.6b. I-V characteristics of grain boundary junction at 40 K.  
A RSJ model fit is shown using  $\beta_c=0$ .

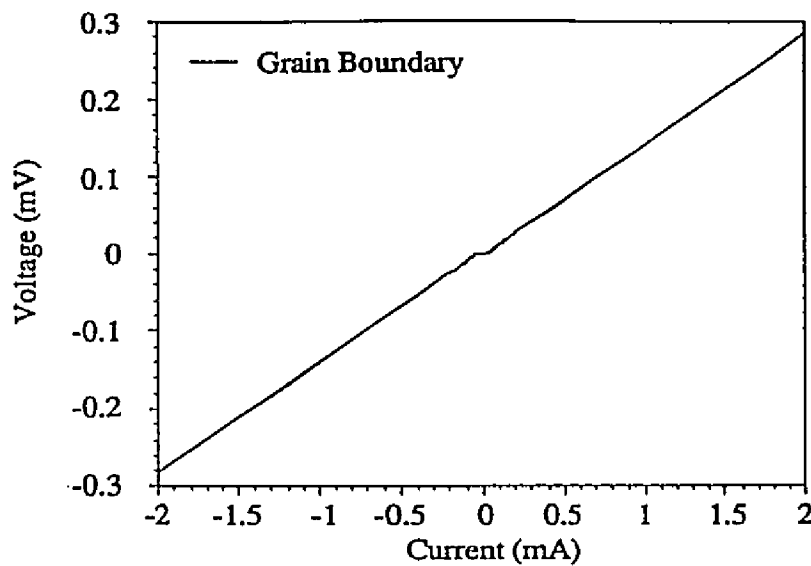


Figure 5.6c. I-V characteristics of grain boundary junction at 60 K.

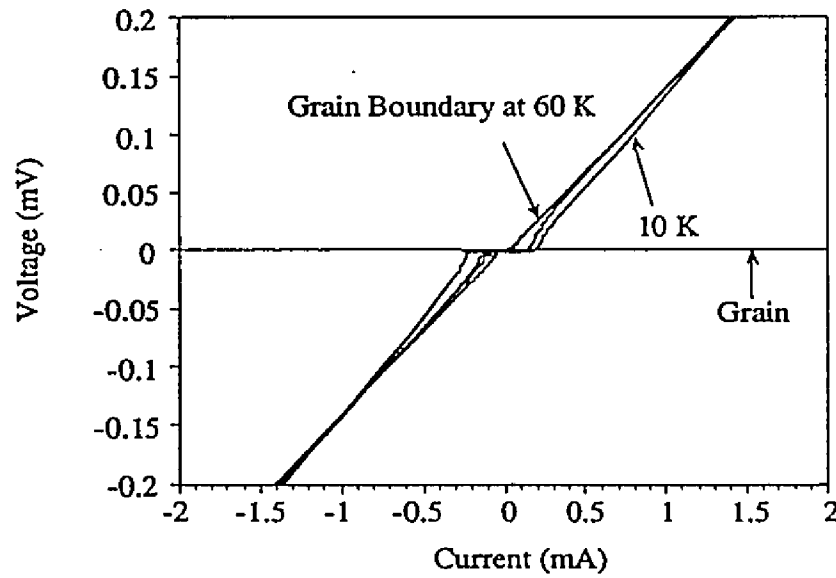


Figure 5.7. I-V characteristics of grain boundary and grain at 10 K, 40 K and 60 K.

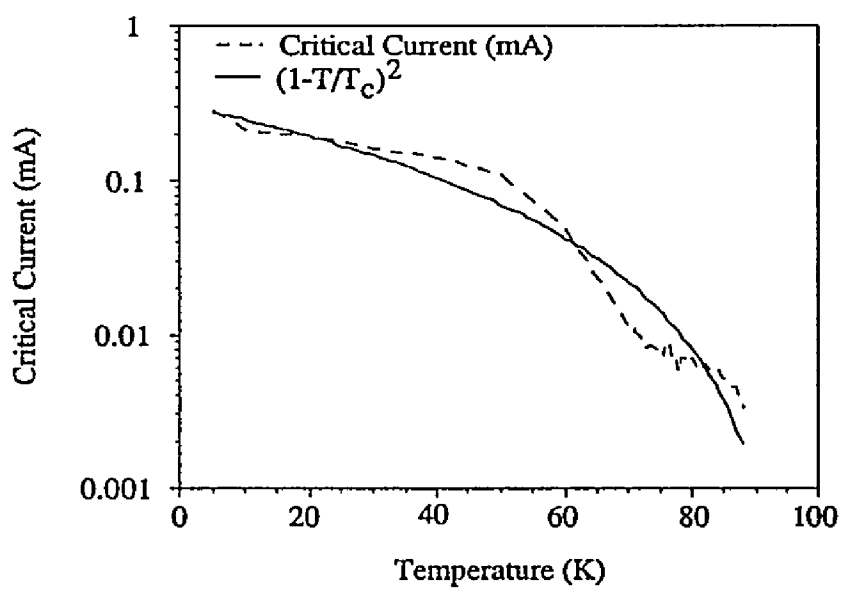


Figure 5.8a. Critical current dependence on temperature for a multilayer sputter induced grain boundary junction.

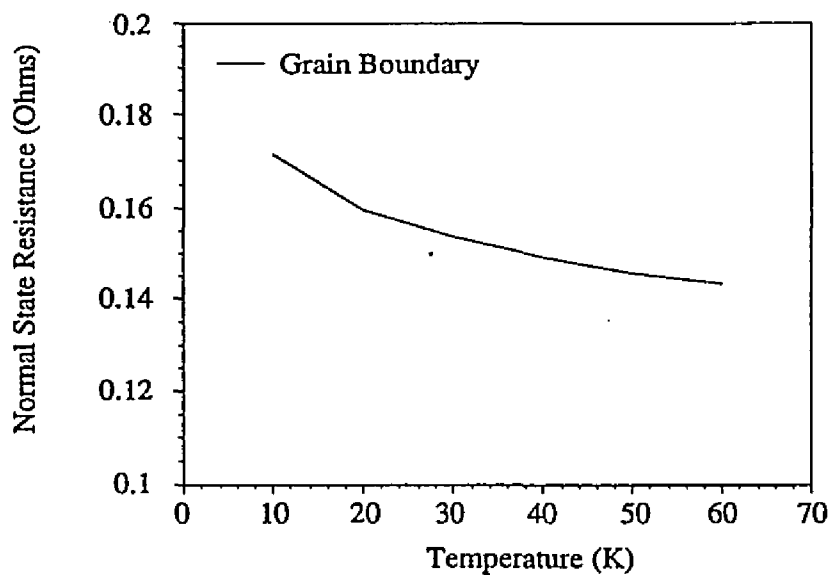


Figure 5.8b. Normal state resistance vs. temperature for a grain boundary junction.

the change in the shape as the temperature is increased. Figure 5.8a. is the critical current as a function of temperature. There is the usual decay with temperature similar to the behavior seen in the sputter induced epitaxy samples on the bulk MgO with a fit to  $(1-T/T_c)^2$ . Another notable aspect is a decrease in the normal state resistance as the temperature is increased. Figure 5.8b. is the normal state resistance as a function of temperature showing a relatively linear decrease. This was also seen in some of the sputter-induced grain boundaries on bulk MgO and in the bi-epitaxial substrates. The decreasing resistance is typical of semiconducting behavior as discussed previously indicating that there are thermally activated resistive channels parallel to superconducting channels.

#### V.2.3. Magnetic Field Behavior

The critical current was measured as a function of magnetic field. Figures 5.9 and 5.10 show the magnetic field behavior applied in two different directions. The first measurement is for the magnetic field applied parallel to the grain boundary and normal to the sample surface. The second measurement applies the field parallel to the grain boundary and parallel to the film surface. The minimum voltage is the maximum critical current (details of the measurement technique are specified in Chapter III).

The results for the field perpendicular to the film surface show the maximum critical current occurring slightly below zero field. The critical current had a relatively sharp drop off, and has relatively large fluctuations for small variations in the applied field. There appears to be minima at 8 G and -7 G, adjacent to two lobes that have a width,  $\Delta B$ , of about 3 G.

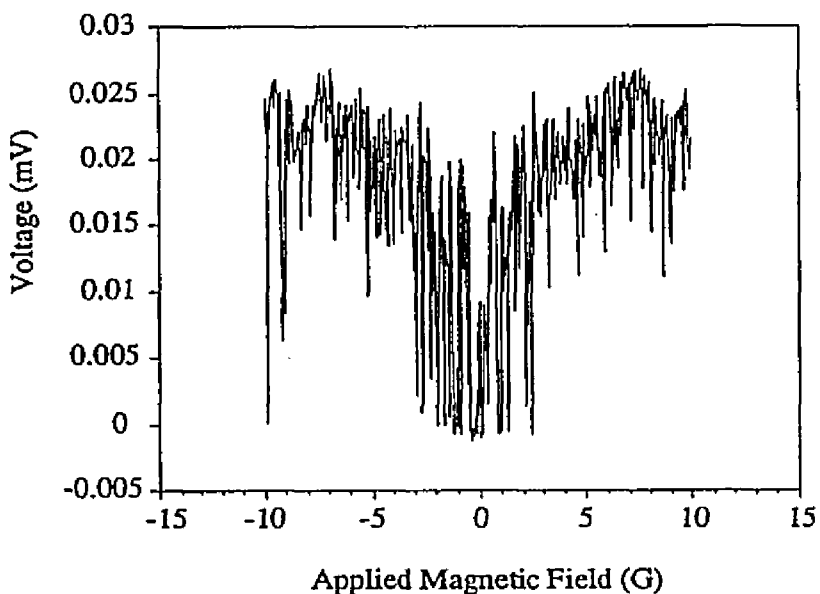


Figure 5.9. Voltage vs. applied magnetic field for a sputter induced grain boundary junction. The applied current bias is 0.2 mA.

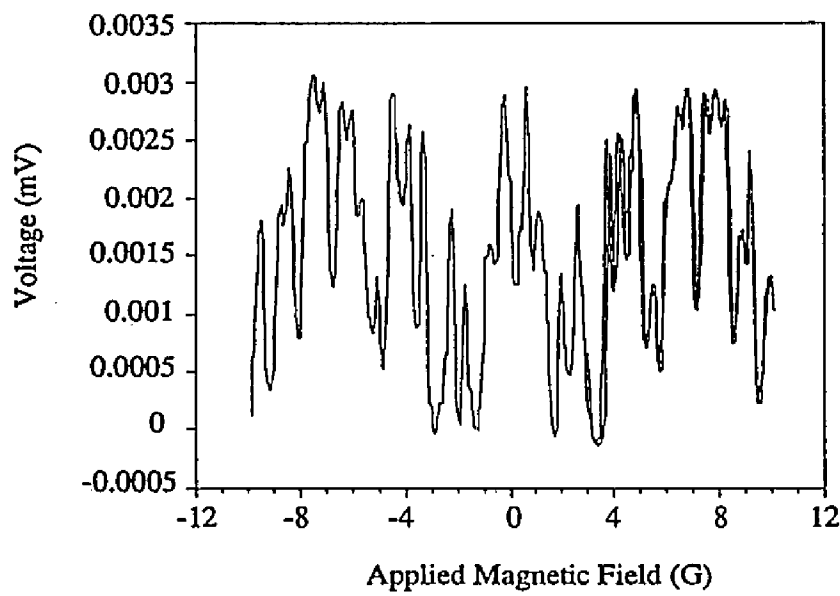


Figure 5.10. Voltage vs. applied magnetic field for field applied parallel to the grain boundary and the thin film surface.

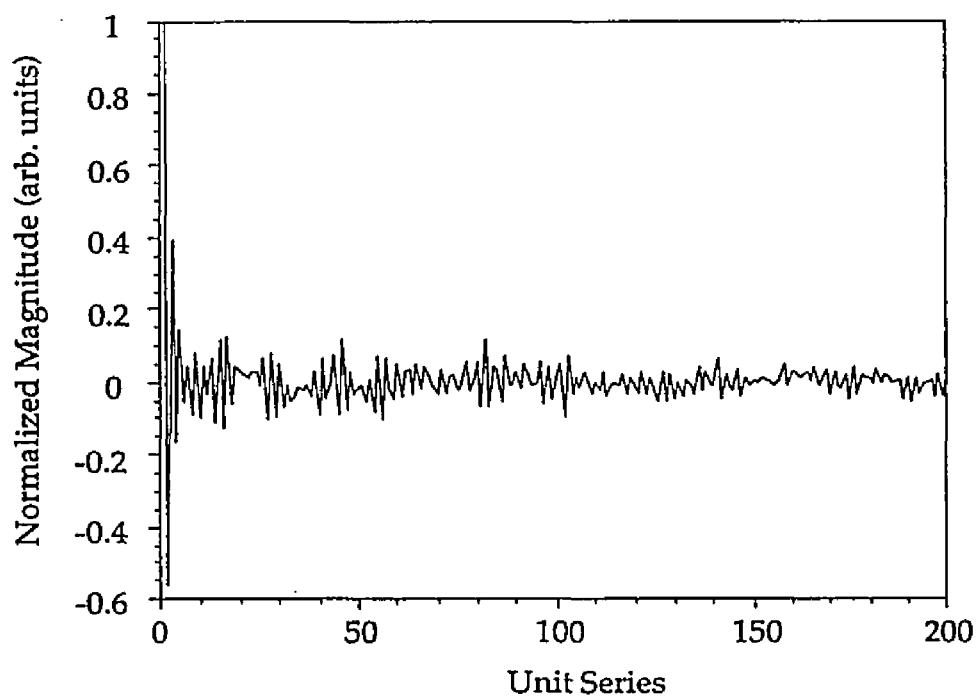


Figure 5.11. Patterson function of magnetic field data in figure 5.9.  
The pattern exhibits a Moire interference between two frequencies.

The pattern is symmetric as expected for the d.c. Josephson effect. The minima never reach zero which is consistent for a non-uniform distribution of the critical current across the junction. A slight hysteresis is observed as the magnetic field is increased and then decreased and is caused by trapped flux along the boundary. The curve is reproducible, other than the offset from the hysteresis.

The Patterson function of this data is shown in figure 5.11. The resulting function is a Moire interference pattern of two superimposed frequencies. This effect can arise from junction size effects, which cause the penetration of the field not only in the normal regions but also in the superconducting areas. This suggests a more uniform current distribution than seen in the sputter-induced epitaxy junction and is still consistent with an asymmetric parallel junction model. The data is explained in more detail in chapter VII and appendix I.

With the magnetic field applied parallel to the film surface a much smoother curve is obtained. The lack of small modulations is because the "width" of the boundary is only the film thickness. Therefore the smaller modulations that correspond to larger real distances are not observed. The behavior of the junction was reproducible and did not show significant hysteresis. This suggests a non-uniform penetration of the field in this direction. Field penetration along the a-b axis would force screening currents along the c-axis. The major point is that there is penetration of the field creating a modulation in the  $I_c(B)$ .

### V.3. Conclusions

Multilayered sputter induced grain boundary junctions were formed on (100) MgO thin films deposited on (100) LaAlO<sub>3</sub>. This proves that the sputter

induced epitaxy technique is not linked to the bulk substrate surface properties that significantly differ from a deposited thin film. There are no inherent barriers to improving the transport properties of these junctions to those of the bulk sputter induced junctions. The improvement in properties should come with higher quality films that are already being made.

There are several important technological implications of junctions formed on multilayers. The major implication is that sputter induced epitaxy grain boundary junctions can be formed on virtually any substrate that a high quality epitaxial (100) MgO film can be deposited. The MgO thin films in this experiment are at least 1000 Å thick, so there should not be any bulk substrate effect on the YBCO film. Using different substrates simplifies integration of grain boundary junctions into other materials systems that are incompatible with bulk MgO substrates. The technique maintains all the advantages of the sputter induced junctions on the bulk substrate discussed previously including versatility, reproducibility and simplicity. For multilayers it is also very important that the technique is planar for subsequent film depositions. Other multilayer systems are currently being explored including GaAs and SrTiO<sub>3</sub> bulk substrates.

Ultimately if the ion implantation mechanism is better understood and can be utilized in a different materials system, the technique can in principle be used to control epitaxy in other multilayer materials. Simple control of epitaxial relations for multilayered designs can be potentially extremely valuable, such as for ferroelectric materials in controlling domain size. The technology uses standard industry thin film growth equipment (OMCVD growth technique and a low voltage ion source) that can easily be modified and scaled for production.

## **VI. Bi-Epitaxial Grain Boundary Junctions**

The bi-epitaxial process was developed by Conductus as a method to form thin film grain boundaries in YBCO. These junctions were used in SQUIDs as one of the first commercial products available using the high-T<sub>c</sub> materials. This technique (described in more detail in sections II.4 and III.2.1) uses a seed and buffer layer to create two different epitaxial conditions on a substrate for a deposited YBCO thin film. The bi-epitaxial boundaries are 45° [001] tilt grain boundaries that have the same misorientation as the sputter induced epitaxy junctions discussed previously.

Two sets of grain boundaries, one grown by POMBE and one grown by pulsed laser deposition (PLD), are compared. Individual grain boundaries were isolated for direct transport measurements, subsequently, the same grain boundaries measured were thinned for TEM and HREM microstructural analysis. The two different growth techniques yielded samples with resistive and superconducting boundaries. The transport properties are directly related to the microstructure to gain an understanding of the grain boundary weak link behavior.

### **VI.1. Thin Film Growth**

A set of bi-epitaxial substrates were made with 100 μm spaced parallel grain boundaries. The junctions were designed so that the transport properties of two grain boundaries on the same sample as well as the grain in between could be measured. The 100 μm spacing also allowed an opportunity to

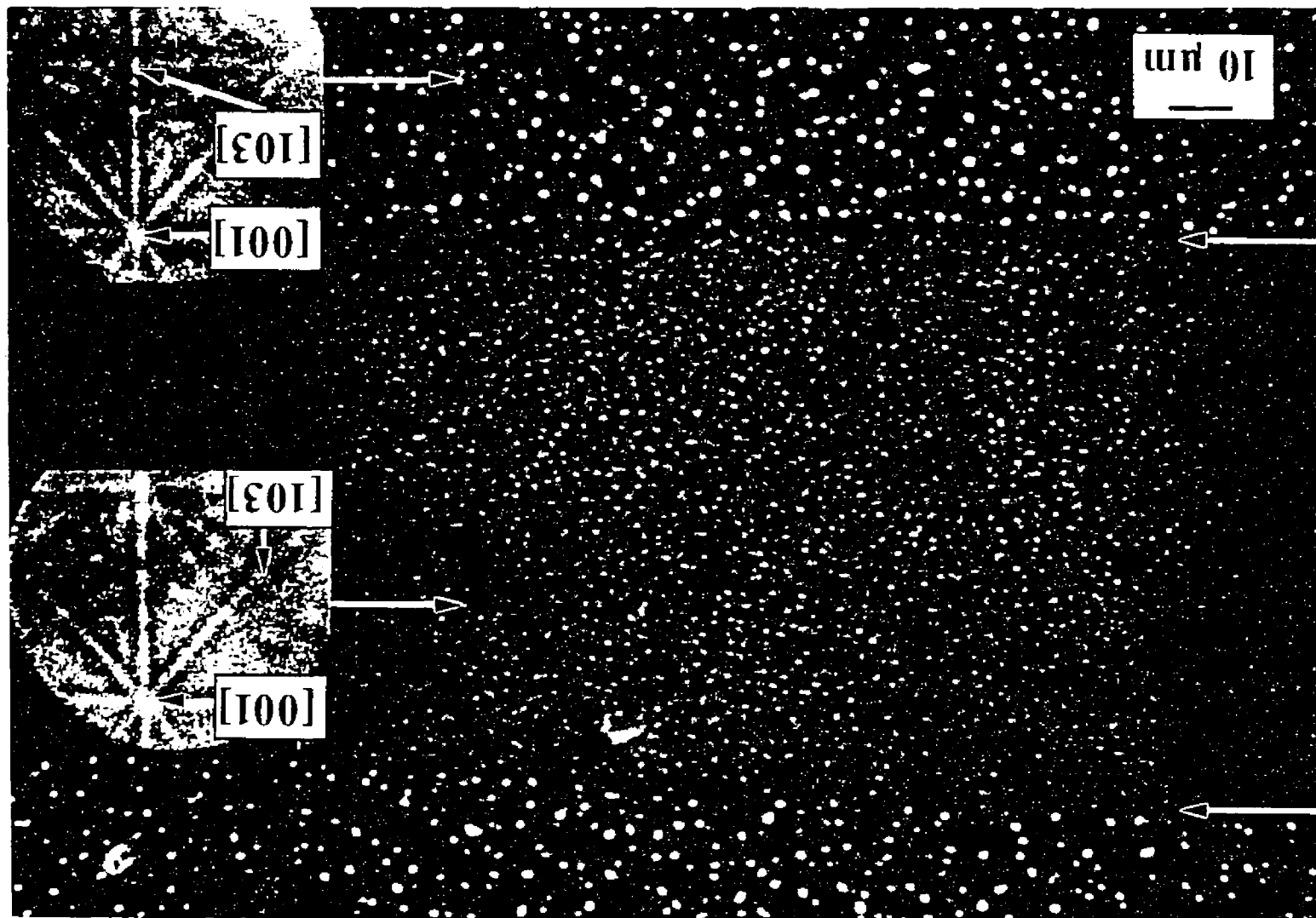
successfully make an electron transparent sample of the measured boundaries. YBCO thin films were deposited using POMBE (grown by D.B Buchholz, K.A. Dean and R.P.H. Chang from Northwestern University) and PLD (grown by G. Zaharchuk and K. Char from Conductus) for comparison of growth techniques. These techniques are described in more detail in sections II.2.4.1 and III.2.2.

All of the samples were optically reflective indicating good quality film. Higher magnification images, using the SEM, showed that the film surface structure varied significantly from sample to sample. Figure 6.1a. is a secondary electron image of a POMBE grown bi-epitaxial grain boundary junction. The two inset EBSP diffraction patterns confirm that the films are all [001] epitaxial. The [103] axis is shown to rotate by 45° about the [001] indicating a grain boundary formed where the grains meet.

The two grains have significant precipitation of copper rich precipitates. On these substrates, for the bi-epitaxial process, one of the grains is grown on CeO<sub>2</sub> and the other grain is grown on SrTiO<sub>3</sub>. As shown in figure 6.1, the precipitation varies depending on which substrate material the YBCO film is grown. Figure 6.1b shows a sample with a high density of smaller precipitates on the SrTiO<sub>3</sub> region. In other samples this condition was reversed, and the higher concentration of precipitates formed on the CeO<sub>2</sub> (figure 6.1c-d). The precipitates also appear to line up along the grain boundary, which proves to be detrimental for transport properties (see figure 6.1d). The variation in the surface morphology between the grains on the different substrate material, is of significant concern. The growth conditions necessary to optimize the surface smoothness on SrTiO<sub>3</sub> is different from those needed to grow smooth films on CeO<sub>2</sub>. Certain conditions can minimize this effect, but the two grains will

Figure 6.1a. SEM image of two parallel bi-epitaxial grain boundaries 100  $\mu\text{m}$  apart. The inset backscattered electron Kikuchi patterns confirm the 45° rotation about [001]. The difference in precipitation in the two grains is due to the substrate materials used.

245



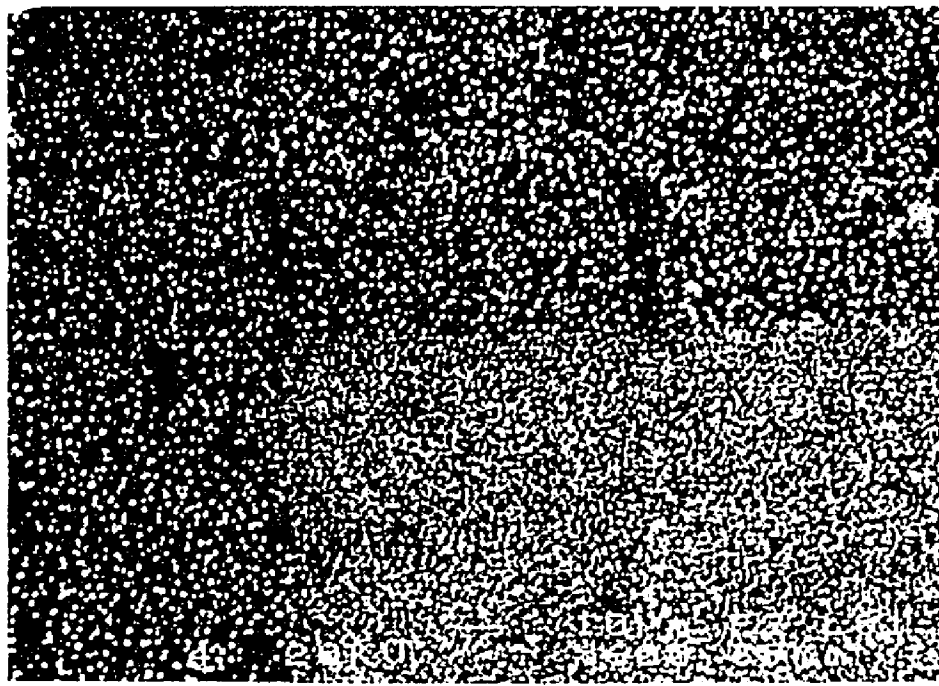


Figure 6.1b. Secondary electron image of a POMBE grown bi-epitaxial grain boundary junction. The density of precipitates is higher in the YBCO grown on the cerium oxide substrate region.



Figure 6.1c. A secondary electron image of a set of bi-epitaxial grain boundary junctions. The higher concentration of smaller precipitates are in the YBCO grown on the strontium titanate regions of the substrate.

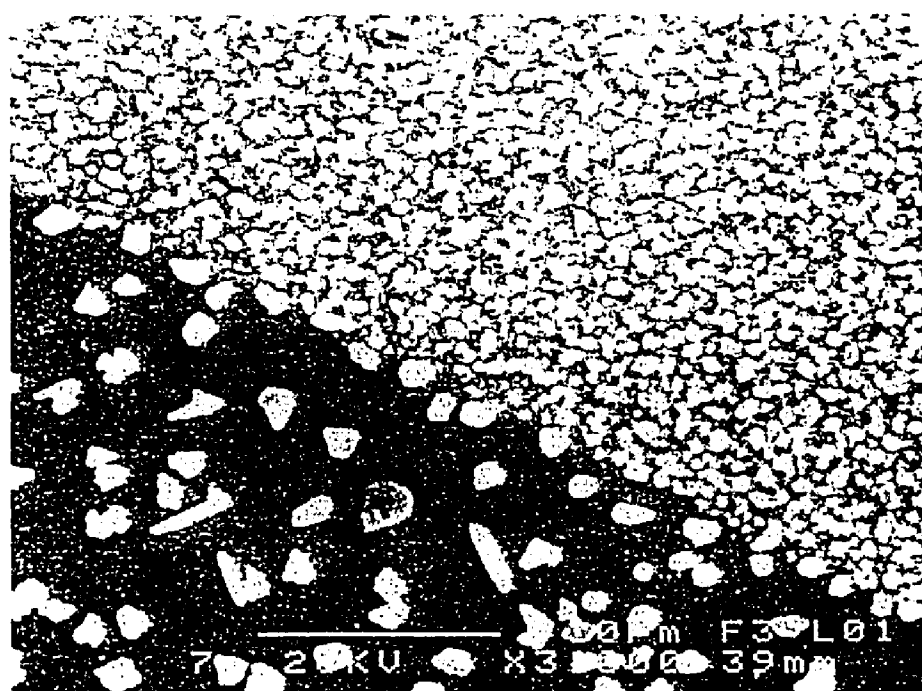


Figure 6.1d: A secondary electron image of a bi-epitaxial grain boundary junction. The higher concentration of precipitates is in the YBCO grown on the strontium titanate.

generally have different surface structures. The implications of the different grain qualities are manifested in the transport characteristics which are discussed below.

## VI.2. Transport Properties

Individual grain boundaries were isolated for cryogenic transport measurements as discussed in section III.2.3. The grain boundaries were made so that two separate grain boundaries could be measured at one time, as well as the grain in between. The following section discusses the transport properties of the bi-epitaxial junctions and in particular highlights the differences between the POMBE grown and the PLD grown samples.

### VI.2.1. Resistance-Temperature Characteristics

Figures 6.2a-c. show the R-T behavior for a POMBE grown thin film junction. The grain has a normal linear decrease from room temperature to the transition temperature. The transition temperature for this sample is 90.5 K, with a width of approximately 1 K. Both the high transition temperature and the narrow transition width indicate that the grain is of high quality. The grain boundaries, however, have a starkly different behavior from the grain and from other grain boundaries measured. The  $dR/dT$  above the transition for the grains is almost flat (as opposed to the positive slope seen for the grain). This is particularly intriguing since the grain clearly has a linear decrease in resistance with temperature. At the transition temperature, there is a sharp decrease in resistance that can be attributed to the transition in the grains on either side of the boundary. Below the critical temperature of the grain, there is an increasing

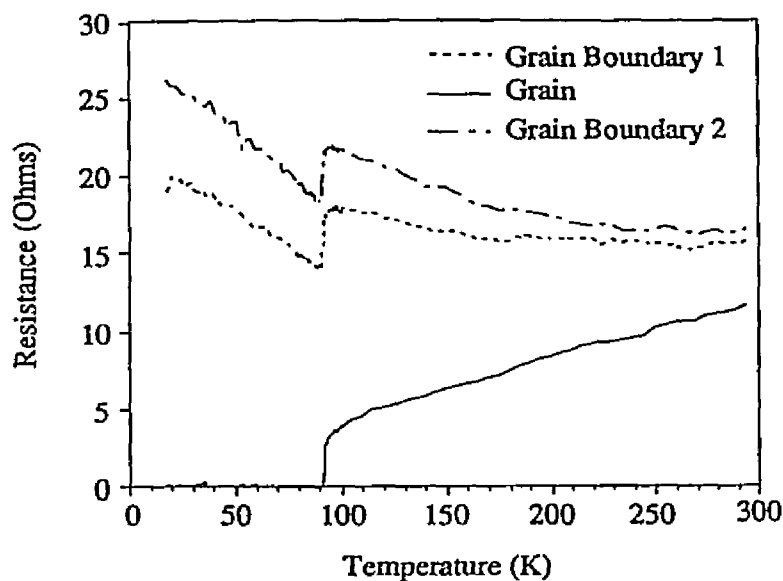


Figure 6.2a. R-T curve for a POMBE grown bi-epitaxial grain boundary with resistive behavior.

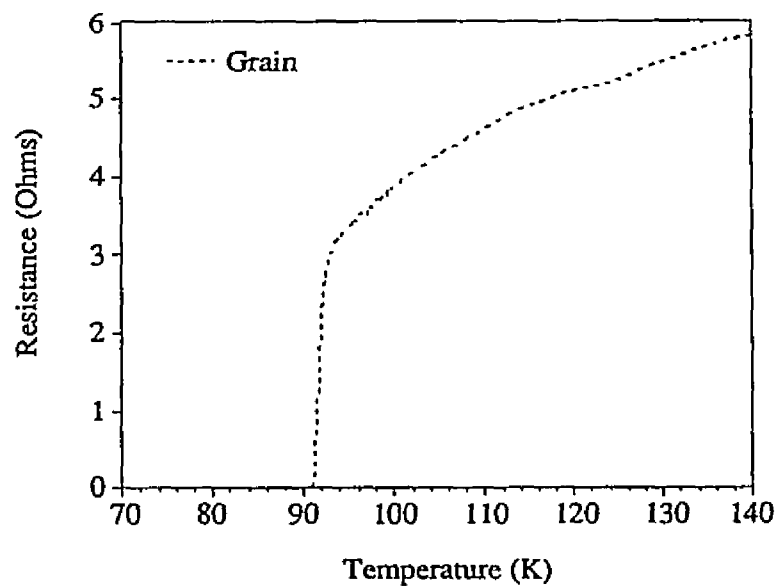


Figure 6.2b. Superconducting transition of the grain with a  $T_c = 90.5$  K.

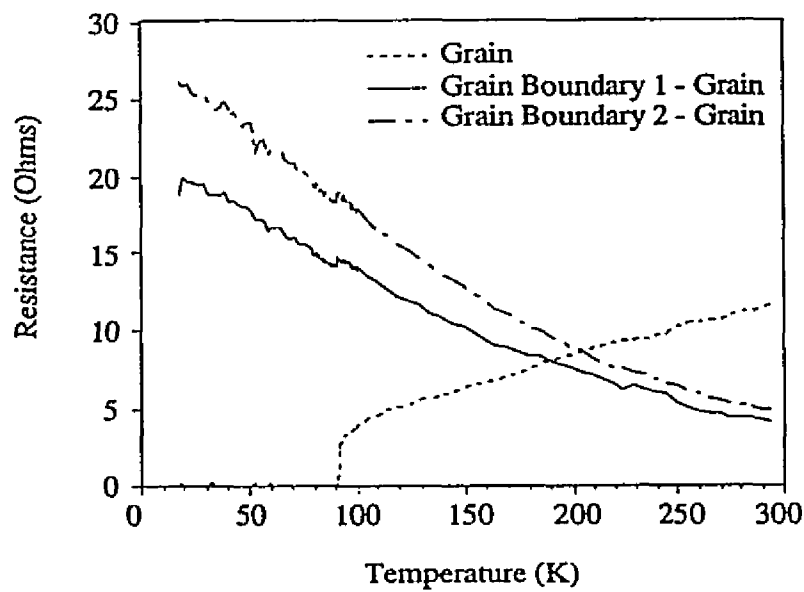


Figure 6.2c. R-T curve of resistive grain boundaries with grain resistance subtracted out.

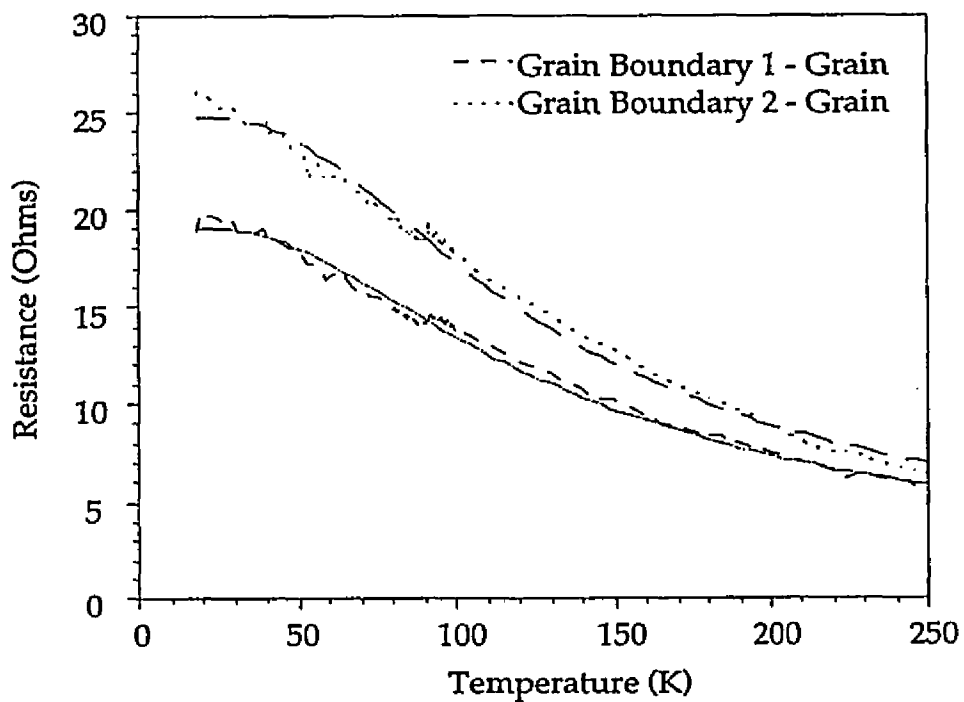


Figure 6.2d. R-T curve of grain boundaries with grain resistance removed.  
The curve fit is with a series of thermally activated conduction paths.

resistance with decreasing temperature, which is linear to the lowest temperature measured.

In the measurement, the channel that measures the voltage drop across the grain boundary consists of the two grains on either side of the boundary as well as the boundary itself. Below  $T_C$  the grains are superconducting so all the resistance is from the grain boundary. Above the grain  $T_C$ , the resistance of the measurement channel across the grain boundary is the sum of the two grains and the grain boundary. If the two grains are assumed to have approximately the same resistivity, the grain resistance can be subtracted from the total measured resistance to determine the grain boundary resistance. Figure 6.2c shows the grain resistance removed from the channel across the grain boundary. There is a linear decrease in resistance from 20 K to 175 K. This indicates that there is a thermally activated transport process because of the decreasing resistance with increasing temperature at the grain boundary and suggests semiconducting type behavior. This behavior is well modeled with a set of thermally activated parallel conduction paths along the boundary (see discussion in section IV.2.1.1). The fit to this model gives values for  $R_0$  (24.78 Ohms and 19.05 Ohms),  $\beta$  (0.0182/K and 0.0151/K), and  $E_{min}$  (0.0123 eV and 0.0111 eV) for each of the boundaries. The magnitude of  $R_0$  scales with  $\beta$ , indicating that the higher the 0 K resistance, the more parallel conduction channels exist. The R-T behavior indicates that there is no superconducting path that could support the measuring current (1  $\mu$ A) at any temperature. These grain boundaries will be referred to in this text as "resistive".

One sample used for 1/f noise measurements described below had a transition at low temperature to the superconducting state. The resistance of the

grain boundary below  $T_c$  was increasing with decreasing temperature as seen in other POMBE samples, but at very low temperatures and measuring currents, a transition was seen. This indicates that the thermally activated channels lie in parallel to superconducting paths. The total number of superconducting channels is inversely proportional to the amount of superconducting regions, as can be seen by the different normal state resistances of the superconducting grain boundaries and the resistive boundaries. This will be discussed in more detail in chapter VII and appendix I.

The R-T behavior of the PLD grown samples is markedly different from the POMBE grown samples. Figures 6.3a-c. show the R-T characteristics of a PLD grown bi-epitaxial junction. The grain and the two grain boundaries measured all have linearly decreasing resistance with temperature above  $T_c$  (see figure 6.3a.). The grain measured has a relatively abrupt superconducting transition onset at 86.5 K, and goes superconducting at 85 K. The grain boundaries both have a transition onset at 88.5 K, where the resistance changes from 6 ohms to 4 ohms. There is a second transition, or "hump", at 86.5 K where the resistance drops to 0.5 Ohms (see figure 6.3c.). The transition then has a foot-like structure, indicating a finite grain boundary resistance down to almost 40 K, before going fully superconducting (see figure 6.3b.).

The transition of the grain boundary has two separate onsets and a foot-like structure at the base of the transition. The first onset is from the grain on one side of the grain boundary (which in this situation is not measured separately). It has a  $T_c$  of 88 K, which is 3 K higher than the other grain. The hump in the grain boundary transition is due to the transition onset of the second grain (which is measured) at 86.5 K. The two grains clearly have

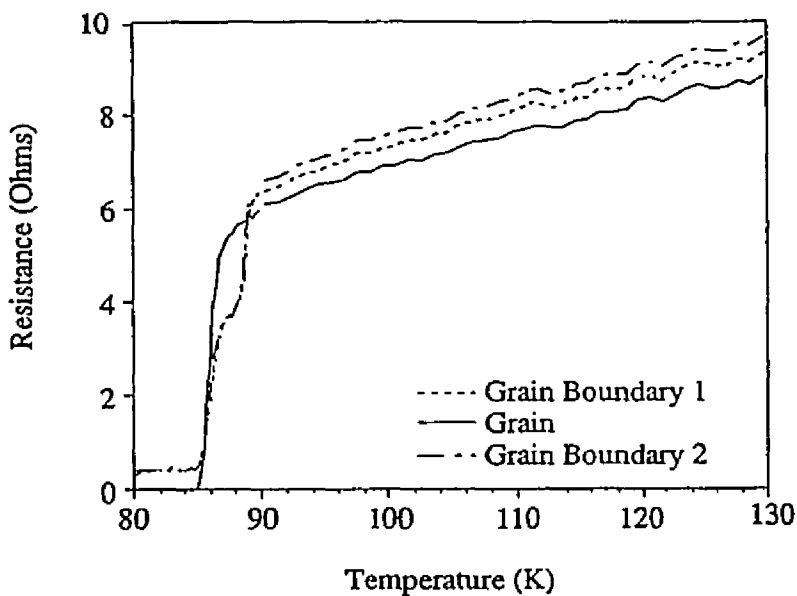


Figure 6.3a. R-T curve of PLD grown bi-epitaxial junctions.

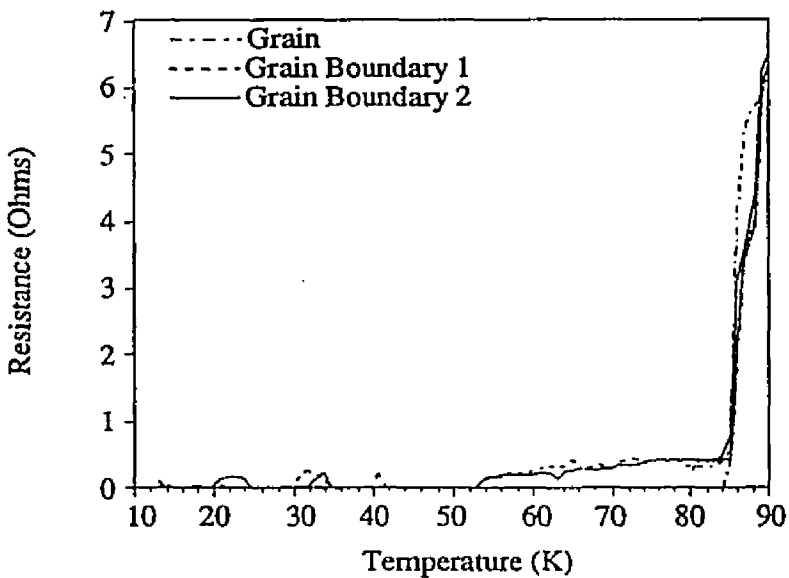


Figure 6.3b. R-T curve showing foot-like structure due to TAPS.

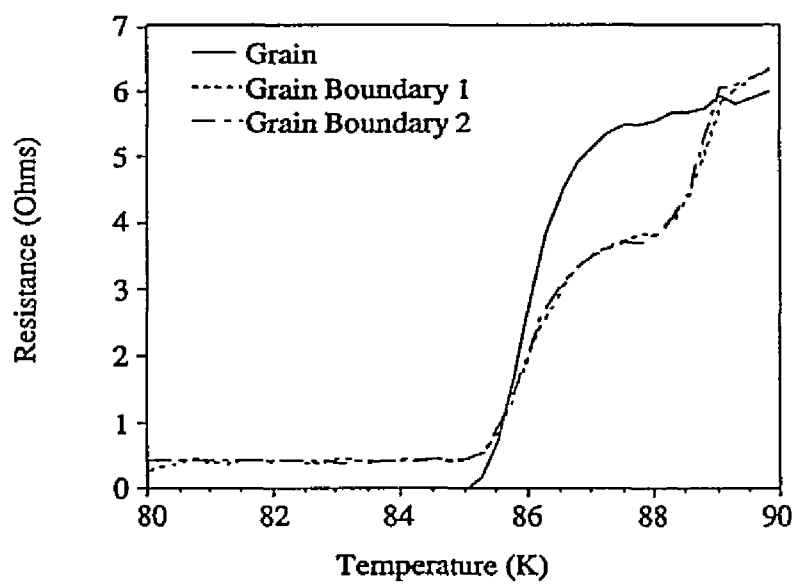


Figure 6.3c. Superconducting transition of grain and double "hump" transition onset in grain boundaries.

different transition temperatures, which can be easily understood from the microstructural variation observed in the SEM. At temperatures below which both the grains go superconducting (85 K) the remaining resistance is directly attributable to the grain boundary. The resistance can be explained by thermally activated phase slippage (Gross *et al.* 1990). The foot-like structure indicates that the grain boundary cannot support a 1  $\mu$ A supercurrent down to 40 K. For this type of critical current a finite resistance due to TAPS is expected down to 40 K due to the small coupling energy of this junction relative to the thermal energy.

It should be noted that these junctions were highly sensitive to magnetic fields and trapped flux (which will be detailed below). Any remnant field in the system caused different I-V behavior in the samples due to trapped flux along the boundary (potentially from asymmetric critical currents along the boundary). The R-T measurements were not optimized for maximum critical current (the maximum  $I_c$  often was not at "zero" field despite great care in isolating the sample).

#### VI.2.2. Current-Voltage Characteristics

The current-voltage characteristics were measured for the grains and the grain boundaries as was described previously in chapter III. The I-V characteristics of the resistive sample had linear ohmic behavior even at the lowest temperature measured, therefore will not be discussed further. Typical I-V characteristics for a superconducting bi-epitaxial sample is shown in figure 6.4. Weak link behavior is seen as the grain boundary has a critical current of about 0.2 mA (2000 A/cm<sup>2</sup>) and the grain remains superconducting. The grain

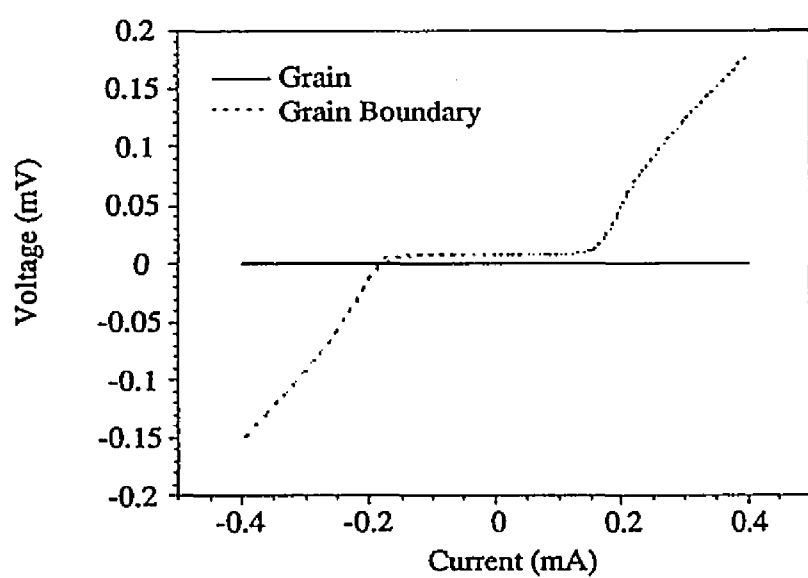


Figure 6.4. I-V characteristics of PLD grown bi-epitaxial grain boundary junction exhibiting weak link behavior at 5 K.

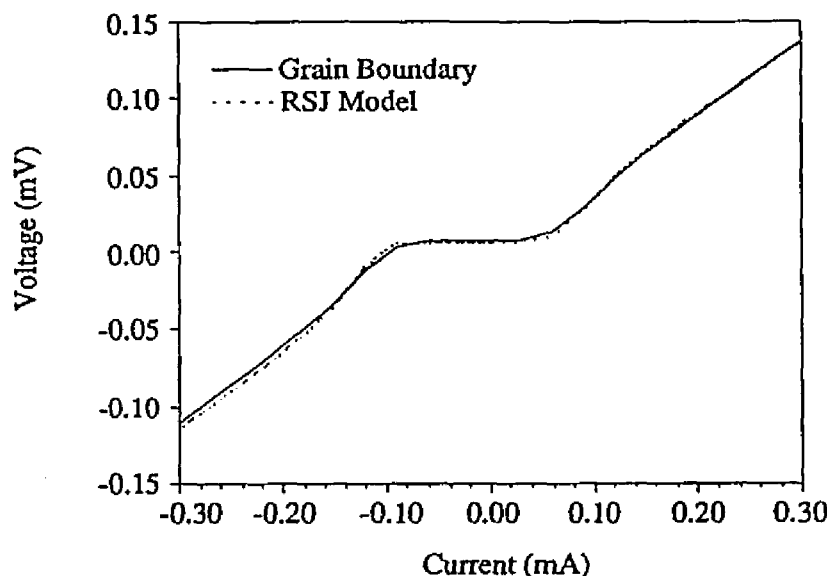


Figure 6.5a. I-V characteristics of bi-epitaxial junction at 9.6 K and 0.24 G applied magnetic field. RSJ model fit with no capacitance.

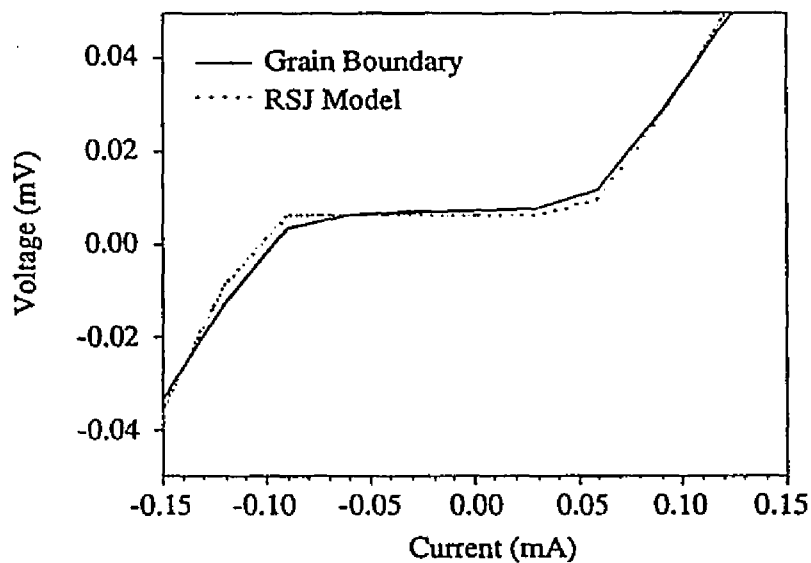


Figure 6.5b. Enlarged transition region showing slight deviations from the RSJ model.

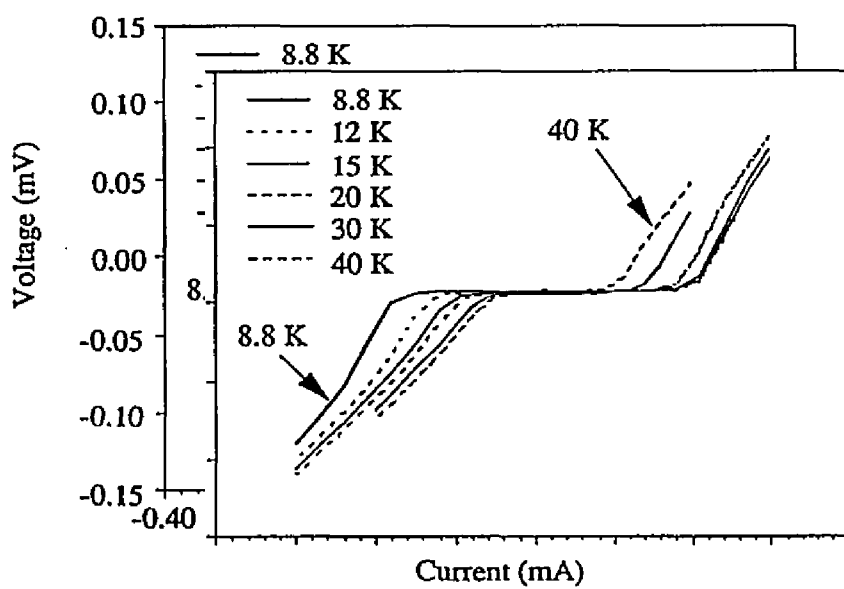


Figure 6.6. I-V characteristics of a bi-epitaxial grain boundary junction at a series of temperatures from 8.8 K to 40 K.

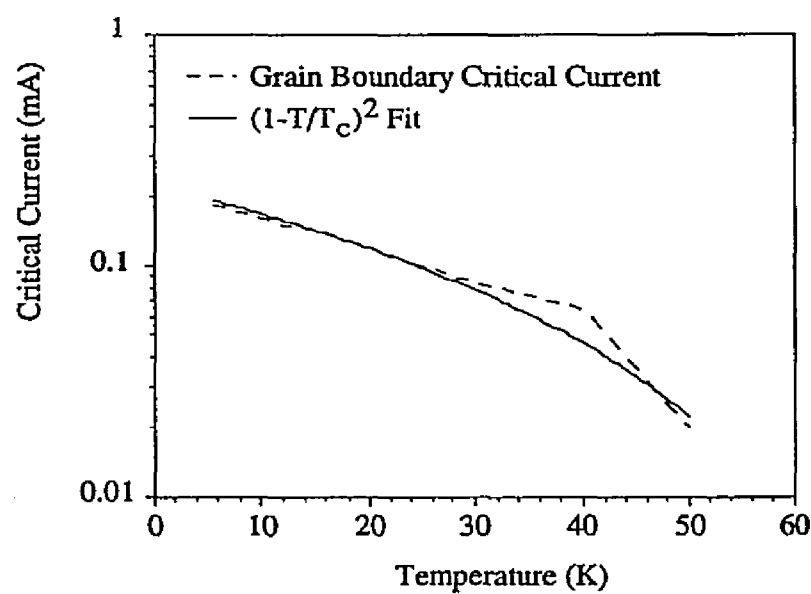


Figure 6.7. Critical current vs. temperature for a grain boundary junction fitted with a  $(1-T/T_c)^2$  fit.

critical current was never approached because resistive heating would destroy the boundary in the process. Typically the I-V curve was asymmetric about zero current due to trapped flux along the boundary (see chapter VII and appendixI).

The boundary has RSJ-like behavior at low temperatures as is modeled in figures 6.5a-b. The best fit is obtained with no capacitance in the junction and a slight thermal offset added. There is a slight deviation of the RSJ model near  $I_c$  due to rounding of the critical current onset from flux motion along the boundary (Gross 1992)

The I-V characteristics for several temperatures are shown in figure 6.6. The critical current density varies from  $2000 \text{ A/cm}^2$  at 5 K to  $700 \text{ A/cm}^2$  at 40 K. At 50 K the I-V curve is already significantly rounded due to TAPS and a critical current density can not be measured accurately. The critical current as a function of time is plotted in figure 6.7. It is fitted relatively well with a  $(1/T_c)^2$  fit. Deviations from the fit are from not having sufficiently accurate  $I_c$  measurements, and the inability to accurately determine  $I_c$  above 40 K, with the onset of TAPS.  $I_c R_n$  products range from  $95 \mu\text{V}$  at 5 K to  $28 \mu\text{V}$  at 40 K, which is a very low value due to the small critical currents of the junction. The normal state resistance only decreases slightly from 5 K to 40 K.

### VI.2.3. Magnetic Field Behavior

The bi-epitaxial grain boundary junctions were extremely sensitive to applied magnetic fields as small as 0.01 G. The magnetic field strongly affected the I-V characteristics of the boundary as shown in figures 6.8a-b. The two I-V curves are of the two grain boundaries in the same film 100  $\mu\text{m}$  apart. At -1.25 G (T=5 K) grain boundary 1 has a critical current of only 0.015 mA and grain

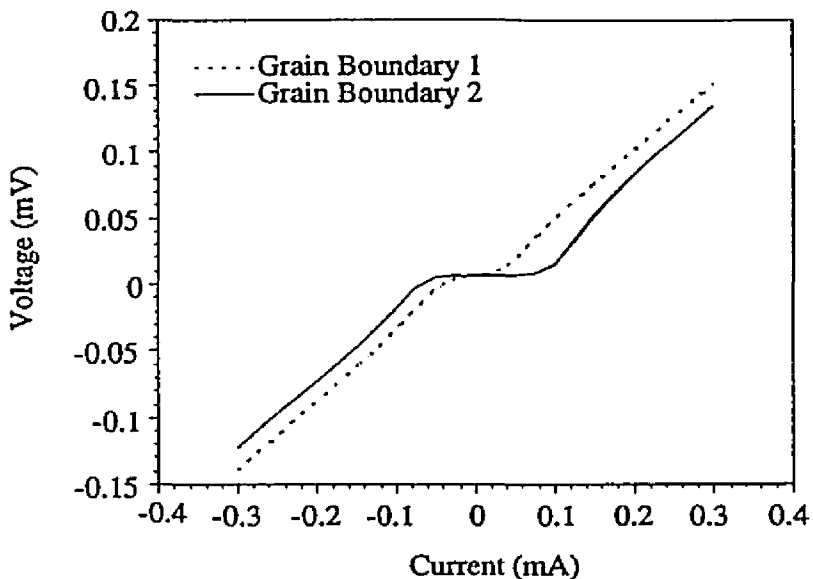


Figure 6.8a. I-V characteristics of two bi-epitaxial boundaries on one sample showing markedly different behavior. Measurement at  $T=5$  K, applied magnetic field =  $-1.25$  G.

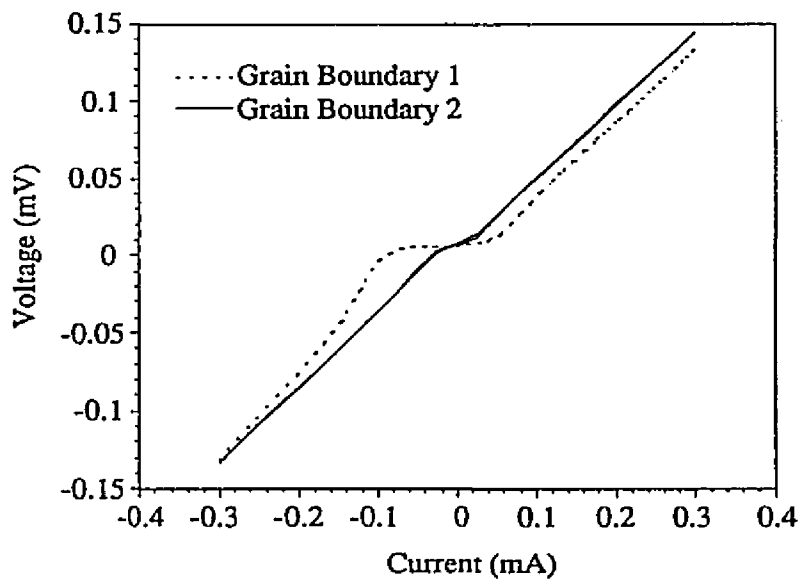


Figure 6.8b. I-V characteristics of same boundaries as in figure 6.8a. at  $T=5$  K, applied magnetic field =  $1.5$  G.

boundary 2 has an  $I_c$  of 0.8 mA. The same boundaries at 1.50 G (T=5 K) reverse behavior with grain boundary 1 having a critical current of about 0.08 mA and grain boundary 2 being almost fully resistive. The different behavior in the two grain boundaries is due to the inhomogeneities of the critical current along the boundary causing non-uniform penetration of the magnetic field. The non-uniformity is also not reproducible from grain boundary to grain boundary, which is why the applied field behavior varies significantly even on the same chip. If the inhomogeneity along the boundaries is not reproducible, the two boundaries behave completely differently. A model of the grain boundary that describes these characteristics is suggested in chapter VII and appendix I.

The dependence of the critical current on the applied magnetic field was measured using techniques described in chapter III. Figures 6.9-6.12. are plots of the voltage across the boundary as a function of applied magnetic field, perpendicular to the film surface with a current bias. The voltage is inversely proportional to the critical current, so the maximum critical current is at the minimum measured voltage.

Figure 6.9 is a plot at T=5 K using 0.01 G steps from 0 to 1 G. The critical current has significant oscillations even for very small applied fields. This is not a clean Fraunhofer pattern as expected for a junction with homogeneous current flow. Therefore this is an indication that the current flow is non-uniform across the grain boundary. From I-V measurements at various points along the curve it is known that the grain boundary is never fully resistive. The slope of the I-V curve changes significantly, but there is always some transition. The fact that the critical current never goes to zero is also indicative of inhomogeneous current flow across the boundary. This type of pattern could also be from a

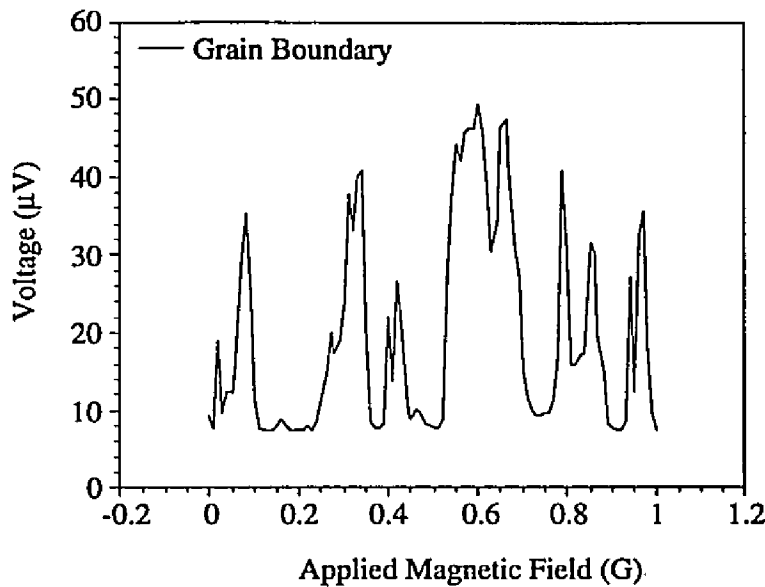


Figure 6.9. Voltage vs. applied magnetic field perpendicular to the film surface stepped in 0.01 G increments.

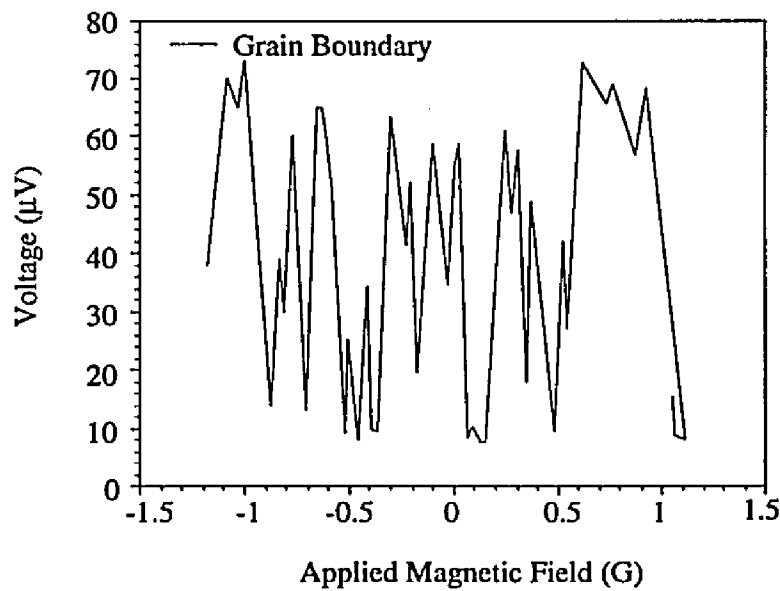


Figure 6.10. Voltage vs. applied magnetic field perpendicular to the film surface from -1 G to 1 G.

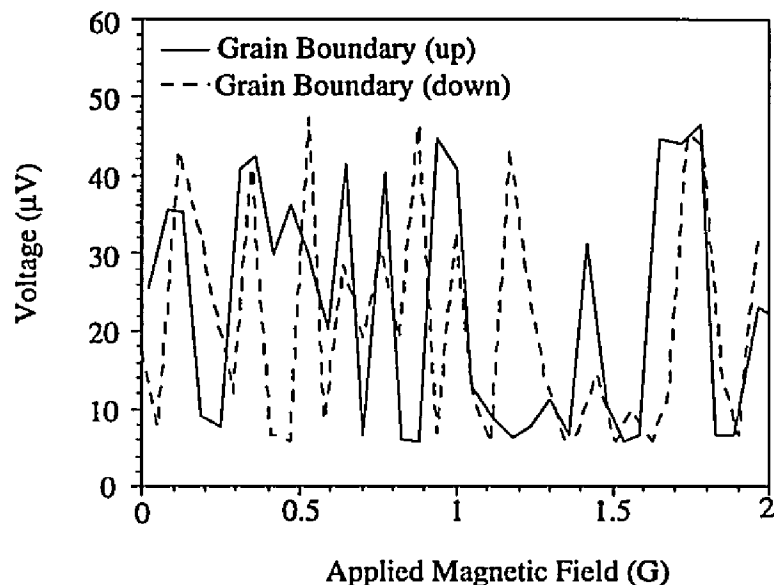


Figure 6.11. Voltage vs. increasing and decreasing applied magnetic field.

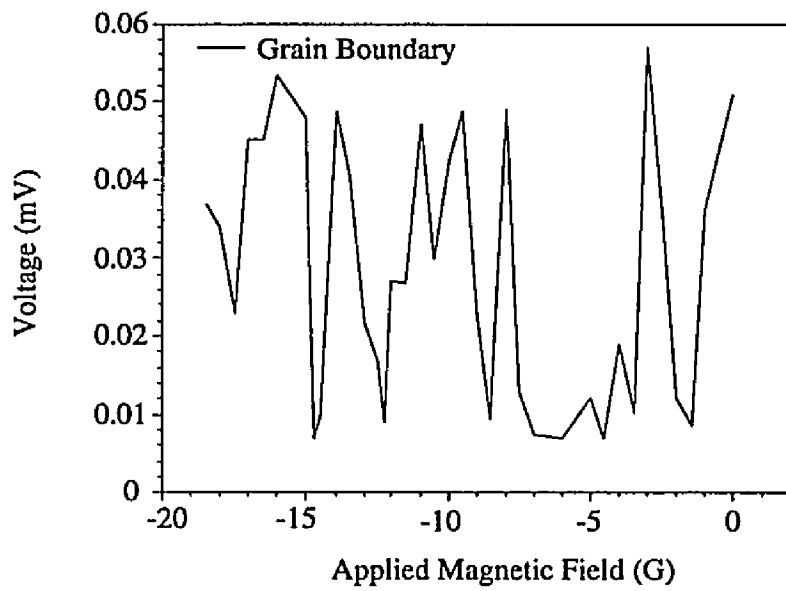


Figure 6.12. Voltage vs. applied magnetic field to -18 G.

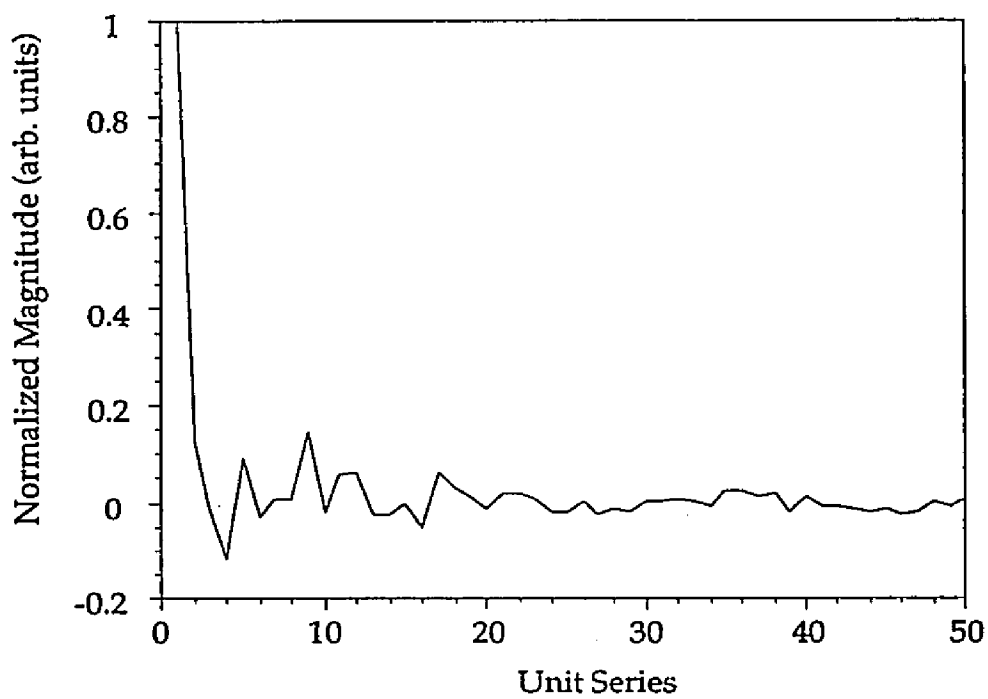


Figure 6.13. Patterson function of magnetic field data in figure 6.9.

series of junctions in parallel along the junction if self-inductance, junction asymmetry, size effects and non-uniform junction penetration are included. The Patterson function of this junction does indicate a frequency in the  $I_c(B)$  behavior (see figure 6.12b). The frequency is due to very small oscillations (0.11 G) that also suggest many junctions in parallel with varying critical currents (a detailed explanation is in chapter VII and appendix I). Figure 6.10 is the magnetic field behavior from 1 to -1 G in 0.05 G steps. The basic shape is similar to figure 6.9, and again shows strong oscillations in the critical current, but does not have a periodicity because there was not sufficient resolution in the measurement. The maximum critical current lies at approximately 0.2 G (this is where some of the I-V characteristics were taken in the previous section).

A set of measurements with increasing and decreasing applied magnetic field are shown in figure 6.11. There is a difference in the two plots for two reasons. First a hysteresis can be detected by some features being offset. Second trapped flux actually modifies some of the peaks in the curve. Figure 6.12 is a plot to somewhat higher fields (18 G) taken with a coarser magnetic field step (0.5 G). The basic fluctuations are still present in the curve showing strong oscillations in the critical current. The magnitude of the variation in the critical current at higher fields does not change relative to the oscillations at low field.

#### VI.2.4. Noise Measurements

A set of low frequency ( $1/f$ ) noise measurements were made on these resistive and superconducting grain boundaries by Liu *et al.* (Liu *et al.* 1995) The noise power was shown to decrease with increasing temperature for all the grain boundaries measured. The dependence of the noise power for a tunnel

junction with defects is attributed to changes in the effective charge carrier density or junction transmission at the barrier.(Liu *et al.* 1995) This type of a model suggests temperature-independent noise power behavior, or slightly increasing noise power with increasing temperature, which was not seen in the grain boundaries.

The noise power behavior is modeled with thermally activated parallel conduction paths at the grain boundary. The same model is used as for the normal state resistance with a temperature independent value and a set of parallel conduction paths (eq. 4.5).

$$R_{gb} = \frac{R_0}{1 + \beta T \exp\left(\frac{-E_{\min}}{k_B T}\right)} \quad (4.5)$$

It is assumed that there are uncorrelated fluctuations for both the temperature independent and temperature dependent processes. The normalized grain boundary noise power is then given by eq. 6.1:

$$\gamma_0 \left( \frac{R_{GB}(T)}{R_0} \right)^2 \quad (6.1)$$

where  $\gamma_0$  is the relative conductance fluctuations for the temperature independent channels. Therefore the noise power is dependent on the grain boundary normal state resistance. The model fits the data well for both the superconducting and resistive grain boundary junctions. The resistive junction has decreasing noise with increasing temperature due to the fluctuations at the boundary. The superconducting junction also had a negative slope in the

normal state until the fluctuations from the grain exceeded the noise fluctuations from the boundary. The major difference between the resistive and superconducting boundaries is the magnitude of the noise power, which is related to the total number of parallel channels. A comparable grain boundary free epitaxial thin film has an even smaller noise power that decreases with decreasing temperature (Liu *et al.* 1994). This result indicates that there are parallel conduction paths in both the superconducting and resistive samples, with the number or size of conduction paths varying inversely with the critical current across the boundary.

### VI.3. Microstructure

#### VI.3.1. Transmission Electron Microscopy

The samples that were characterized for transport measurement were subsequently thinned for TEM analysis. Both resistive and superconducting samples were prepared in order to compare variations in the grain boundary structure. The first analysis was standard bright field/dark field imaging to determine the general microstructure of the boundary.

Several bright field images of a resistive grain boundary are shown in figures 6.13-14. The grains have a high density of (110) twins with spacings ranging from 40 nm to 100 nm. The twins compensate for the strain caused by the phase transformation from a tetragonal to an orthorhombic structure that occurs during the cooldown from the growth temperature. The high field measurements of this film indicated that the grain critical current did not diminish significantly at fields up to 6 T. This is consistent with the high twin density, where the twins can act as flux pinning sites. The rest of the grain

Figure 6.13a. Bright field micrograph of a resistive bi-epitaxial grain boundary. The two arrows indicate the ends of the grain boundary.



Figure 6.13b.Bright field micrograph of a resistive bi-epitaxial grain boundary. The arrows marked A show two different type of disruptions at the boundary. The arrows marked B show the boundary.



Figure 6.14. A region of the resistive grain boundary showing significant disruption along the boundary length.



also exhibited precipitation similar to the precipitation at the boundary, which agrees with the SEM images of the sample.

The micrographs show grain boundary meandering along the length of the film. The boundary deviates by up to 500 nm from a straight line, which is significantly more than seen in bicrystal boundaries (from 10-250 nm) (Traeholt *et al.* 1994b; Miller *et al.* 1995; Alarco *et al.* 1993). The enhanced meandering is caused for similar reasons as in the sputter-induced epitaxy samples. The first effect is from the photolithographic process used to define the boundaries in the bi-epitaxial junction (see chapter III). The photoresist mask does not produce a straight line across the sample, rather has some variation along its length. The second effect is the enhanced grain growth along the a-b directions in the YBCO film. The faster growth in these directions allows the grains to interpenetrate across the predefined patterned lines. Cross-sectional TEM analysis of bi-epitaxial grain boundaries confirms that interpenetration occurs, by observing a tilted grain boundary relative to the substrate surface (Rosner *et al.* 1992).

Several studies have confirmed meandering of YBCO on different substrates Alarco, 1993 #238)(Miller *et al.* 1995; Traeholt *et al.* 1994b; McKernan *et al.* 1992). The waviness of the boundary has been correlated to the growth rate with slower growth rates producing a smaller magnitude of waviness (Miller *et al.* 1995). By observing the phenomena on a 24° bicrystal substrate where the second orientation is not a favorable orientation for the film, the interpenetration of the grains is shown to be a generic phenomenon. Therefore the grain growth coupled with the imperfect photoresist template enhances the effect due to the two processes involved. The magnitude of the waviness in the POMBE grown bi-epitaxial sample (up to 500 nm) is several times greater than

the POMBE grown sample on a bicrystal (approximately 100 nm),(Miller *et al.* 1995) which is consistent with the idea that the grain growth and imperfect template contribute to the effect. The sputter-induced epitaxy samples also exhibited meandering on the same length scale because the boundaries are also formed with photoresist masks. The major implication of the meandering grain boundary is that the microscopic symmetry varies significantly from the macroscopic symmetry. This has implications for the transport properties as discussed in section VI.4.

The boundaries had large amounts of precipitation along their length. The precipitation was determined to be copper-rich using EDS. In this particular sample, precipitates formed at the grain boundary for over 60% of the length. The width of the precipitates at the boundary varied up to 200 nm, with an average value of approximately 40 nm. These disruptions at the boundary are much larger than the coherence length ( $\xi_{a-b} = 1-1.5$  nm) and would therefore be barriers to the supercurrent across the boundary.

The superconducting grain boundaries exhibited meandering behavior, similar to the resistive samples (see figure 6.15). The magnitude of the meandering was somewhat smaller than that of the resistive boundaries probably due to the very different growth conditions used. The major difference on this length scale, is the lack of significant precipitation along the boundary. There was an occasional precipitate, but only along approximately 10% of the boundary. The lack of precipitation significantly increases the length of the boundary that provides a direct contact between the grains.

**Figure 6.15a.** A bright field image of a superconducting bi-epitaxial grain boundary. The arrows denote similar locations in the corresponding bright field images. The arrow A is a precipitate at the boundary.

280



Figure 6.15b. A dark field image corresponding to the figure 6.15a. The arrows indicate similar positions in the micrographs.



Figure 6.15c. A dark field image of the opposing grain from figure 6.15b. The arrows indicate similar positions along the boundary. Note that the region denoted by the arrow A remains dark in both images.



### VI.3.2. High Resolution Electron Microscopy

The two different boundaries were analyzed using HREM to provide a more detailed analysis of the local grain boundary structure. Figures 6.17-18 are high resolution electron micrographs of the resistive and superconducting grain boundaries. The regions where there were no precipitates in the resistive grain boundaries the images show a narrow disordered region. This disordered region varied somewhat in width, but was approximately 1 nm wide. A structural distortion on a length scale of the coherence length could prevent transport, which supports the resistive transport properties of this sample.

The structure of the superconducting grain boundary indicates a much cleaner boundary. The boundary changes local symmetry due to the meandering, but will occasionally exhibit asymmetric facets. These facets form in the same configuration as the facets in the sputter-induced epitaxy samples. The orientation is (100) of one grain is parallel to the (110) of the adjacent grain. The facets observed only extended approximately 50 Å, which is significantly shorter than observed in the sputter-induced epitaxy samples (up to 100 nm). The asymmetric facets are well structured up to the boundary, but other regions along the boundary appear to be less ordered. Some areas along the boundary show overlap between the adjacent grains as expected from the cross-sectional TEM work that indicates an inclined grain boundary (Rosner *et al.* 1992).

It is important to note that the beam damage on these samples was uniform across the grains and the boundaries. The disordered region at the boundary did not grow with time indicating that it was not beam induced grain boundary grooving as has been seen at 400 kV(McKernan *et al.* 1992) The conventional TEM was done with a 100 kV beam, and the HREM was done with

Figure 6.17. A HREM image of a POMBE grown bi-epitaxial junction. A 1 nm disordered region is seen at the boundary.

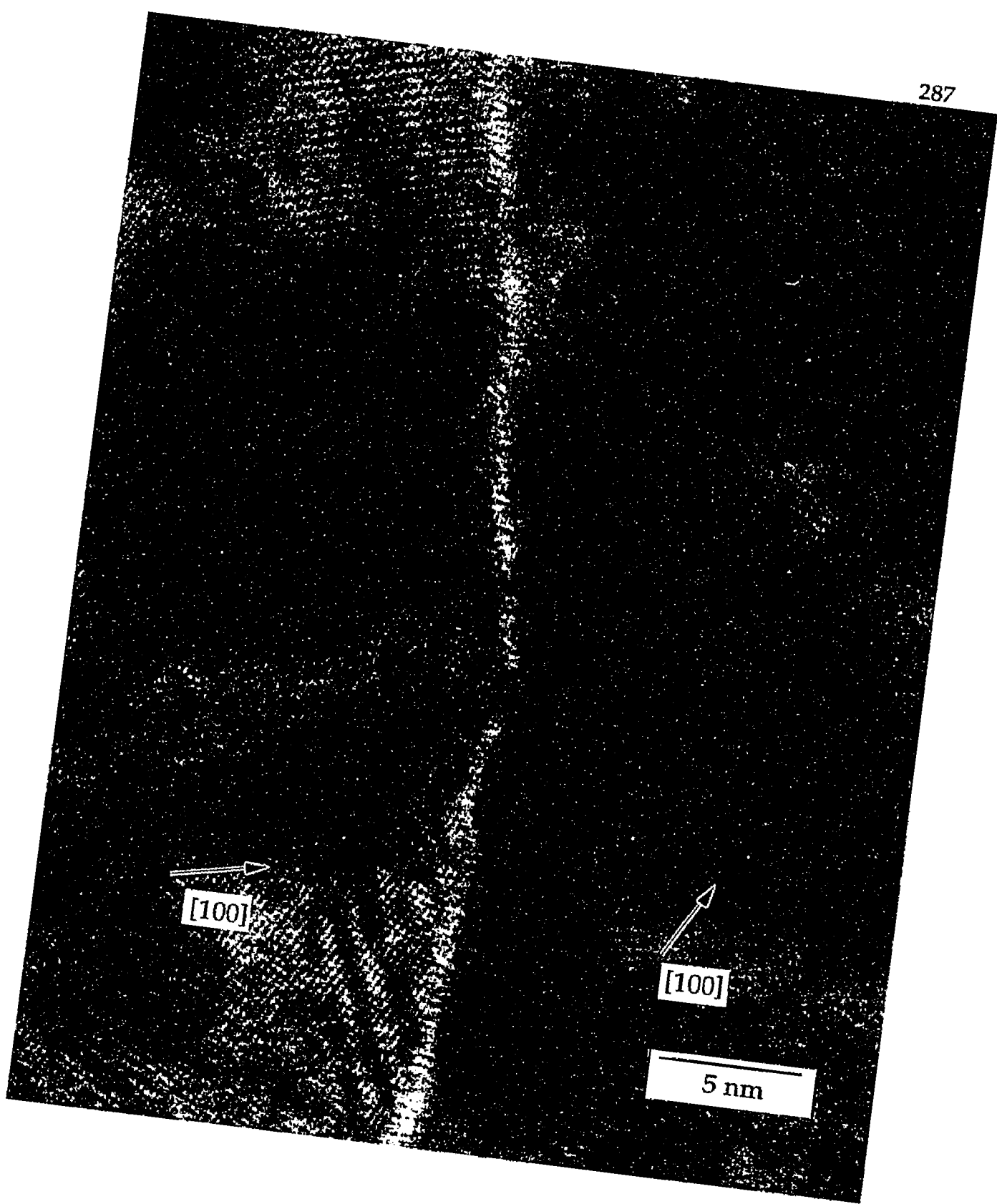


Figure 6.18a. A HREM image of a PLD grown bi-epitaxial junction. The boundary is well structured and exhibits some (100)(110) asymmetric facets.

289

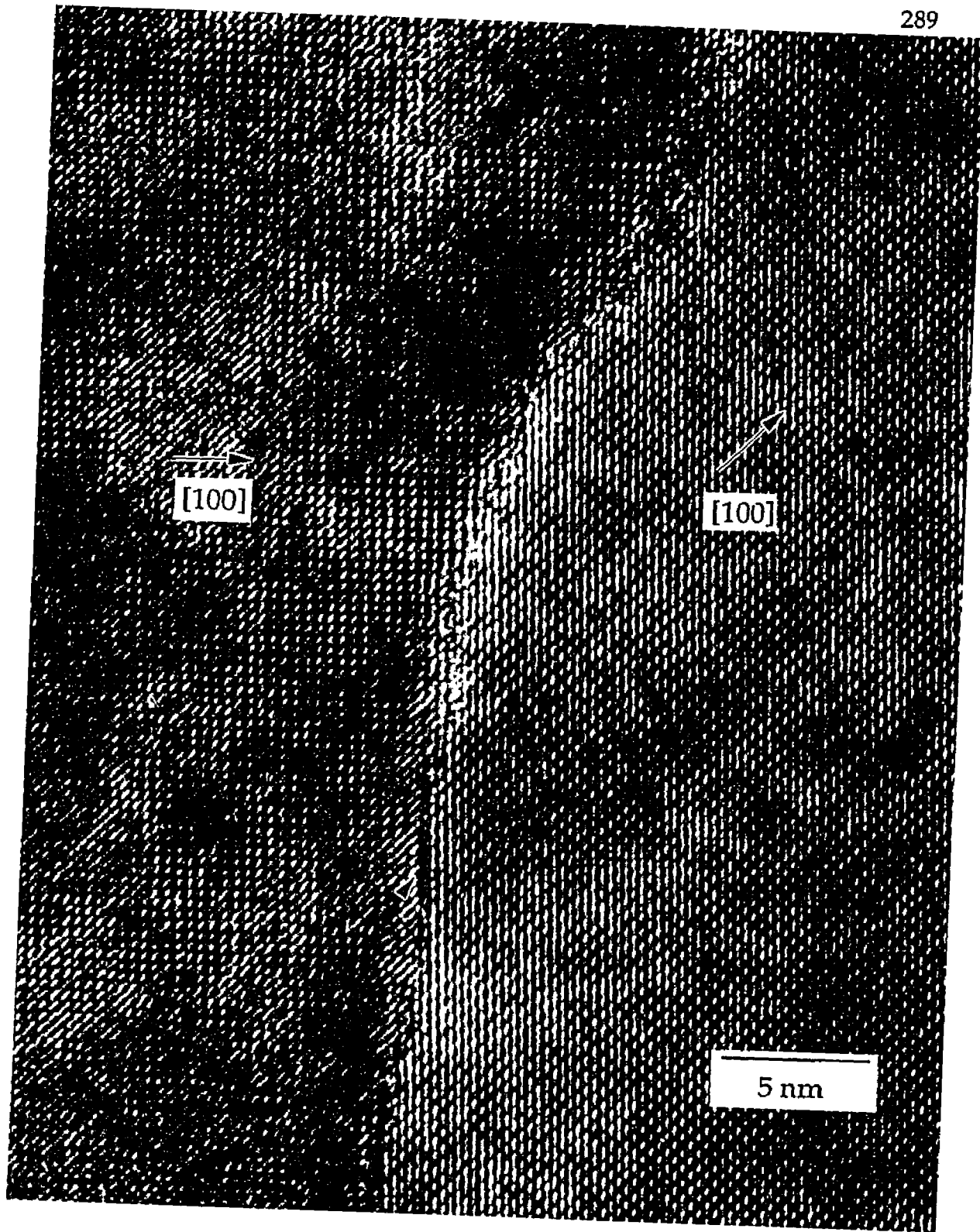


Figure 6.19b. A HREM image of PLD grown bi-epitaxial grain boundary. The arrow indicates a region where the grain boundary plane is inclined relative to the beam direction.



a 200 kV beam in order to minimize any damage. All the samples were prepared in identical manner as described in chapter III. The samples were all viewed in the microscope for approximately the same amounts of time, so there should be no discrepancy due to effects from the electron microscope.

#### VI.4. Structure - Property Relations

The comparison of the microstructure and transport properties of a superconductive and resistive sample can provide insight into the weak link behavior of high-T<sub>c</sub> grain boundaries. The properties of the two boundaries are very different in some respects, i.e. one is superconducting and the other is resistive throughout the entire measurement regime. However, the noise data suggests that they inherently have similarities, which vary from the grain. The model of a series of parallel thermally activated conduction paths across the boundary agrees well with the data for the two samples.

The microstructure does indicate differences in the two samples. Both chemical and structural effects appear to be important. The resistive boundary clearly has a significant length covered by precipitation that reduces the contact area across the boundary. The superconductive sample definitely does not have nearly as much, but this is not sufficient to explain the discrepancy in the transport properties. If the resistive grain boundary still had 40% of its length superconducting, it would be detected by the measurements, assuming it had similar critical current densities to the superconducting samples. Therefore the 1 nm wide disordered region at the boundary probably plays a role in the resistivity. Assuming a width of 1 nm along 20  $\mu\text{m}$  of the boundary with a 15 Ohm resistance gives a resistivity 9 Ohm-cm, which is on the order of a

semiconductor. There is still the possibility that only very small regions of the boundary are superconducting, and cannot be detected. The basis for this is one sample measured (Liu *et al.* 1995) has a transition at very low temperature (approximately 10 K) for a small measuring current. This further supports the idea of parallel conduction paths along the boundary.

The microstructure of the superconducting boundary shows much better connection without significant interruption by precipitates. The boundaries features are definitely inhomogeneous along its length, which explains the significantly different transport properties between grain boundaries on the same sample. There is substantial meandering along the length, and a small amount of precipitation. The actual grain boundary plane did have some regions that microfaceted along the (100) and (110) planes of adjacent grains. The boundary plane was also inclined to the substrate in certain regions suggesting an additional [100] (or [110]) tilt component to the grain boundary. All of these features can affect the transport properties. The comparison of these [001] tilt boundaries to the sputter-induced epitaxy samples with identical misorientation provides a more complete picture of the role of the microstructure in the transport properties (see chapter VII and appendix I). The next chapter deals with the comparison of all the boundaries discussed to form a grain boundary model.

## VII. Grain Boundary Model

The development of the sputter-induced epitaxy grain boundaries provides a unique opportunity to compare three 45° [001] tilt grain boundaries with significantly different transport properties. A model is developed that can consistently explain the transport phenomena observed and provide a connection between structure and property. A description of the model is made, followed by a direct comparison to the results on the boundaries studied and in the literature. The sputter-induced epitaxy junctions, superconducting bi-epitaxial junctions and resistive bi-epitaxial junctions are used for the comparison of grain boundaries with identical macroscopic misorientation and significantly differing properties. The most recent developments in the assumptions of this model have been incorporated in a paper presented in appendix I. This paper shows simulations of the model with very good qualitative agreement with the experimental data.

### VII.1 Asymmetric Parallel Junction Model

There are several different models for grain boundaries in high- $T_c$  superconductors, which were discussed in II.3.5. None of these fully explain all the transport properties, particularly the magnetic field data, and microstructural aspects of the boundary. By extending the models to include additional effects, a more complete description of the grain boundary properties can be made, and connected to microstructural observations. The transport properties of the 45° [001] tilt grain boundaries suggest a parallel multi-junction model that accounts for self-inductance, asymmetric current flow and junction

size effects. The Dayem bridge model(Sarnelli 1993a; Sarnelli *et al.* 1993b; Sarnelli *et al.* 1993c; Sarnelli *et al.* 1994) and the modified Dayem bridge model(David *et al.* 1993) develop the idea of parallel junctions, but without consideration for junction size and asymmetry. With these additional parameters, a better understanding of the grain boundary can be obtained. It should be made clear that asymmetry refers to the unequal current distribution along the grain boundary, not the local symmetry.

The basic concept of the asymmetric parallel junction model is to simulate a grain boundary with a series of N number of Josephson junctions in parallel along the boundary separated by normal regions (see figure 7.1). The analogous circuit diagram of the junction is shown in figure 7.1, with a set of parallel Josephson junctions of differing sizes and critical currents in parallel with shunt resistances (both temperature dependent and independent). The circulating currents, caused by penetrating flux, around each superconducting loop produce an additional term due to self-induced flux. These currents modify the local difference in the phase across the boundary. Then, if the junctions are sufficiently large, there will be a junction size effect due to penetration of flux in the junction in addition to penetration in the separating normal regions.

A schematic diagram of the microstructural comparison to the parallel junction model is shown in figure 7.2. The boundary consists of different microstructural features, each of which is represented by a given circuit element. The precipitates and second phases along the boundary are the parallel resistive regions that produce a shunt resistance (both temperature dependent and temperature independent). The remainder of the boundary consists of relatively

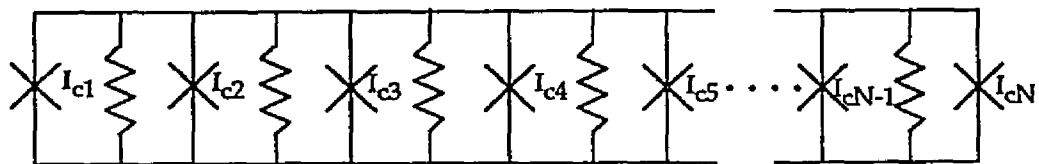


Figure 7.1 Circuit diagram to simulate grain boundary junction. A series of parallel Josephson junctions shunted by resistors, analogous to an interferometer. The junctions have unequal critical currents.

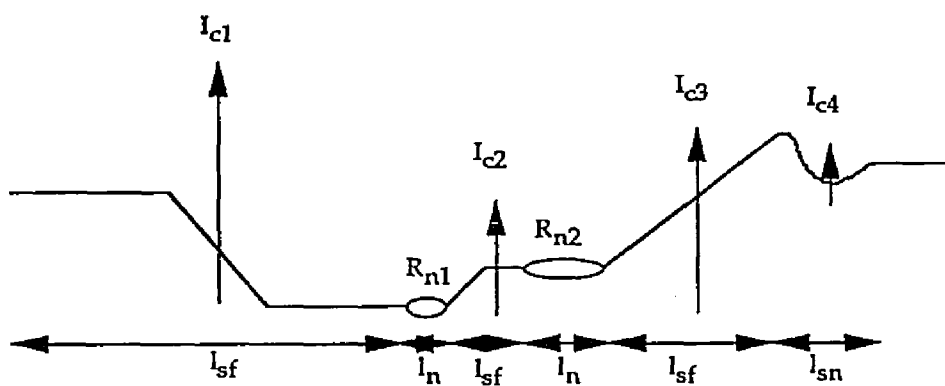


Figure 7.2a. Comparative region of the grain boundary junction with parallel junctions shunted by resistive regions.

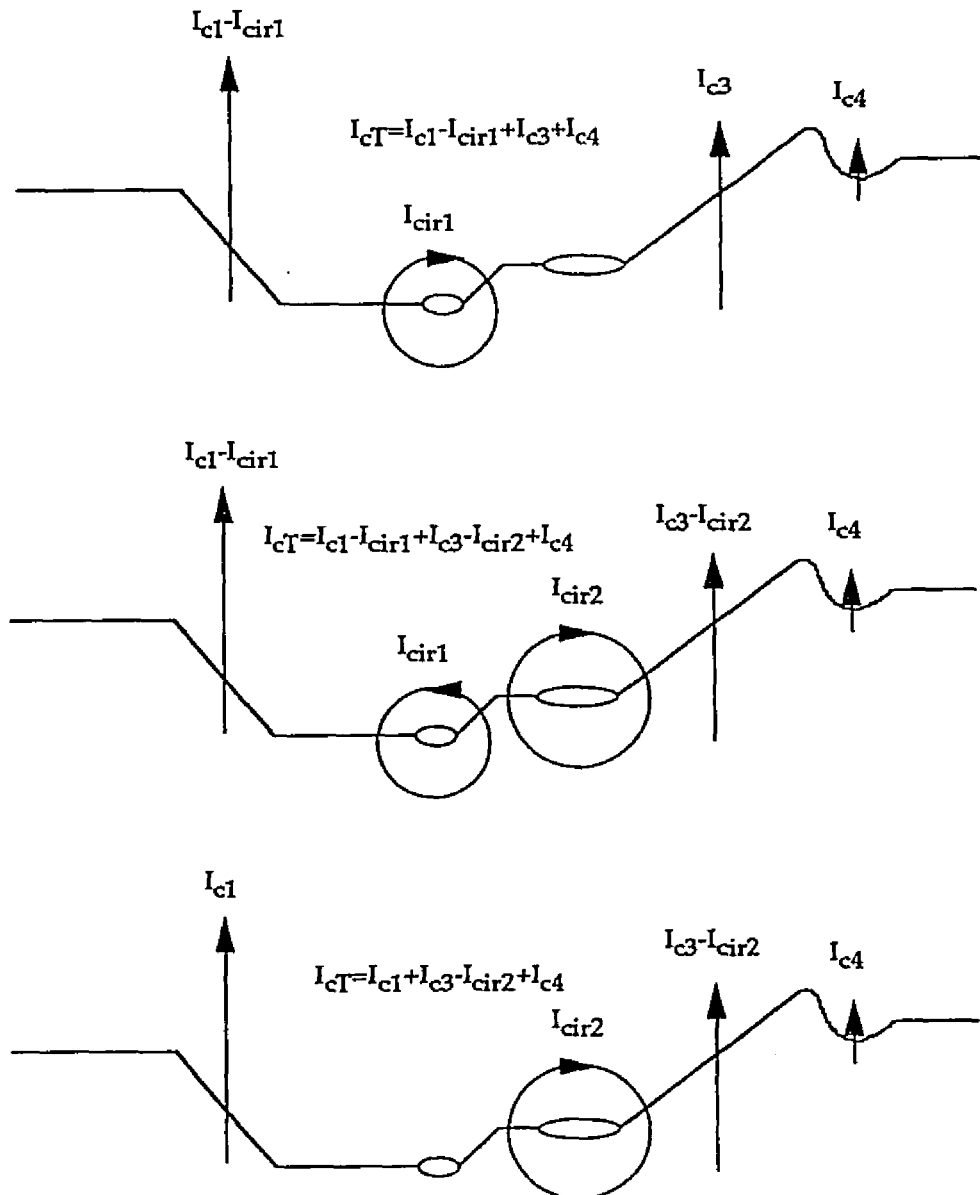


Figure 7.2b. Schematic diagram of the grain boundary junction showing the total critical current for three different applied flux states.

well connected areas of the grains with the same macroscopic symmetry, but a variation in the microscopic symmetry due to meandering. The better connected regions can then be further broken up into regimes with low index plane facets and non-faceted areas. By comparison of the structural data of the different superconducting samples the faceted regions should maintain higher critical current densities than unfaceted regions. These different faceted regions along the boundary can then be considered parallel junctions, with differing critical currents separated by varying amounts of normal material.

From this model various predictions can be made with the R-T and I-V behavior. The regions along the boundary can be broken up into superconducting faceted,  $I_{sf}$ , superconducting non-faceted,  $I_{sn}$  and non-superconducting,  $I_n$ . The two types of superconducting areas are assumed to have significantly different critical current densities (based on the transport data). Obviously the boundary consists of even more distributions of  $J_c$ , but only two will be considered for simplification. The total critical current will be the critical current density of the superconducting region times the total length of superconducting area along the boundary

$$I_{cT} = J_{sf} L_{sfT} t + J_{sn} L_{snT} t \quad (7.1)$$

where

$$L_{sfT} = \sum_{Boundary} l_{sf}$$

$$L_{snT} = \sum_{Boundary} l_{sn}$$

$t$  is the film thickness, the facets are assumed to extend through the entire film thickness. Therefore the magnitude of the critical current is directly dependent on the amount of asymmetric faceting along the boundary. From the I-V measurement, some idea of the total superconducting length can be obtained, but not of the current distribution.

Since the total length of the boundary is constant ( $L_{sf} + L_{sn} + L_n$ ), the length of normal regions is inversely proportional to the length of superconducting regions. This would indicate that assuming a constant resistivity, the normal state resistance of the boundary would increase with decreasing critical current (for a given temperature). Therefore, the normal state resistance can give a magnitude of resistive regions along the boundary. This is explained further in the section on the R-T behavior.

The critical current oscillations as a function of applied field can also be understood from this model. The interactions of the junctions can be described as an interferometer with shunted resistance (as shown in figure 7.1). The basis of this model is a SQUID with two parallel junctions, which can then be modified to accommodate N junctions in parallel. For simplification, the basic ideas are developed in two parallel junctions (a SQUID) following van Duzer(Van Duzer *et al.* 1981). Assume that the junctions are symmetrically placed in a loop and have critical currents  $I_{c1}$  and  $I_{c2}$  respectively. The phase differences in the two junctions ( $\phi_1, \phi_2$ ) can be related by integrating the gradient of the phase of the pair wave function around the loop of the SQUID(Van Duzer *et al.* 1981). The phase difference is then given by:

$$\phi_2 = \phi_1 - \left( \frac{2\pi\Phi}{\Phi_0} \right) \quad (7.2)$$

where  $\Phi$  is the applied flux and  $\Phi_0$  is the flux quantum ( $h/2e$ ). The total current across the two junctions is then given by the sum of the two individual currents:

$$I_T = I_{c1} \sin \phi_1 + I_{c2} \sin \left( \phi_1 - \frac{2\pi\Phi}{\Phi_0} \right) \quad (7.3)$$

By ignoring self-inductance (hence  $\Phi=\Phi_{app}$ ), and maximizing eq. 7.3 with respect to  $\phi_1$ , the total critical current becomes eq. 7.4:

$$I_{Tc}(\Phi_{app}) = \left[ (I_{c1} - I_{c2})^2 + 4I_{c1}I_{c2} \cos^2 \left( \frac{\pi\Phi_{app}}{\Phi_0} \right) \right]^{\frac{1}{2}} \quad (7.4)$$

This relation indicates that if the critical currents across the junctions are equivalent, the total critical current is reduced to a cosine term forming a series of cusps, with  $I_{Tc}=0$  at  $B=n(\Phi_0/2)$ . An asymmetry in the critical currents ( $I_{c1} \neq I_{c2}$ ) will not allow perfect cancellation of the critical currents in the circuit, therefore there are no applied fields for which there is no critical current (see figure 7.3). In the case of the asymmetric critical currents, the ratio of the two junction currents is inversely proportional to the difference between the maxima and minima of the critical current as a function of magnetic field.

Equation 7.4 assumes no self-induced flux, which is not the case for any situation where  $LJ_c \geq \Phi_0/6$  ( $L$  is the inductance of the loop). Self-induced flux arises from the circulating currents in the loop(Van Duzer *et al.* 1981). The circulating currents create an additional flux term:

$$\Phi_{ind} = LJ_{cir} \quad (7.5)$$

The circulating currents are defined by  $I_{\text{cir}} = (1/2)(I_2 - I_1)$ . Substituting into 7.5 and adding to the applied flux the total flux in the loop is then:

$$\Phi = \Phi_{\text{app}} + \frac{1}{2}LI_{\text{cir}}(\sin \phi_2 - \sin \phi_1) \quad (7.6)$$

The phase difference (eq. 7.2) now becomes:

$$\phi_2 = \phi_1 - \left( \frac{2\pi}{\Phi_0} \right) \left[ \Phi_{\text{app}} + \frac{1}{2}LI_{\text{cir}}(\sin \phi_2 - \sin \phi_1) \right] \quad (7.7)$$

The total flux can now be determined as a function of  $\Phi_{\text{app}}$  and  $\phi_1$ . The total current can therefore be maximized for a given applied flux. The numerical solution is illustrated in figure 7.4. The two different critical currents have complementary behavior due to the reversal of current at half-flux intervals. The circulating currents induce a flux that tries to make the total penetrating flux an integral value. Therefore as the applied flux increases beyond  $1/2 \Phi_0$  the lowest energy state is for the circulating currents to reverse in direction. The channels then essentially switch from a constant critical current to a critical current varying with field depending on the direction of the circulating current. This implies that a series of parallel junctions could be a set of parallel switches that vary between the two states as the flux is changed. Figure 7.5 shows how the self-induced flux strongly affects the difference between the maximum and minimum critical currents (as did the junction asymmetry discussed above).

Both the self-induced flux and the asymmetry of the boundary critical currents will diminish the peak to valley ratio of the maximum critical current

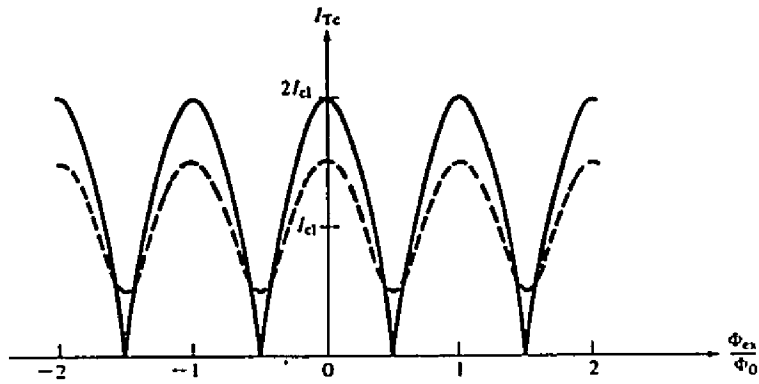


Figure 7.3. The dependence of the critical current on applied flux for a two junction model. The dotted line is for two junctions with unequal critical currents (from Van Duzer 1981).

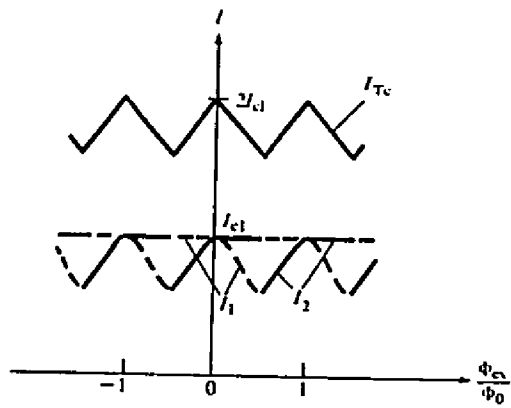


Figure 7.4. The critical current response for two parallel junctions with self-induced fields included. The lower two curves break down the currents in either junction (from Van Duzer 1981).

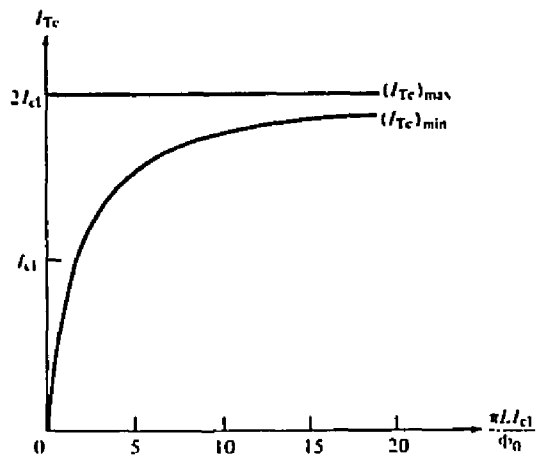


Figure 7.5. The effect of self-inductance on the difference of the maximum and minimum critical currents. At higher self-inductances the peak to valley ratio in the  $I_c(B)$  relation diminishes (from Van Duzer 1981).

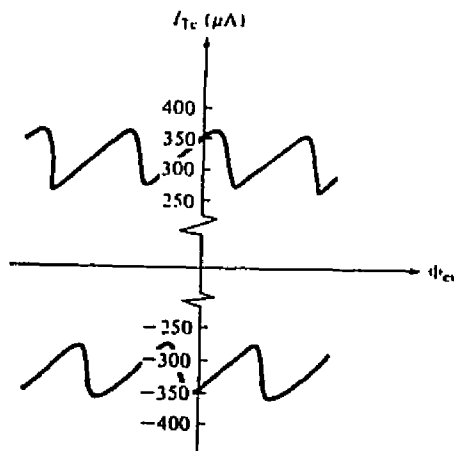


Figure 7.6. The  $I_c(B)$  behavior for an asymmetric (unequal critical currents) junction with self-induced fields (from Van Duzer 1981).

as a function of magnetic field. These two effects can actually be differentiated by determining the modulation depth as a function of temperature. As  $T_c$  is approached, the self-inductance is minimized due to the decreasing critical current. Therefore the modulation should increase significantly if the self-inductance is the major effect on the behavior. The behavior of a junction displaying both asymmetry and self-inductance is shown in figure 7.6. This graph shows that the absolute value of the positive critical current and the negative critical current can be different due to the combination of asymmetry and self-inductance, which is consistent with the results on the grain boundaries.

The final effect on the junction behavior is the finite junction size. If the junction size is relatively large compared to the loop, there will be flux penetration in the junction, not just in the loop as previously assumed. The effect will be to add an envelope term due to the additional modulation in the junction itself causing a double modulation in the  $J_c(B)$  behavior.

The basic concepts expressed for two junctions can be extended to multiple junctions, but becomes extremely complex. In particular, the high- $T_c$  grain boundaries, depending on the microbridge width, are probably composed of up to hundreds of junctions with differing sizes and critical currents, complicating the matter further. There are, however, some basic predictions that can come from this model. The transport measurements of the different samples are discussed with respect to the asymmetric parallel junction model. Some differences between the Dayem bridge model and the asymmetric parallel junction model will also be mentioned.

## VII.2. Transport Properties

### VII.2.1. Resistance-Temperature

The R-T behavior of the different grain boundaries all agree with the behavior for a set of Josephson junctions in parallel with a set of thermally activated conduction paths. The R-T curve of three grain boundaries is shown in figures 4.11, 6.2, and 6.3 . The sputter-induced epitaxy grain boundary exhibits TAPS at the boundary, and has the highest transition temperature of the three boundaries. The superconducting boundary has an extended foot-like structure due to the reduced critical current at the boundary. The resistive bi-epitaxial junction displays an increasing resistance with decreasing temperature.

The grain transition temperatures for the samples are all within 5 K. The grain in the resistive sample actually has the highest of all the samples measured. The microstructure of the boundary suggests that the excess material was preferentially precipitated at the boundary, indicating that the high quality grain can force non-stoichiometric structures to form at the boundary under suitable conditions. The other two samples had grains with similar transition temperatures suggesting that the grain quality does not play an important role between the two samples. The extended foot-like structure in the curves is from TAPS, and indicates that the two different have significantly different critical currents, which is confirmed by I-V measurements later.

The R-T curve provides one more insight into the grain boundary behavior. By driving the sample normal, the boundary properties of both the bi-epitaxial and sputter-induced epitaxy samples suggest a series of thermally activated parallel conduction paths along the boundary. This behavior was modeled in both types of boundaries as well as the resistive boundary. The

major difference between the boundaries is the number of parallel conduction paths, with the resistive boundary having the most and the sputter-induced epitaxy boundary having the least. This data is also corroborated by noise power measurements on the bi-epitaxial samples (see section VI.2.4).

The R-T behavior of the boundaries is well described by the model. The parallel junctions should not modify the transition temperature relative to one junction with an equal length of superconducting region. The different junctions can all have different critical currents, but the same critical temperatures. The normal state resistances also indicate that in all the samples there are parallel conduction paths along the boundary. The total resistance of the sample is given by the sum of all the resistive channels as was described in chapter IV.

### VII.1.2. Current-Voltage

The two superconducting boundaries had RSJ-like behavior typical for grain boundary weak links. The major difference between the two boundaries is the critical current density across the boundary. The sputter induced grain boundary has a critical current density of  $5 \times 10^4$  A/cm<sup>2</sup> at 5 K as opposed to the critical current density of the bi-epitaxial junctions  $2 \times 10^3$  A/cm<sup>2</sup> at 5 K. This indicates that the sputter-induced samples could support over an order of magnitude more supercurrent than the bi-epitaxial junctions. The I-V characteristics also provide information on the normal state resistance of the boundaries. The normal state resistance of the sputter-induced epitaxy grain boundary is 0.025 Ohms at 5 K and for the bi-epitaxial junctions it is 0.475 Ohms. This directly supports the idea of the parallel conduction paths being

inversely proportional to the superconducting paths along the boundary. Therefore the larger the critical current the more superconducting paths it has along the boundary (assuming the same critical current density along the boundary). The I-V characteristics for the junction at zero field should be the sum of all the critical currents along the parallel paths. This also agrees with the RSJ-like behavior of the boundary.

The asymmetry of the I-V characteristics is a unique feature of the high- $T_c$  grain boundaries that has been observed by other groups as well (Dimos *et al.* 1990). This asymmetry is also exhibited by a two junction SQUID with both unequal critical currents across the junctions and self-inductance(Fulton *et al.* 1972). The combination of these two effects creates an asymmetric I-V characteristic as described in the previous section.

### VII.1.3. Magnetic Field

The dependence of the critical current on the applied magnetic field for the three different samples is shown in figures 4.20-21, 5.9 and 6.9-12. The Patterson functions of both sets of data suggest that there is a definite periodicity of approximately 2 G in the sputter-induced epitaxy, and no distinct periodicity in the bi-epitaxial data. The periodicity of the multilayer even shows a Moire interference pattern of two periodicities. The period in the  $J_c(B)$  behavior cannot be directly predicted by modeling for a given  $J_c(x)$  and Fourier transforming the data. This is because of the additional self-inductance that locally varies the phase along the boundary.

As the magnetic field is applied the various junctions will behave differently along the length of the boundary. Figure 7.2b. is a schematic

diagram for different applied fields along the boundary. The flux will penetrate unevenly along the junction and different circulating screening currents will be set up to compensate. Thus, as flux penetrates one region, the circulating currents travel clockwise for example, then when the flux is greater than  $(1/2)n\Phi_0$  the circulating currents will reverse the direction to maintain the lowest energy configuration. Also as the flux increases the circulating current increases up to half a flux quantum. Therefore each region will have varying circulating currents set up for flux compensation. If the junctions have differing critical current values, there will be a current going through the junction even when the maximum screening current is present. The current is why there is no perfect cancellation of the currents across the boundary. The self-induced currents will further modify the local field seen by the junctions. This will cause variations in the screening currents along the boundary. Mutual inductance is probably minimized due to the low Josephson current values.

Other measurements in the literature also agree with the parallel conduction model. High field measurements show a residual current, that would agree with this model (Sarnelli *et al.* 1993b; Sarnelli *et al.* 1993c; Froehlich *et al.* 1995). One interesting prediction of the model is the differentiation between self-induced flux and asymmetric critical currents in the parallel junctions. At temperatures approaching  $T_c$ , the asymmetric currents would diminish the difference between  $I_{max}$  and  $I_{min}$  in the magnetic field data, whereas self-inductance would maximize it (due to a decrease in the self-inductance from smaller critical currents near  $T_c$ ). The data on the junctions produced by sputter-induced epitaxy shows that at higher temperature the difference is

Boundary Type	Grain T <sub>c</sub> (K)	Grain Boundary T <sub>c</sub> (K)	I <sub>c</sub> (mA) @ 5 K	R <sub>n</sub> (Ohms) @ 5 K	I <sub>c</sub> R <sub>n</sub> (mV) @5 K	ΔB (G)
Resistive Bi-epitaxial	90.5	NA	NA	20	NA	NA
Superconducting Bi-epitaxial	86.5	40	0.2	0.475	0.095	<0.2
Sputter Induced Epitaxy	86	81	5	0.025	0.125	2.2

Table 7.1. Synopsis of transport data for three representative types of grain boundary junctions.

minimized implying the dominant feature is the asymmetric critical currents along the boundary.

The period of  $J_c(B)$  should vary with an increasing number of junctions for a fixed grain boundary length. This is confirmed by Early et al. (Early *et al.* 1994) which showed that the periodicity decreases with increasing microbridge width. As the number of junctions increases, there are more permutations of the junction "switching" states. This will make a finer  $J_c(B)$  pattern without a characteristic period, unless the junctions are evenly spaced.

## VII.2. Microstructure

The microstructure of the three boundaries showed both similarities and differences. SEM analysis of the samples would often show varying surface morphology, which has been directly related to specific growth conditions (Buchholz *et al.* 1994). The bi-epitaxial samples tend to form precipitates preferentially at the boundary. This is detrimental for the transport properties, but can be minimized using optimal growth conditions. The sputter-induced epitaxy samples did not have this type of surface morphology probably due to the growth of the YBCO on the MgO on both sides of the boundary.

TEM analysis of the boundaries showed that they all exhibited a characteristic meandering along their length. The meandering on approximately the same length scale for each, typically deviating as much as 500 nm from a hypothetical straight line. As discussed previously (sections IV.3.2 and VI.3.1.), this effect is from both the faster grain growth along the a-b plane relative to the c-axis growth, and from the imperfect photoresist. Both the sputter-induced epitaxy and bi-epitaxial samples are made using a photoresist

process, therefore this is consistent with the magnitude of the meandering along the boundary. The meandering is about a factor of two greater than that seen in bicrystal samples, which is consistent with having only one contribution to the meandering in the bicrystal samples (i.e. grain growth).

The resistive boundary had significant precipitation preferentially occurring at the boundary. The precipitates appeared along over 60% of the boundary length indicating a large reduction of the contact area at the boundary. The superconductive bi-epitaxial and sputter-induced epitaxy boundaries did have some precipitation at the boundary, but it was less than 10% of the length. The precipitation is a major microstructural difference between the resistive and superconducting samples, implying that it plays a major role in the resistance of the boundary.

HREM provides even more insight into the atomic scale differences of the three boundaries. In the resistive boundary along the regions of the grain boundary that are not interrupted by precipitates, there is a 1 nm wide disordered region. A region on the length scale is a sufficient barrier that can prevent superconductivity across the junction.

The major difference between the two superconducting grain boundaries is the localized symmetry at the grain boundary plane. The superconducting bi-epitaxial junction meanders exhibiting a few asymmetric facets, on the order of 10% of the boundary length. There are also regions that have an additional [100] tilt component (also confirmed with cross-sectional TEM(Rosner *et al.* 1992)). The grain boundary plane is therefore non-uniform along its length. In contrast, the sputter-induced grain boundary junction has extensive regions of the boundary that have asymmetric faceting of the (100) plane parallel to the (110)

plane of the adjacent grain. Around 70% of the boundary is faceted in this manner. What is particularly striking is how even in regions where the boundary is strongly curved, it is accommodated with small asymmetric microfacets. The asymmetric facets appear to be well structured to within 4 Å of the grain boundary plane indicating minimal strain.

### VII.3. Structure-Property Relationship

The study between the three different grain boundaries provides an opportunity to compare [001] 45° tilt grain boundaries with strikingly different properties. By controlling the variables (e.g. macroscopic misorientation, microbridge width etc.), the connection between structure and properties can be made more directly. The most obvious differences in the samples is between the resistive and the superconducting samples. Clearly both precipitation and a localized disordered region along the boundary cause the resistive behavior. The other boundaries did not display either of these characteristics and were superconducting. The difference between the effect of the precipitation and the disordered region on the resistance is not fully understood.

The two superconducting samples have over an order of magnitude difference in their critical current densities. The sputter-induced epitaxy sample had a definite periodicity of critical current as a function of applied magnetic field, as opposed to the bi-epitaxial sample that did not exhibit a clear periodicity. These variations in the transport data are too large to be explained by small variations along the boundary. Microstructurally, most of the features of the junctions were similar, few precipitates, meandering along the length (same magnitude) and structure of the boundary. Therefore these effects can be

assumed to have a minimal effect on the transport properties in this situation. There was one primary difference, however, the local boundary symmetry. The sputter-induced epitaxy samples had long asymmetric (100) (110) facets on the order of 50-100 nm. The bi-epitaxial sample only showed faceting along short lengths of the boundary, and had regions where the boundary had a [100] twist component.

There have been no studies that document the transport properties of asymmetric vs. symmetric grain boundary planes. There have been varying predictions of the two types of boundaries, both theoretical calculations(Meilikhov 1994) and microchemical analyses(Browning *et al.* 1993). The calculations by Meilikhov use a dislocation model to predict the stress along the boundary. Then, based on a reduced order parameter at high stress regions, he predicts that an asymmetric boundary can maintain higher critical currents than symmetric boundaries (by more than one order of magnitude). In contrast, the work by Browning *et al.* suggests that the symmetric grain boundary did not have a depletion in hole carrier concentration, but the asymmetric facet did. This work was done on two different facets with grain boundary misorientations of 29.5° and 36°. Different misorientation angles could have different stoichiometries at the boundary. Also, no electrical transport measurements were made to confirm whether the critical current densities of the facets were different.

The full estimates of this model would require extensive calculations for just one grain boundary. The smaller the junction width, the fewer parallel junctions would have to be simulated. The critical measurement would be low magnetic field behavior of the critical current.

## **Chapter VIII. Conclusions and Future Work**

The major results of this work are in the development of sputter-induced epitaxy grain boundary formation and the understanding of the microstructure-transport property relationship in 45° [001] YBCO thin film grain boundary junctions. Sputter-induced epitaxy is a unique technique for the control of the epitaxial orientation relationship between a YBCO thin film and a (100) MgO substrate. A pre-growth substrate treatment using a low voltage argon ion source has been developed to reproducibly form 45° [001] grain boundary junctions on MgO. The modification of the substrate is due to two primary effects of the ion damage. Atomic force microscopy studies clearly exhibit a roughened surface morphology on the pre-sputtered region relative to the unspattered regions. The surface roughening is accompanied with argon and tungsten ion implantation in the top surface layer of the MgO as indicated by RBS results. The argon and tungsten ration is approximately 10:1 under standard pre-treatment conditions. The results of numerous pre-growth treatments under varying incident ion energies, sputter durations and incident ion angles indicate that the modified epitaxy is due to a combination of ion implantation and surface roughening.

The sputter-induced epitaxy grain boundary junctions have good junction transport characteristics. The junctions had high transition temperatures and exhibited thermally activated phase slippage across the boundary. At higher measuring currents the normal state resistance of the junction has a temperature dependence that can be modeled by a series of

thermally activated resistors in parallel with a set of Josephson junctions.. The I-V characteristics are modeled by a resistively shunted junction with no capacitance and noise rounding at higher temperatures. The critical current densities were as high as  $5 \times 10^4$  A/cm<sup>2</sup> at 5 K and  $1.6 \times 10^3$  A/cm<sup>2</sup> at 77 K. At higher temperatures the behavior became more flux flow like. The critical current as a function of applied magnetic field exhibited a periodic structure indicating a relatively uniform current distribution across the boundary.

The microstructure of sputter-induced epitaxy junctions suggest the reason for the good transport properties. There were very few precipitates along the boundary length. The grains on either side of the boundary maintained structural integrity up to a 4 Å disordered region localized at the grain boundary. The most unique aspect of the boundaries are the long low-index plane asymmetric facets along 70% of the grain boundary with the (100) of one grain parallel to the (110) of the adjacent grain. These microfacets have been observed as long as 100 nm in length. Even in regions of meandering the grain boundary will often reverse symmetry at the grain boundary plane and maintain the low-index microfacets.

Sputter-induced epitaxy junctions have several significant advantages over other grain boundary junctions. The technique is extremely simple and versatile in implementation. Grain boundaries can be made in any configuration dictated by the physical mask. The necessary components for the entire procedure (including an ion source, thin film growth technique and photolithography capabilities) are already standard in the semiconductor industry and can be readily scaled to production sizes. The junctions have excellent transport properties considering the high-angle of the grain

boundaries. The two grains are formed on the same substrate material (as opposed to bi-epitaxial junctions) allowing uniform grain growth on both sides of the junction. The structure of the boundaries has a characteristic low-index plane asymmetric faceting. The faceting allows more uniform current distribution across the boundary. The drawbacks of the technique are the limited geometry of the grain boundary, which ultimately limits the  $I_c R_n$  value. Also, sputter-induced epitaxy initially required a bulk MgO substrate that was not always the desired substrate material depending on the application.

The sputter-induced epitaxy process was then extended to a multilayer system to remove the constraints of using the bulk (100) MgO substrate. A layer of 1000 Å - 1500 Å of high quality epitaxial (100) MgO is deposited on (100) LaAlO<sub>3</sub>. The MgO is then patterned using photolithographic techniques and the sputtered with 250 - 300 eV argon ions. A final layer of YBCO is subsequently grown on the MgO. The resulting orientation is YBa<sub>2</sub>Cu<sub>3</sub>O<sub>7-x</sub> [001] || MgO [001] and YBa<sub>2</sub>Cu<sub>3</sub>O<sub>7-x</sub> [100] || MgO [110] on the pre-sputtered region with the cube-on-cube orientation on the unsputtered region. This junction has all the advantages of the sputter-induced epitaxy junction on bulk MgO, but is not limited to the bulk MgO substrate. The YBCO grain boundary transport properties showed characteristic single junction behavior. The R-T exhibited TAPS with a relatively high- $T_c$ . Typical RSJ I-V characteristics were observed with no capacitance. The Patterson function of the  $I_c(B)$  data exhibited a Moire pattern indicating two different periodicities superimposed. The major implication of the multilayer grain boundary junction is the ability to integrate a junction into different materials systems in a relatively simple manner.

The structure-property relationship of the bi-epitaxial grain boundary junctions was studied. Two different types of junctions were observed, superconducting and resistive. The resistive junctions exhibited an increasing resistance with decreasing temperature. This behavior was modeled by a set of parallel thermally activated resistive regions. The superconducting regions had very low  $T_c$  (40-50 K) with an extended regions of TAPS due to the significantly depressed critical current across the boundary. The critical current density at 5 K was  $2 \times 10^3$  A/cm<sup>2</sup>. The I-V characteristics were modeled using the RSJ model with no capacitance. The magnetic field behavior of the critical current had strong oscillations as a function of very small changes in applied magnetic field. This behavior is consistent with a set of parallel Josephson junctions with a variable phase difference along the grain boundary. The microstructure of the resistive grain boundaries had precipitation and second phases along their length including a 1 nm disordered region at the boundary. The superconducting grain boundary meandered significantly, but had about 10% of the boundary formed by low-index asymmetric facets.

By comparing the structure-property relationship in the three different grain boundary junctions, a phenomenological model has been developed to explain the observed behavior. The junction is modeled with a series of Josephson junctions in parallel with a set of resistors. The R-T and I-V characteristics can be directly interpreted from this model, as it has been using other proposed models. However, the  $I_c(B)$  behavior can also be qualitatively described using the parallel junctions. The key aspect of the parallel junctions is the inclusion of self-inductance, asymmetric current flow and junction size effects. These will all contribute to the phase shift along the boundary

indicating that there is a non-uniform phase shift. The implication is that the magnetic field data is not directly interpretable using an apriori current distribution along the boundary. Non-uniform penetration of the magnetic field coupled with the additional multiple junction effects create a complex pattern of current flow across the boundary in response to small applied fields. This model is also connected to the microstructure of the grain boundary. The long asymmetric facets in the sputter-induced epitaxy junctions provide more uniform current flow, which is not apparent in the bi-epitaxial junctions. Therefore the Josephson junctions are the low-index plane asymmetric facets separated by regions of lower critical current density (other grain boundary regions) and normal regions (precipitates along the boundary).

The correlation of the structure-property relationship provides insight into the weak link nature. The best way to improve the junction behavior is to form long regions of uniform current flow. In the 45° [001] grain boundary junctions this can be done by maximizing the asymmetric microfaceted regions of the boundary. The sputter-induced epitaxy junctions are made under near thermodynamic equilibrium conditions implying that the asymmetric facets are energetically favorable.

This project has contributed both to the technological development of grain boundary junctions and the scientific understanding of the weak link behavior of high-angle grain boundaries. In so doing, a new set of questions arise to obtain a deeper understanding of the scientific issues and further development of the technology. Future work is suggested in both the analysis of the phenomenon of sputter-induced epitaxy and in the area of grain boundary transport.

The ultimate benefit of sputter-induced epitaxy might be in a completely different materials system. A somewhat more thorough understanding of the mechanism would allow the translation of this technique to other thin films on MgO, YBCO on different bulk substrates or on an altogether different system. Cross-sectional TEM analysis of the grain boundary junctions could provide more insight into the mechanism. Perhaps the most useful would be an in-situ analysis of the nucleation and growth of the thin film using surface science monitoring techniques such as low energy electron diffraction (LEED) or reflective high energy electron diffraction (RHEED). In order to study the surface lattice parameter a method such as total external reflection (TER) x-ray diffraction could possibly be used. This would not be a trivial experiment due to the surface roughness of the MgO, but could conceivably be performed. After a thorough understanding of the mechanism is obtained, other systems where the epitaxial relation between the substrate and the thin film is crucial, or grain boundaries control critical properties can be identified. As for the YBCO, other multilayer systems on semiconductors can be developed to determine integration capabilities with other materials techniques. The optimization of the thin film growth process would allow a better determination of the critical current density reproducibility both in one chip and from chip-to-chip. This would also determine the best critical current density and  $I_c R_n$  values obtainable with this technology. Other aspects of the technique could be further developed such as using a diamond-like carbon thin film as a mask to provide extremely sharp edges.

The structure-property relationship in the sputter-induced epitaxial grain boundaries can be further developed to ultimately obtain a thorough

quantitative agreement with the grain boundary model. The key studies would be a series of careful applied magnetic field measurements at both low (up to 200 G) and high (5-10 T) fields. Using a series of different width boundaries (even on the same chip) will allow better understanding of the current flow across the junction. It would be critical to have high quality films to separate intrinsic from extrinsic boundary effects. The ultimate goal would be to isolate an individual microfacet to perform transport measurements, but this appears to be extremely difficult if not impossible with current technology. Noise measurements on these grain boundaries would allow comparison to the bi-epitaxial to determine the role of the microfacets in these properties. Microwave response would also be interesting to determine the strength of the A.C. Josephson effect in these junctions. The development of junction implementation would be of interest. An immediate possibility would be to make a SQUID and determine its noise properties and field sensitivity (critical parameters in SQUID design).

The structure of the grain boundaries can be further analyzed. An extensive set of simulations of the grain boundary could provide more insight into the nature of the 4 Å disordered region. Also small probe PEELS analysis would allow comparison of the hole carrier concentration of different facets in these grain boundaries. Perhaps designing an experiment using tripod polishing techniques could provide larger thin regions to analyze longer regions of the boundary. If more extensive regions of the boundary can be observed a better understanding of the structure-property relationship can be obtained.

# **Appendix I. Structure-Property Relationship in YBa<sub>2</sub>Cu<sub>3</sub>O<sub>7-x</sub> Thin Film Grain Boundaries: A Grain Boundary Model**

## **Structure-Property Relationship in YBa<sub>2</sub>Cu<sub>3</sub>O<sub>7-x</sub> Thin Film Grain Boundaries: A Grain Boundary Model**

B.V. Vuchic<sup>a,b</sup>, L.D. Marks<sup>b</sup> and K.L. Merkle<sup>a</sup>

<sup>a</sup>Materials Science Division, Argonne National Laboratory, Argonne, IL 60439

<sup>b</sup>Materials Science and Engineering Department, Northwestern University,  
Evanston, IL 60208

### **Abstract**

Transport in magnetic field across 45° [001] tilt grain boundaries in YBa<sub>2</sub>Cu<sub>3</sub>O<sub>7-x</sub> thin films is studied for samples whose microstructure has been well characterized down to the atomic scale. A grain boundary model is proposed of parallel superconducting paths separated by normal regions. The key parameter necessary to qualitatively match the low magnetic field data is that the magnetic field penetration is minimal in the superconducting regions relative to the normal regions. The effects of varying the components of the boundary (such as conduction path size and precipitate size) are discussed. This result implies that a substantial improvement in the control of the microstructure to electronic grade levels is necessary to form reproducible junction properties.

## Introduction

One of the predominant materials issues both scientifically and technologically in the high- $T_c$  materials has been the role of grain boundaries. Previous studies have shown that most high- $T_c$  high-angle grain boundaries behave as weak links.(Dimoset *al.* 1988; Dimoset *al.* 1990; Ivanovet *al.* 1991) The weak link behavior is detrimental for high current density applications. However the Josephson-like characteristics of the grain boundaries can be used in microelectronic devices such as superconducting quantum interference devices (SQUIDs). The basic understanding of the weak link behavior is still incomplete and prevents the incorporation of grain boundaries into many potential applications.

Numerous studies have analyzed the transport properties of thin film grain boundaries with many different macroscopic misorientations (see e.g.: (Gross 1992)). Likewise there has been substantial work to study the microstructure and chemistry of grain boundaries.(Rosneret *al.* 1992; Alarcoet *al.* 1993; Browninget *al.* 1993; Dravidet *al.* 1993; Jiaet *al.* 1993; Babcocket *al.* 1994; Traeholtet *al.* 1994) Unfortunately there is seldom a direct connection made between the structure and transport properties.

There have been several proposed grain boundary models to explain the observed weak link behavior in high angle grain boundaries. The microfilamentary model suggests that there are a few strongly coupled regions along the boundary where superconducting filaments, or fully oxygenated regions from the grains on either side join.(Moecklyet *al.* 1993)(Earlyet *al.* 1994) The areas surrounding the superconducting filaments are proposed to be oxygen deficient normal regions. The model is based on the transport data from

MgO grain boundaries, however there is no direct evidence that structurally or chemically confirms this. Another grain boundary model was suggested by Sarnelli et al. based on high magnetic field measurements.(Sarnelli 1993a; Sarnelli *et al.* 1993b) They used a Dayem bridge model ascribing the weak link behavior to a set of superconducting regions on the order of a coherence length (1-1.5 nm in the a-b direction) separated by a set of normal regions. Dravid et al. extended this model studying the hole carrier concentration along the boundary.(Dravid *et al.* 1993) There are two major drawbacks of both models. First, none of the models have been used to correctly interpret the low magnetic field behavior of the grain boundaries. Secondly the microstructure of the boundary has never been correlated to the transport properties to confirm the models with respect to the transport data.

The present work studies grain boundaries with the same macroscopic misorientation, but with three markedly different transport properties, varying from resistive to superconducting. Microstructural features of the boundaries were analyzed using transmission electron microscopy (TEM) and high resolution electron microscopy (HREM) to determine consistent differences in the boundary structure (for further details see references Vuchic *et al.* 1995a; Vuchic *et al.* submitted(a); Vuchic *et al.* submitted(b)). A grain boundary model is proposed here based on the observed microstructure and transport data. Simulations of the magnetic field behavior based on the microstructural model are then made to show the effects of the microstructural features on the transport with qualitative agreement.

### **Experimental Procedure**

Both bi-epitaxial grain boundaries(Charet *et al.* 1991a; Charet *et al.* 1991b) and sputter-induced epitaxy grain boundaries(Chewet *et al.* 1992; Vuchic *et al.* 1995c; Vuchic *et al.* 1995d) were formed in YBCO thin films. The thin films all had 45° [001] tilt grain boundaries and thus had macroscopically identical misorientations. The details of the formation of the grain boundaries using these techniques is described elsewhere.(Charet *et al.* 1991a; Charet *et al.* 1991b; Vuchic 1995a)

The YBCO films were grown between 2500Å and 3000Å thick using two different growth techniques: pulsed laser deposition (PLD) and pulsed organo metallic beam epitaxy (POMBE). The growth techniques are described in more detail by others.(Charet *et al.* 1991a; Buchholz *et al.* 1994) The orientation relation between the two epitaxial variants was confirmed using backscatter electron Kikuchi patterns. The films were then patterned using a molybdenum shadow-mask and low voltage (500 eV) argon ion milling to generate microbridges which allowed measurement of the voltage drop in three separate channels. The microbridge was 35-40 µm wide and allowed comparison between the grain boundary and grain properties. The contacts were formed using a short sputter treatment of the contact pads and subsequent *in situ* silver evaporation. The samples were annealed for 4-8 hours at 450° C in flowing high purity oxygen. Gold leads were placed on the sample using silver paint. Low temperature measurements were performed using a He flow cryostat. Resistance vs. temperature, current vs. voltage as a function of temperature and magnetic field were studied.

Samples were thinned for transmission electron microscopy (TEM) analysis using standard grinding, dimpling and ion milling procedures. The

samples were never exposed to water or high temperature to minimize sample damage. TEM was performed on a Phillips CM30 with energy dispersive x-ray (EDX) capability and high resolution electron microscopy was performed on a JEOL 4000 EXII. All microscopy was performed at an accelerating voltage of 200 kV or less to minimize beam damage.

## Results

Three types of grain boundaries will be compared in this work. They are all macroscopically similar, 45° [001] tilt grain boundaries, but with strikingly different transport properties and microstructure. The detailed analysis of the transport properties and the microstructure of all the boundaries discussed is shown elsewhere.(Vuchic 1995a) In this work the critical current vs. magnetic field behavior of the boundaries is presented in light of the microstructural observations and the interpretation will be discussed in the following section.

For the magnetic field behavior measurements discussed below the sample was biased just below the maximum critical current value with a d.c. constant current. The magnetic field was applied perpendicular to the film surface and parallel to the grain boundary plane. The voltage was measured as the applied magnetic field was increased and decreased. The voltage is related to the critical current such that the minimum voltage is equivalent to the maximum critical current of the boundary. The Patterson function of the  $I_c(B)$  data is also presented. The Patterson function is the inverse Fourier transform of  $I_c^2(B)$  which, if one can use the simple interpretation of  $I_c(B)$  as the Fourier transform of the conduction paths across the boundary, is the autocorrelation of

these (see later). The term Patterson function is used here since it is (in this approximation) identical to the usage in x-ray or electron diffraction.

The first set of samples were POMBE grown bi-epitaxial boundaries which were fully resistive. The grains had a very narrow superconducting transition at 91 K, however the grain boundaries had an increasing resistance with decreasing temperature down to the lowest temperatures measured (4.2 K). The resistance was very high, being on the order of 15 to 20 Ohms at 4.2 K. The boundaries were covered by precipitates over 50% of their length. More importantly, however, there was a 1 nm wide disordered region along all the areas of the boundary that were not disrupted by precipitates. These boundaries will be referred to as "resistive bi-epitaxial" boundaries.

The second set of bi-epitaxial grain boundaries were made using PLD and were superconducting. The R-T behavior showed the grains going superconducting at approximately 86-88 K, but a finite resistance remaining across the grain boundary down to almost 40 K. This extended foot-like structure is due to the reduced Josephson coupling energy across the boundary from the low critical current densities. The reduced coupling energy allows the thermal energy to create a finite resistance due to thermally activated phase slippage (TAPS) which is described in more detail by others (Gross et al.)(Gross 1992). Despite being superconducting, the boundaries did have relatively low values for the critical current densities ( $2 \times 10^3$  A/cm<sup>2</sup> at 4.2 K). TEM analysis shows that these grain boundaries have precipitates along only approximately 10% of their length. They appear to be structurally well connected at the boundary with some short asymmetric (100) (110) facets (up to 10 nm in length). The grain boundary plane was inclined in many regions, changing the local

grain boundary symmetry completely from the microfaceted regions, this has also been proven by cross-sectional analysis done by Rosner et al.(Rosner *et al.* 1992) These grain boundaries will be referred to as "superconducting bi-epitaxial" boundaries (for more details on the microstructure and transport see references (Vuchic *et al.* submitted (b); Vuchic 1995a).

The sputter-induced epitaxy grain boundaries had the best superconducting properties of the boundaries measured. The R-T behavior also exhibited a foot-like structure with a finite resistance across the boundary down to approximately 80 K (for the same measuring current density as for the superconducting bi-epitaxial samples). The critical current density ( $5.1 \times 10^4$  A/cm<sup>2</sup> at 4.2 K) was more than an order of magnitude larger than the superconducting bi-epitaxial boundaries. The dominant microstructural feature of these grain boundaries is low index (100) (110) asymmetrically faceted regions over 70% of the grain boundary length. These facets extended as long as 100 nm along the grain boundary (an order of magnitude longer than observed in the bi-epitaxial boundaries). This is a clear distinction between the bi-epitaxial and sputter-induced epitaxy grain boundaries. The details of the structure and transport properties are in references (Vuchic 1995a; Vuchic *et al.* 1995c; Vuchic *et al.* submitted(a)).

The magnetic field behavior of a superconducting bi-epitaxial grain boundary is shown in figures A1 a-b with the corresponding Patterson function of figure A1a shown in figure A2 (see below for a discussion on the units used in the Patterson function). The corresponding figures for the sputter-induced epitaxy grain boundaries are shown in figures A3-A6. There are some general comments that can be made about these results:

- The data was hysteretic (with increasing and decreasing field - see figure A1b) indicating the presence of trapped flux as noted by others.
- The critical current never went fully to zero indicating inhomogeneous current flow across the boundary.
- There is clearly no simple Fraunhofer-like interference function which is expected for a Josephson junction with uniform current flow across the junction and homogeneous magnetic field penetration.
- There is an oscillating structure in the low frequency part of the Patterson function.
- From the bi-epitaxial to the sputter-induced epitaxy to the second sputter-induced epitaxy (see figures A5-A6) sample the "noise" level in the high frequency regime of the Patterson function increases (see below).

The features of the raw data have been observed in both bi-epitaxial and bi-crystal grain boundaries by other groups (Mayer et al. and Early et al.)(Mayer et al. 1993)(Early et al. 1994) It has also been observed that oscillations in the critical current of the grain boundaries exist up to fields as high as 12 T (Daumling et al. 1992; Sarnelli et al. 1993b; Froehlich et al. 1995).

### Numerical Grain Boundary Model

Our experimental results as well as those of others (Mayer et al. 1993)(Early et al. 1994) clearly show that at least for boundaries of size about 40 microns, simple Fraunhofer-like patterns are not observed. However, this does

not mean that the basic ideas of Josephson junctions do not apply, rather that a more complicated model of an inhomogeneous boundary is required.

In order to simulate the grain boundary model it is appropriate to start by analyzing the equations which govern the behavior of the current in field. In the most general case we can write:

$$I_c(B) = \left| \int J_c(r, B) dr \right|$$

$$I_c(B) = \left| \int A(r) \exp\left(\frac{2\pi i \Phi(r, B)}{\Phi_0}\right) dr \right|$$

where:

$J_c(r, B)$  is the critical current density at any point,  $r$ , for a given field,  $B$ .

$\Phi(r, B)$  is the total flux between 0 and  $r$  at a given applied field,  $B$ .

$\Phi_0$  is the flux quantum.

$A(r)$  includes the transmittance across the grain boundary.

This equation only depends on the existence of magnetic field as a vector potential, and therefore should be valid unless some very exotic mechanism governs superconductivity in these materials. To reduce this equation to the more standard form with simple Fraunhofer-like diffraction effects two approximations are required. The first of these is that  $\Phi(r, B)$  is linear with the external field across the entire junction, i.e. that there is little to no flux-trapping. From the hysteresis in the data we know that this is not strictly true. However, to include this is a formidable problem probably requiring a Monte-Carlo simulation; we will assume here that this effect is small. The second approximation is that the field penetration is constant across the boundary. We will assume that this is not the case and there is non-uniform penetration of the field in the junction as shown in figure A7. Therefore in this simulation the

value for the flux between two points is varied depending on whether there is a superconducting or normal region. In this case the current is given by an equation of form

$$\begin{aligned} I_c(B) &= \left| \int A(r) \exp(2\pi i \alpha(r)B) dr \right| \\ &= \left| \int t(r) \exp(2\pi i \alpha'(r)rB) dr \right| \end{aligned}$$

where:

$$t(r) = A(r) \exp(2\pi i [\alpha(r) - \alpha'(r)r]B)$$

$$\alpha'(r) = \text{gradient of the phase } \alpha(r).$$

We have here a (complex) transmission term  $t(r)$  for any region of the boundary with at least locally something similar to a Fourier Transform provided that the gradient of the phase is constant. (We are using terms such as a transmission function for consistency with electron diffraction where similar integrals occur.) The above equation is useful to describe the numerical model (see below), but is best written in a more conventional (diffraction) form:

$$I_c(B) = \left| \int T(r) \exp(2\pi i \beta r B) dr \right|$$

with:

$$T(r) = A(r) \exp(2\pi i [\alpha(r) - \beta r]B)$$

In this case the Patterson function is equal to:

$$P(r) = \int T^*(r - r') T(r') dr$$

The Patterson function is the autocorrelation of the (complex) transmission function  $T(r)$ , and can also be interpreted in an optical sense as the transverse coherence (see for example Born and Wolf (Bornet *al.* 1975)) of the (pair) current

across the boundary. If the boundary is very homogeneous, a high degree of coherence is preserved; if the boundary is inhomogeneous the current between two point  $r-r'$  and  $r'$  will be incoherent when averaged along the boundary length ( $r'$ ). No pair-breaking is involved here, and a simple analogue is transmission of a laser beam through a slit versus transmission through a piece of glass with a rough surface that provides an inhomogeneous transmission function over its area. Note that the units of the Patterson function are distance although scaling is highly problematic because it involves an assumption about a width normal to the grain boundary, within where penetration occurs, which is unknown and may itself vary from point to point.

The numerical model simulates the microstructure observed experimentally as illustrated in figure A7. The grain boundary is simulated using a random number generator to produce a distribution of normal and superconducting regions. Random numbers with a standard deviation of one are generated, the modulus squared is calculated and a cutoff point is selected to roughly simulate the amount of normal regions experimentally observed. We took  $t(r)=0$  for precipitates (or other normal regions) and  $t(r)=1$  otherwise over the total length of the boundary (2048 points). Two different values of the phase gradient ( $\alpha'(r)$ ) were taken for the normal regions and superconducting ones. For different values of the applied field the integrals were performed numerically. The simulations were all performed using SEMPER software.

The first variable analyzed is the effect of varying the magnetic field penetration into the superconducting regions of the junction (varying the slope of the phase as shown in figure A7). Figures A8-A10 show the results for a set of parallel junctions with the amount of field penetration into the

superconducting regions increasing. Figure A8 is actually a very realistic simulation for the magnetic field behavior exhibited by the bi-epitaxial grain boundary shown in figure A1. This simulation assumes that there is no field penetration into the superconducting regions. Holding everything else constant (average conduction path size, average precipitate size, microbridge width etc.) and increasing the field penetration the magnetic field behavior begins to show much more of a Fraunhofer like pattern as shown in figure A10a.

In calculating the Patterson function of the data, the central peak is removed from all the spectra (except figure A10c.) to include residual flux penetration at the boundary. The corresponding Patterson functions have a substantial broadening at the origin as the field penetration is increased. It is important to note that the Patterson function for a Fraunhofer pattern is triangular as is seen in figure A10c (figure A10c is calculated from the  $I_c(B)$  data with a central peak while figure A10b is calculated for the same curve with the peak removed). The Patterson function in figure A8b. is most similar to that of figure A2 for the bi-epitaxial. The broadening of the central peak in the Patterson function is clearly not observed in any of the experimental data. The combination of the Patterson function data and the magnetic field behavior suggest that the assumption of minimal field penetration into the superconducting regions is valid.

The current distribution at given applied fields provides further insight into the current transport. This information cannot be obtained in the experimental  $I_c(B)$  data because the phase information is lost. Figures A11 and A12 are the real and imaginary parts of the current along the length of the boundary for different magnetic field values. Figure A11 has more uniform field

distribution along the boundary with penetration at relatively evenly spaced regions. In comparison figure A12 shows non-uniform penetration of the field along the boundary. These are only two specific examples used for comparison, often a even less uniform field penetration than in figure A12 is observed. This is further evidence that the distribution of the field is critical in determining the  $I_c(B)$  behavior.

The effect of the conduction path size (i.e. the well connected regions of the boundaries) is significant. As the conduction size is increased (from figure A13 to A14) a more periodic low frequency structure appears in the magnetic field behavior with a higher frequency oscillation superimposed. These two simulations match the data very well and will be discussed more later. The size of the precipitates or normal regions also affects the magnetic field behavior as shown in figures A15 and A16. Figure A15 has larger precipitates and starts showing some periodic resonances. This supports the concept that the normal regions can control the junction transport behavior. The total junction width shows an increase in the higher frequency oscillations in the magnetic field data as the total microbridge width is increased (compare figure A13 with a narrower total bridge width to figure A17 with a wider bridge). The final variable modified is the critical current density along differing superconducting regions. This resulted in a decrease in the high frequency in the Patterson function suggesting that the current densities are not uniform along the boundary.

## Discussion

The trends found based on this model can successfully explain much of the magnetic field data. First of all figures A13 and A14 are the best fits with the data. All of these assume minimal field penetration into the superconducting regime, and only change the conduction path size. Therefore a change in conduction path size can explain the evolution of the periodic structure observed in the  $I_c(B)$  behavior of the sputter-induced epitaxy grain boundary. This is consistent with the microstructural observations that show a significant increase in the amount of faceted regions along the boundary in the sputter-induced epitaxy junctions. The inference is that the (100) (110) facets maintain higher critical currents than unfaceted regions. Also the increasing amplitude of the high frequency regime of the Patterson function is consistent with the simulations. The basic shape of the Patterson function is observed in the experimental data, but more variables could be introduced to better match the data such as a smoothing of the field penetration at the edges of the superconducting regions. Obviously a perfect quantitative match is virtually impossible with the number of variables, but the simulations qualitatively match the data.

Several observations can be made about the comparison between the data and the simulations. In both the simulations and the experimental data the critical current does not go to zero (this is also observed experimentally by other groups (Early *et al.* 1994)). The hysteretic behavior and the lack of a zero field peak in the experimental data can be explained by trapped flux in the boundary. The fact that there is no zero field peak in the bi-epitaxial data can be due to the normal regions that allow flux penetration in minimal fields, which is not accounted for in the simulation. Increases in the total junction width (shown in

figures A13 and A17) agree well with other published data which exhibit similar behavior.(Early *et al.* 1994) Furthermore this model predicts that the oscillations in the critical current would continue to high magnetic fields as has been observed by others (Daumling *et al.* 1992; Sarnelli *et al.* 1993b; Froehlich *et al.* 1995).

The grain boundary model does not assume *a priori* that the boundary is a weak link. The strong match with the data suggests that it is not inconceivable that a well structured region of the grain boundary could maintain a respectable critical current relative to the grain at zero field penetration. Furthermore the majority of the  $I_c(B)$  characteristics are dominated by the inhomogeneity of the normal regions along the boundary length. The important parameter is the ratio of total flux in the superconducting region to the total flux in the normal regions (as shown in figures A8-A10). The smaller this ratio is the more dominant are the normal regions. The width normal to the grain boundary of the magnetic field penetration may have a large influence here as mentioned previously. This implies that not only the length of the normal region (e.g. precipitates or structurally disordered regions of the boundary), but also the width will dictate where preferential penetration can first occur. A simple Fraunhofer pattern can be recovered using this model by increasing the field penetration into the superconductor or just having uniform superconducting regions along the entire length of the boundary. Currently we cannot differentiate between a grain boundary consisting of small precipitates with high flux penetration per unit area relative to the superconducting regions vs. a boundary with large precipitates with proportionally less flux penetration per unit area relative to the superconducting regions. Therefore it is not possible to make a definitive

comparison to the microstructure. In order to gain a more quantitative understanding of the role of the microstructure it will be necessary to study very narrow microbridges, perhaps as small as 1 micron, and counting the size and number of precipitates and faceted boundary regions to compare with the magnetic field data. This will have to be done for a range of boundaries with varying structure and properties to determine, for instance, the properties vs. number and size density of a given feature.

The result of penetration primarily in the normal regions of the boundary could even have implications in bulk samples where the low current carrying boundaries are a problem. The bulk boundaries could have low critical currents primarily due to statistical incoherence across the large set of parallel junctions and not necessarily be due to poor transport across the grain boundary.

The results of this work clearly indicate the importance of correlating microstructure to properties in grain boundary junctions. The structure along the boundary allows non-uniform magnetic field penetration. The simulations that match the data indicate that the field penetrates normal regions preferentially with almost none penetrating at the superconducting areas of the boundary. This results in highly complex magnetic field behavior that qualitatively matches the experimental results. The major implication of this result is that the engineering of grain boundaries must immensely improve to electronic grade material quality (defect densities in the boundary of  $\sim 10^{-8}$  cm<sup>-2</sup>) in order to form highly reproducible junction behavior.

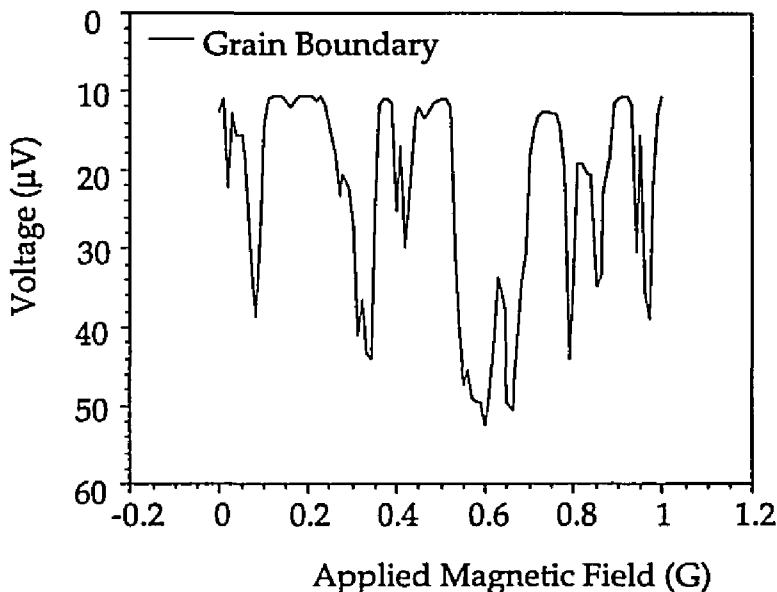


Figure A1a. The critical current vs. magnetic field behavior for a bi-epitaxial grain boundary junction at 5 K.

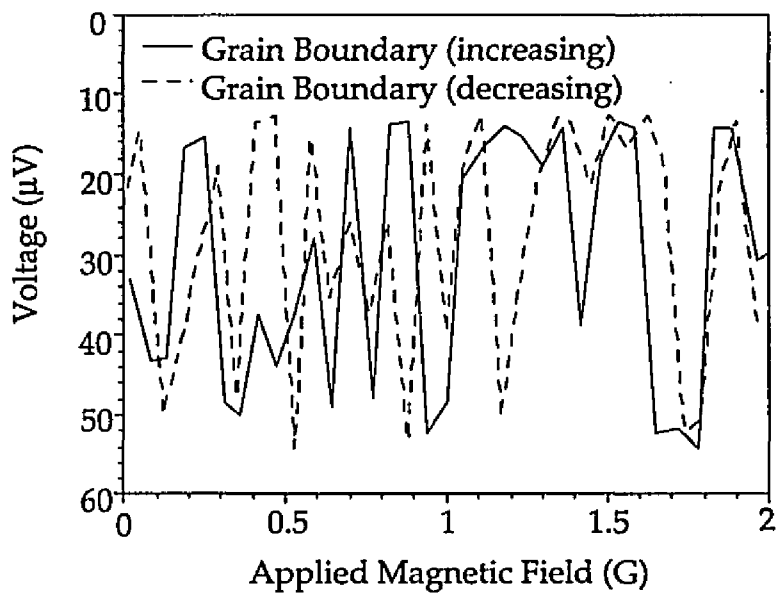


Figure A1b. The critical current vs. magnetic field behavior for increasing and decreasing field with hysteretic behavior.

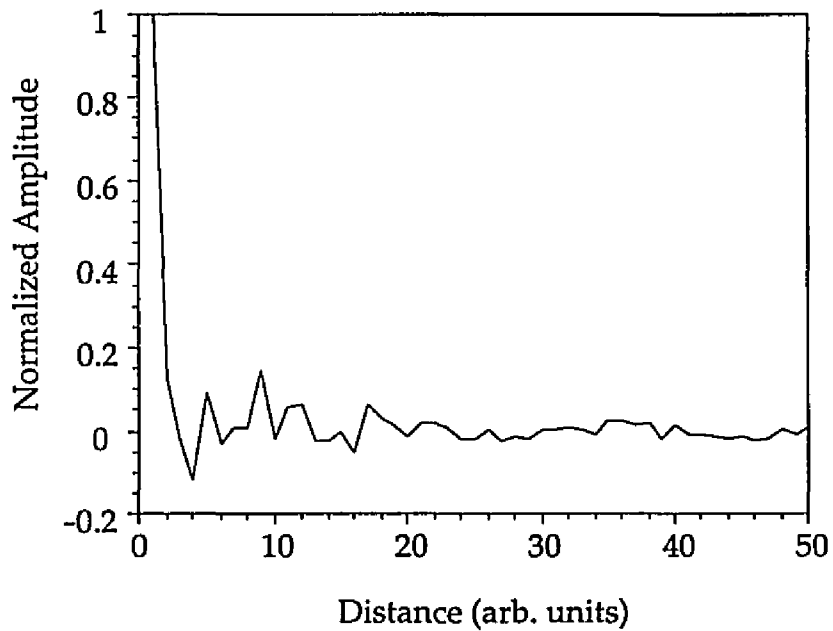


Figure A2. The Patterson function for the bi-epitaxial grain boundary junction characteristics shown in figure A1a.

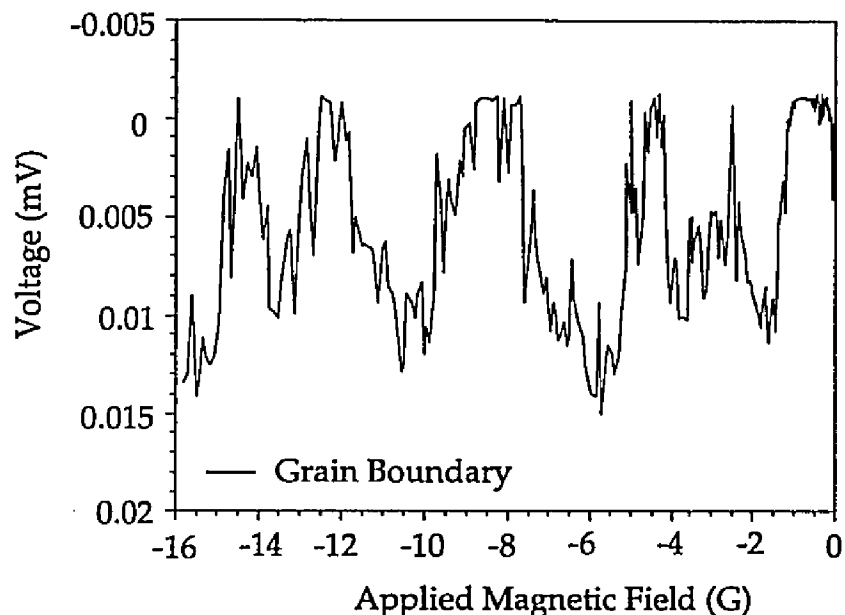


Figure A3. The magnetic field behavior for a sputter-induced epitaxy sample at 5 K.

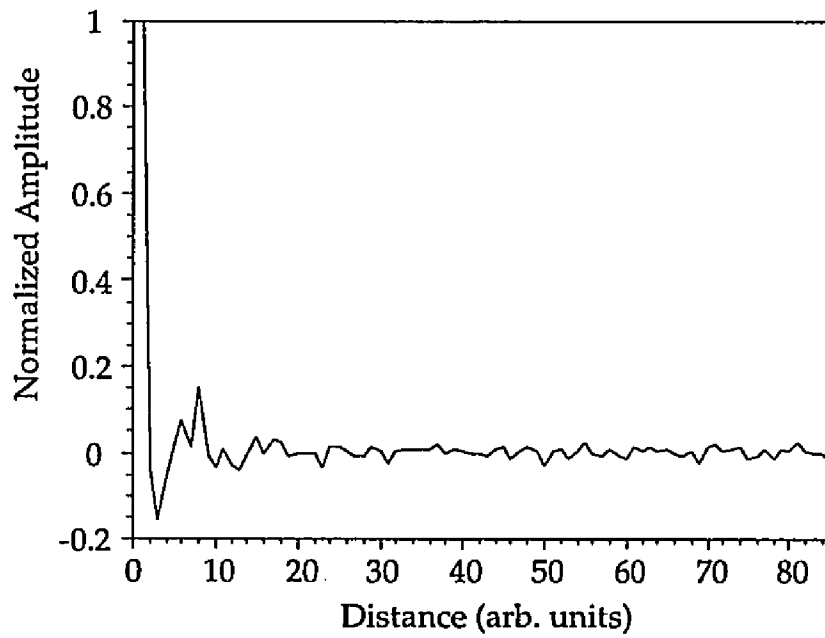


Figure A4. The Patterson function for the curve in figure A2.

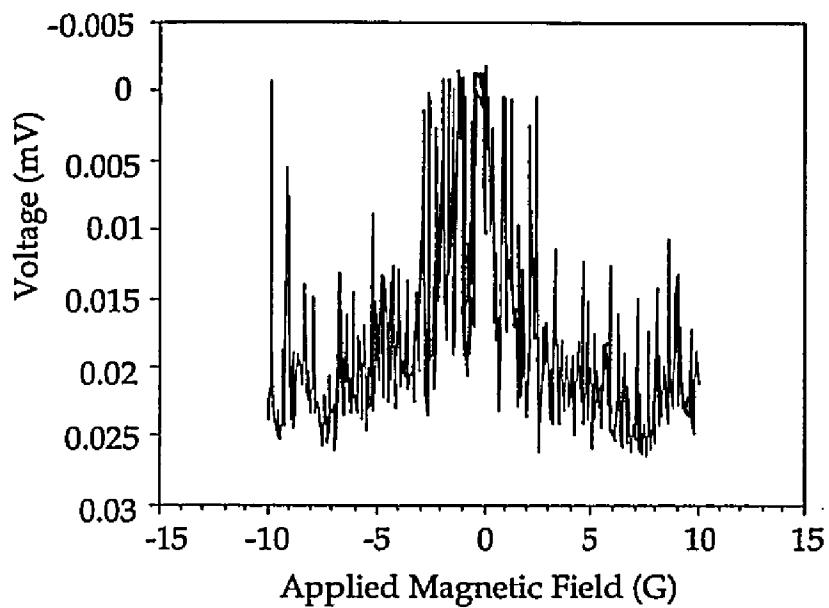


Figure A5. The critical current vs. magnetic field behavior for a multilayer sputter-induced epitaxy sample.

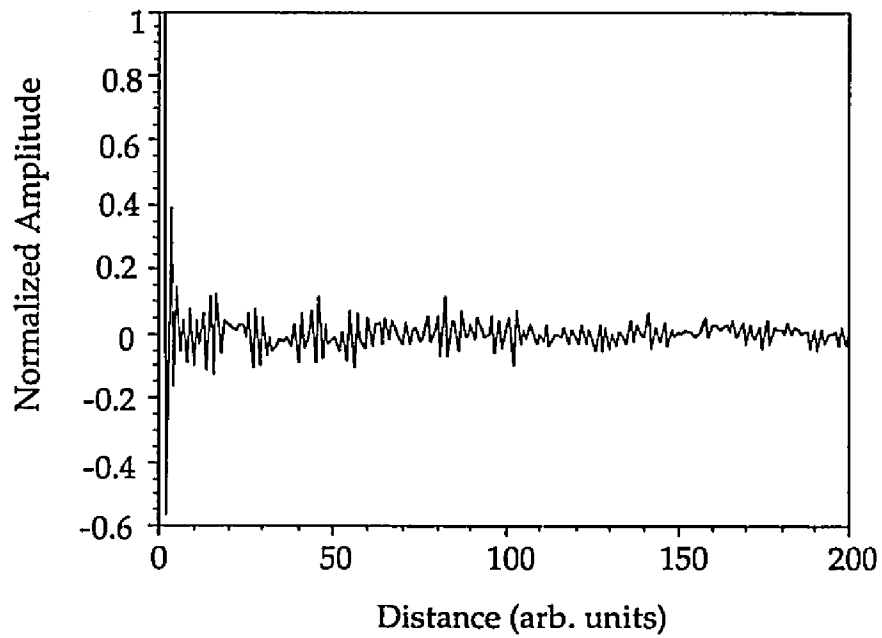


Figure A6. The corresponding Patterson function for figure A5.



Figure A7a. A micrograph of a sputter-induced epitaxy grain boundary showing the variation in the microstructure. The boundary has a precipitate (arrow) and exhibits different regions of faceting along its length.

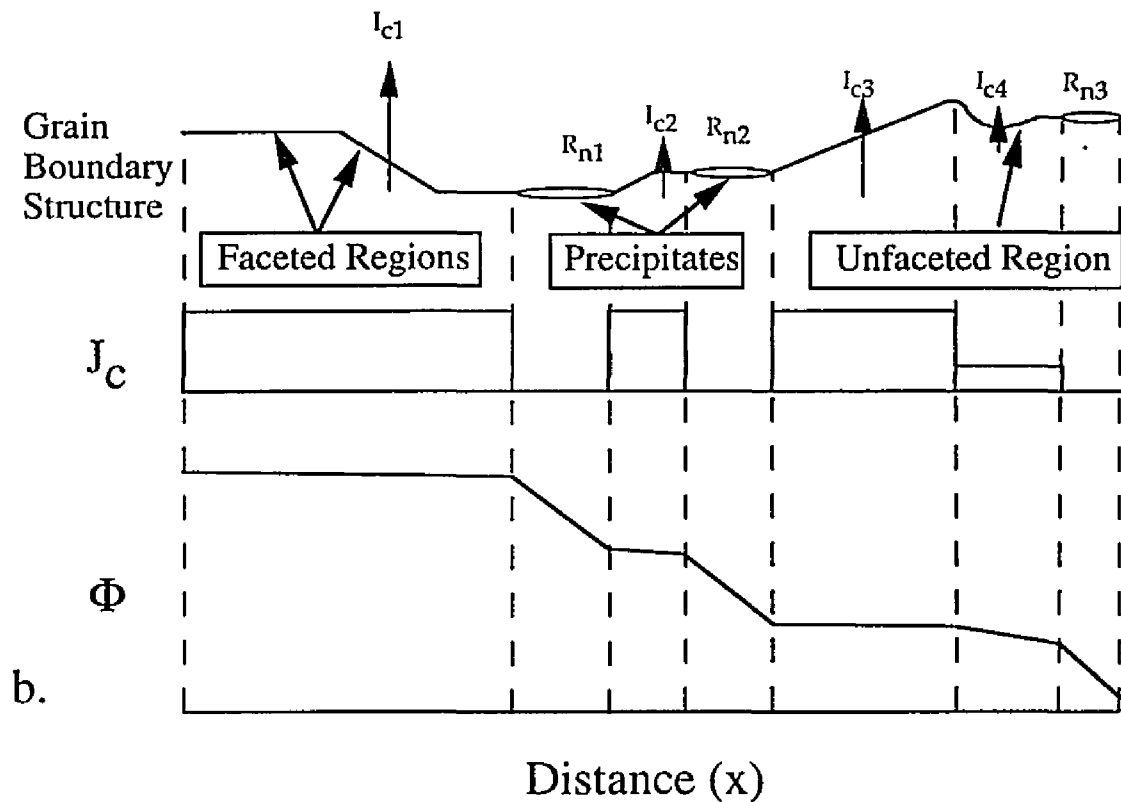


Figure A7b. A schematic representation of a grain boundary with precipitates and different types of grain boundary structure (faceted and non-faceted) along its length. The corresponding variation in critical current density and the phase along the boundary length are also shown.

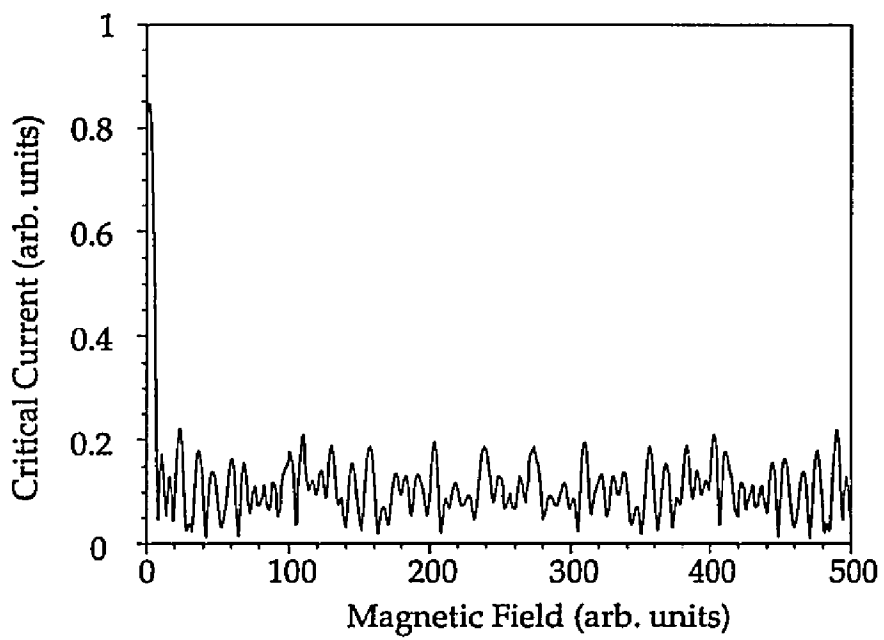


Figure A8a. The simulated critical current vs. magnetic field behavior for a grain boundary with minimal magnetic field penetration into the superconducting regions.

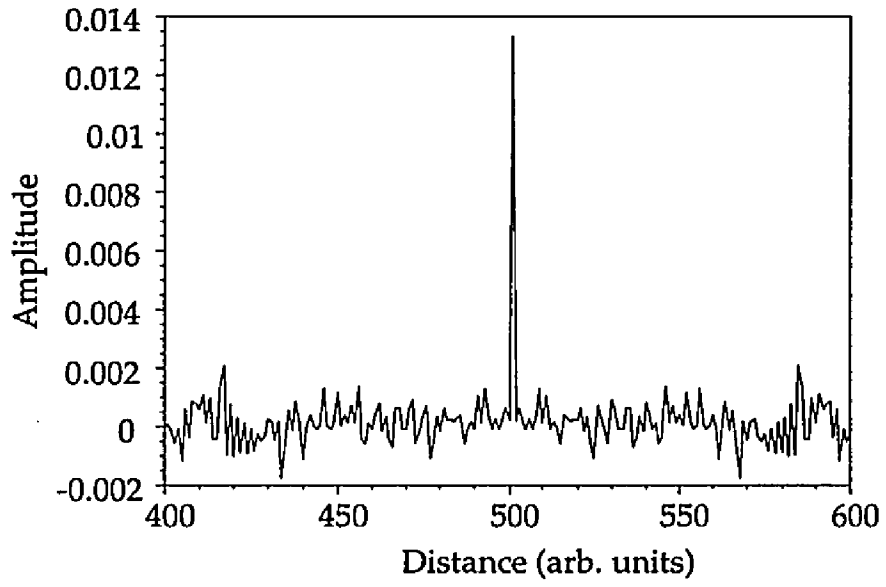


Figure A8b. The corresponding Patterson function for figure A8a with a very narrow central peak.

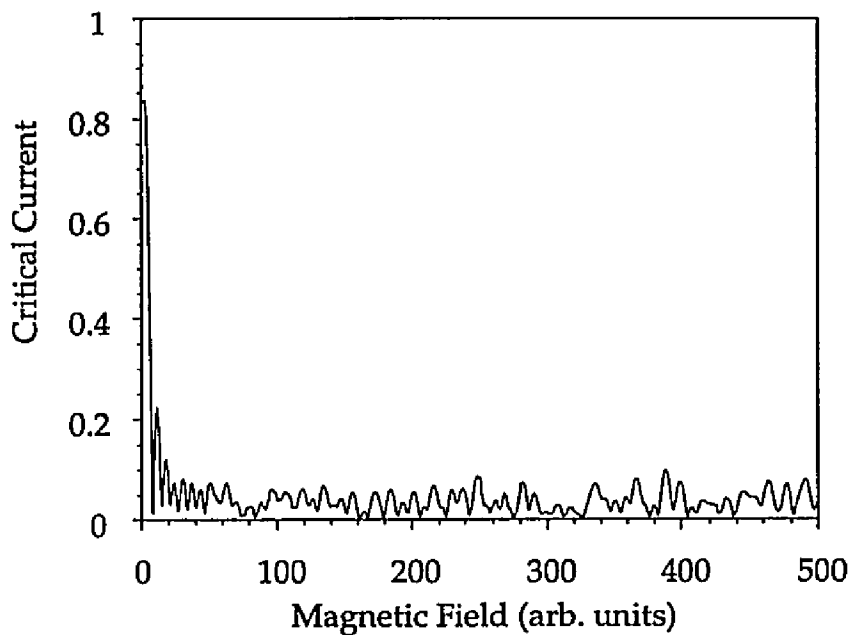


Figure A9a. The simulated critical current vs. magnetic field behavior for a grain boundary with larger penetration of the field into the superconducting region than figure A8.

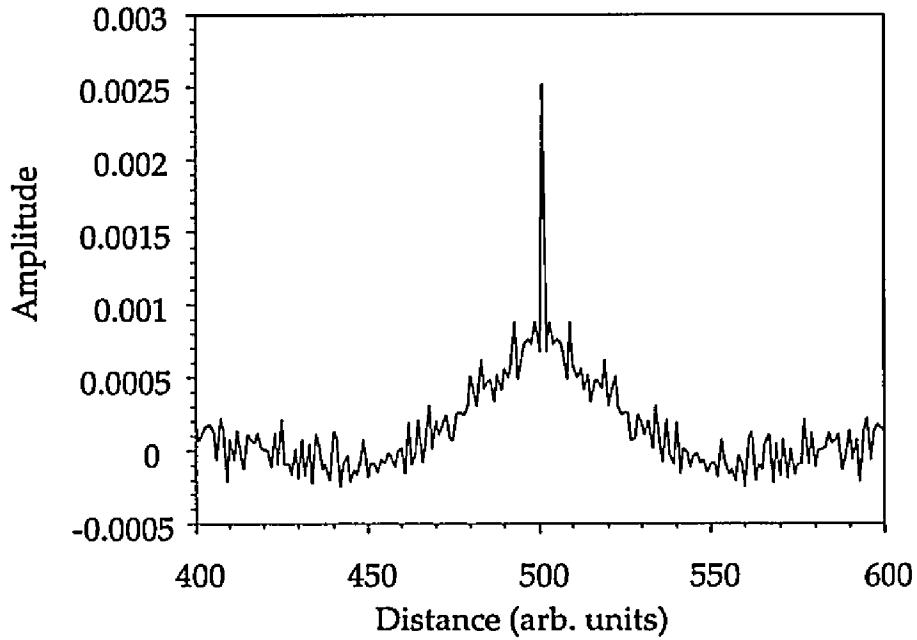


Figure A9b. The corresponding Patterson function for figure A9a with a broadening central peak relative to figure A8b.

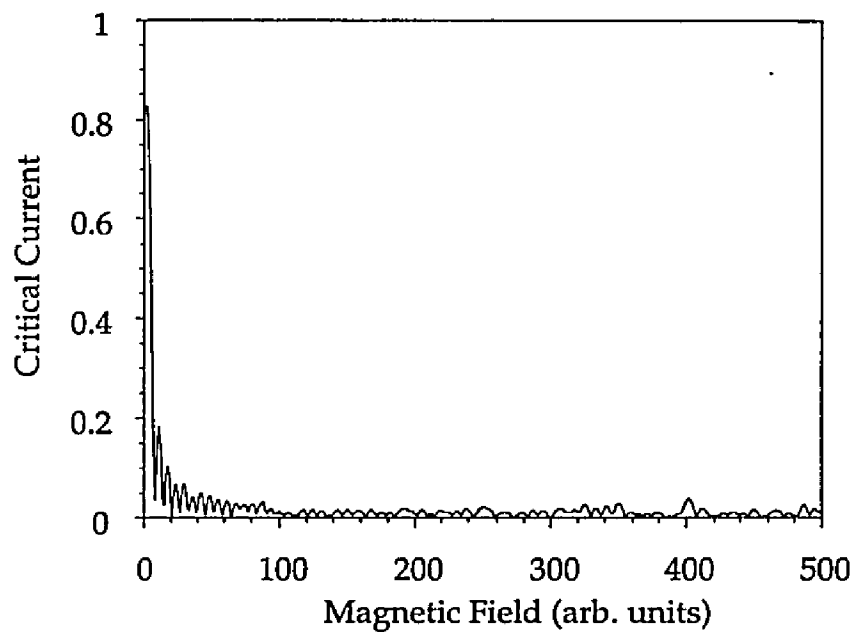


Figure A10a. The simulated behavior for a junction with almost complete penetration of the superconducting regions (virtually the same penetration as in the normal regions).

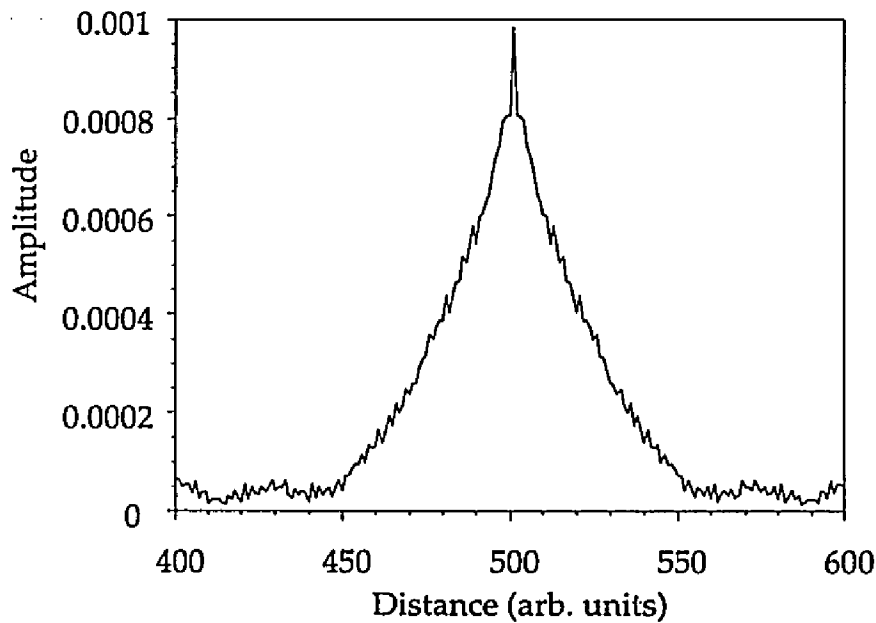


Figure A10b. The corresponding Patterson function for figure A10a with the central peak removed showing a further broadening of the central peak.

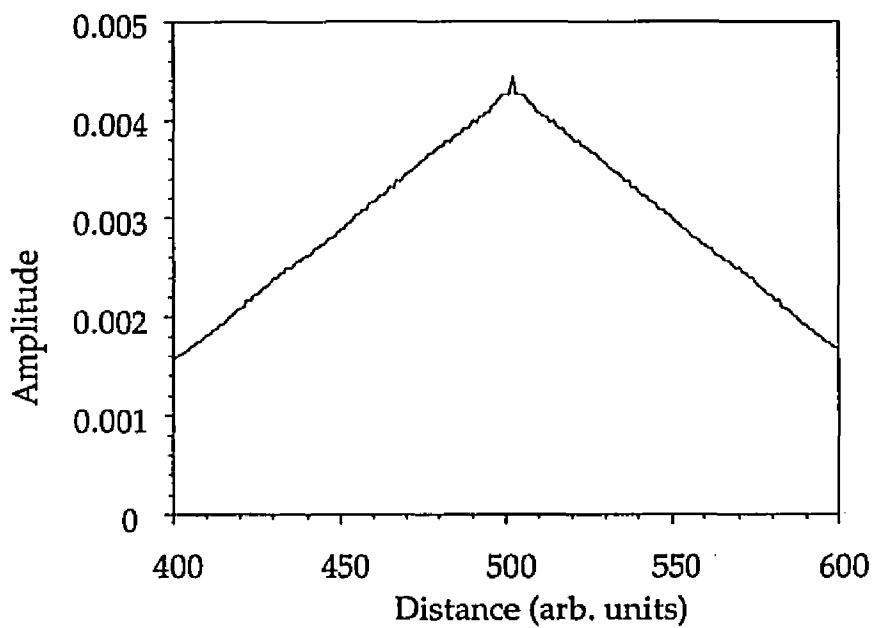


Figure A10c. The Patterson function for figure A10a without the central peak removed showing a triangular shape expected for a standard Fraunhofer pattern.

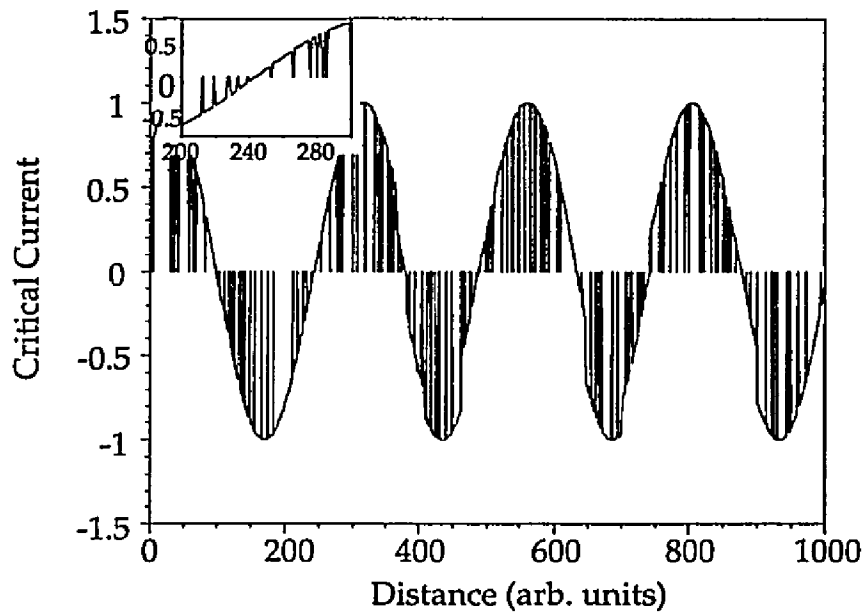


Figure A11a. The real part of the critical current traversing the boundary with relatively uniform magnetic field penetration. The inset is an enlargement of a region of the curve.

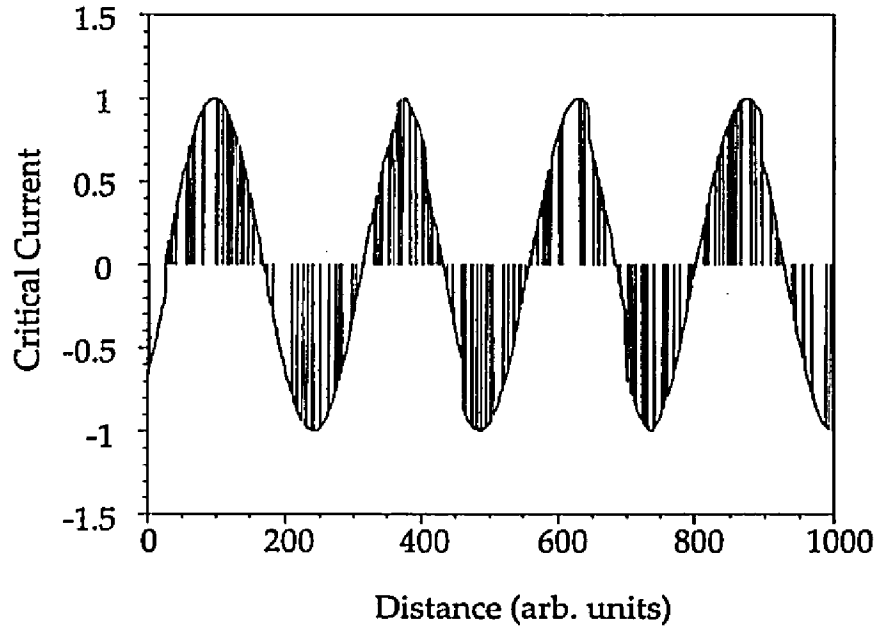


Figure A11b. The imaginary part of the critical current traversing the boundary corresponding to figure A11a.

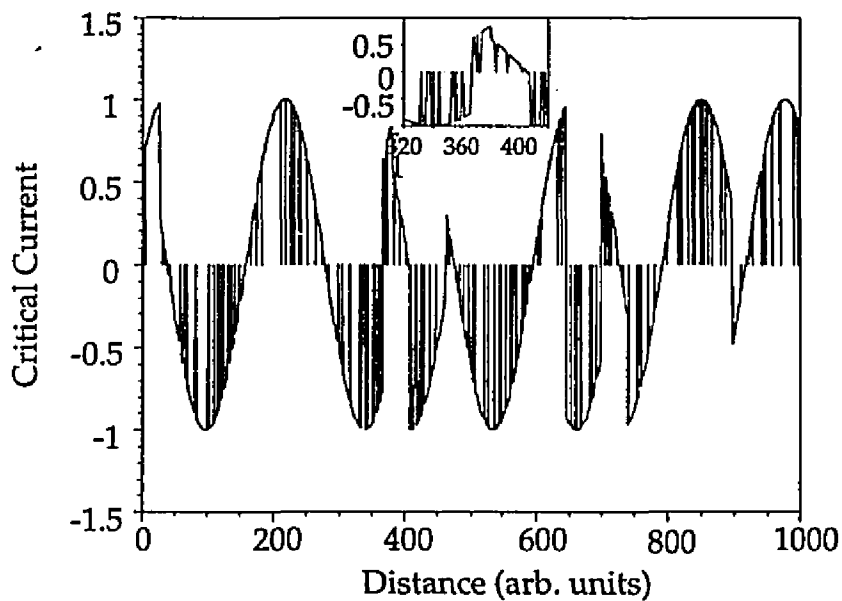


Figure A12a. The real part of the critical current traversing the boundary with non-uniform magnetic field penetration. The inset is an enlargement of a region of the curve.

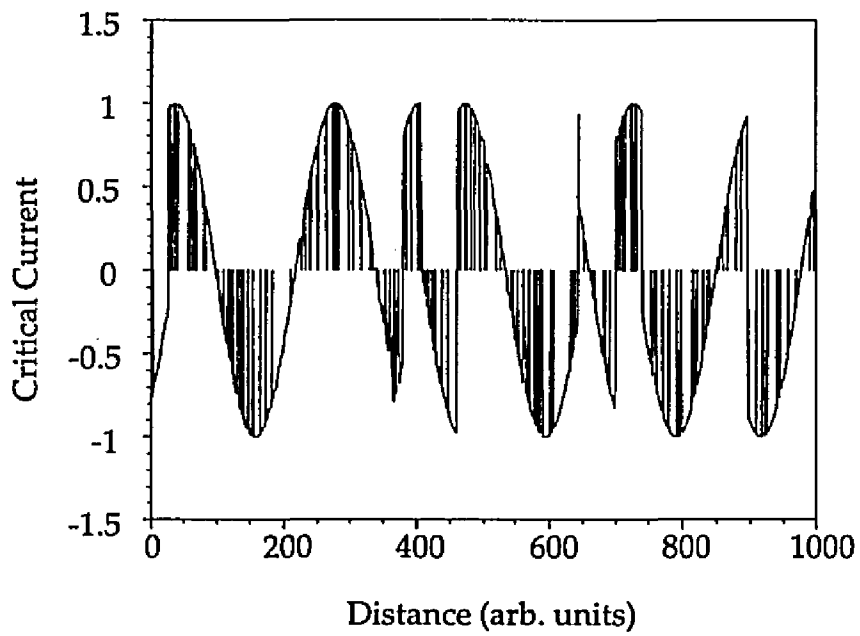


Figure A12b. The imaginary part of the critical current traversing the boundary corresponding to figure A12a.

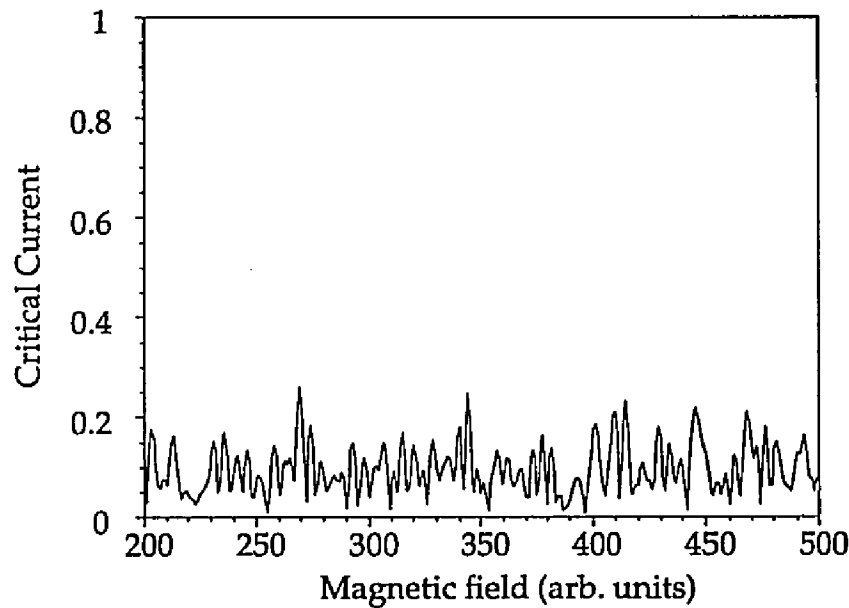


Figure A13a. The simulated behavior for a grain boundary with a relatively small average superconducting region distribution. This graph is a good match with the bi-epitaxial data.

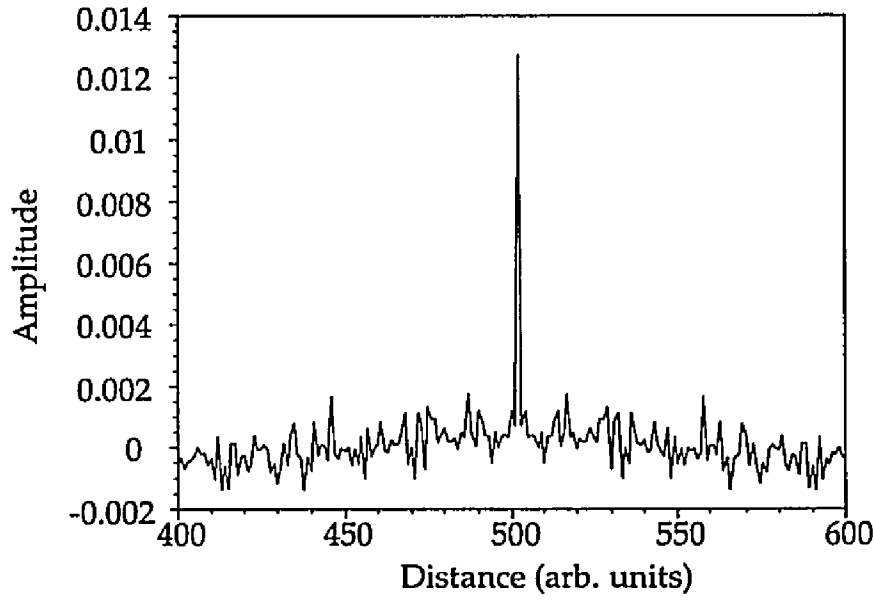


Figure A13b. The Patterson function for figure A13a.

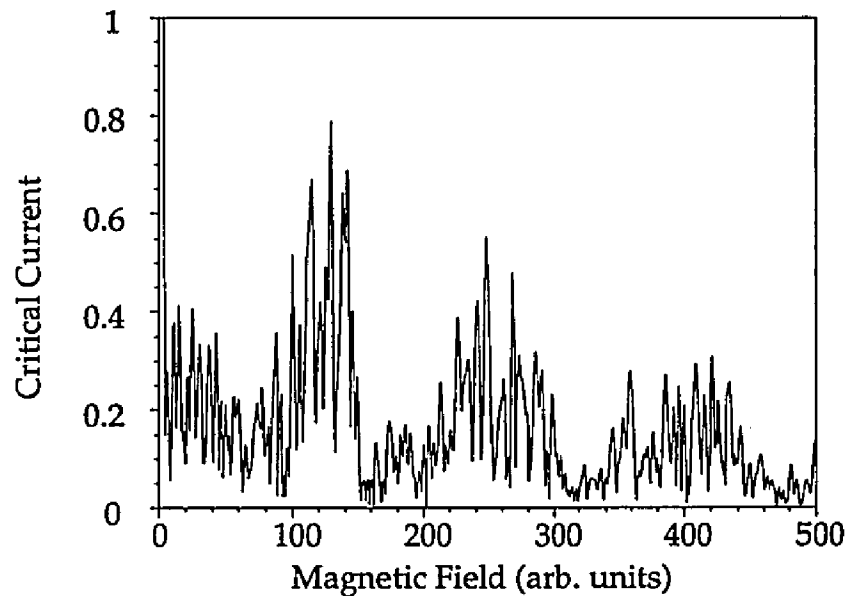


Figure A14a. The simulated behavior for a grain boundary with a 10-fold increase in the size of conduction paths across the boundary. This matches the experimental results for the sputter-induced epitaxy grain boundaries.

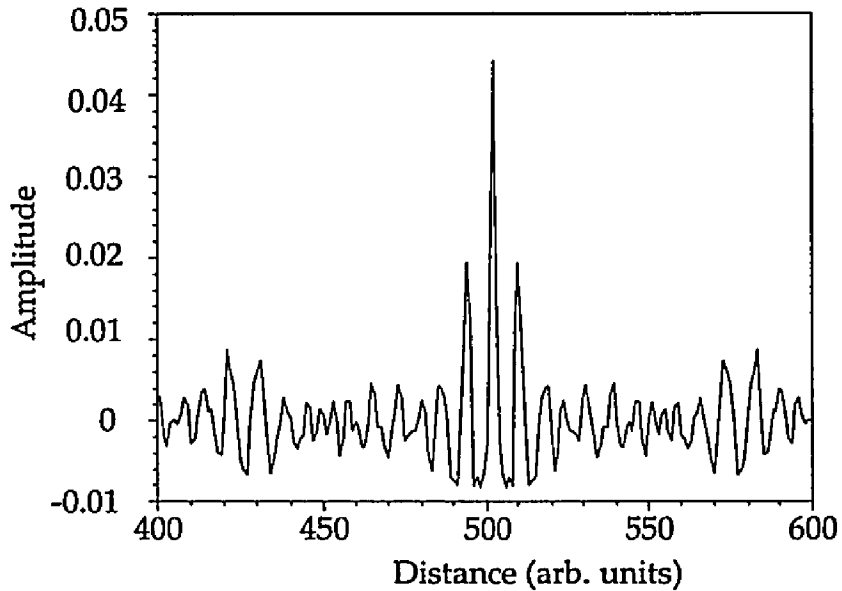


Figure A14b. The corresponding Patterson function for figure A14a that is in good agreement with figure A6.

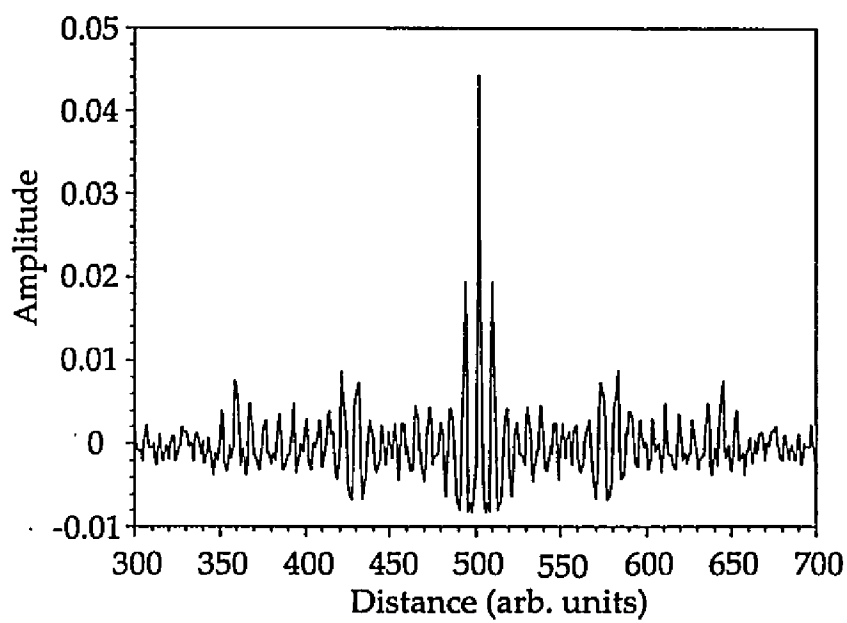


Figure A14c. Enlargement of figure A14b to show Moire interference pattern in Patterson function.

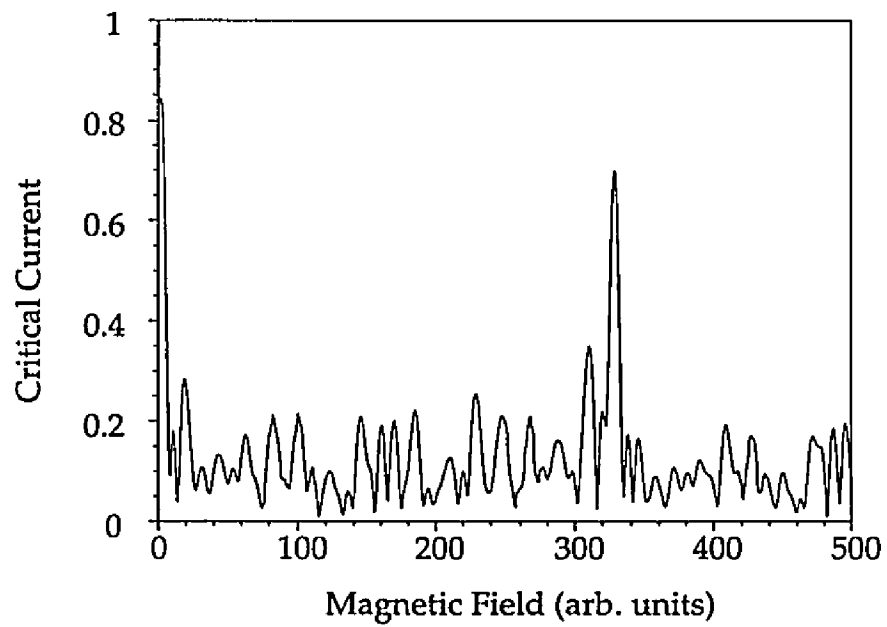


Figure A15. The simulated behavior for a grain boundary with small precipitates.

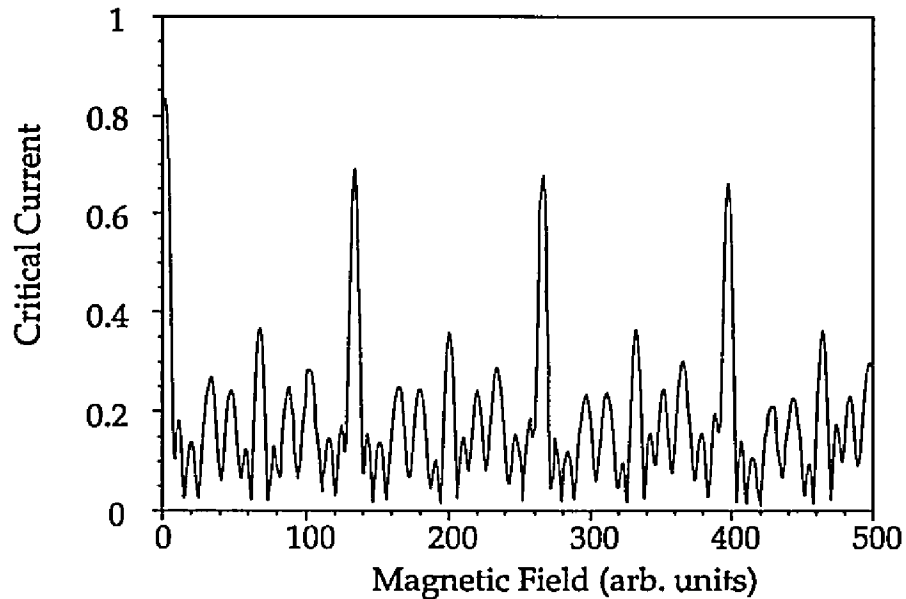


Figure A16. The simulated behavior for the identical boundary as in figure A15 except for double the size for the precipitates.

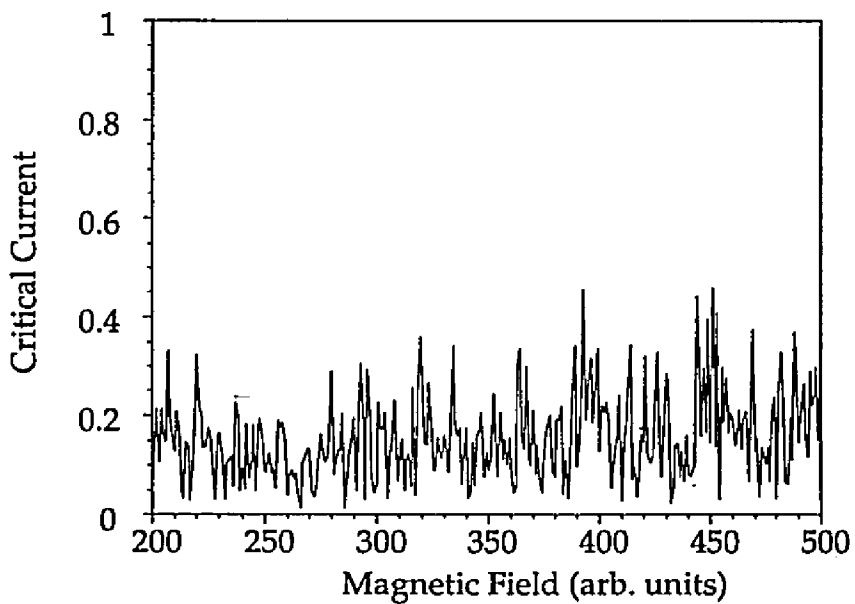


Figure A17. The same grain boundary as in figure A13, but for a microbridge that is twice as wide. There is an increase in the higher frequency modulations relative to figure A13.

## References

- Alarco, J.A., Olsson, E., Ivanov, Z.G., Nilsson, P.A., Winkler, D., Stepansov, E.A. and Tzalenchuk, A.Y. "Microstructure of an artificial grain boundary weak link in an  $\text{YBa}_2\text{Cu}_3\text{O}_{7-\delta}$  thin film grown on a (100)(110), [001]-tilt  $\text{Y-ZrO}_2$  bicrystal." Ultramicroscopy 51 (1993): 239-246.
- Babcock, S.E., Cai, X.Y., Larbalestier, D.C., Shin, D.H., Zhang, N., Zhang, H. and Kaiser, D.L. "A TEM-EELS study of hole concentrations near strongly- and weakly-coupled grain boundaries in electromagnetically-characterized  $\text{YBa}_2\text{Cu}_3\text{O}_{7-\delta}$  bicrystals." Physica C (1994):
- Born, M. and Wolf, E. *Principles of Optics*, London: Pergamon Press (1975).
- Browning, N.D., Chisholm, M.F. and Pennycook, S.J. "Cell-by-cell mapping of carrier concentrations in high-temperature superconductors." Interface Science 1 (1993): 309-320.
- Buchholz, D.B., Duray, S.J., Schulz, D.L., Marks, T.J., Ketterson, J.B. and Chang, R.P.H. "Surface morphology studies of Y-Ba-Cu-oxide thin films prepared by pulsed organometallic beam epitaxy." Materials Chemistry and Physics 36 (1994): 377-382.

Char, K., Colclough, M.S., Garrison, S.M., Newman, N. and Zaharchuk, G. "Bi-epitaxial grain boundary junctions in  $\text{YBa}_2\text{Cu}_3\text{O}_7$ ." Appl. Phys. Lett. **59** (1991a): 733-735.

Char, K., Colclough, M.S., Lee, L.P. and Zaharchuk, G. "Extension of the bi-epitaxial Josephson junction process to various substrates." Appl. Phys. Lett. **59** (1991b): 2177-2179.

Chew, N.G., Goodyear, S.W., Humphreys, R.G., Satchell, J.S., Edwards, J.A. and Keene, M.N. "Orientation control of  $\text{YBa}_2\text{Cu}_3\text{O}_7$  thin films on  $\text{MgO}$  for epitaxial junctions." Applied Physics Letters **60** (1992): 1516-1518.

Daumling, M., Sarnelli, E., Chaudhari, P., Gupta, A. and Lacey, J. "Critical current of a high-T<sub>c</sub> Josephson grain boundary junction in high magnetic field." Appl. Phys. Lett. **61** (1992): 1355-1357.

Dimos, D., Chaudhari, P. and Mannhart, J. "Superconducting transport properties of grain boundaries in  $\text{YBa}_2\text{Cu}_3\text{O}_7$  bicrystals." Phys. Rev. B **41** (1990): 4038-4049.

Dimos, D., Chaudhari, P., Mannhart, J. and LeGoues, F.K. "Orientation Dependence of Grain-Boundary Critical Currents in  $\text{YBa}_2\text{Cu}_3\text{O}_7$  Bicrystals." Phys. Rev. Lett. **61** (1988): 219-222.

David, V.P., Zhang, H. and Wang, Y.Y. "Inhomogeneity of charge carrier concentration along the grain boundary plane in oxide superconductors." Physica C 213 (1993): 353-358.

Early, E.A., Steiner, R.L., Clark, A.F. and Char, K. "Evidence for parallel junctions within high-T<sub>c</sub> grain-boundary junctions." Phys. Rev. B 50 (1994): 9409-9418.

Froehlich, O.M., Schulze, H., Beck, A., Mayer, B., Alff, L., Gross, R. and Huebener, R.P. "Analysis of the critical current density in grain boundary Josephson junctions on a nanometer scale." Appl. Phys. Lett. 66 (1995): 2289-2291.

Gross, R. "Grain boundary Josephson junctions in the high temperature superconductors." In *Interfaces in superconducting systems* edited by S. L. Shinde and D. Rudman. New York: Springer Verlag, (1992).

Ivanov, Z.G., Nilsson, P.Å., Winkler, D., Alarco, J.A., Claeson, T., Stepantsov, E.A. and Tzalenchuk, A.Y. "Weak links and dc SQUIDs on artificial nonsymmetric grain boundaries in  $\text{YBa}_2\text{Cu}_3\text{O}_{7-\delta}$ ." Appl. Phys. Lett. 59 (1991): 3030-3032.

Jia, C.L. and Urban, K. "Structure of grain boundaries in  $\text{YBa}_2\text{Cu}_3\text{O}_7$  thin-film step-edge junctions." Interface Science 1 (1993): 291-308.

Mayer, B., Schuster, S., Beck, A., Alff, L. and Gross, R. "Magnetic field dependence of the critical current in  $\text{YBa}_2\text{Cu}_3\text{O}_{7-\delta}$  bicrystal grain boundary junctions." Appl. Phys. Lett. **62** (1993): 783-785.

Moeckly, B.H., Lathrop, D.K. and Buhrman, R.A. "Electromigration study of oxygen disorder and grain-boundary effects in YBCO thin films." Phys. Rev. B **47** (1993): 400-417.

Rosner, S.J., Char, K. and Zaharchuk, G. "Microstructure of biepitaxial grain boundary junctions in  $\text{YBa}_2\text{Cu}_3\text{O}_7$ ." Appl. Phys. Lett. **60** (1992): 1010-1012.

Sarnelli, E. "A two-channel model for transport across high- $T_c$  bicrystal grain boundary junctions." Interface Science **1** (1993a): 287-290.

Sarnelli, E., Chaudhari, P. and Lacey, J. "Residual critical current in high  $T_c$  bicrystal grain boundary junctions." Appl. Phys. Lett. **62** (1993b): 777-779.

Traeholt, C., Wen, J.G., Zandbergen, H.W., Shen, Y. and Hilgenkamp, J.W.M. "TEM investigation of  $\text{YBa}_2\text{Cu}_3\text{O}_7$  thin films on  $\text{SrTiO}_3$  bicrystals." Physica C **230** (1994): 425-434.

Vuchic, B.V. "The formation, transport properties and microstructure of  $45^\circ$  [001] tilt grain boundaries in  $\text{YBa}_2\text{Cu}_3\text{O}_{7-x}$  thin films" Northwestern University. (1995a).

Vuchic, B.V., Merkle, K.L., Baldo, P., Dean, K.A., Buchholz, D.B., Chang, R.P.H., Zhang, H. and Marks, L.D. "The formation, transport properties and microstructure of individual sputter-induced epitaxy grain boundaries in YBCO thin films." (submitted(a)).

Vuchic, B.V., Merkle, K.L., Char, K., Buchholz, D.B., Chang, R.P.H. and Marks, L.D. "Bi-epitaxial grain boundaries in YBCO thin films prepared by pulsed laser deposition and pulsed organometallic beam epitaxy: Direct comparison of transport properties and grain boundary structure." (submitted(b)).

Vuchic, B.V., Merkle, K.L., Dean, K.A., Buchholz, D.B., Chang, R.P.H. and Marks, L.D. "Integrated multi-layer sputter-induced 45° YBCO grain boundary junctions." Appl. Phys. Lett. 67 (1995b): 1013-1016.

Vuchic, B.V., Merkle, K.L., Dean, K.A., Buchholz, D.B., Chang, R.P.H. and Marks, L.D. "Sputter-induced grain boundary junctions in  $\text{YBa}_2\text{Cu}_3\text{O}_{7-\text{x}}$  thin films on MgO." Journal of Applied Physics 77 (1995c): 2591-2594.

Vuchic, B.V., Merkle, K.L., Funkhouser, J.W., Buchholz, D.B., Dean, K.A., Chang, R.P.H. and Marks, L.D. "YBaCuO 45° [001] tilt grain boundaries induced by controlled low-energy sputtering of MgO substrates: transport properties and atomic-scale structure." IEEE Transactions on Applied Superconductivity 5 (1995d): 1225-1228.

## References

- Alarco, J.A., Olsson, E., Ivanov, Z.G., Nilsson, P.A., Winkler, D., Stepansov, E.A. and Tzalenchuk, A.Y. "Microstructure of an artificial grain boundary weak link in an  $\text{YBa}_2\text{Cu}_3\text{O}_{7-\delta}$  thin film grown on a (100)(110), [001]-tilt  $\text{Y-ZrO}_2$  bicrystal." Ultramicroscopy 51 (1993): 239-246.
- Ambegaokar, V. and Baratoff, A. "Tunneling between superconductors." Phys. Rev. Lett. 10 (1963): 486-489.
- Ambegaokar, V. and Halperin, B.I. "Voltage due to thermal noise in the dc Josephson effect." Phys. Rev. Lett. 22 (1969): 1364-1366.
- Anderson, P.W. and Rowell, J.M. "Probable observation of the Josephson superconducting tunneling effect." Phys. Rev. Lett. 10 (1963): 230-232.
- Babcock, S.E., Cai, X.Y., Kaiser, D.L. and Larbalestier, D.C. "Weak-link-free behaviour of high-angle  $\text{YBa}_2\text{Cu}_3\text{O}_{7-\delta}$  grain boundaries in high magnetic fields." Nature 347 (1990): 167-169.
- Babcock, S.E., Cai, X.Y., Larbalestier, D.C., Shin, D.H., Zhang, N., Zhang, H. and Kaiser, D.L. "A TEM-EELS study of hole concentrations near strongly- and weakly-coupled grain boundaries in electromagnetically-characterized  $\text{YBa}_2\text{Cu}_3\text{O}_{7-\delta}$  bicrystals." Physica C 227 (1994): 183-196.
- Babcock, S.E. and Larbalestier, D.C. "Evidence for local composition variations within  $\text{YBa}_2\text{Cu}_3\text{O}_{7-\delta}$  grain boundaries." Appl. Phys. Lett. 55 (1989): 393-395.
- Baglin, J.E.E. "Interface tailoring for adhesion using ion beams." Nuclear Instruments and Methods in Physics Research B B39 (1989): 764-768.
- Baglin, J.E.E. "Interface design for thin film adhesion." In *Fundamentals of Adhesion* edited by L. H. Lee. Plenum Publishing Corporation, (1991): 363-382.
- Baglin, J.E.E. "Interface structure, adhesion and ion beam processing." NATO ASI on Materials and Processes for Surface and Interface Engineering, Dordrecht, The Netherlands, Kluwer Academic Publishers, (1995): 1-39.

Baglin, J.E.E. "Thin film bonding using ion beam techniques- A review." IBM Journal of Research and Development 38 (1994): 413-422.

Bardeen, J., Cooper, L.N. and Schrieffer, J.R. "Theory of superconductivity." Phys. Rev. 108 (1957): 1175.

Barone, A. and Paterno, G. *Physics and Applications of the Josephson Effect*, New York: John Wiley & Sons (1982).

Batson, P.E. "Simultaneous STEM imaging and electron energy-loss spectroscopy with atomic-column sensitivity." Nature 366 (1993): 727-728.

Bednorz, J.G. and Müller, K.A. "Possible high  $T_c$  superconductivity in the Ba-La-Cu-O system." Z. Phys. B 64 (1986): 189-193.

Browning, N.D., Chisholm, M.F. and Pennycook, S.J. "Cell-by-cell mapping of carrier concentrations in high-temperature superconductors." Interface Science 1 (1993): 309-320.

Browning, N.D., Yuan, J. and Brown, L.M. "Determination of the local oxygen stoichiometry in  $\text{YBa}_2\text{Cu}_3\text{O}_{7-\delta}$  by electron energy loss spectroscopy in the scanning transmission electron microscope." Physica C 202 (1992): 12-18.

Buchholz, D.B., Duray, S.J., Schulz, D.L., Marks, T.J., Ketterson, J.B. and Chang, R.P.H. "Surface morphology studies of Y-Ba-Cu-oxide thin films prepared by pulsed organometallic beam epitaxy." Materials Chemistry and Physics 36 (1994): 377-382.

Carter, C.B. and Tietz, L.A. "Interfaces in high-T<sub>c</sub> superconducting oxides." Meeting of the Electron Microscopy Society of America, San Francisco Press, Inc. (1989): 178-179.

Cava, R.J., Hewat, A.W., Hewat, E.A., Batlogg, B., Marezio, M., Rabe, K.M., Krajewski, J.J., Peck Jr., W.F. and Rupp Jr., L.W. "Structural anomalies, oxygen ordering and superconductivity in oxygen deficient  $\text{Ba}_2\text{YCu}_3\text{O}_x$ ." Physica C 165 (1990): 419-433.

Chan, S.-W., Hwang, D.M., Ramesh, R., Sampere, S.M., Nazar, L., Gerhardt, R. and Pruna, P. "Study of Y-Ba-Cu-O thin films grown on single crystal SrTiO<sub>3</sub>: not all high angle grain boundaries destroy  $J_c$ ." AIP Conference Proceedings 200, High T<sub>c</sub> Superconducting Thin Films, American Institute of Physics, (1990): 172-185.

- Chapman, B. *Glow Discharge Processes*, New York: John Wiley & Sons (1980).
- Char, K., Antognazza, L. and Geballe, T.H. "Study of interface resistances in epitaxial  $\text{YBa}_2\text{Cu}_3\text{O}_{7-x}$ /barrier/ $\text{YBa}_2\text{Cu}_3\text{O}_{7-x}$  junctions." *Appl. Phys. Lett.* **65** (1994): 904-906.
- Char, K., Colclough, M.S., Garrison, S.M., Newman, N. and Zaharchuk, G. "Bi-epitaxial grain boundary junctions in  $\text{YBa}_2\text{Cu}_3\text{O}_7$ ." *Appl. Phys. Lett.* **59** (1991a): 733-735.
- Char, K., Colclough, M.S., Lee, L.P. and Zaharchuk, G. "Extension of the bi-epitaxial Josephson junction process to various substrates." *Appl. Phys. Lett.* **59** (1991b): 2177-2179.
- Chaudhari, P., Koch, R.H., Laibowitz, R.B., McGuire, T.R. and Gambino, R.J. "Critical-current measurements in epitaxial films of  $\text{YBa}_2\text{Cu}_3\text{O}_{7-x}$  compound." *Phys. Rev. Lett.* **58** (1987): 2684-2686.
- Chaudhari, P., Mannhart, J., Dimos, D., Tsuei, C.C., Chi, J., Oprysko, M.M. and Scheuermann, M. "Direct measurement of the superconducting properties of single grain boundaries in  $\text{YBa}_2\text{Cu}_3\text{O}_{7-x}$ ." *Phys. Rev. Lett.* **60** (1988): 1653-1656.
- Cheney, K.B. and Pitkin, E.T. "Sputtering at acute incidence." *J. Appl. Phys.* **36** (1965): 3542-3544.
- Chew, N.G. Private Communication, (1992).
- Chew, N.G., Goodyear, S.W., Humphreys, R.G., Satchell, J.S., Edwards, J.A. and Keene, M.N. "Orientation control of  $\text{YBa}_2\text{Cu}_3\text{O}_7$  thin films on MgO for epitaxial junctions." *Appl. Phys. Lett.* **60** (1992): 1516-1518.
- Chiang, Y., Ikeda, J.A.S. and Roshko, A. "Grain boundary segregation and critical current density in  $\text{YBa}_2\text{Cu}_3\text{O}_{7-x}$  superconductors." In *Ceramic Superconductors* edited by M. F. Yan. Westerville, OH: The American Ceramic Society, (1988): 607-617.
- Chisholm, M.F., Pennycook, S.J., Norton, D.P. and Browning, N.D. "Atomic structure of grain boundaries in  $\text{YBa}_2\text{Cu}_3\text{O}_{7-x}$  as observed by Z-contrast imaging." *Interface Science* **1** (1993): 339-346.
- Chu, W.K., Mayer, J.W. and Nicolet, M.A. *Backscattering Spectrometry*, New York: Academic Press (1978).

Cooper, L.N. "Bound electron pairs in a degenerate Fermi gas." Phys. Rev. **104** (1956): 1189-1190.

Daly, K.P., Dozier, W.D., Burch, J.F., Coons, S.B., Hu, R., Platt, C.E. and Simon, R.W. "Substrate step-edge  $\text{YBa}_2\text{Cu}_3\text{O}_7$  rf SQUIDs." Appl. Phys. Lett. **58** (1991): 543-545.

Daumling, M., Sarnelli, E., Chaudhari, P., Gupta, A. and Lacey, J. "Critical current of a high-T<sub>c</sub> Josephson grain boundary junction in high magnetic field." Appl. Phys. Lett. **61** (1992): 1355-1357.

Dayem, A.H. and Wiegand, J.J. "Behavior of thin-film superconducting bridges in a microwave field." Phys. Rev. **155** (1967): 419-428.

de Bruyn Outboter, R. "Superconductivity: discoveries during the early years of low temperature research at Leiden, 1908-1914." IEEE Trans. on Magn. **MAG-23** (1987): 355-370.

Dean, K.A., Buchholz, D.B., Marks, L.D., Chang, R.P.H., Vuchic, B.V., Merkle, K.L., Studebaker, D.B. and Marks, T.J. " $\text{YBa}_2\text{Cu}_3\text{O}_{7-x}$  on MgO films grown by pulsed organometallic beam epitaxy for fabrication of grain boundary junctions." J. of Mat. Res. submitted.

Deutscher, G. and Müller, K.A. "Origin of superconductive glassy state and extrinsic critical currents in high-T<sub>c</sub> oxides." Phys. Rev. Lett. **59** (1987): 1745-1747.

Dimos, D., Chaudhari, P. and Mannhart, J. "Superconducting transport properties of grain boundaries in  $\text{YBa}_2\text{Cu}_3\text{O}_7$  bicrystals." Phys. Rev. B **41** (1990): 4038-4049.

Dimos, D., Chaudhari, P., Mannhart, J. and LeGoues, F.K. "Orientation dependence of grain-boundary critical currents in  $\text{YBa}_2\text{Cu}_3\text{O}_{7-x}$  bicrystals." Phys. Rev. Lett. **61** (1988): 219-222.

Dingley, D.J. "Backscattering in the scanning electron microscope." Proceedings of EMAG 91, Bristol, UK. (1991), 551-558.

Dingley, D.J. and Baba-Kishi, K. "Electron backscatter diffraction in the scanning electron microscope." Microscopy and Analysis (1990): 32-35.

- Dravid, V.P., Zhang, H. and Wang, Y.Y. "Inhomogeneity of charge carrier concentration along the grain boundary plane in oxide superconductors." *Physica C* 213 (1993): 353-358.
- Duray, S.J., Buchholz, D.B., Song, S.N., Richeson, D.S., Ketterson, J.B., Marks, T.J. and Chang, R.P.H. "Pulsed organometallic beam epitaxy of complex oxide films." *Appl. Phys. Lett.* 59 (1991): 1503-1505.
- Early, E.A., Clark, A.F. and Char, K. "Half-integral constant voltage steps in high-T<sub>C</sub> grain boundary junctions." *Appl. Phys. Lett.* 62 (1993): 3357-3359.
- Early, E.A., Steiner, R.L., Clark, A.F. and Char, K. "Evidence for parallel junctions within high-T<sub>C</sub> grain-boundary junctions." *Phys. Rev. B* 50 (1994): 9409-9418.
- Edwards, J.A., Satchell, J.S., Chew, N.G., Humphreys, R.G., Keene, M.N. and Dosser, O.D. "YBa<sub>2</sub>Cu<sub>3</sub>O<sub>7</sub> thin-film step junctions on MgO substrates." *Appl. Phys. Lett.* 60 (1992): 2433-2435.
- Ekin, J.W. "Offset criterion for determining superconductor critical current." *Appl. Phys. Lett.* 55 (1989): 905-907.
- Ekin, J.W., Braginski, A.I., Panson, A.J., Janocko, M.A., Capone II, D.W., Zaluzec, N.J., Flandermeyer, B., de Lima, O.F., Hong, M., Kwo, J. and Liou, S.H. "Evidence for weak link and anisotropy limitations on the transport critical current in bulk polycrystalline Y<sub>1</sub>Ba<sub>2</sub>Cu<sub>3</sub>O<sub>x</sub>." *J. Appl. Phys.* 62 (1987): 4821-4828.
- Eom, C.B., Marshall, A.F., Suzuki, Y., Boyer, B., Pease, R.F.W. and Geballe, T.H. "Absence of weak-link behaviour in Y<sub>1</sub>Ba<sub>2</sub>Cu<sub>3</sub>O<sub>x</sub> grains connected by 90 [010] twist boundaries." *Nature* 353 (1991): 544-547.
- Eom, C.B., Phillips, J.M., Marshall, A.F. and Geballe, T.H. "Microstructure and transport properties of various 90° grain boundaries in YBa<sub>2</sub>Cu<sub>3</sub>O<sub>7</sub> thin films." *Interface Science* 1 (1993): 267-286.
- Field, M.B., Cai, X.Y. and Larbalestier, D.C. "Transport properties across individual grain boundaries in melt-textured YBa<sub>2</sub>Cu<sub>3</sub>O<sub>6+x</sub> bi-crystals." *preprint* (1992): 1479-1482.
- Field, M.B., Pashitski, A., Polyanskii, A., Larbalestier, D.C., Parikh, A.S. and Salama, K. "Experimental evidence for electromagnetic coupling inhomogeneity along the grain boundary plane in high angle melt-textured YBa<sub>2</sub>Cu<sub>3</sub>O<sub>6+x</sub>

bicrystals." to be published IEEE Transactions on Applied Superconductivity (1995).

Fleshler, S., Kwok, W.K., Welp, U., Vinokur, V.M., Smith, M.K., Downey, J. and Crabtree, G.W. "Anisotropy and Lorentz-force dependence of twin-boundary pinning and its effect on flux-lattice melting in single-crystal  $\text{YBa}_2\text{Cu}_3\text{O}_{7-\delta}$ ." Phys. Rev. B 47 (1993): 14448-14461.

Froehlich, O.M., Schulze, H., Beck, A., Mayer, B., Alff, L., Gross, R. and Huebener, R.P. "Analysis of the critical current density in grain boundary Josephson junctions on a nanometer scale." Appl. Phys. Lett. 66 (1995): 2289-2291.

Fulton, T.A., Dunkleberger, L.N. and Dynes, R.C. "Quantum interference properties of double Josephson junctions." Phys. Rev. B 6 (1972): 855-875.

Gao, Y., Merkle, K.L., Bai, G., Chang, H.L.M. and Lam, D.J. "Structure and composition of grain boundary dislocation cores and stacking faults in MOCVD-grown  $\text{YBa}_2\text{Cu}_3\text{O}_{7-x}$  thin films." Physica C 174 (1991a): 1-10.

Gao, Y., Merkle, K.L., Bai, G., Chang, H.L.M. and Lam, D.J. "[001] tilt grain boundaries in  $\text{YBa}_2\text{Cu}_3\text{O}_{7-x}$  thin films." Ultramicroscopy 37 (1991b): 326-340.

Giaever, I. "Electron tunneling between two superconductors." Phys. Rev. Lett. 5 (1960): 464-466.

Giess, E.A., Sandstrom, R.L., Gallagher, W.J., Gupta, A., Shinde, S.L., Cook, R.F., Cooper, E.I., O'Sullivan, E.J.M., Roldan, J.M., Segmuller, A.P. and Angilelio, J. "Lanthanide gallate perovskite-type substrates for epitaxial, high-T<sub>c</sub> superconducting  $\text{Ba}_2\text{YCu}_3\text{O}_{7-x}$  films." IBM Journal of Research Development 34 (1990): 916-925.

Gross, R. "Grain boundary Josephson junctions in the high temperature superconductors." In *Interfaces in superconducting systems* edited by S. L. Shinde and D. Rudman. New York: Springer Verlag, (1992): 176-209.

Gross, R., Chaudhari, P., Dimos, D., Gupta, A. and Koren, G. "Thermally activated phase slippage in high-T<sub>c</sub> grain boundary Josephson junctions." Phys. Rev. Lett. 64 (1990): 228-231.

Gross, R., Kaplan, S.J., Chi, J. and Dimos, D. Unpublished

Gyorgy, E.M., van Dover, R.B., Schneemeyer, L.F., White, A.E., O'Bryan, H.M., Felder, R.J., Waszczak, J.V., Rhodes, W.W. and Hellman, F. "Sharp angular sensitivity of pinning due to twin boundaries in  $\text{Ba}_2\text{YCu}_3\text{O}_7$ ." Appl. Phys. Lett. 56 (1990): 2465-2467.

Hollmann, E.K., Vendik, O.G., Zaitsev, A.G. and Melekh, B.T. "Substrates for high-T<sub>c</sub> superconductor microwave integrated circuits." Superconductor Science and Technology 7 (1994): 609-622.

Hwang, D.M., Ravi, T.S., Ramesh, R., Chan, S.-W., Chen, C.Y., Nazar, L., Wu, X.D., Inam, A. and Venkatesan, T. "Application of a near coincidence site lattice theory to the orientations of  $\text{YBa}_2\text{Cu}_3\text{O}_{7-x}$  grains on (001) MgO substrates." Appl. Phys. Lett. 57 (1990): 1690-1692.

IJsselsteijn, R.P.J., Hilgenkamp, J.W.M., Eisenberg, M., Vittoz, C., Flokstra, J. and Rogalla, H. "Bi-epitaxial template grain boundaries with different in-plane angles on (100) MgO substrates." Journal of Alloys and Compounds 195 (1993): 231-234.

Ivanov, Z.G., Nilsson, P.Å., Winkler, D., Alarco, J.A., Claeson, T., Stepansov, E.A. and Tzalenchuk, A.Y. "Weak links and dc SQUIDs on artificial nonsymmetrical grain boundaries in  $\text{YBa}_2\text{Cu}_3\text{O}_{7-\delta}$ ." Appl. Phys. Lett. 59 (1991a): 3030-3032.

Ivanov, Z.G., Nilsson, P.A., Winkler, D., Bronsson, G., Claeson, T., Stepansov, E.A. and Tzalenchuk, A.Y. "YBa<sub>2</sub>Cu<sub>3</sub>O<sub>7</sub> DC-SQUIDs on Y-ZrO<sub>2</sub> Bicrystals." IV. International Conference on Superconducting and Quantum Effect Devices and their Applications, Berlin, Germany, (1991b): 42-45.

Jia, C.L., Kabius, B., Urban, K., Herrmann, K., Cui, G.J., Schubert, J., Zander, W., Braginski, A.I. and Heiden, C. "Microstructure of epitaxial YBa<sub>2</sub>Cu<sub>3</sub>O<sub>7</sub> films on step edge SrTiO<sub>3</sub> substrates." Physica C 175 (1991): 545-554.

Jia, C.L., Kabius, B., Urban, K., Herrmann, K., Schubert, J., Zander, W. and Braginski, A.I. "The microstructure of epitaxial YBa<sub>2</sub>Cu<sub>3</sub>O<sub>7</sub> films on steep steps in LaAlO<sub>3</sub> substrates." Physica C 196 (1992): 211-226.

Jia, C.L. and Urban, K. "Structure of grain boundaries in YBa<sub>2</sub>Cu<sub>3</sub>O<sub>7</sub> thin-film step-edge junctions." Interface Science 1 (1993): 291-308.

Jirmanus, M.N. "Introduction to laboratory cryogenics" Janis Research Company. (1990).

- Jorgensen, J.D., Beno, M.A., Hinks, D.G., Soderholm, L., Volin, K.J., Hitterman, R.L., Grace, J.D., Schuller, I.K., Segre, C.U., Zhang, K. and Kleefisch, M.S. "Oxygen ordering and the orthorhombic-to-tetragonal phase transition in  $\text{YBa}_2\text{Cu}_3\text{O}_{7-x}$ ." Phys. Rev. B 36 (1987): 3608-3616.
- Jorgensen, J.D., Veal, B.W., Paulikas, A.P., Nowicki, L.J., Crabtree, G.W., Claus, H. and Kwok, W.K. "Structural properties of oxygen-deficient  $\text{YBa}_2\text{Cu}_3\text{O}_{7-\delta}$ ." Phys. Rev. B 41 (1990): 1863-1877.
- Josephson, B.D. "Possible new effects in superconductive tunneling." Physical Letters 1 (1962): 251-253.
- Kroeger, D.M., Choudhury, A., Brynestad, J., R.K., W., Padgett, R.A. and Coghlan, A. "Grain-boundary compositions in  $\text{YBa}_2\text{Cu}_3\text{O}_{7-x}$  from Auger electron spectroscopy of fracture surfaces." J. Appl. Phys. 64 (1988): 331-335.
- Kwok, W.K., Welp, U., Crabtree, G.W., Vandervoort, K.G., Hulscher, R. and Liu, J.Z. "Direct observation of dissipative flux motion and pinning by twin boundaries in  $\text{YBa}_2\text{Cu}_3\text{O}_7$  single crystals." Phys. Rev. Lett. 64 (1990): 966-969.
- Lathrop, D.K., Moeckly, B.H., Russek, S.E. and Buhrman, R.A. "Transport properties of high-angle grain boundary weak links in Y-Ba-Cu-O thin films." Appl. Phys. Lett. 58 (1991): 1095-1097.
- Laval, J.Y., Drouet, M., Delamarre, C., Cabanel, C., Swiatnicki, W. and Leliboux, M. "Atomic structure and local electrical behaviour of grain boundaries in  $\text{YBa}_2\text{Cu}_3\text{O}_{7-x}$ ." Physica C 185-189 (1991): 2449-2450.
- Likharev, K.K. "Superconducting weak links." Reviews of Modern Physics 51 (1979): 101-159.
- Liu, L., Nowak, E.R., Jaeger, H.M., Vuchic, B.V., Merkle, K.L., Buchholz, D.B. and Chang, R.P.H. "High-angle grain boundary junctions in YBCO: Normal-state resistance and  $1/f$  noise." Phys. Rev. B 51 (1995): 16164-16167.
- Liu, L., Zhang, K., Jaeger, H.M., Buchholz, D.B. and Chang, R.P.H. "Normal-state resistance fluctuations in high- $T_c$  cuprate films." Phys. Rev. B 49 (1994): 3679-3682.
- Lu, H.B., Huang, T.W., Wang, J.J., Lin, J., Tu, S.L., Yang, S.J. and Hsu, S.E. "Artificial grain boundaries of  $\text{YBa}_2\text{Cu}_3\text{O}_{7-x}$  on MgO bicrystals." IEEE Transactions on Applied Superconductivity 3 (1993): 2325-2328.

Maeda, H., Tanaka, Y., Fukutomi, M. and Asano, T. "A New high-T<sub>c</sub> Oxide Superconductor Without a Rare Earth Element." Japanese Journal of Applied Physics 27 (1988): L209-L210.

Mannhart, J., Bednorz, J.G., Catana, A., Gerber, C. and Schlom, D.G. "High-T<sub>c</sub> thin films. Growth modes - structure - applications." Materials and Crystallographic Aspects of HTc-Superconductivity, NATO ASI, Erice, Sicily, Italy, Kluwer Academic Publishers, (1993), 453-470.

Marezio, M. "Oxygen stoichiometry in high-T<sub>c</sub> superconductors." Acta Cryst. A 47 (1991): 640-654.

Marshall, A.F. and Eom, C.B. "Microfaceting of 90° [001] tilt boundaries in YBa<sub>2</sub>Cu<sub>3</sub>O<sub>7-x</sub> thin films." Physica C 207 (1993): 239-246.

Mayer, B., Schuster, S., Beck, A., Alff, L. and Gross, R. "Magnetic field dependence of the critical current in YBa<sub>2</sub>Cu<sub>3</sub>O<sub>7-δ</sub> bicrystal grain boundary junctions." Appl. Phys. Lett. 62 (1993): 783-785.

McCumber, D.E. "Effect of ac impedance on dc voltage-current characteristics of superconductor weak-link junctions." J. Appl. Phys. 39 (1968): 3113-3118.

McKernan, S., Norton, M.G. and Carter, C.B. "The 45° grain boundaries in YBa<sub>2</sub>Cu<sub>3</sub>O<sub>7-δ</sub>." J. Mat. Res. 7 (1992): 1052-1059.

Meilikhov, E.Z. "Intergrain boundary asymmetry and the critical current of HTSC ceramics." Physica C 226 (1994): 69-75.

Miller, D.J., Roberts, T.A., Kang, J.H., Talvacchio, J., Buchholz, D.B. and Chang, R.P.H. "'Meandering' grain boundaries in YBa<sub>2</sub>Cu<sub>3</sub>O<sub>7-δ</sub> bi-crystal thin films." Appl. Phys. Lett. 66 (1995): 2561-2563.

Miller, J.H., Gunaratne, G.H., Huang, J. and Golding, T.D. "Enhanced quantum interference effects in parallel Josephson junction arrays." Appl. Phys. Lett. 59 (1991): 3330-3332.

Moeckly, B.H., Lathrop, D.K. and Buhrman, R.A. "Electromigration study of oxygen disorder and grain-boundary effects in YBa<sub>2</sub>Cu<sub>3</sub>O<sub>7-δ</sub> thin films." Phys. Rev. B 47 (1993): 400-417.

Neumann, C., Suzuki, K., Enomoto, Y. and Tanaka, S. "Fabrication of YBaCuO-Josephson-junctions on MgO-substrates damaged by a focused ion beam prior

to film deposition." Japanese Journal of Applied Physics Part 2 **32** (1993a): L727-L729.

Neumann, C., Yamaguchi, K., Hayashi, K., Suzuki, K., Enomoto, Y. and Tanaka, S. "Fabrication of high  $I_c \times R_n$  YBCO-Josephson-junctions on MgO-substrates using a focused-ion-beam system." Physica C **210** (1993b): 138-146.

Norton, M.G. and Carter, C.B. (1990). "Effect of substrate on the early stages of the growth of  $\text{YBa}_2\text{Cu}_3\text{O}_{7-x}$  thin films." Proceedings of Materials Research Society, Boston, MA (1990): 165-170.

Norton, M.G. and Carter, C.B. "The nucleation and heteroepitactic growth of  $\text{YBa}_2\text{Cu}_3\text{O}_{7-\delta}$  thin films on MgO." J. Crys. Growth **110** (1991): 641-651.

Norton, M.G. and Carter, C.B. "Growth of  $\text{YBa}_2\text{Cu}_3\text{O}_{7-\delta}$  thin-films - nucleation, heteroepitaxy, and interfaces." Scanning Microscopy **6** (1992): 385-397.

Norton, M.G. and Carter, C.B. "Observations on the growth of YBCO thin films." In Interfaces in High-T<sub>c</sub> Superconducting Systems edited by S. L. Shinde and D. A. Rudman. New York: Springer-Verlag, (1994): 1-27.

Nücker, N., Fink, J., Fuggle, J.C., Durham, P.J. and Temmerman, W.M. "Evidence for holes on oxygen sites in the high-T<sub>c</sub> superconductors  $\text{La}_{2-x}\text{Sr}_x\text{CuO}_4$  and  $\text{YBa}_2\text{Cu}_3\text{O}_{7-y}$ ." Phys. Rev. B **37** (1988): 5158-5163.

Nücker, N., Romberg, H., Alexander, M. and Fink, J. "Electronic structure studies of high-T<sub>c</sub> cuprate superconductors by electron energy-loss spectroscopy." In Studies of High Temperature Superconductors edited by A. Narlikar. New York: Nova Science Publishers, (1990): 145-194.

Nücker, N., Romberg, H., Xi, X.X., Fink, J., Gegenheimer, B. and Zhao, Z.X. "Symmetry of holes in high-T<sub>c</sub> superconductors." Phys. Rev. B **39** (1989): 6619-6629.

Oh, B., Char, K., Kent, A.D., Naito, M., Beasley, M.R., Geballe, T.H., Hammond, R.H., Kapitulnik, A. and Graybeal, J.M. "Upper critical field, fluctuation conductivity, and dimensionality of  $\text{YBa}_2\text{Cu}_3\text{O}_{7-x}$ ." Phys. Rev. B **37** (1988): 7861-7864.

Olsson, E. Private Communication (1994).

Olsson, E. and Char, K. "The role of interfacial morphology in multilayers based on high-T<sub>c</sub>  $\text{YBa}_2\text{Cu}_3\text{O}_{7-x}$ ." Interface Science **1** (1993): 371-384.

Pashley, D.W. "The growth and structure of epitaxial layers." Materials Research Society, (1985): 67-76.

Putilin, S.N., Antipov, E.V., Chmaissem, O. and Marezio, M. Nature 362 (1993): 226-228.

Ramesh, R., Hwang, D., Ravi, T.S., Inam, A., Barner, J.B., Nazar, L., Chan, S.W., Chen, C.Y., Dutta, B., Venkatesan, T. and Wu, X.D. "Epitaxy of Y-Ba-Cu-O thin films on single-crystal MgO." Appl. Phys. Lett. 56 (1990a): 2243-2245.

Ramesh, R., Hwang, D.M., Barner, J.B., Nazar, L., Ravi, T.S., Inam, A., Dutta, B., Wu, X.D. and Venkatesan, T. "Defect structure of laser deposited Y-Ba-Cu-O thin films on single crystal MgO substrate." J. Mat. Res. 5 (1990b): 704-716.

Ramesh, R., Inam, A., Hwang, D.M., Ravi, T.S., Sands, T., Xi, X.X., Wu, X.D., Li, Q., Venkatesan, T. and Kilaas, R. "The atomic structure of growth interfaces in Y-Ba-Cu-O thin films." J. Mat. Res. 6 (1991): 2264-2271.

Ramos, J., Ivanov, Z.G., Olsson, E., Zarembinski, S. and Claeson, T. "YBa<sub>2</sub>Cu<sub>3</sub>O<sub>7-δ</sub> Josephson junctions on directionally ion beam etched MgO substrates." Appl. Phys. Lett. 63 (1993): 2141-2143.

Rickards, J., Oliver, A. and José-Yacamán, M. "Electron beam damage in high T<sub>c</sub> superconductor materials." Ultramicroscopy. 30 (1989): 425-428.

Rosenthal, P.A., Beasley, M.R., Char, K., Colclough, M.S. and Zaharchuk, G. "Flux focusing effects in planar thin-film grain-boundary Josephson junctions." Appl. Phys. Lett. 59 (1991): 3482-3484.

Rosner, S.J., Char, K. and Zaharchuk, G. "Microstructure of biepitaxial grain boundary junctions in YBa<sub>2</sub>Cu<sub>3</sub>O<sub>7</sub>." Appl. Phys. Lett. 60 (1992): 1010-1012.

Russek, S.E. "Growth, microstructure and transport properties of high T<sub>c</sub> superconducting yttrium barium copper oxide thin films" Ph. D. Thesis, Cornell University. (1990).

Sarma, C., Schindler, G., Haase, D.G., Koch, C.C., Saleh, A.M. and Kingon, A.I. "Measurement of current voltage characteristics of single grain boundaries in melt textured bulk YBa<sub>2</sub>Cu<sub>3</sub>O<sub>x</sub>." Appl. Phys. Lett. 64 (1994): 109-111.

Sarnelli, E. "A two-channel model for transport across high-T<sub>c</sub> bicrystal grain boundary junctions." Interface Science 1 (1993a): 287-290.

- Sarnelli, e., Chaudhari, P., Däumling, M. and Lacey, J.A. "Magnetic field dependence of critical currents of single grain boundary junctions in  $\text{Y}_1\text{Ba}_2\text{Cu}_3\text{O}_{7-\delta}$  superconductor." IEEE Transactions on Applied Superconductivity 3 (1993b): 2329-2332.
- Sarnelli, E., Chaudhari, P. and Lacey, J. "Residual critical current in high Tc bicrystal grain boundary junctions." Appl. Phys. Lett. 62 (1993c): 777-779.
- Sarnelli, E., Testa, G. and Esposito, E. "A two channel model as a possible microscopic configuration of the "barrier" in high-Tc grain boundary junctions." Journal of Superconductivity 7 (1994): 387-390.
- Schieber, M. "Deposition of high temperature superconducting films by physical and chemical methods." Journal of Crystal Growth 109 (1991a): 401-417.
- Schieber, M., Han, S.C., Ariel, Y., Chokron, S., Tsach, T., Maharizi, M., Deutscher, C., Racah, D., Raizman, A. and Rotter, S. "Comparison of thin films of YBCO deposited by physical (laser ablation) and chemical (OMCVD) methods for device applications." Journal of Crystal Growth 115 (1991b): 31-42.
- Schindler, G., Sarma, C., Haase, D.G., Koch, C.C. and Kingon, A.I. "Techniques for the isolation and the electrical characterization of individual grain boundaries in polycrystalline superconductors." Cryogenics (1994): 287-292.
- Schindler, G., Seebacher, B., Kleiner, R., Müller, P. and Andres, K. "Electrical characterisation of single grain boundaries in  $\text{DyBa}_2\text{Cu}_3\text{O}_{7-x}$  ceramics." Physica C 196 (1992): 1-6.
- Schlom, D.G. "Epitaxial growth of high temperature superconductors from the gas phase." International Workshop on Superconductivity, Honolulu, HI, (1992a): 34.
- Schlom, D.G., Anselmetti, D., Bednorz, J.G., Gerber, C. and Mannhart, J. "Defect-mediated growth of YBCO films." Materials Research Society, Boston (1992b): 58-60.
- Shaked, H., Keane, P.M., Rodriguez, J.C., Owen, F.F., Hitterman, R.L. and Jorgensen, J.D. *Crystal structures of the high-Tc superconducting copper-oxides*, Amsterdam: Elsevier Science B.V. (1994).

- Shapiro, S., Janus, A.R. and Holly, S. "Effect of microwaves on Josephson currents in superconducting tunneling." Reviews of Modern Physics (1964): 223-225.
- Sheng, Z.Z., Kiehl, W., Bennett, J., El Ali, A., Marsh, D., Mooney, G.D., Arammash, F., Smith, J., Viar, D. and Hermann, A.M. "New 120 K Tl-Ca-Ba-Cu-O Superconductor." Appl. Phys. Lett. 52 (1988): pp. 1738-1740.
- Shin, D.H., Silcox, J., Lathrop, D.K., Russek, S.E. and Buhrman, R.A. "High-resolution STEM study of grain boundaries in high-T<sub>c</sub> superconducting YBa<sub>2</sub>Cu<sub>3</sub>O<sub>7-x</sub> thin films." Electron Microscopy Society of America, San Francisco, CA, San Francisco Press, Inc. (1989): 174-175.
- Stewart, W.C. "Current-Voltage Characteristics of Josephson Junctions." Appl. Phys. Lett. 12 (1968): 277-280.
- Streiffer, S.K., Lairson, B.M. and Bravman, J.C. "Growth of YBa<sub>2</sub>Cu<sub>3</sub>O<sub>7-x</sub> on vicinally polished MgO substrates." Appl. Phys. Lett. 57 (1990): 2501-2503.
- Tietz, L.A., Carter, C.B., Lathrop, D.K., Russek, S.E. and Buhrman, R.A. "Grain boundaries in YBa<sub>2</sub>Cu<sub>3</sub>O<sub>7-x</sub>." Materials Research Society, Boston, MA (1988): 715-718.
- Traeholt, C., Wen, J.G., Svetchnikov, V. and Zandbergen, H.W. "HREM study of the YBCO/MgO interface on an atomic scale." Physica C 230 (1994a): 297-305.
- Traeholt, C., Wen, J.G., Zandbergen, H.W., Shen, Y. and Hilgenkamp, J.W.M. "TEM investigation of YBa<sub>2</sub>Cu<sub>3</sub>O<sub>7</sub> thin films on SrTiO<sub>3</sub> bicrystals." Physica C 230 (1994b): 425-434.
- Van Duzer, T. and Turner, C.W. *Principles of Superconductive Devices and Circuits*, New York: Elsevier North Holland, Inc. (1981).
- Venables, J.A. and Harland, C.J. "Electron back-scattering patterns - A new technique for obtaining crystallographic information in the scanning electron microscope." Phil. Mag. 27 (1973): 1193-1200.
- Vuchic, B.V., Merkle, K.L., Dean, K.A., Buchholz, D.B., Chang, R.P.H. and Marks, L.D. "Sputter-induced grain boundary junctions in YBa<sub>2</sub>Cu<sub>3</sub>O<sub>7-x</sub> thin films on MgO." J. Appl. Phys. (1995a): 2591-2594.
- Vuchic, B.V., Merkle, K.L., Funkhouser, J.W., Buchholz, D.B., Dean, K.A., Chang, R.P.H. and Marks, L.D. "YBa<sub>2</sub>Cu<sub>3</sub>O<sub>7-x</sub> 45° [001] tilt grain boundaries induced

by controlled low-energy sputtering of MgO substrates: transport properties and atomic-scale structure." to be published in IEEE Transactions on Applied Superconductivity (1995b).

Wang, Z.L., Kontra, R., Kroeger, D.M., Goyal, A. and Williams, R.K. "Interface and grain boundary structures in  $\text{YBa}_2\text{Cu}_3\text{O}_{7-x}$  and  $\text{YBa}_2\text{Cu}_3\text{O}_8$  materials." Interface Science 1 (1993): 321-338.

Welp, U., Gardiner, T., Gunter, D., Fendrich, J., Crabtree, G.W., Vlasko-Vlasov, V.K. and Nikitenko, V.I. "Magneto-optical study of twin boundary pinning in  $\text{YBa}_2\text{Cu}_3\text{O}_{7-\delta}$ ." Physica C 235 (1994): 241-244.

Welp, U., Kwok, W.K., Crabtree, G.W., Vandervoort, K.G. and Liu, J.Z. "Magnetic measurements of the upper critical field of  $\text{YBa}_2\text{Cu}_3\text{O}_{7-\delta}$  single crystals." Phys. Rev. Lett. 62 (1989): 1908-1911.

Wolf, D. and Merkle, K.L. "Correlation between the structure and energy of grain boundaries in metals." In *Materials Interfaces Atomic-level structure and properties* edited by D. Wolf and S. Yip. London: Chapman & Hall, (1992).

Wu, M.K., Ashburn, J.R., Torng, C.J., Hor, P.H., Meng, R.L., Gao, L., Huang, Z.J., Wang, Y.Q. and Chu, C.W. "Superconductivity at 93 K in a new mixed-phase Y-Ba-Cu-O compound system at ambient pressure." Phys. Rev. Lett. 58 (1987): 908-910.

Zandbergen, H.W., Fu, W.T., de Jong, L.J. and van Tendeloo, G. "Electron microscopy study of grain boundaries in 1-2-3 superconductors." Cryogenics 30 (1990): 628-632.

Zhu, Y., Corcoran, Y.L. and Suenaga, M. "Grain boundary chemistry and grain boundary dislocations in bulk  $\text{YBa}_2\text{Cu}_3\text{O}_{7-x}$ ." Interface Science 1 (1993a): 361-370.

Zhu, Y., Wang, Z.L. and Suenaga, M. "Grain-boundary studies by the coincident-site lattice model and electron-energy-loss spectroscopy of the oxygen K edge in  $\text{YBa}_2\text{Cu}_3\text{O}_{7-x}$ ." Phil. Mag. A 67 (1993b): 11-28.



3 5556 021 657 358